ANALYSIS OF DATA FROM THE PLASMA COMPOSITION EXPERIMENT ON THE INTERNATIONAL SUN-EARTH EXPLORER (ISEE 1)

O.W. Lennartsson
Lockheed Missiles & Space Company, Inc.
Research and Development Division
3251 Hanover Street
Palo Alto, CA 94304

May 1994
Final Report
Contract NAS5-33047

Prepared for:
Goddard Space Flight Center
Greenbelt, MD 20771

1. Report No. CR-189353	2. Government Accession No.	3. Recipient's Catalog No.
4. Title and Subtitle ANALYSIS OF DATA FROM THE PLASMA COMPOSITION EXPERIMENT ON THE INTERNATIONAL SUN-EARTH EXPLORER (ISEE 1)		5. Report Date 5/10/94
		6. Performing Organization Code
7. Author(s) O.W. Lennartsson		8. Performing Organization Report No. F254279
9. Performing Organization Name and Address Lockheed Missiles & Space Company, Inc. Research and Development Division 3251 Hanover Street Palo Alto, CA 94304		10. Work Unit No.
		11. Contract or Grant No. NAS5-33047
		13. Type of Report and Period Covered
12. Sponsoring Agency Name and Address NASA/ Goddard Space Flight Center Greenbelt, Maryland 20771 Technical Officer: G.D. Bullock, Code 602		Draft Final Report 1 Jan 90 - 31 May 94
		14. Sponsoring Agency Code

15. Supplementary Notes

3|c 88

16. Abstract

The Lockheed Plasma Composition Experiment on the ISEE 1 spacecraft has provided one of the largest and most varied sets of data on Earth's energetic plasma environment, covering both the solar wind, well beyond the bow shock, and the near-equatorial magnetosphere to a distance of almost 23 earth radii. This report is an overview of the last four years of data analysis and archiving.

The archiving for NSSDC includes most data obtained during the initial 28-month of instrument operation, from early November 1977 through the end of February 1980 ("prime period"). The data products are a combination of spectra (mass and energy-angle) and velocity moments. A copy of the Data User's Guide and examples of the data products are attached (Appendix A).

The data analysis covers three major areas: (1) solar wind ions upstream and downstream of the dayside bowshock, especially He^{++} ions, (2) terrestrial ions flowing upward from the auroral regions, especially H^+, O^+ and He^+ ions, and (3) ions of both solar and terrestrial origins in the tail plasma sheet and lobe regions. Copies of publications are attached (Appendix B).

17. Key Words (Selected by Author(s)) Ion Composition, Magnetotail, Tail Lobes, Plasma Sheet, Ion Flows, Auroral Acceleration, Energetic Ions, Solar Wind, Bow Shock	18. Distribution Statement

19. Security Classif. (of this report) Unclassified	20. Security Classif. (of this page) Unclassified	21. No. of Pages 196 *	22. Price*

*For sale by the Clearinghouse for Federal Scientific and Technical Information. Springfield, Virginia 22151.

* including attachments

PREFACE

This report is an overview of science and data archiving results obtained with the Lockheed Plasma Composition Experiment on the International Sun-Earth Explorer One (ISEE 1) spacecraft since January of 1990. The experiment measures the differential flux of positive ions in the energy range from near 0 eV to approximately 18 keV per unit charge. In contrast to the more conventional electrostatic particle analyzers flown on many spacecraft, this experiment has the capability to select the ions to be measured by selecting their mass per unit charge. Relatively few experiments of this type have been flown to date, and no other such experiment has provided the same variety of data in vastly different regions of space.

The science studies reported here have utilized data from both sources of magnetospheric plasmas, namely the solar wind near Earth's bow shock and the high-latitude region of ion outflow from Earth's ionosphere, as well as very extensive data from the confluence region of solar and terrestrial plasmas in Earth's magnetic tail, almost as far out as 23 R_E.

A major effort has been devoted to the preservation and dissemination of data from this experiment by converting more than two years of measurements into various physical quantities and depositing those in the National Space Science Data Center.

TABLE OF CONTENTS

1. INTRODUCTION

This is the final report by Lockheed Missiles & Space Company, Inc., Research and Development Division, to the National Aeronautics & Space Administration, Goddard Space Flight Center, under a contract to process, analyze and interpret data from the Lockheed Plasma Composition Experiment on the International Sun-Earth Explorer One (ISEE 1) spacecraft. The purpose of this report is to review the principal results obtained since 1 January 1990, the starting date of this contract, and to provide a bibliography of scientific papers based on data from this instrument. In addition to the bibliography, which is limited to papers published under this contract, the report also has a more general list of relevant papers from the scientific literature, numbered according to the order of referencing in the text.

1.1 Data Archiving

A major portion of Lockheed's efforts under this contract has been devoted to the archiving of data at the NSSDC under the guidelines of the Preservation and Archiving of Explorer Satellite Data, originally proposed by NSSDC and NASA/Goddard Space Flight Center in December of 1986. The necessary computer code was developed in 1990, and the actual production and delivery of data took place in 1991. Because of unexpected reductions in NASA's funding of this contract in 1991, the scientific efforts had to be essentially abandoned that year in order to complete this archiving for the minimum data period ending 1 March 1980 (end of "Prime" period; see below). These funding reductions also made it necessary to choose magnetic tapes as the archival medium, instead of an optical disc, as had been planned.

1.2 Guest Investigator Support

Although the original work statement for this contract did not specifically require support for ISEE Guest Investigations, such a requirement was implicitly created with the issuance by NASA Headquarters of a Research Announcement under its Space Physics Guest Investigator Program in March of 1990 (NRA-90-OSSA-9). In fact, two of the winning proposals were prepared under the assumption that this contract would provide basic data processing support during the three-year duration of the proposed research, beginning in the Spring of 1991. Despite a small ($15,000) augmentation made available for this purpose by the Headquarters' Operating Satellites Office in January 1992, the unexpected ending of ISEE Project support in 1991, even before fully funding this contract for that same year, made it necessary to revise the spending profile and request no-cost extensions. The problem was greatly alleviated by the fact that one of the Guest Investigations could successfully rely in large part on the newly completed archival data set, thereby avoiding a severe conflict.

2. BRIEF DESCRIPTION OF THE EXPERIMENT

The ISEE 1 spacecraft (along with the ISEE 2) was launched on October 22, 1977, into an orbit with apogee at almost 23 R_E (geocentric), perigee at about 300 km altitude, an inclination of 29°, and an orbital period of 57 hours. It was placed in a spinning mode with the axis nearly perpendicular to the solar ecliptic plane and with a period of approximately 3 seconds.

The Lockheed Plasma Composition Experiment on the ISEE 1 is one of a family of instruments using the same type of ion optics and covering nearly the same range of energies (0 eV/e to about 17 keV/e) which have also been flown on GEOS 1 and 2, DE 1 and AMPTE/CCE [1]. The ISEE 1 instrument consists of two nearly identical mass spectrometers with the respective fields of view centered 5° above and 5° below the spin plane, that is about 5° above and below the solar ecliptic plane. Most of the results reported here, including all of the latest data archiving

products, have been derived from one and the same of these, the one looking below the spin plane (seeing ions moving upward). The other spectrometer was often operated in a special low-energy mode for continuous monitoring of the "cold" component of the magnetospheric plasmas, and it failed much earlier in the mission (mid 1978).

The field of view of each spectrometer is about 10° wide along the spin plane, and some 10° to 50° wide transverse to this plane, being the widest at the low energy end (due to preacceleration) and gradually decreasing toward 10° with increasing energy. Information on the instantaneous pitch angles (at center of field of view) is provided by the ISEE 1 Fluxgate Magnetometer [2].

Each spectrometer consists of an electrostatic analyzer to select energy per charge, followed by a combined electrostatic and magnetic analyzer to select mass per charge. Both analyzer sections have particle detectors, so at each energy setting the experiment provides both the total ion flux and the partial flux at a selected mass per charge. On ISEE 1 each combination of energy and mass is maintained for at least 1/16 sec in high telemetry bit rate and 1/4 sec in low (normal) bit rate. Different combinations are stepped through in a cyclic fashion according to patterns controlled by a random access memory which is programmable from the ground. The various ISEE 1 patterns, or "modes", require anywhere from 1 to 20 minutes to complete, depending on the predicted location of the spacecraft. Modes used inside the magnetosphere usually take the longest.

The mass selections almost always include one that blocks all ions from reaching the second detector, allowing intermittent measurements during each cycle of the noise associated with penetrating radiation. These measurements are later used to correct the count rates of mass analyzed ions. The total count rate in the first detector is not corrected this way, but this detector is much less susceptible to penetrating radiation because of its small size (spiraltron).

The maximum energy range of the ISEE 1 instrument is 0 eV/e (or spacecraft potential) to 17.9 keV/e, divided into 32 contiguous channels, although only a subset of these may be used in a given mode. In data used here, the lowest channel, from 0 eV/e to about 100 eV/e, is limited to energies above 10 eV/e by an RPA (retarding potential analyzer) in the entrance. That same RPA is otherwise used to provide "cold plasma" data from 0 to 100 eV/e (retarding within the lowest channel), a function that was originally reserved for one of the two spectrometers, but later was made part of many standard scan cycles, in order to accommodate such measurements with a single spectrometer. Because of measurement uncertainties associated with spacecraft charging and plasma convection, the lowest energy channel is treated separately when calculating velocity moments. Data from the highest energy channel (above 16 keV/e) are normally excluded altogether from moment calculations, because of a slight variation over time of the mass response of the ISEE 1 instrument in that channel. The numerical procedures used for weighting and summing counts from the various energy channels are such that the velocity moments correspond to an energy range of either 100 eV/e to 16 keV/e (standard tool in most studies) or 10 eV/e to 100 eV/e (used in a few studies), the latter assuming no spacecraft charging.

3. ARCHIVAL DATA FOR THE NSSDC

Data from the Lockheed Plasma Composition Experiment on the ISEE 1 have been archived at the NSSDC in several different formats at different times, most recently in 1991. These last data have the NSSDC index numbers 77-102A-12I (ASCII magnetic tape files) and 77-102A-12J (hardcopy plots). Only a brief description is provided in this section; a complete data user's guide is attached to this report, along with copies of "user-friendly" command files for magnetic tape reading and copying (VAX/VMS) provided for the convenience of the NSSDC and its customers (Appendix A).

The archived data cover the first 28 months of the mission, up through 3/1/80, that is the so called "prime period" of ISEE-1 and -2 investigations (while most experiments were still working).

The format and (variable) time resolution are based on the energy-mass cycle time of the instrument, which varies between about 1 minute and 20 minutes, depending on mode of operation and on the telemetry rate (high or low). The format is specifically designed to answer the most common types of question asked by other ISEE investigators over the years, such as:

What is the local ion composition during time interval T1 - T2?

Is this plasma rich in solar He^{++} ions or terrestrial O^+ ions?

Ion beams are observed by our experiment. Do they contain O^+ ions?

To interpret our flow measurements we need to know the average ion mass.

We observe this plasma wave feature. Can it be due to heavy ions?

In addition, the compact size and extensive time and space coverage (see figure) make the data well suited for large-scale statistical studies. The format may be described briefly as follows:

Each calendar day has five separate ASCII files, named according to date and content, as for example MD78142.DAT, MC78142.DAT, etc. Three of these contain mass-resolved data, with a time resolution defined by the complete instrument cycle (at most 20 minutes), and one contains data from a "total ion" counter (assuming all protons), with a time resolution defined by the energy-spin-angle cycle (usually about 2 minutes long). All these files have their own set of spacecraft ephemeris and contain magnetic field data derived from the ISEE-1 magnetometer [2]. The fifth file is a small auxiliary file ("EX-file") with only ephemeris data to facilitate the labeling of plots. Each file can be viewed on a video screen set at a width of 132 characters, or output on a standard line printer.

One of the mass-resolved files contains velocity moments up to second order for H^+, He^{++}, He^+, and O^+ ions, calculated two different ways, as described below, and covering the energy ranges 10 eV/e - 100 eV/e (density only) and 100 eV/e - 16 keV/e. Each moment has a statistical uncertainty (standard deviation) associated with it, calculated with standard formulas for the propagation of counting statistics (see [3], pp. 56-64), including the uncertainty in background subtraction [4]. This is the principal file providing relative ion composition ("MD-file").

The second file ("MC") contains spin-averaged energy spectra of the same four ions plus O^{++} ions, covering the energy range 10 eV/e - 17.9 keV/e in 32 energy channels, as well as information about the peak count rate in each channel during each energy-mass scan cycle. This information includes the time (in seconds) and spin angle of the peak, the maximum rate, and the angular range of count rates greater than 1/3 of the maximum rate ("full peak width at 1/3 of maximum"). This is the best file to use for studying the composition and probable origin of ion beams or flows, for example.

The third file ("MS") contains mass spectra in four energy ranges, whenever the instrument cycle included complete scans of the mass-per-charge range (from less than 1 amu/e to about 150 amu/e). Most cycles did include at least a few such scans.

The "total ion" file ("ED") contains velocity moments up to second order as well, assuming that the counts are due entirely to H^+ ions, but only for the 100 eV to 16 keV range. Since H^+ ions usually dominate the count rate (proportional to the square root of charge/mass at given energy), this file typically provides an approximate and nearly continuous measure of the H^+ at higher time resolution.

These ASCII files with numbers are complemented with hardcopy plots (current NSSDC index number 77-102A-12J) showing selected moments as a function of time, including the total ion pressure perpendicular to the local magnetic field, as well as the magnetic pressure and field direction angles.

This 28-month data set occupies 545 megabytes and resides on six 6250 bpi magnetic tapes produced with the VAX/VMS backup procedure. The NSSDC has been furnished with VAX/VMS command procedures for easy transfer of any number of days of data to disk and subsequent transfer to new tapes using the more universal COPY procedure. The NSSDC has the complete User's Guide for these data, both on tape and in hardcopy format (see Appendix A).
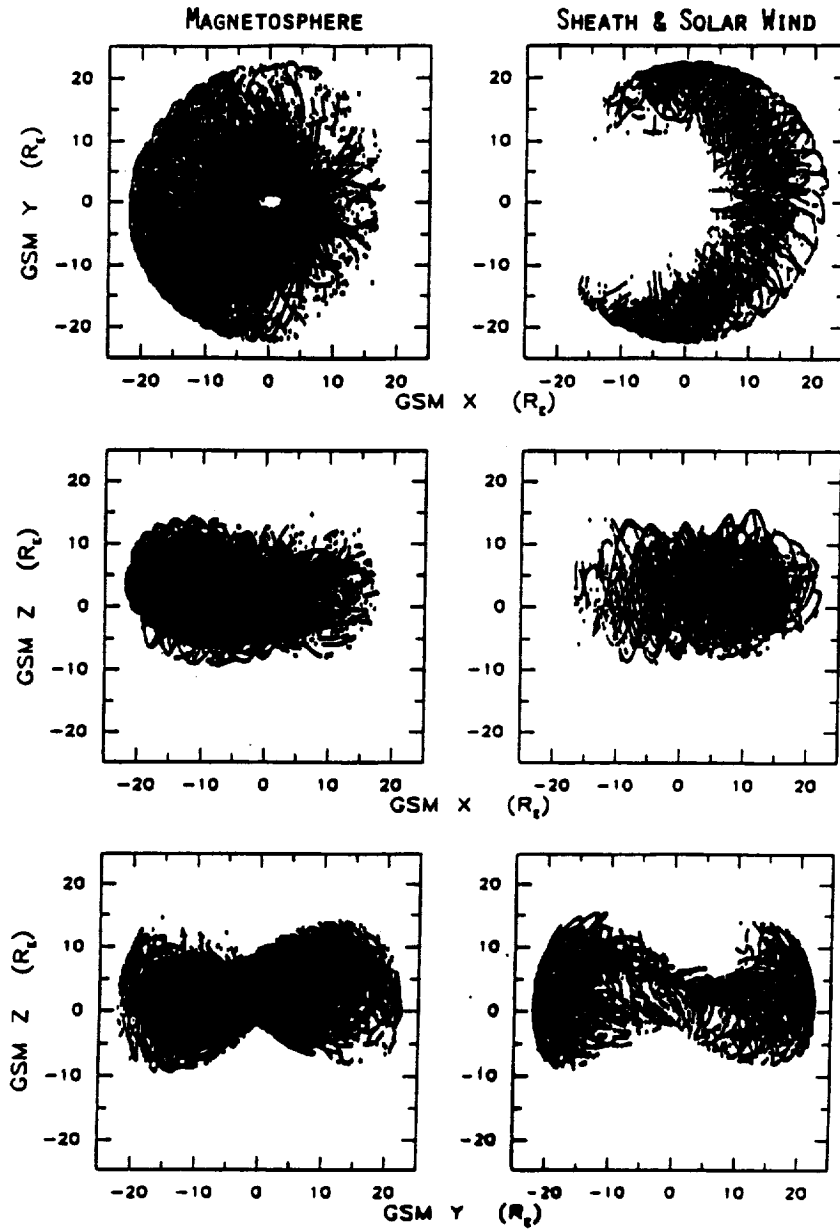
Spatial coverage of archival data (in GSM coordinates). Solar wind data (right panels) have been included only when obtained in the same types of instrument operating mode used in the magnetosphere (complete spin-angle coverage). The "butterfly" patterns in the bottom panels reflect the pivoting motion of the GSM system around the sun-earth line (only figure in main part of this document).

4

3.1 Velocity Moment Calculations

To calculate full three-dimensional velocity moments from the raw ISEE 1 data, the ion fluxes measured within the near-ecliptic field of view have been extrapolated to other angles using either of two sets of approximating assumptions:

1. The principal ion flow is parallel to the solar ecliptic plane and the ion fluxes have rotational symmetry around the flow vector, regardless of the magnetic field orientation. The direction of the flow vector within this plane is determined by the measured flow within the instrument field of view. The single angular variable in this case is divided among twelve 30° spin-angle bins, roughly approximating the inherent angular resolution of the ISEE 1 instrument in normal low-bit-rate operation.

2. Fluxes are gyrotropic (independent of gyration angle) over the sampled range of pitch angles, and isotropic outside of this range, maintaining the values measured at the smallest and largest pitch angles, respectively. The pitch angles are divided among nine 20° bins. This assumption is only applied to number densities, mean energies, parallel and perpendicular to the magnetic field, and energy densities. It ignores any net bulk flow perpendicular to the magnetic field.

The two sets of assumptions usually provide about the same densities and total mean energies, within statistical uncertainties, but the numbers obtained with 1 are believed to be at least marginally more accurate in most cases, except when it is necessary to separate components parallel and perpendicular to the magnetic field. Although the drift direction in 1 is determined from average fluxes in 30° wide bins, the weighting involved in the integrations usually provides an accuracy much better than 30°. In either case, whenever the energy scans have left some channels unsampled, sometimes every other channel, an interpolation procedure has been employed, essentially assuming a linear variation of the differential flux.

4. BRIEF REVIEW OF SCIENCE EFFORTS

The versatility of the Lockheed Plasma Composition Experiment, including its exceptional sensitivity and flexible operating modes [1], and the extremely large and eccentric orbit of the ISEE 1 spacecraft have combined to create what is arguably the most varied set of space plasma data in existence, and one of the largest as well. This great resource has continued to yield many new and very significant scientific results in the last four years. The varied nature of the data is well represented by the diverse nature of the three main topics of study under this contract: solar wind alpha particles (He^{++}) at Earth's bow shock, plasma waves and ions on auroral magnetic field lines, and plasma sheet and tail lobe ion populations.

4.1 Solar Wind Alpha Particles (He^{++}) at Earth's Bow Shock

The ISEE 1 orbit had its apogee sufficiently high (at nearly 23 R_E geocentric distance) to allow measurements at the interface between the solar wind and Earth's magnetosphere, including the magnetosheath and the bow shock, during virtually all normal solar wind conditions and over a very broad local-time sector. This is in contrast to other spacecraft with similar instruments which have had lower orbits and only encountered this region during times of extremely large solar wind pressure, if at all. In spite of this, data obtained beyond the magnetopause by the Lockheed experiment have not yet been explored very extensively, due primarily to shortage of funds. During the brief (less than two years) period of ISEE Project funding for science under this contract, work in this area was limited to the study of He^{++} ions upstream and downstream of the dayside bowshock. This work was led by Dr. S.A. Fuselier, who had extensive experience with data from the Fast Plasma Experiments (for total ion counts) on ISEE 1 and 2 from his previous

research at the Los Alamos National Laboratory. The research conducted under this contract was a cooperative effort between Lockheed and the LANL.

The He^{++} ions, or alpha particles, are a much smaller component of the solar wind than are the protons (H^+ ions), typically only 3% to 5% of the total ion density, but they are expected to provide important clues in regard to the various plasma processes taking place at the bow shock. One process investigated with the Lockheed data involves the partial reflection of incoming solar wind ions at the bow shock. There were some outstanding questions as to the relative importance of electric and magnetic fields in this reflection process at the quasi-parallel shock, that is a shock configuration where the solar wind magnetic field (the IMF) is nearly parallel to the shock normal (nearly perpendicular to the shock surface). The solar wind He^{++} ions, which have an energy/charge about twice that of protons (about the same bulk velocity) would be far less affected than the protons by the retarding electric field believed present at the shock. They were found to be reflected to about the same extent as the protons, implying that magnetic forces play a large roll also at the quasi-parallel shock, at least when the solar wind Mach number is high. These results are presented in Ref. [5].

A second process studied involves beam-plasma interactions between the reflected protons and the upstream solar wind. The question of main interest here was whether these interactions, in the case of the quasi-parallel shock, were of resonant (resonating with protons) or non-resonant nature. Only non-resonant interactions would affect the He^{++} ions, by heating them. The Lockheed data showed that the He^{++} ions were indeed heated in a manner consistent with non-resonant interactions under certain circumstances, as described in Refs. [6] and [7].

4.2 Plasma Waves and Ions on Auroral Magnetic Field Lines

Although the ISEE 1 and 2 spacecraft were launched into a near-equatorial orbit, the subsequent precession caused the outbound leg of the orbit to traverse the near-earth, high-latitude auroral regions, between about 2 and 7 R_E, after a couple of years. This had not been foreseen during the original planning of the experiment, but was fairly easy to take advantage of by devising special operating modes for the proper orbit segment, beginning in 1980. The resulting data set is in some regards superior to any obtained by polar orbiting spacecraft, since the ISEE orbit was often nearly parallel to the geomagnetic field over distances of several R_E, offering a unique opportunity to study the altitude dependence of the acceleration of outflowing ionospheric ions. Studies in this area have been a cooperative effort between Lockheed and the University of California at Berkeley, comparing the ion data with electric field data from the UCB Double Probe Experiment on ISEE 1.

In one study, led by Dr. C.A. Cattell of the UCB, the objective has been to establish the detailed relationship between upflowing H^+ and O^+ beams and the various possible plasma wave modes during a specific but probably typical event. During this event, which took place while the ISEE 1 was at a geocentric distance of 2.5 to 4.5 R_E, the ion beams were observed associated with large localized quasi-static electric fields (a type often called "shocks"), directed essentially perpendicular to the magnetic field, and with plasma waves identified as current-driven oblique electrostatic cyclotron waves near the H^+, He^+, and O^+ cyclotron frequencies. In addition, the H^+ and O^+ velocity distributions showed evidence of H^+ -O^+ two-stream instability at lower altitudes. The data do not by themselves reveal the exact physical process involved, but the popular interpretation would suggest that the ion acceleration is due to some combination of a net upward component of the quasi-static electric field, the mirroring force of the magnetic field, and the plasma waves. The results are presented and discussed in Ref. [8].

In another study, also led by Dr. Cattell, the objective has been to establish the main long-term, solar-cycle related variations in the auroral acceleration processes, by comparing many events observed both by the ISEE 1 and by the polar orbiting S3-3 spacecraft. As described in Ref. [9], the principal long-term effects, going from solar minimum to solar maximum, have been found to be: (1) a general increase in altitudinal location of regions of magnetic field-aligned electric field,

(2) a possible weakening of this field, (3) an increase in the rate of transverse ion acceleration (transverse to the magnetic field), and (4) an increase in the rate of outflow of O^+ ions.

4.3 Plasma Sheet and Tail Lobe Ion Populations

Since about the mid 1980's the ISEE data analysis at Lockheed has placed the greatest emphasis on Earth's magnetic tail region, for a number of reasons. One is that the ISEE 1 was in that region a very large portion of the time, and the Lockheed experiment was the first ion mass spectrometer to fly there. Actually, the Lockheed ISEE 1 data are still the only extensive ion composition data from the tail, covering the crucial energy range from near 0 eV/e to about 18 keV/e. This is in contrast to the inner magnetosphere, inside of about 9 R_E, where several spacecraft have carried ion mass spectrometers, both before and after. Another reason is that the energy range of the Lockheed experiment appears, most of the time, to cover the bulk of the ions in the tail region, beyond 9 or 10 R_E, as opposed to the relative coverage in the inner magnetosphere, where more energetic (of the order 100 keV) ring current ions have a strong influence on the bulk ion properties. A third reason is that the tail region is probably where some of the most important solar-terrestrial processes are initiated, including the entry of solar wind plasma into the magnetosphere and the generation of auroras and magnetic storms.

This philosophy has continued under this contract, as far as internal Lockheed efforts are concerned. Studies in this area have attempted to make the most complete use possible of the large quantity of data acquired, by making large-scale statistical comparisons between the ion data and widely available geomagnetic and solar indices, especially the auroral electrojet (AE) indices (see Ref. [10] and subsequent data books in that series) and the Ottawa daily index for solar radio flux, the so called F10.7 index. Large-scale comparisons have also been made between the tail ion data and concurrent data on the solar wind plasma and the solar wind magnetic field, the IMF, as made available through the NSSDC OMNI file (see Ref. [11]). These studies have been led by Dr. O.W. Lennartsson.

In one such study the objective has been to try to determine what solar wind parameter, or combination of parameters, has the strongest influence on the concentration of energetic (keV) O^+ ions in the plasma sheet. Preliminary results, reported in Ref. [12], indicate that one of the most important parameters, if not the most imprtant, is the solar wind electric field, that is the field associated with the solar wind flow accross the IMF, defined by the negative cross product between the flow velocity and magnetic field vectors, $-v \times B$. The peculiar aspect of this result is that the O^+ concentration is very strongly positively correlated with the average magnitude of this field during a couple of hours preceding the plasma sheet measurements, but it does not appear to depend very strongly on the direction of the field. Stated differently, the plasma sheet O^+ density does not seem to depend strongly on the sign of the GSM Z-component of the IMF, which is strange in view of the well-known strong dependence of the AE and other geomagnetic indices on this IMF component. This "paradox" is currently being studied under a NASA/Lockheed SR&T contract.

In a second study the objective has been to try to identify the principal means and route of solar plasma entry into the tail. The results of this study, reported in Ref. [13], indicate that the solar wind enters along slots between the plasma sheet and the tail lobes, convected inward by the electric fringe field of the low latitude magnetopause boundary layer (LLBL) on the tail flanks. This entry appears to take place at all times, and contrary to popular belief, there is no evidence in the combined plasma-sheet-solar-wind data that the entry is generated or even facilitated by the IMF.

In a third study, which has taken advantage of the high sensitivity of the Lockheed instrument, the objective has been to investigate the variation of the ion bulk properties across the boundary between the plasma sheet and the tail lobes. One of the most interesting results, as reported in Ref. [14], is that the density gradient of the H^+ ions is significantly steeper than that of the heavier ions, especially when compared with the O^+ gradient. An attempt has been made to

model this in simple terms of the different characteristic gyroradii of the different ions, and some agreement is achieved that way, although only partially. This feature, along with some other results in [14], lends further support to the arguments in [13] that solar ions enter from the tail flanks.

In a fourth study, the large set of ISEE 1 plasma sheet ion composition data has been utilized to determine whether the O^+ ions may have a feedback effect on auroral substorms, as has been suggested in the literature. According to this idea, which has become increasingly popular in recent years, the O^+ ions, because of their very large mass/charge, may have a destabilizing effect on the tail current sheet (center plane of plasma sheet), where the magnetic field is weak, causing tearing-mode perturbations that may trigger or enhance the substorms. To address this issue, the ion data have been compared very thoroughly with both geomagnetic and solar indices. The statistical correlations between the ion data and these indices, and between the different indices, all point in the same direction: there is probably no feedback specific to the O^+ ions, in spite of the fact that they often contribute most of the ion mass density in the tail current sheet. This result, perhaps somewhat disappointing to many, but nevertheless very important, is reprted in Ref. [15].

The last three studies have been supported for the most part under the NASA Guest Investigator Program, but this contract has provided important support for computer programming and basic data processing. The last two studies have been based entirely on the archival data produced under this contract, with some additional support from this contract to produce the required analysis programs.

5. NEW TECHNOLOGY

The analysis of data from the Lockheed Plasma Composition Experiment on the ISEE 1 spacecraft has been carried out with conventional tools and methods and has not led to the development of new technology. The data from the instrument, although refined in the final archival formats, have the same basic form that has been utilized with spaceborne electrostatic particle analyzers for decades. The only fundamental difference between these and most earlier data lies in the selection of ions by mass per charge. Our knowledge about the ion mass has so far been utilized for scientific purposes only, and no technological application has yet been discovered.

6. CONCLUSIONS

Twelve years after the end of data collection by the Lockheed Plasma Composition Experiment on the ISEE 1, the data continue to yield new results of fundamental importance to solar-terrestrial physics. This is in part an attestation to the scientific importance of the ISEE Mission as a whole, but it certainly affirms the significance of this particular experiment, and the significance of ion composition data.

Of all the unexpected results obtained with spaceborne ion mass spectrometers, the mere fact that Earth contributes significantly to the energetic plasmas (first reported in [16]) has probably had the greatest mental impact. Especially the results obtained from near-earth polar orbiting spacecraft have encouraged some to postulate that the earth is even the principal source [17]. The Lockheed ISEE 1 data have indeed confirmed the omnipresent nature of energetic terrestrial ions, in particular the O^+ ions, but they have also helped to paint a more balanced picture, one in which the ions of solar origin still have a prominent position. Data obtained in the tail, beyond 10 R_E, imply that the solar source may supply the larger part of the vast plasma sheet most of the time, if not all the time [14], and therefore act as the more important source of magnetospheric plasma by sheer volume.

7. RECOMMENDATIONS

During its approximately 4 1/2 years of operation (until March 20, 1982) the Lockheed Plasma Composition Experiment on ISEE 1 gathered a very large and in many respects entirely unique set of data on the ion populations with energies in the 0-18 keV/e range. Due to the orbital characteristics of the ISEE 1 spacecraft, data have been obtained in regions of space where no ion mass spectrometer had been flown before, and the few such instruments that have since been flown in the same general regions, especially the geomagnetic tail beyond 10 R_E, have either been designed for much more energetic ions or have failed to provide useful data.

Barely more than half (2 1/3 years) of these Lockheed data were archived at the NSSDC by the end of the three-spacecraft ISEE mission, both because of the emphasis on the first two years of data by the ISEE Project and because of rapidly dwindling funding towards the end of the mission. In light of the very uncertain future of new NASA missions, including the GGS/Polar, it would seem to be prudent on the part of NASA to make some additional funding available to Lockheed to complete this archiving, funding that would have to be very modest by the standards that apply to new missions. It is therefore recommended by this author that such funding be made available, and that NASA acts on this matter very soon, before the Lockheed magnetic tape records of the raw ISEE 1 data risk disposal as obsolete in these times of cost savings in the aerospace industry, or otherwise become illegible.

8. REFERENCES

1. Shelley, E.G., R.D. Sharp, R.G. Johnson, J. Geiss, P. Eberhardt, H. Balsiger, G. Haerendel, and H. Rosenbauer, Plasma composition experiment on ISEE-A, *IEEE Trans. Geosci. Electron., GE-16*, 266, 1978.

2. Russell, C.T., The ISEE 1 and 2 fluxgate magnetometers, *IEEE Trans. Geosci. Electron., GE-16*, 239, 1978.

3. Bevington, P.R., *Data Reduction and Error Analysis for the Physical Sciences*, McGraw-Hill, New York, 1969.

4. Lennartsson, W., and R.D. Sharp, A comparison of the 0.1-17 keV/e ion composition in the near equatorial magnetosphere between quiet and disturbed conditions, *J. Geophys. Res., 87*, 6109, 1982.

5. Fuselier, S.A., O.W. Lennartsson, M.F. Thomsen, and C.T. Russell, Specularly reflected He^{2+} at high Mach number quasi-parallel shocks, *J. Geophys. Res., 95*, 4319, 1990.

6. Galvez, M., S.A. Fuselier, S.P. Gary, M.F. Thomsen, and D. Winske, Alpha particle heating in hot diamagnetic cavities, *J. Geophys. Res., 95*, 11975, 1990.

7. Fuselier, S.A., O.W. Lennartsson, M.F. Thomsen, and C.T. Russell, He^{2+} heating at a quasi-parallel shock, *J. Geophys. Res., 96*, 9805, 1991

8. Cattell, C.A., F.S. Mozer, I. Roth, R.R. Anderson, R.C. Elphic, W. Lennartsson, K. Ogilvie, R. Fitzenreiter, and E. Ungstrup, ISEE-1 observations of electrostatic ion cyclotron waves in association with ion beams on auroral field lines from ~ 2.5 to 4.5 R_E, *J. Geophys. Res., 96*, 11421, 1991.

9. Cattell, C.A., T. Nguyen, M. Temerin, W. Lennartsson, and W. Peterson, Effects of solar cycle on auroral particle acceleration, in *Auroral Plasma Dynamics*, Geophysical Monograph 80, American Geophysical Union, 219, 1994.

10. Kamei, T., and H. Maeda, Auroral electrojet indices (AE) for January-June 1978, *Data Book 3*, World Data Center C2 for Geomagn., Kyoto, Japan, April 1981.

11. Couzens, D.A., and J.H. King, Interplanetary medium data book, supplement 3, 1977-1985, Rep. *NSSDC/WDC-A-R&S 86-04*, NASA Goddard Space Flight Cent., Greenbelt, Md., 1986.

12. Lennartsson, W., Solar control of the earth's emission of energetic O^+, *J. Atmospheric and Terrestrial Phys., 53*, 1103, 1991.

13. Lennartsson, W., A scenario for solar wind penetration of Earth's magnetic tail based on ion composition data from the ISEE 1 spacecraft, *J. Geophys. Res., 97*, 19221, 1992.

14. Lennartsson, O.W., Tail lobe ion composition at energies of 0.1 to 16 keV/e: evidence for mass-dependent density gradients, *J. Geophys. Res., 99*, 2387, 1994.

15. Lennartsson, O.W., D.M. Klumpar, E.G. Shelley, and J.M. Quinn, Experimental investigation of possible geomagnetic feedback from energetic (0.1 to 16 keV) terrestrial O^+ ions in the magnetotail current sheet, *J. Geophys. Res., 98*, 19443, 1993.

16. Shelley, E.G., R.G. Johnson, and R.D. Sharp, Satellite observations of energetic heavy ions during a geomagnetic storm, *J. Geophys. Res., 77*, 6104, 1972.

17. Chappell, C.R., T.E. Moore, and J.H. Waite, Jr., The ionosphere as a fully adequate source of plasma for the Earth's magnetosphere, *J. Geophys. Res., 92*, 5896,1987.

ACKNOWLEDGMENTS

BIBLIOGRAPHY

PUBLICATIONS AND PRESENTATIONS 1990-94 (Papers based in large part or entirely on data from the Lockheed Plasma Composition Experiment on the ISEE 1)

1. Publications

Cattell, C.A., F.S. Mozer, I. Roth, R.R. Anderson, R.C. Elphic, W. Lennartsson, K. Ogilvie, R. Fitzenreiter, and E. Ungstrup, ISEE-1 observations of electrostatic ion cyclotron waves in association with ion beams on auroral field lines from ~ 2.5 to 4.5 RE, *J. Geophys. Res., 96,* 11421, 1991.

Cattell, C.A., T. Nguyen, M. Temerin, W. Lennartsson, and W. Peterson, Effects of solar cycle on auroral particle acceleration, in *Auroral Plasma Dynamics,* Geophysical Monograph 80, American Geophysical Union, 219, 1994.

Fuselier, S.A., O.W. Lennartsson, M.F. Thomsen, and C.T. Russell, Specularly reflected He^{2+} at high Mach number quasi-parallel shocks, *J. Geophys. Res., 95,* 4319, 1990.

Fuselier, S.A., O.W. Lennartsson, M.F. Thomsen, and C.T. Russell, He^{2+} heating at a quasi-parallel shock, *J. Geophys. Res., 96,* 9805, 1991

Galvez, M., S.A. Fuselier, S.P. Gary, M.F. Thomsen, and D. Winske, Alpha particle heating in hot diamagnetic cavities, *J. Geophys. Res., 95,* 11975, 1990.

Lennartsson, W., Solar control of the earth's emission of energetic O^+, *J. Atmospheric and Terrestrial Phys., 53,* 1103, 1991.

Lennartsson, W., A scenario for solar wind penetration of Earth's magnetic tail based on ion composition data from the ISEE 1 spacecraft, *J. Geophys. Res., 97,* 19221, 1992.

Lennartsson, O.W., Tail lobe ion composition at energies of 0.1 to 16 keV/e: evidence for mass-dependent density gradients, *J. Geophys. Res., 99,* 2387, 1994.

Lennartsson, O.W., D.M. Klumpar, E.G. Shelley, and J.M. Quinn, Experimental investigation of possible geomagnetic feedback from energetic (0.1 to 16 keV) terrestrial O^+ ions in the magnetotail current sheet, *J. Geophys. Res., 98,* 19443, 1993.

2. Presentations

Fuselier, S.A., Ion composition measurements in the earth's magnetosheath (abstract; invited paper), *Eos Trans. AGU, 71(43),* 1521, 1990.

Huang, C.Y., W. Lennartsson, and L.A. Frank, Low-energy ions in the plasma sheet boundary layer (abstract), *Eos Trans. AGU, 72(44),* Fall Meeting suppl., 424, 1991.

Lennartsson, W., Solar control of the earth's emission of energetic O^+, presented at the COSPAR XXVIII Plenary Meeting in the Hague, the Netherlands, 25 June - 6 July 1990.

Lennartsson, W., Solar wind parameters influencing the magnetospheric content of energetic O^+ (abstract), *Eos Trans. AGU, 71(43),* 1522, 1990.

Lennartsson, W., Tailward flows of solar-wind like plasma in the plasma sheet boundary layer inside of 23 earth radii, presented at the XX General Assembly of the IUGG in Vienna, Austria, 11-24 August 1991.

Lennartsson, W., Tailward flows of solar-wind like plasma in the plasma sheet boundary layer inside of 23 earth radii (abstract), *Eos Trans. AGU, 72(44)*, Fall Meeting suppl., 424, 1991.

Lennartsson, W., Evidence for separation of solar ions by mass in the earth's magnetotail (abstract), *Eos Trans. AGU, 73(43)*, Fall Meeting suppl., 471, 1992.

Lennartsson, W., Correlation of magnetospheric O^+ content with IMF B_Z (abstract), *Eos Trans. AGU, 74(43)*, Fall Meeting suppl., 519, 1993.

Schmidt, W.K.H., and S.A. Fuselier, On solar wind O^{6+} ions reflected off the earth's bow shock (abstract), *Eos Trans. AGU, 71(43)*, 1515, 1990.

APPENDIX A

Data User's Guide and VAX/VMS Command Files

ISEE-1 ION COMPOSITION DATA (10 eV/e to 16 keV/e);
A GUIDE TO READING THE ED-, MD-, MC-, MS-, AND EX-FILES

By O. W. Lennartsson

Lockheed Missiles and Space Company, Inc.
Research and Development
Palo Alto, California

PREFACE

The data and data formats described herein have been produced in cooperation with several people at the Lockheed Research and Development Division, in particular with R. D. Sharp, E. G. Shelley, W. K. Peterson, D. L. Carr, and W. E. Francis

The magnetic fields included here are based on ISEE-1 magnetometer data made available by C. T. Russell of the Institute for Geophysics and Planetary Physics at the University of California, Los Angeles, California. The processing and editing of the magnetometer data are the sole responsibility of the author.

Any questions regarding these data files should be directed to:

Dr. O. W. Lennartsson
Lockheed Missiles and Space Company, Inc.
Research and Development
Dept. 91-20, Bldg. 255
3251 Hanover St.
Palo Alto, CA 94304

Telephone: (415) 424-3259
Telefax: (415) 424-3333
SPAN: LOCKHD::LENN

1. INTRODUCTION

The ISEE-1 spacecraft (along with the ISEE-2) was launched on October 22, 1977, into an orbit with apogee at almost 23 RE (geocentric), perigee at about 300 km altitude, an inclination of 29 deg, and an orbital period of 57 hours. It was placed in a spinning mode with the axis nearly perpendicular to the solar ecliptic plane and with a period of approximately 3 seconds. It reentered almost 10 years later, on September 26, 1987.

The Lockheed Plasma Composition Experiment flown on ISEE-1 is one of a family of instruments using the same type of ion optics and covering nearly the same range of energies (0 eV/e to about 17 keV/e) which have also been flown on GEOS 1 and 2, Dynamics Explorer One, and AMPTE CCE [Shelley et al., IEEE Trans. Geosci. Electron., GE-16, 266, 1978]. The Principal Investigator of the ISEE-1 experiment during its development and during its several years of operation in orbit was R. D. Sharp. In the later phase of data analysis this role was transferred to O. W. Lennartsson. For a review of the first few years of data analysis see Sharp et al. in Energetic Ion Composition in the Earth's Magnetosphere, edited by R. G. Johnson, TERRAPUB, Tokyo, 231, 1983.

The ISEE-1 instrument consists of two nearly identical mass spectrometers with the respective fields of view centered 5 deg above and 5 deg below the spin plane, that is about 5 deg above and below the solar ecliptic plane. Each field of view is 10 deg wide along the spin plane, and 10 to 50 deg wide transverse to this plane, being the widest at the low energy end and gradually decreasing to 10 deg with increasing energy. All data used for this archiving were obtained with one spectrometer, the one viewing below the spin plane. Information on the instantaneous pitch angles is provided by the ISEE-1 Fluxgate Magnetometer [Russell, IEEE Trans. Geosci. Electron., GE-16, 239, 1978].

Each spectrometer consists of an electrostatic analyzer to select energy per charge, followed by a combined electrostatic and magnetic analyzer to select mass per charge. Both analyzer sections have particle detectors, so at each energy setting the experiment provides both the total ion flux and the partial flux at a selected mass per charge. The detector in the energy analyzer is offset from the center path of ions and corresponds to a view direction that is slightly different from the nominal mass spectrometer field of view, being more nearly within the spin plane. To be more specific, the two detectors have about the same size fields of view at all energies, but the "energy detector" central view direction varies, being some 15 deg away from the spin plane on the opposite side of the "mass detector" view direction at near-zero energies, and gradually approaching the spin plane with increasing energy.

Each combination of energy and mass is maintained for at least 1/16 sec in high telemetry bit rate and 1/4 sec in low (normal) bit rate. Different combinations are stepped through in a cyclic fashion according to various patterns controlled by a random access memory which is programmable from the ground. Some patterns, or "modes", may require only a couple of minutes per cycle, others may take 15 to 20 minutes.

The mass selections usually include one that blocks all ions from reaching the second detector, which is a modified Johnston electron multiplier, allowing intermittent measurements of the noise associated with penetrating radiation (mostly MeV electrons and associated bremsstrahlung). These measurements are

later used to correct the count rates of mass analyzed ions. The background count rate in the first detector, which is a so called spiraltron, is generally negligible and is not corrected for.

The maximum energy range is 0 eV/e (or spacecraft potential) to 17.9 keV/e, divided into 32 contiguous channels, but the lowest channel, from 0 eV/e to about 100 eV/e, is normally limited to energies above 10 eV/e by an RPA (retarding potential analyzer) in the entrance. That same RPA is used to provide "cold plasma" data from 0 to 100 eV/e (retarding within the lowest channel) during part of some measurement cycles. Because of measurement uncertainties associated with spacecraft charging and plasma convection, the "cold plasma" data have not been included here. The lowest "hot plasma" channel, the one covering 10 eV/e to 100 eV/e, has been used only sparingly for those same reasons.

All velocity moments, with one exception (see below), use 100 eV/e as the lower energy limit. As far as moments are concerned, the highest energy channel (above 16 keV/e) has not been used either, because of a slight variation over time of the mass peak locations in that channel. The energy range of moments is therefore generally 100 eV/e to (about) 16 keV/e, unless further limited by a particular instrument energy/mass scan mode (see below).

The mass range is from below 1 amu/e to about 150 amu/e, divided into 64 channels, but the most common scan cycles only sample 4 to 5 channels, corresponding to the principal ions, plus a background channel (below 1 amu/e).

2. ARCHIVAL DATA FORMAT

These archival data are a combination of ion data, magnetic field data, and s/c ephemeris, generally sorted by instrument energy/mass scan cycle and placed in five kinds of ASCII files, called the ED-, MD-, MC-, MS-, and EX-files, respectively. There is one set of these files for each day of data, and the date is part of the file names, represented by the last two digits of the year, followed by three digits for the day of the year, as for example ED78057.DAT, etc. The format and content of each kind of file are described in detail in following sections.

The ion data are a combination of velocity moments, calculated two different ways (using two different sets of assumptions about symmetry in velocity space), and energy and mass spectra. The velocity moments are calculated both from the total ion count rates in the energy analyzer, assuming that all counts are due to H+ ions (and using one set of symmetry assumptions), and from the partial count rates at M/Q = 1, 2, 4, and 16 in the mass analyzer, assuming those counts to be due to the four principal magnetospheric ions H+, He++, He+, and O+, respectively (and using both sets of symmetry assumptions). The "total ion" moments are listed in the ED-file, the partial (mass analyzed) moments are listed in the MD-file.

The energy spectra are based on mass analyzed counts only, and are listed in the MC-file for the same four principal ions (same four M/Q values), plus a fifth ion, namely the O++ (M/Q= 8). The five energy spectra are a compacted representation of the raw count rates at each energy (spin-averaged and maximum).

The mass spectra (when produced) show the accumulated raw counts (and number of samples) in each of the 64 mass channels in four energy ranges. These are listed in the MS-file.

The magnetic field data (time averaged) are listed in all of the ED-, MD-, MC-, and MS-files. In addition, the magnetic field measurements have been used in conjunction with the ion data to determine pitch angles and ion plasma beta.

The s/c ephemeris is also listed with the ion data in the ED-, MD-, MC-, and MS-files, but an extra set of half-hour interval parameters are listed in the EX-file. That file contains only ephemeris, and has been used to label certain data plots. These plots are available in hardcopy (see end of this document for description).

3. TIME COVERAGE

These data have been produced to cover the PRIME archival period for the ISEE-1 and ISEE-2, from launch (October 22, 1977) through February of 1980. The coverage is continuous with the following exceptions:

a.   The initial two weeks were devoted to extensive in-flight testing and calibration of the experiment. The resulting data have not been used for this archiving, so the beginning date is day 312 of 1977.

b.   The instrument was normally turned off for 1.5 to 2 hours at perigee, occasionally longer (primarily to avoid the inner radiation belts).

c.   Extended periods of "cold plasma" measurements (a few tens of hours all together). No such measurements are included here, but they were normally carried out as brief (few minutes) interruptions of longer energy/mass scan cycles and do not normally show up as data gaps.

d.   Solar wind measurements in the so called "sun-synchronous" mode. In this mode data were taken at an increased rate in a narrow spin angle sector around the sun direction, and no data were taken at other angles, in order to maintain the same average data rate per spin. These data have been judged too cumbersome to treat within the particular format of this archiving. The resulting data gaps are numerous and extensive, sometimes leaving an entire day blank.

e.   Gaps in the data transmission/reception or poor quality reception. These are usually of modest duration (few hours) but fairly common.

4. NUMERICAL ACCURACY

The absolute calibration of the instrument is believed to have been accurate to better than 30% in the early phase of in-flight operations. This estimate is based mostly on pre-flight tests in the laboratory, but also on extensive early in-flight confirmation of the location and shape of major peaks in M/Q spectra. As discussed below (in connection with the MC-file), the mass analyzed portion of these archival data have been derived from counts acquired at the higher of two detector triggering levels, in order to minimize the effect of background.

This triggering level has become progressively less sensitive over the years, but it has been monitored, and the count rates have been adjusted accordingly, before being used in the moment calculations. These adjustments are believed to have maintained the absolute calibration accuracy to within about 30% to 35% during high (normal) sensitivity operations.

4.1 Normal High Sensitivity Mode

These estimates assume ideal conditions, however, which means that the differential flux of any ion species is isotropic within the field of view of each sampling, constant in energy over the width of each energy channel, and constant in time during each sampling. Any or all of these conditions may be violated in a real situation, and the resulting error may be significantly greater than 35%. To take an extreme example: if a phase space density is inferred from the count rate in the lowest energy channel, from between 10 eV/e and slightly beyond 100 eV/e, that count rate is divided by 40 eV/e (the weighted center energy). If in fact the ions all have energies near the lower or upper edges of this channel, then the phase space density will be either four times too small or almost three times too large. Errors of a similar magnitude may occur when the ion flux has an extremely narrow angular distribution, or when it varies rapidly in time. The energy distribution is of less concern at higher energies (smaller delta-E over E), but the potential error in phase space density due to narrow angular distributions can be large at any energy, especially in low (normal) bit rate, where the instrument sweeps through 30 deg of spin angle during a sampling (1/4 sec).

Summing (weighted) phase space densities into moments does reduce the relative measuring errors, but to infer complete three-dimensional moments from these data requires assumptions about that part of the unit sphere which is not being sampled. The potential new errors are impossible to calculate, of course, but they can be minimized by making realistic assumptions. The moments listed in the MD-file have been calculated two ways, using two entirely different sets of assumptions (see file description), each set being optimal in some part of the ISEE-1 environment. As can be seen from the listed numbers, the two ways of calculating number densities, for example, produce nearly the same result much of the time, at least in the magnetosphere. If the respective set of assumptions is correct, then the moment calculations are intrinsically accurate to within a few percent.

4.2 Low Sensitivity Mode

If operated normally, the particle counters will saturate when exposed to the high directional flux of H+ in the magnetosheath and solar wind. Even the He++ may cause saturation in these regions of space. To avoid this and to increase the dynamical range of the data, the instrument was designed to have a second commandable detector function that would reduce the sensitivity by about two orders of magnitude. This is accomplished in one case by turning off one of two power supplies (in the mass analyzer) and by shifting the power to another detector in the other case (in the energy analyzer). For the most part, this sensitivity change is programmed to occur automatically when the count rate exceeds a certain threshold, and to be deactivated at the start of the next group of commands, that is typically within 8 sec in low bit rate and within 2 sec in

high. New commands are activated at intervals that are multiples of 32 sam-
plings, called "octaves", usually at every such octave. Normally the instrument
maintains the same mass channel for one or more whole octaves at a time as well.

In theory this dual sensitivity function is simple enough, but it has several
practical problems, especially when it is set to be automatic. The change to
low sensitivity takes a finite known time (close to one second), but the telem-
etry bit stream does not allow the exact starting time to be shown, only the af-
fected octave is flagged. Instead the time of change must be estimated from the
sequence of count rates, which is hampered by rapid strong variations in the ion
flux. In automatic operation it is also reset to normal in an automatic fashion
(takes negligible time), so the change to low sensitivity may be repeated as of-
ten as every octave (or every other octave in high bit rate).

During the computer processing of these archival data, the transitions from high
to low sensitivity have been treated as data dropouts, for simplicity, and only
counts taken at least 1.5 seconds (1/2 spin) beyond the estimated start of each
transition have been included, after multiplication by a constant scaling factor
representing the end state (no such multiplication in the MS-file). This method
avoids having the transient count rates multiplied by the wrong variable scaling
factor, due to uncertainties in the exact timing, but it creates a systematic
undersampling of the ion flux near its maximum and on one side of this maximum.
The situation is further aggravated by the fact that these automatic sensitivity
changes tend to occur where the ion fluxes have the strongest anisotropies and
the narrowest energy distributions.

In view of these difficulties, all data obtained in low sensitivity mode should
be treated with suspicion. They show the gross and qualitative plasma proper-
ties very well, but the tabulated numbers may be substantially wrong. If it is
important to establish absolute values, it is worth comparing these numbers with
archived data from some of the other particle instruments on the ISEE-1 and -2.
The data most often obtained in this mode are those in the ED-file and the H+
data in the MD-, MC-, and MS-files. Sometimes the He++ data are also affected.
All data obtained this way are clearly flagged (see file descriptions).

5. KNOWN ERRORS

All data, including the magnetic field data, have been screened very rigorously
with respect to potential problems in the telemetry transmission and reception.
Any time the telemetry quality flags suggest a potential problem, all data that
could possibly be affected have been discarded without further investigation.
In addition, every ion count rate and every magnetic field reading have been
examined for clearly "unrealistic" values, that is unrealistically large values
under given circumstances (given region of space). Such values have been dis-
carded on an individual basis (sample by sample).

5.1 Ion Data

The remaining errors, as far as they are known, are very few and ought to be
obvious from the wider context, especially when the various files are intercom-
pared. One group of known errors consists of a few isolated "bursts of counts"
in the MS-file (mass spectra) at M/Q values where no significant ions are to be

expected. Another group of suspected errors consists of a few isolated "bursts of ions" having strangely repetitive count rate and angle of motion, as evident in the MC-file.

5.2 Magnetic Field Data

These have more errors in them, unfortunately, but that is offset by the fact that expertly processed values can be obtained from other archival files sup- plied by the Principal Investigator for the ISEE-1 Fluxgate Magnetometer (C. T. Russell; NSSDC identification No. 77-102A-04). There are two main types of er- rors occurring here, one brief error often present at the gain changes (at most once or twice per orbit) due to a misalignment of the gain flag and the actual data on the tape, and another less common but longer lasting error that may ap- pear in connection with certain offset corrections (related to the antenna flip status). These errors are more fully explained in the descriptions of the ED- and MD-files, along with methods to recognize the errors (see also description of hardcopy plots at the end of this document). Errors in the magnetic field only affect part of the ion data, namely the beta value and the moments that are based on pitch-angle binning (the second method used in the MD-file).

6. THE ED-FILE

This file contains data from a particle counter called the "energy detector", or "ED", which intersects the ions after energy analysis but before mass analysis. The count rates have been converted to certain velocity moments assuming that all counts are due to protons. These moments are thus not directly comparable to any of the moments in the MD-files, unless the protons are indeed the dominant species. Even in that case, there may often be significant differences between the ED and MD proton moments, because the ED and MD particle counters respond to ions with slightly different external angles of motion (see above), and the two sets of count rates are usually averaged over different times.

Since the ED count rates are independent of the mass channel selection, and the energy channels are normally scanned at a higher rate than are the mass channels, it is usually possible to obtain several consecutive sets of ED moments during each complete instrument scan cycle. This advantage has been utilized whenever possible, and the ED averaging intervals are more or less independent of the phase of the instrument cycle. The criterion most commonly used for defining the ED intervals is to have a "sufficiently dense" coverage in energy and spin phase angle. This criterion varies with different types of energy and mass scan patterns, but typically amounts to having at least every other energy channel sampled in each of 12 spin angle sectors (30 deg wide sectors). The missing matrix points are filled in by interpolation between adjacent points before the moments are calculated.

The criterion for ending each ED averaging interval is modified when the instrument is in low sensitivity mode (usually set by automatic triggering at extreme count rates) and, at the same time, the count rates show strong (10-fold or stronger) spin phase modulation. At such times the ED intervals are made equal to the instrument scan cycle. This situation occurs most often in the solar wind. The purpose is to suppress artificial oscillations in the moments caused (in some modes) by spin phase dependent energy samplings. The modification has not been applied uniformly throughout the entire data set, however, so there are periods of "strange" and non-physical modulations in the ED moments, especially in the densities. At any rate, all data taken in low sensitivity mode should be treated with care; they are not intended to represent accurate quantitative measurements, but they have been included to complete the gross qualitative picture and to provide continuity between times of normal magnetospheric data. All low sensitivity data are flagged as such (see below).

Unlike the MD data, the ED data have not been corrected for background counts due to penetrating radiation (not measured), but they are known to be much less affected by that problem than are the MD data (different kinds of detectors). The ED data also differ from the MD data in that no standard deviations are calculated from the combination of counts (a saving in CPU time and output volume). If necessary, approximate upper limits on the ED standard deviations can be estimated from the corresponding standard deviations in the MD-file (the MD data have additional variance associated with background correction).

6.1 File Format

The ED-file has been written by a formatted sequential FORTRAN WRITE:

```
      WRITE(9,210) IYYDDD,IUTSEC,BXED,BYED,BZED,BTED,ITHETB,IPHIB,
     *EDDNS,EDEMN,EDVEL,IEDANG,ACSEC,XCSEC,ENRG1,ENRG2,RX,RY,RZ

  210 FORMAT(2I6,4F8.1,I4,I5,3(1PE10.2),I5,2(0PF8.2),2F5.1,3F6.1)
```

The variable names represent the following quantities:

IYYDDD is the year (two digits) and day of year (three digits).

IUTSEC is the universal time in seconds at the midpoint of the averaging
       interval. The nominal length of each interval is defined by the
       distance between adjacent midpoints, but the actual length may vary
       somewhat because of time gaps (noise) in the data (see ACSEC below).

BXED, BYED, BZED, and BTED are the GSE components and absolute value, respec-
       tively, of the measured magnetic field, each averaged over the ED
       interval (for data quality check, see next section). The unit is
       "nanotesla" ("nT"), or equivalently, "gamma".

ITHETB and IPHIB are, respectively, the magnetic field elevation and longitude
       angles in GSE coordinates. ITHETB ranges from -90 deg (southward) to
       +90 deg (northward), IPHIB from -180 deg (antisunward) to +180 deg (anti-
       sunward), with 0 deg being sunward and 90 deg duskward. These angles
       have been calculated from the time averaged field components, and are
       rounded to the nearest integer.

EDDNS is the ion number density in "/cm3" (assuming protons) contained in the
       nominal energy range from 100 eV to about 16 keV (see also next section).

EDEMN is the "thermal" ion energy in "keV", that is the mean energy (0.1 -
       16 keV) minus the energy associated with the common drift motion.

EDVEL is the common drift speed in "km/sec" in a plane parallel to the s/c
       spin plane, that is approximately in the solar ecliptic plane.

IEDANG is the longitudinal direction angle of that same drift, with 0 deg
       being sunward, and 90 deg duskward (-180 deg to +180 deg).

ACSEC is the number of seconds of data included in the moments. This number
       is normally at least 6% smaller than the length of the averaging inter-
       val, since neither the lowest nor the highest energy channels are in-
       cluded (may be further reduced by data gaps).

XCSEC is the number of seconds during the averaging interval when the ED detec-
       tor was in low sensitivity mode. This number is almost always zero in
       the magnetosphere, but usually nonzero in the magnetosheath and solar
       wind. If nonzero, it implies that at least some of the count rates have
       been multiplied by a crude scaling factor (= 130) to compensate for the
       reduced sensitivity.

ENRG1 and ENRG2 are, respectively, the lower and upper energy limits used in the moment calculations, in units of "keV". These are normally 0.1 and 16.1, but may be modified in some modes (cf. comments on energies above).

RX, RY, and RZ are the GSM coordinates of the s/c (at midpoint of interval) in units of "earth radii". On the rare occasions when the GSM coordinates are unavailable (due to faulty ephemeris tape) the GSE coordinates are used instead (available on raw data tape). Those occasions are flagged in the EX-file (also flagged in the MC-, MD- and MS-files).

6.2 Further Explanations of Certain Variables.

The magnetic field values provided here may to some extent duplicate what has already been archived at the NSSDC by the magnetometer principal investigator (Prof. C. T. Russell; NSSDC identification number 77-102A-04), but are not intended to supplant those. The values derived here may not have been adequately screened against telemetry noise or adjusted for instrument anomalies, so it is recommended that the PI provided data be consulted whenever there is doubt about accuracy. There are two types of errors known to occur here:

a.   When the magnetometer is commanded to low gain on the inbound leg of the s/c orbit, usually between R = 8 Re and = 5 Re, the corresponding flag may show up slightly too late on the raw data tape, resulting in a brief underrepresentation of the field by a factor of 32. This may last for about a minute or less (part of one major frame) and affects a single ED interval. This error ought to be fairly obvious in the ED data, and therefore traceable in the MD data as well (by comparing the times). The corresponding mismatch at high gain command on the outbound leg, that is a sudden 32-fold increase of the field, is usually discovered as "unreal" and corrected.

b.   Occasionally, it appears that the wrong antenna flip status has been inferred from the raw data behavior (pertains to the s/c Y and Z coordinates), resulting in anomalous modulations of the GSE components. These modulations cause the sum BXED**2+BYED**2+BZED**2 to be much smaller than the square of the time-averaged absolute field strength BTED**2. It is recommended that the two measures of field strength be compared routinely, and that other magnetic field data be consulted if those two differ by more than a few percent. An additional (or alternative) check can be made using certain MD data (see below).

The velocity moments have been calculated from a 32 energy channel (covering the entire range from 10 eV to about 18 keV) by 12 spin angle sector (30 deg each) matrix of time-averaged count rates in the following steps:

I.   A phase space density is assigned to each matrix point, using the local count rate when available, or interpolating between adjacent count rates if the point has not been sampled. The bottom and top energy channels are included in the interpolation procedure, when necessary, but not in the integration (summation) over energy.

II.   Within each energy channel the phase space densities are weighted
       by cosines or sines of the spin angle (center of sector) and summed
       over angle to form two orthogonal projections. These projections
       are in turn weighted by energy and by an energy bandwidth (see below)
       and summed over energy channels, forming two orthogonal components,
       approximately the GSE X and Y components, of a vector that is pro-
       portional to number flow density. Both components are then divided
       by a total (scalar) sum of phase space densities weighted by the
       energy bandwidth and by the square root of the energy, that is by a
       sum proportional to number density, to form (approximate) X and Y
       drift velocity components, and an angle IEDANG.

III.   A spherical coordinate system is envisioned with its polar axis along
       the drift velocity vector, that is in the GSE X-Y plane. It is now
       assumed that the phase space density has azimuthal symmetry in this
       coordinate system (rotational symmetry around drift velocity vector).
       The number density, drift speed (but not angle), and mean energy are
       recalculated by summing over solid angle and energy in this system.
       The solid angle weighting factors in this case are zones on a unit
       sphere, each defined at the intersection with the GSE X-Y plane by the
       boundaries of a 30 deg spin angle sector, or by one boundary and the
       drift velocity vector. These zones are partially overlapping, and
       summing over 12 spin angle sectors (typically = 14 zones) means cover-
       ing the unit sphere twice, so a factor 1/2 is applied to each sum.
       The drift speed (EDVEL) and mean energy (EDEMN) are obtained by divid-
       ing flow density and energy density, respectively, by the number den-
       sity (EDDNS). The mean energy is converted to "thermal" energy by
       subtracting the equivalent drift energy.

If the drift speed in step II is less than 14 km/sec (less than 1 eV energy),
the coordinate system is instead aligned with the X-Y projection of the magnetic
field, that is with the angle IPHIB, provided the elevation angle ITHETB is be-
tween -45 and +45 deg. If the latter is not the case, and if the drift speed is
below 14 km/sec, the coordinate system is aligned with the s/c spin axis, and
the phase space densities are treated as isotropic. Only density and mean en-
ergy are recalculated in these two cases.

The summation over energy treats each energy channel, except the second one
(first channel not included), as a point measurement at the center energy, and
takes the energy bandwidth to be the distance between adjacent channels in the
trapezoidal fashion. At the second channel an extra term is added to extend the
integral from the center energy downward to about 0.1 keV, assuming the flux to
be a constant. This addition brings the mathematical energy range in better
agreement with the instrumental range of acceptance.

The variable ACSEC is a sum of elementary time segments associated with each
commanded setting of the power supplies controlling energy and mass channels.
These elementary times are 1/4 sec during low bit rate operation (about 80% of
the time) and 1/16 sec during high bit rate operation. These times include the
resetting of the power supplies, however, and are slightly longer than the times
associated with particle counting. For simplicity, the particle counting is
interrupted for about 12% of the elementary time segments in both low and high
bit rate operation to allow for resetting. The ACSEC therefore exceeds the ac-
tual particle counting time by about 14% in both cases.

7. THE MD-FILE

This file contains data from a particle counter called the "mass detector", or "MD", which receives the ions after both energy and mass analysis. Count rates of the four principal magnetospheric ion species, the H+, He++, He+, and O+, have been sorted by 32 energy channels (10 eV/e to 18 keV/e), 12 spin angle sectors (30 deg each) and 9 pitch-angle ranges (20 deg each) and averaged over each complete energy/mass scan cycle of the instrument. At the end of each cycle the averaged count rates have been converted to certain velocity moments using two different assumptions: the velocity distributions have rotational symmetry a- round either (A) the bulk flow vector or (B) the local magnetic field direction (see below). Note: the ion labels are applied to certain M/Q values (the in- strument does not measure mass per se) and may be inappropriate in the magneto- sheath and solar wind, especially at M/Q= 4 (He+).

The energy/mass scan cycles vary in length from a few minutes to about 20 min or more, depending on the instrument mode of operation. Each cycle may cover only a few mass channels and a reduced energy range, or it may cover the full energy range at each of 64 mass channels (load mode). The most common modes in the magnetosphere provide for multiple energy scans at each of 5 to 7 mass chan- nels (including a background channel at M/Q < 1), where each energy scan may sample a different subset of the 32 energy channels (e.g. every fourth channel in four interleaving scans), and each energy channel is maintained for about four seconds (1.3 s/c spin cycles). In addition, each cycle may contain a few scans through all 64 mass channels at a few energies, as well as one or two brief scans through the RPA voltages in the lowest energy channel (cold plasma measurements not included here). In order to simplify tabulation of moments, no distinction is made here between different phases of a given cycle. That is, all moments are treated as averages over the same cycle, although different ions were in fact sampled at different phases (the same ion often more than once per cycle).

All MD moments have been corrected for background counts due to penetrating radiation (mostly MeV electrons and associated bremsstrahlung). This has been done by subtracting an average background, that is the average sampled during a given energy/mass scan cycle, from the average ion count rates in each energy and angle bin. As a consequence, normally non-negative moments such as number density may end up negative, when the count rate of a given ion is very close to background levels, and the count rate in the background channel happens to be on the high side due to normal statistical or temporal fluctuations. This is to be expected, and negative values ought to be included in any statistical averaging of number densities from these files, in order not to bias the result.

All MD moments have a standard deviation assigned to them. This one accounts for purely statistical uncertainties, those associated with Poisson counting statistics. In all cases but one, the tabulated value is an integer number be- tween 0 and 999, which represents the ratio in percent (%) between the standard deviation and the absolute value of the moment itself, rounded downward (values greater than 999 assumed irrelevant). The one exception is the bulk flow angle (drift direction angle) in the GSE X-Y plane (spin plane), where the standard deviation is expressed as an angle between 0 and 360 deg, rounded to the nearest integer.

The variance (square of standard deviation) of a given moment, or a given combination of moments (as in bulk velocity and mean energy), has been calculated in a customary fashion by taking the partial derivative with respect to the count rate in each energy and angle bin included in the moment (in both numerator and denominator, where applicable), squaring the derivative, multiplying it with the variance of the associated count rate, and adding such terms over all bins. If the same count rate is used twice, in order to replace a missing sample in an adjacent bin (see below), its contribution to the variance is adjusted so as to reflect the reduced number of independent samplings. All standard deviations, except the one assigned to bulk flow angle (see below), include a contribution from the variance of the background measurement. The reason for the exception is that the background measurement, although subtracted from all other count rates, is a scalar (single number) that cancels out from the calculation of flow angle.

For various reasons, the data may be statistically insufficient to allow a given moment (or combination of moments) to be calculated. If the number density has been calculated to be a negative number (background measurement too high), for example, it makes no sense to even attempt to calculate a mean energy. And if only a few energy channels have been sampled (due to noisy data), it makes no sense to calculate any of the moments, since the output format presumes a certain degree of consistency. Whenever a moment calculation fails, the corresponding standard deviation is set equal to -1.

7.1 File Format

The MD-file has been written in groups of five lines (records), using formatted sequential FORTRAN WRITE statements as follows:

The first of five lines is a title line:

        WRITE(8,230) IYYDDD,JSTART,JSTOP,RX,RY,RZ,RT,DZ,IMLAT,TLOCL,
      *BXMD,BYMD,BZMD,BTMD,BETA,IDBETA,BCTR,MDTCR,
      *ENEMAX,IRATE,RSEY,RSEZ

    230 FORMAT(I6,2I5,5F6.1,I4,F5.1,4F8.1,1PE10.2,I3,1PE10.2,I3,
      *0PF5.1,I2,2F6.1)

The variable names represent the following quantities:

IYYDDD is the year (two digits) and day of year (three digits).

JSTART is the universal time in minutes at the beginning of the averaging
        interval, that is the time of the first good data in that interval.
        This is normally at the start of an energy/mass scan cycle, unless
        some initial data in that cycle are bad.

JSTOP is the universal time in minutes at the end of the averaging interval,
        that is the time of the last good data in that interval. This is
        normally at the end of an energy/mass scan cycle, unless the last
        data in that cycle are bad.

RX, RY, RZ, and RT are, respectively, the GSM X, Y, Z, and radial distance
    at the midpoint of the averaging interval, all in units of "earth
    radii" ("Re"). RY and RZ are set to 999. if GSM coordinates not
    available (RX same in GSE).

DZ   is the distance in "earth radii" (at midpoint) from the nominal neutral
        sheet in the geotail according to Fairfield and Ness [J.Geophys. Res.,
        75, 7032, 1970]. This is only displayed for GSM X < -11 Re, otherwise
        set to 999. If no GSM coordinates available, it is set to 0.

IMLAT   is the geomagnetic latitude in degrees (at midpoint), rounded to the
        nearest integer. This is set to 0, if no ephemeris tape available.

TLOCL   is the geographic local time in hours and 1/10 hours (at midpoint).
        This is set to 0.0, if no ephemeris tape available.

BXMD, BYMD, BZMD, and BTMD are the GSE components and absolute value, respec-
    tively, of the measured magnetic field, each averaged over the whole
    MD interval (for data quality check, see next section). The unit is
    "nanotesla" ("nT"), or equivalently, "gamma".

BETA and IDBETA are a simplified representation of the ion plasma beta and its
    standard deviation (% of absolute value). Its definition is explained
    in the next section.

BCTR   is the average background count rate in counts/sec.

MDTCR   is a flag showing which of two detector pulse hight triggering levels
        has been used (= 2 in these data).

ENEMAX is the maximum energy sampled, in units of "keV/e", or equal to 16.1,
        whichever is smaller (16.1 is maximum in moments). Even if it is listed
        as 16.1 (typical) the moments of some ion species may sometimes be lim-
        ited to lower energies, depending on the energy/mass scan mode (see next
        section).

IRATE   is a flag showing which of two data accumulation (and telemetry trans-
        mission) rates has been used. The low or normal rate (80% of the time)
        is shown by IRATE = 1, the high rate by IRATE = 4. Note: low rate means
        four (4) samplings/sec, high rate means sixteen (16) samplings/sec.

RSEY and RSEZ are the GSE Y and Z (at midpoint of averaging interval) in units
        of "earth radii".

The next four lines list, respectively, the moments for H+ (K= 1), He++ (K= 2),
He+ (K= 3), and O+ (K= 4) (that is actually for M/Q= 1, 2, 4, and 16):

```
      DO 270 K=1,4

      WRITE(8,240)DNS5,ID0,DNS8,ID1,EMN8,ID2,
     *VDRFT,ID3,IDRFT,ID4,
     *BGD,ID6,ACSEC,XCSEC,
     *IPAMIN,IPAMAX,DENS8,ID7,EPER8,ID8,EPAR8,ID9

  240 FORMAT(4(1PE10.2,I3),I5,I4,1PE10.2,I3,0PF7.2,0PF6.2,
     *I4,I4,1PE10.2,I3,2(1PE9.2,I3))

  270 CONTINUE
```

The variable names represent the following quantities:

DNS5 and ID0 are the number density in "/cm3" and standard deviation (% of ab-
      solute value) of ions with energies between 10 eV/e and about 100 eV/e,
      that is of ions in the lowest energy channel (with RPA voltage fixed at
      10 V).

DNS8 and ID1 are the number density in "/cm3" and standard deviation (% of ab-
      solute value) of ions with energies between about 100 eV/e and 16 keV/e
      (normally).

EMN8 and ID2 are the mean energy in "keV" and standard deviation (%) of ions in
      the nominal energy range from 100 eV/e to 16 keV/e. Note: this is total
      energy, including bulk motion, and it is in units of "keV", not "keV/e".

VDRFT and ID3 are the common (among those ions) drift speed (bulk flow speed)
      in "km/sec" and standard deviation (%) of ions in that same energy range
      (100 eV/e - 16 keV/e). This drift speed is in the s/c spin plane, that
      is approximately in the GSE X-Y plane.

IDRFT and ID4 are the longitudinal direction angle of that same drift and its
      standard deviation, both in "degrees". IDRFT = 0 is sunward and = 90 is
      duskward (-180 deg to +180 deg). ID4 is between 0 and 360 deg.

These moments, from DNS5 through IDRFT, assume that the velocity distribution
has rotational symmetry around the drift (flow) vector (in the GSE X-Y plane).

BGD and ID6 are the equivalent isotropic density in "/cm3", over the 100 eV/e
      to 16 keV/e range, and standard deviation (%) corresponding to the meas-
      ured average background count rate. That is, BGD is equal to the total
      background correction of DNS8 (a number already subtracted from DNS8).
      The ID6, when expressed in absolute terms, is part of ID1.

ACSEC is the number of seconds of data included in the moments for that ion
       species. This number is normally a small fraction of the length of the
       averaging interval (energy/mass scan cycle).

XCSEC is the number of seconds during the averaging interval when the MD detec-
       tor was in low sensitivity mode and, at the same time, was sampling that
       particular ion species. This number is almost always zero in the magne-
       tosphere, but usually nonzero for H+ in the magnetosheath and solar wind.
       In the latter cases it is often nonzero for He++ ions as well. If it is

not zero, it implies that at least some of the count rates of that ion species have been multiplied by a crude scaling factor (= 65 for MDTCR = 2) to compensate for the reduced sensitivity.

IPAMIN and IPAMAX are the minimum and maximum pitch angles in "degrees" sampled for those ions, rounded to the nearest integer. Note: if the magnetic field is properly measured and corrected for magnetometer offsets, then the sum of these angles, IPAMIN + IPAMAX, should range between about 170 deg and 190 deg.

DENS8 and ID7 are the number density in "/cm3" and standard deviation (% of absolute value) of ions in the 100 eV/e - 16 keV/e range, assuming that the velocity distribution has rotational symmetry around the local magnetic field vector (see next section for further explanations).

EPER8 and ID8 are the mean perpendicular energy (perpendicular to magnetic field; two degrees of freedom) in "keV" and standard deviation (%) of ions in the 100 eV/e - 16 keV/e range, assuming that same kind of symmetry.

EPAR8 and ID9 are the mean parallel energy (parallel to magnetic field; one degree of freedom) in "keV" and standard deviation (%) of ions in the 100 eV/e - 16 keV/e range, assuming that same kind of symmetry.

7.2 Further Explanations of Certain Variables.

The magnetic field values provided here may to some extent duplicate what has already been archived at the NSSDC by the magnetometer principal investigator (Prof. C. T. Russell; NSSDC identification number 77-102A-04), but are not intended to supplant those. The values derived here may not have been adequately screened against telemetry noise or adjusted for instrument anomalies, so it is recommended that the PI provided data be consulted whenever there is doubt about accuracy. There are two types of errors known to occur here:

a.   When the magnetometer is commanded to low gain on the inbound leg of the s/c orbit, usually between R = 8 Re and = 5 Re, the corresponding flag may show up slightly too late on the raw data tape, resulting in a brief underrepresentation of the field by a factor of 32. This may last for about a minute or less (part of one major frame) and affects a single MD interval. This error ought to be fairly obvious in the ED data, and therefore traceable in the MD data as well (by comparing the times). The corresponding mismatch at high gain command on the outbound leg, that is a sudden 32-fold increase of the field, is usually discovered as "unreal" and corrected.

b.   Occasionally, it appears that the wrong antenna flip status has been inferred from the raw data behavior (pertains to the s/c Y and Z coordinates), resulting in anomalous modulations of the GSE components. These modulations cause the sum BXMD**2+BYMD**2+BZMD**2 to be much smaller than the square of the time-averaged absolute field strength BTMD**2. It is recommended that the two measures of field strength be compared routinely, and that other magnetic field data be consulted if those two differ by more than a few percent. An additional (or

alternative) check can be made by summing IPAMIN and IPAMAX. If the
sum is several degrees smaller than 170 deg or several degrees larger
than 190 deg, then the magnetic field should be in doubt.

The velocity moments have been calculated two ways, A and B, using either of two
energy-angle matrices. Both matrices consist of 32 energy channels (covering
the entire range from 10 eV/e to about 18 keV/e), but one has 12 spin angle sec-
tors (30 deg each) and no pitch angles, the other has 9 pitch-angle sectors (20
deg each) and no spin angles. In method A, using 12 spin angle sectors, the
calculations consist of the following steps:

A.I   A phase space density and a corresponding standard deviation are
        assigned to each matrix point that has been sampled, using the
        local average count rate, minus an average background count rate,
        and the number of samplings. No interpolations are made at this
        stage.

A.II   Within each energy channel that has been sampled (usually all have),
        except the bottom and top ones, the phase space densities are weighted
        by cosines or sines of the spin angle (center of sector) and summed
        over angle to form two orthogonal projections. At this stage the
        phase space densities are interpolated in angle, if some angular bins
        have no samples. These projections are in turn weighted by energy and
        by an energy bandwidth (see below) and summed over energy channels,
        forming two orthogonal components, approximately the GSE X and Y com-
        ponents, of a vector that is proportional to number flow density.
        Both components are then divided by a total (scalar) sum of phase
        space densities weighted by the energy bandwidth and by the square
        root of the energy, that is by a sum proportional to number density,
        to form (approximate) X and Y drift velocity components, and a drift
        angle IDRFT. Similar summations are carried out with the variances
        (square of standard deviations), using the corresponding partial de-
        rivatives (squared) as weights, to derive the standard deviation of
        the drift angle (ID4).

A.III   A spherical coordinate system is envisioned with its polar axis along
        the drift velocity vector, that is in the GSE X-Y plane. It is now
        assumed that the phase space density has azimuthal symmetry in this
        coordinate system (rotational symmetry around drift velocity vector).
        The number density, flow density (but not angle), and energy density
        are recalculated by summing over solid angle and energy in this system.
        The solid angle weighting factors in this case are zones on a unit
        sphere, each defined at the intersection with the GSE X-Y plane by the
        boundaries of a 30 deg spin angle sector, or by one boundary and the
        drift velocity vector. These zones are partially overlapping, and
        summing over 12 spin angle sectors (typically = 14 zones) means cover-
        ing the unit sphere twice, so a factor 1/2 is applied to each sum.
        The drift speed (VDRFT) and mean energy (EMN8) are obtained by dividing
        flow density and energy density, respectively, by the number density
        (DNS8). No drift energy is subtracted from this mean energy. The cor-
        responding standard deviations (ID3, ID2, and ID1) are derived from
        similar sums of variances, using partial derivatives as weights.

A.IV   The partial number density of ions in the bottom energy channel (DNS5)
       and the corresponding standard deviation (ID0) are also calculated in
       this coordinate system, although in this case the energy "sum" has a
       single term covering the channel width (10 eV/e to about 100 eV/e).

If the drift speed in step A.II corresponds to less than 1 eV (less than 14
km/sec for H+, less than 4 km/s for O+, etc.), then the coordinate system is
instead aligned with the X-Y projection of the magnetic field (calculated from
BXMD and BYMD), provided the field elevation angle (including BZMD) is between
-45 and +45 deg. If the latter is not the case, and if the drift speed is be-
low minimum, the coordinate system is aligned with the s/c spin axis, and the
phase space densities are treated as isotropic. Only density and mean energy
are recalculated in these two cases.

In method B, using 9 pitch-angle ranges (0.0 - 19.9, 20.0 - 39.9, etc.),
the steps are as follows:

B.I   A phase space density and a corresponding standard deviation are
       assigned to each matrix point that has been sampled, using the
       local average count rate, minus an average background count rate,
       and the number of samplings.

B.II   If only part of the pitch-angle range has been sampled, which is
       often the case (indicated by IPAMIN and IPAMAX), then the empty
       angular bins near 0 deg and 180 deg are assigned the same phase
       space density as the nearest sampled bin (closer to 90 deg) at
       the same energy.

B.III A spherical coordinate system is envisioned with its polar axis
       along the magnetic field vector (arbitrary direction). It is now
       assumed that the phase space density has azimuthal symmetry in this
       coordinate system (rotational symmetry around magnetic field vector),
       which is to say that the phase space densities in the 9 pitch-angle
       bins represent the entire unit sphere. The number density and the
       parallel (axial) and perpendicular energy densities are calculated
       by summing over solid angle and energy in this system. When summing
       over solid angle, the parallel and perpendicular energies are repre-
       sented by, respectively, the cosine square and the sine square of
       the pitch angle at the center of each bin. The solid angle weighting
       factors in this case are 9 contiguous zones on a unit sphere, each
       defined by the boundaries of a 20 deg pitch-angle sector. The two
       mean energies (EPAR8 and EPER8) are obtained by dividing the respec-
       tive energy densities by the number density (DENS8). The correspond-
       ing standard deviations (ID9, ID8, and ID7) are derived from similar
       sums of variances, using partial derivatives as weights. Only the
       standard energy range (0.1 - 16 keV/e) is included here.

EPER8 and EPAR8 should have a ratio of 2:1 if the velocity distribution is iso-
tropic (or if the count rates have been extrapolated from a single bin at 90 deg
pitch angle), since EPER8 represents two degrees of freedom and EPAR8 only one.
Due to rounding-off errors in the summation over angle, however, the isotropic
ratio is not exactly 2, but about 1.969. More specifically, if statistical and
instrumental errors are neglected, EPER8 is very nearly exact (about 0.02% too
small), but EPAR8 is about 1.55% too large. Naturally, neither energy will be

very meaningful if the magnetic field is in error (see above).

The "ion plasma beta" listed in the title line, BETA, is actually calculated with method A. The ion pressure used here is equal to 2/3 (two degrees of freedom) of the sum of "thermal" energy densities of the four ion species, that is total energy densities minus the energy densities associated with the respective drift speed, as calculated assuming symmetry around the respective drift velocity vector. This pressure has been divided by a magnetic pressure based on BTMD. An alternative and more formally correct value may be calculated using the "gyrotropic" density DENS8 and perpendicular energy EPER8, although those quantities do not account for bulk flow (drift). In case the magnetic field is suspect, and other field measurements are available, the beta can only be recalculated with method A (using DNS8, EMN8, and VDRFT for each ion).

The summation over energy treats each energy channel, except the first and second ones, as a point measurement at the center energy, and takes the energy bandwidth to be the distance between adjacent sampled channels in the trapezoidal fashion, ignoring intermediate channels with no samples. At the second channel an extra term is added to extend the standard energy integral from the center of the channel downward to about 0.1 keV, assuming the flux to be a constant. This addition brings the mathematical energy range into better agreement with the instrumental range of acceptance. At the first energy channel, which is treated separately, the energy summation has only one term that includes the channel width (10 eV/e - 100 eV/e) as a factor (only DNS5 and ID0 calculated).

Since the summations are done after the completion of an energy/mass scan cycle, the energy channels have normally been sampled in a contiguous fashion, but the summation procedures are set up to accept gaps of as many as four channels (due to noisy data), before declaring the data insufficient.

Depending on the scan mode, the lowest and highest energy channels sampled may vary, and are sometimes different for different ions. The summation procedure uses the actual lower and upper channels, so the moments of different ions may on occasion cover different energy ranges. There are no flags to separate ions in that regard in the MD-file (insufficient space), but the actual energy coverage is shown for each ion in the MC-file (see below). See also the explanation of ENEMAX above.

The variable ACSEC is a sum of elementary time segments associated with each commanded setting of the power supplies controlling energy and mass channels. These elementary times are 1/4 sec during low bit rate operation (about 80% of the time) and 1/16 sec during high bit rate operation. These times include the resetting of the power supplies, however, and are slightly longer than the times associated with particle counting. For simplicity, the particle counting is interrupted for about 12% of the elementary time segments in both low and high bit rate operation to allow for resetting. The ACSEC therefore exceeds the actual particle counting time by about 14% in both cases.

This file is essentially an abbreviated listing of the count rates that have been converted to velocity moments in the MD-file. All relevant energy channels are represented, but the spin angle bins have been replaced, in each separate energy channel, by the peak count, the time of the peak (in seconds), the spin angle of the peak (angle of motion of ions), a measure of the angular width of the ion flux, and the spin-averaged count rate with standard deviation. No pitch-angle information is listed, but the approximate pitch angle at the peak count can be derived from the spin angle and the magnetic field orientation.

Count rates are listed for five ion species, that is for the same four species included in the MD-file: H+, He++, He+, and O+ (actually for M/Q= 1, 2, 4, and 16), and, in addition, for doubly charged oxygen: O++ (M/Q= 8). The listing for O++ is usually incomplete (contains fill) because it has only been measured over part of the energy range, or it has not been measured at all, depending on the energy/mass scan mode. It is common to limit the measurement of the O++ to the lowest 24 energy channels (to energies below about 10 keV/e), to avoid contamination by the more abundant O+, whose M/Q response function partially overlaps with that of the O++ at the highest energies.

Usually the MC-file displays count rates from all 32 energy channels, but if the energy/mass scan cycle is limited to a lower portion of the energy range (as may be the case when the instrument has been commanded for solar wind or magnetosheath observations), then the MC-file is also limited to lower energies. In such cases, it is not uncommon to have a different energy coverage for different ions, but the MC-file lists the same number of channels (same number of lines) for all five ion species, displaying dummy fill where data are missing. The fill consists of -1 or -1.00.

Note: The MC-file is the only documentation of the actual energy ranges used in the MD-file, in case different ions have been measured over different energy ranges. The MD moment calculations will extend across missing intermediate energies, up to four contiguous missing channels (see above), but they will not extrapolate below or above the end channels, and they will not extend above 16 keV/e (or below 100 eV/e in most cases). The actual ranges can be deduced from the MC-file by the lowest and highest channels (lines) that have data (rather than fill). Usually the only places where the energy sweep is shortened and made different for different ions are in the solar wind and in the magnetosheath, as predicted from average magnetosphere configurations.

In order to simplify the file format, all averaged counts are treated as representing the whole energy/mass scan cycle, even though different ions were in fact sampled at different phases of the cycle (the same ion often more than once). However, the time labels on the peak counts do refer to the respective times of sampling, rounded downward to the whole second.

All MC counts and count rates are raw data, except when the instrument has been operating in low sensitivity mode. In that case the peak count and some counts included in the spin-averaged rate have been multiplied by a crude scaling factor (= 65) to compensate for the reduced sensitivity. Such counts are flagged accordingly (see below). None of the counts or count rates has been corrected for background counts due to penetrating radiation (mostly MeV electrons and associated bremsstrahlung). However, the average background count rate measured

during each energy/mass scan cycle is listed as average counts per sample, along
with the sampling rate, which is expressed in number of samples per second here.

The MC counts and count rates may be converted to differential fluxes or phase
space densities using the instrument parameters listed in a separate section
below.

8.1 File Format

The MC-file has been written in groups of up to 34 lines (up to 33 records),
using formatted sequential FORTRAN WRITE statements as follows:

The first line in each group has a single character indicating the format of
the counts (1 or 2), the second line is a title line that also indicates how
many lines (energy channels) are to follow in the current group:

```
     WRITE(11,243)IFORMT,IYYDDD,JSTART,JSTOP,RX,RY,RZ,RT,RSEY,RSEZ,
    *DZ,IMLAT,TLOCL,BXMD,BYMD,BZMD,BTMD,BETA,IDBETA,BGND,IDBGND,
    *MAXESO,NSPLPS

 243 FORMAT(I2/3I6,7F6.1,I4,F5.1,4F8.1,1PE10.2,I3,1PE9.2,I3,2I3)
```


The variable names represent the following quantities:

IFORMT is the format flag for the counts, showing either of two formats.
    The standard format (IFORMT = 1) lists the averaged count rates in
    floating point with two decimal places, the other one (IFORMT = 2)
    rounds them to the nearest integer in order to allow more positions
    for the peak counts (always integers) on the same line.

IYYDDD is the year (two digits) and day of year (three digits).

JSTART is the universal time in seconds (not minutes) at the beginning of
    the averaging interval, that is the time of the first good data in
    that interval. This is normally at the start of an energy/mass scan
    cycle, unless some initial data in that cycle are bad.

JSTOP is the universal time in seconds (not minutes) at the end of the
    averaging interval, that is the time of the last good data in that
    interval. This is normally at the end of an energy/mass scan cycle,
    unless the last data in that cycle are bad.

RX, RY, RZ, and RT are, respectively, the GSM X, Y, Z, and radial distance
    at the midpoint of the averaging interval, all in units of "earth
    radii" ("Re"). RY and RZ are set to 999. if GSM coordinates not
    available (RX same in GSE).

RSEY and RSEZ are the GSE Y and Z (at midpoint of averaging interval) in units
    of "earth radii".

DZ   is the distance in "earth radii" (at midpoint) from the nominal neutral
        sheet in the geotail according to Fairfield and Ness [J.Geophys. Res.,
        75, 7032, 1970]. This is only displayed for GSM X < -11 Re, otherwise
        set to 999. If no GSM coordinates available, it is set to 0.

IMLAT   is the geomagnetic latitude in degrees (at midpoint), rounded to the
        nearest integer. This is set to 0, if no ephemeris tape available.

TLOCL   is the geographic local time in hours and 1/10 hours (at midpoint).
        This is set to 0.0, if no ephemeris tape available.

BXMD, BYMD, BZMD, and BTMD are the GSE components and absolute value, respec-
        tively, of the measured magnetic field, each averaged over the whole
        interval (for data quality check, see description of MD-file). The unit
        is "nanotesla" ("nT"), or equivalently, "gamma".

BETA and IDBETA are a simplified representation of the ion plasma beta and its
        standard deviation (% of absolute value). Its definition is explained
        in the description of the MD-file.

BGND and IDBGND are the average background count rate in counts per sample
        (not per second) and standard deviation (%).

MAXES0 is the number of lines to follow in the current group (usually = 32,
        sometimes less). Each line represents one energy channel, always
        starting with the lowest channel (10 eV/e - 100 eV/e), whether or not
        that channel was sampled, and running through the channels contiguously.
        MAXES0 is the number of the highest energy channel sampled at any phase
        of the energy/mass scan cycle.

NSPLPS is the number of samples per second taken during the current energy/mass
        scan cycle, either 4 (low bit rate) or 16 (high bit rate).

The next N = MAXES0 lines list counting data in N contiguous energy channels,
starting at the bottom channel (I= 1), for H+ (J= 1), He++ (J= 2), He+ (J= 3),
O+ (J= 4), and O++ (J= 5) (M/Q= 1, 2, 4, 16, and 8):

        DO 248 I=1,MAXES0

        IF(IFORMT.EQ.1)THEN
        WRITE(11,246)
       *(ACTR(J),IDCTR(J),IPCTR(J),IUTPC(J),IPDEG(J),IWDEG(J),J=1,5)

    246 FORMAT(X,F7.2,I3,I4,I5,I4,I4,4(F7.2,I3,I3,I5,I4,I4))

        ELSE
        WRITE(11,247)
       *(IACTR(J),IDCTR(J),IPCTR(J),IUTPC(J),IPDEG(J),IWDEG(J),J=1,5)

    247 FORMAT(X,I5,I3,I6,I5,I4,I4,4(I5,I3,I5,I5,I4,I4))

        ENDIF
    248 CONTINUE

The variable names represent the following quantities:

ACTR   is the average (spin-averaged) count rate in floating point represen-
        tation (IFORMT = 1), that is the average number of counts per sample
        (4 or 16 samples per second).

IACTR   is an integer approximation of ACTR, that is ACTR rounded to the nearest
        integer. This format (IFORMT = 2) is used when some ion (usually H+) at
        some energy (usually around one keV) has a value of ACTR that would cause
        the standard format to overflow (IACTR is capped in the rare event that
        it would also overflow). This same integer representation is used for
        all ions at all energies, regardless of where the overflow would have
        ocurred. This condition is usually associated with a change of instru-
        ment operation to low sensitivity mode, so the largest IACTR values
        usually contain counts that have been "corrected", that is multiplied
        by a scaling factor (= 65), and are flagged accordingly (by IDCTR).

IDCTR   is normally the Poisson standard deviation of ACTR (or IACTR), expressed
        in percent and rounded downward to an integer value. That is, IDCTR
        represents the ratio (in %) between the square root of the sum of counts
        and the sum of counts (sum = ACTR * No of samples). In case the instru-
        ment has been in low sensitivity mode at any time while a particular ACTR
        (or IACTR) was being averaged, the IDCTR is instead used as a flag and
        set equal to -9. In that case ACTR (or IACTR) contains "corrected"
        counts and should be treated with some care.

IPCTR   is the maximum number of counts during any single sample (about 1/4:th
        or 1/16:th of a second) of a given ion at a given energy. If IDCTR= -9,
        then IPCTR probably contains a "correction factor" (= 65).

IUTPC   is the (approximate) time of maximum count rate (IPCTR), expressed as
        integer number of seconds after the beginning of the current averaging
        interval. That is, the universal time in seconds is = JSTART + IUTPC.

IPDEG   is the angle of motion in the s/c spin plane of those ions that cause
        the maximum count rate. The angle refers to the midpoint of the samp-
        ling interval (and the midpoint of the instrument field of view), and
        is rounded to the nearest integer. During each sampling interval the
        instrument sweeps (spins) through about 30 deg of angle in low bit rate
        (4 samplings/sec), and about 7.5 deg in high bit rate (16 samplings/sec).

IWDEG   is a measure of the angular width (nearest integer) of the ion flux dis-
        tribution around the maximum. It is a sum of two angles, one being the
        closest spin angle from IPDEG with a count rate less than 1/3 of IPCTR,
        the other being the most distant spin angle from IPDEG with a count rate
        at least 1/3 of IPCTR. That is, IWDEG is a crude measure of the full
        width at 1/3 of maximum. It is measured after IUTPC if more than 1/2
        s/c spin remains, otherwise set to -1. If IPCTR is more than 3 times
        greater than any subsequent counts, IWDEG is set to 30 deg in low bit
        rate and 8 deg in high bit rate (or -1 if too close to end of interval).

8.2 Relevant Instrument Parameters.

To convert counts per sample, or CTS, to counts per second, or CTRATE, use

$$CTRATE = CTS *RATE /0.21865$$

where RATE = 1.0 in low bit rate, and RATE = 4.0 in high bit rate.

However, the count rates in the MC-file are raw counts and need to be adjusted for detector degradation (including peak counts and background). These count rates have been obtained at the higher of two pulse hight triggering levels in the MD particle detector, at the MDTCR = 2 level. The lower level, MDTCR = 1, provides a more nearly one to one detection level, that is one count for every ion entering the detector, but it also admits more false counts due to penetrating radiation than does the higher level. The reason for using the MDTCR = 2 level is to minimize the background. The lower sensitivity to ions is not a problem in itself as long as it is well known, since the count rate can be adjusted accordingly, but it has slowly declined over time, making it necessary to do periodic in-flight calibrations. These have consisted of intercomparing the count rates at the MDTCR = 1 and = 2 levels, which are both part of the instrument output, during times of extremely low background. Fortunately, the MDTCR = 1 level has shown no degradation, and can be used as a standard reference. The following table shows the results of these intercomparisons in the lowest and highest energy channels for the four principal ions (date refers to beginning of month). The intercomparisons for O++ (ION= 5) have been less extensive but suggest that the O+ (ION= 4) ratios can be used for the O++ as well.

```
c Ratios of MDTCR= 2 count rate to MDTCR= 1 count rate in flight;
c
c in lowest energy channel:
     DATA CMD01/
c  launch - Jan 78,    Jul 78,    Jan 79,    Jul 79,    Jan 80,    Jul 80
c ION= 1
     *        .90,       .81,       .60,       .48,       .36,       .24,
c ION= 2
     *        .95,       .90,       .80,       .70,       .60,       .50,
c ION= 3
     *        .95,       .85,       .70,       .60,       .50,       .40,
c ION= 4
     *        .95,       .89,       .75,       .65,       .55,       .45/
c
c in highest energy channel:
     DATA CMD32/
c  launch - Jan 78,    Jul 78,    Jan 79,    Jul 79,    Jan 80,    Jul 80
c ION= 1
     *        .94,       .93,       .82,       .72,       .61,       .50,
c ION= 2
     *        .97,       .95,       .90,       .85,       .80,       .75,
c ION= 3
     *        .97,       .95,       .90,       .85,       .80,       .75,
c ION= 4
     *        .97,       .95,       .90,       .85,       .80,       .75/
```

Intercomparisons have been made at many energies, and it appears that the ratios vary about linearly with energy channel number (1 through 32). That relation has been used when converting count rates to velocity moments in the MD-file, that is, the ratios have been interpolated linearly in energy channel number. They have also been interpolated linearly in time between the dates above. For dates beyond July of 1980 this scheme has been abandoned, and MDTCR = 1 counts have been used exclusively. Given count rates from before July 1980, these are thus to be adjusted by

CTRATE = CTRATE /CMD(IE, date, ION)

where IE is the energy channel No, and CMD(...) is obtained by linear interpolation in IE and date between the CMD01 and CMD32 in the table. For ION= 5 (O++) use the same numbers as for ION= 4 (O+).

There is actually one more adjustment that can be made to improve the one to one relationship between counts and ions in the MC-file. This one does not depend on the MDTCR level, but it depends somewhat on the energy/mass scan mode. To have exactly one count for every ion entering the MD detector, on average, requires that the power supplies controlling the M/Q separation be tuned exactly to the peak response for a given ion at every energy. This is impractical, but in all scan modes, except the so called "load mode", the single mass channel chosen to represent a given ion will have let that ion through at about 90% of peak response, or higher. In the "load mode", however, every mass channel has been sampled, and all counts at a response of 40% or higher have been used (for the five ions listed). The average response for those counts ranges between 70% and 90% of the peak, varying somewhat randomly from one energy channel to the next, but is mostly 80% to 85%.

Therefore, if the counts have been obtained in "load mode" it may be worth adjusting the time averaged counts (ACTR and IACTR) by another factor of about 1.2 (average over energy). The peak count rates (IPCTR) cannot be adjusted for this effect at this stage, since the mass channel No. is not listed. The "load mode" can be recognized from the MS-file (see below). By contrast, all counts used when calculating moments for the MD-file were adjusted for off-peak response on a sample by sample basis (after first summing over the mass peak in load mode).

Once adjusted, the count rates in the MC-file can be converted to differential flux "FLUX" and phase space density "F" with the following subroutine.

```fortran
      SUBROUTINE AFLUX( ION, CTRATE, IE, FLUX, F )
c**** Input:   ION= 1 (H+), 2 (He++), 3 (He+), 4 (O+), or 5 (O++)
c****          CTRATE= counts per second (floating point), and
c****          IE= 1, 2, 3, ....., 32 (energy channel)
c****
c**** Output: "FLUX" in units of "/cm2/sec/ster/keV"
c****         "F" in units of "sec3/km6".
c****  _____
      DIMENSION AM(5),Q(5) ! ion mass and charge units
      DATA AM/1.,4.,4.,16.,16./, Q/1.,2.,1.,1.,2./
c**** instrument energies (center of channels):
      DIMENSION ENERGY(32) ! "keV/e"
      DATA ENERGY/
     *    .040,    .212,    .410,    .628,    .851,  1.095,  1.353,  1.633,
     *  1.929,   2.244,   2.580,   2.934,   3.317,  3.718,  4.146,  4.599,
     *  5.080,   5.592,   6.132,   6.713,   7.333,  7.998,  8.701,  9.446,
     * 10.235, 11.076, 11.969, 12.917, 13.927, 14.999, 16.144, 17.364/
c**** instrument geometric factors, including delta-E:
      DIMENSION G(32,5) ! "1.0E-4 cm2 keV"
      DATA G/
c**** ION= 1:
     * 3.60,6.00,6.00,6.00,6.01,6.01,6.01,6.01,6.01,6.01,6.02,6.02,6.02,
     * 6.48,6.94,7.40,7.85,8.31,8.77,9.23,9.69,10.3,10.9,11.5,12.1,12.8,
     * 13.4,14.0,14.6,15.2,15.8,16.4,
c**** ION= 2:
     * 4.50,7.37,7.20,7.04,6.87,6.70,6.54,6.37,6.21,6.04,5.87,5.71,5.54,
     * 5.85,6.17,6.48,6.80,7.11,7.43,7.74,8.06,8.39,8.71,9.04,9.37,9.69,
     * 10.0,10.4,10.8,11.2,11.6,12.0,
c**** ION= 3:
     * 7.20,11.9,11.3,10.7,10.0,9.41,8.79,8.16,7.54,6.92,6.30,5.67,5.05,
     * 5.37,5.69,6.01,6.32,6.64,6.96,7.28,7.60,7.99,8.38,8.77,9.16,9.54,
     * 9.93,10.3,10.7,11.1,11.5,11.9,
c**** ION= 4:
     * 3.10,5.28,5.23,5.17,5.12,5.07,5.01,4.96,4.91,4.86,4.80,4.75,4.70,
     * 4.85,4.99,5.14,5.29,5.44,5.59,5.73,5.88,6.26,6.63,7.02,7.42,7.82,
     * 8.23,8.61,9.02,9.42,9.82,10.2,
c**** ION= 5:
     * 4.71,7.83,7.55,7.28,7.01,6.74,6.47,6.19,5.92,5.65,5.38,5.10,4.83,
     * 5.05,5.26,5.47,5.69,5.90,6.12,6.33,6.54,6.92,7.30,7.68,8.06,8.52,
     * 8.96,9.34,9.72,10.2,10.6,11.0/
c**** normalize:
      GDE= G(IE,ION)*1.0E-4
c**** differential flux:
      FLUX= CTRATE/GDE/Q(ION) ! "/cm2/s/sr/keV)"
c**** phase space density:
      F= 0.5449208*FLUX*AM(ION)*AM(ION)/Q(ION)/ENERGY(IE) ! "s3/km6"
      RETURN
      END
```

The energy channel widths (in keV/e) and the angular fields of view in each energy channel are inherent in the geometric factors listed in this subroutine (G-delta-E), but it may be of interest to know them separately:

The external energy bandwidth is defined by the internal energy resolution of the instrument, which is about a constant 5% at all energies, but the external bandwidth is not a constant fraction of energy, because the ions are pre-accelerated by about 3.0 kV before they enter energy analysis (energy selection). To obtain the absolute energy bandwidth to incoming ions, add 3.0 keV/e to the center energies listed in the subroutine, except the lowest energy, and take 5% of the sum. The lowest energy channel is different, due to the applied RPA voltage, and extends approximately between 10 eV/e and 100 eV/e (more precisely to about 110 eV/e).

As mentioned, the center of the instrument field of view (the one used here) points 5 deg below the spin plane, that is about 5 deg below the GSE X-Y plane (ion velocity vector pointing 5 deg above). In this plane the width is about 10 deg. In the perpendicular (GSE Z) direction it varies with energy (due to the pre-acceleration), from about 45 deg at 10 eV/e to 10 deg at 18 keV/e. To be more specific, if the center energies of the 32 energy channels are used as reference, the corresponding 32 angular widths are as follows (full width at 25% of max; in deg):

```
40.0, 30.0, 26.0, 22.5, 20.0, 18.0, 16.5, 15.5,
15.0, 14.0, 13.5, 13.0, 13.0, 12.5, 12.5, 12.0,
12.0, 11.5, 11.5, 11.0, 11.0, 11.0, 11.0, 10.5,
10.5, 10.5, 10.5, 10.5, 10.5, 10.0, 10.0, 10.0
```

9. THE MS-FILE

This file contains complete mass spectra in four energy ranges, provided the instrument energy/mass scan included complete mass scans at some energies (not always the case). The counts in this file are also from the MD detector, but they are normally not the same counts as those listed in the MC-file, which went into moment calculations for the MD-file. It is only in the mode called "load mode" that the same raw counts have been used in all three files with MD data. This particular mode (hardwired) consists of one complete 32-step energy scan in each successive mass channel over the complete 64 mass-channel range (four such scan cycles have been used to define a full cycle in high bit rate here). This scan mode is used infrequently, and can be recognized by the fact that the number of samplings in the MS-file (see below) add up to cover the entire averaging interval (entire scan cycle). In all other scan modes the mass spectra are obtained as separate and small parts of each energy/mass scan cycle, and are only used to provide data for the MS-file here. For simplicity, the same beginning and ending times are listed here as are listed in the MD-file, even if the mass spectra were obtained for brief intervals well inside those times.

The four mass spectra are listed in four vertical columns, with each line representing one mass channel, beginning with channel No. 1 at the top and ending with No. 64 at the bottom. Each column represents one energy range, with the energy increasing from left to right:

Leftmost energy range: channel No. 1 (about 10 eV/e - 100 eV/e).

Second to the right: channels No. 2 - 5 (about 100 eV/e - 1 keV/e)

Third to the right: channels No. 6 - 12 (about 1 keV/e - 3 keV/e)

Fourth to the right: channels No. 13 - 31 (about 3 keV/e - 16 keV/e)

The counts in each mass channel (on each line) are a sum of counts from all energy channels sampled within each energy range. Along with the sum of counts is the number of samples.

The MS-counts are pure raw counts; no "corrective" factor has been applied when the instrument has been operating in low sensitivity mode. However, each column has a flag above it showing how many of the samples in that column were taken in low sensitivity mode (without specifying mass channel). No background counts have been subtracted either.

Within each mass spectrum (each column) certain mass peaks may be found more often than others. The following is a listing of expected mass channel No. (1 through 64) at peak count rate for certain important M/Q:

M/Q= 16.00   about 16 to 17

   = 8.00   about 21 to 22

   = 4.00   about 29 to 30

   = 2.66   about 35 to 36

   = 2.00   about 40 to 41

   = 1.50   about 45 to 46

   = 1.00   about 55 to 56

9.1 File Format

The MS-file has been written in groups of 68 lines (65 records),
using formatted sequential FORTRAN WRITE statements as follows:

The first line in each group is blank, the second and third make up a title,
and the fourth lists (above each mass spectrum) the No. of samples taken in
low sensitivity mode:

```
     WRITE(12,255)
    *IYYDDD,JSTART,JSTOP,RX,RY,RZ,RT,RSEY,RSEZ,DZ,IMLAT,TLOCL,
    *BXMD,BYMD,BZMD,BTMD,BETA,IDBETA,BGND,IDBGND,MAXEMS,NSPLPS,
    *(IMSLOW(I),I=1,4)

  255 FORMAT(X/I6,2I5,7F6.1,I4,F5.1/X,4F8.1,1PE10.2,I3,1PE9.2,I3,2I3/
    *X,4I13)
```

The variable names represent the following quantities:

IYYDDD is the year (two digits) and day of year (three digits).

JSTART is the universal time in minutes at the beginning of the averaging
       interval, that is the time of the first good data in that interval.
       This is normally at the start of an energy/mass scan cycle, unless
       some initial data in that cycle are bad.

JSTOP is the universal time in minutes at the end of the averaging interval,
       that is the time of the last good data in that interval. This is nor-
       mally at the end of an energy/mass scan cycle, unless the last data in
       that cycle are bad.

RX, RY, RZ, and RT are, respectively, the GSM X, Y, Z, and radial distance
       at the midpoint of the averaging interval, all in units of "earth
       radii" ("Re"). RY and RZ are set to 999. if GSM coordinates not
       available (RX same in GSE).

RSEY and RSEZ are the GSE Y and Z (at midpoint of averaging interval) in units
       of "earth radii".

DZ   is the distance in "earth radii" (at midpoint) from the nominal neutral
          sheet in the geotail according to Fairfield and Ness [J.Geophys. Res.,
          75, 7032, 1970]. This is only displayed for GSM X < -11 Re, otherwise
          set to 999. If no GSM coordinates available, it is set to 0.

IMLAT   is the geomagnetic latitude in degrees (at midpoint), rounded to the
          nearest integer. This is set to 0, if no ephemeris tape available.

TLOCL   is the geographic local time in hours and 1/10 hours (at midpoint).
          This is set to 0.0, if no ephemeris tape available.

BXMD, BYMD, BZMD, and BTMD are the GSE components and absolute value, respec-
          tively, of the measured magnetic field, each averaged over the whole
          interval (for data quality check, see description of MD-file). The unit
          is "nanotesla" ("nT"), or equivalently, "gamma".

BETA and IDBETA are a simplified representation of the ion plasma beta and its
          standard deviation (% of absolute value). Its definition is explained
          in the description of the MD-file.

BGND and IDBGND are the average background count rate in counts per sample
          (not per second) and standard deviation (%).

MAXEMS   is the number of the highest energy channel included in the mass spectra
          (31 or lower).

NSPLPS   is the number of samples per second taken during the current energy/mass
          scan cycle, either 4 (low bit rate) or 16 (high bit rate).

IMSLOW   is the total number of samples taken in low sensitivity mode while
          gathering the mass spectrum below it (regardless of mass channel).

The next 64 lines, one for each mass channel, list the accumulated number of
counts (sums) in each of four energy ranges (explained above), along with the
corresponding number of samples:

      DO 258 J=1,64

      WRITE(12,257)((ISUM04(I),ISPL04(I)),I=1,4)

   257 FORMAT(X,4(I9,I4))

   258 CONTINUE

The variable names represent the following quantities:

ISUM04 is the accumulated number of counts within energy range I, regardless
          of instrument look angle.

ISPL04 is the corresponding number of samples (4 per seconds in low bit rate,
          16 per seconds in high; cf. NSPLPS)

10. THE EX-FILE

This file contains auxiliary ISEE-1 ephemeris that may be used for labeling
plots of data from the other files (see comments on existing plots at the end
of this data user's guide). It is derived from separate ISEE ephemeris tapes
which have a more complete set of coordinates, all listed once per minute. This
file has a subset of the ephemeris, and it only lists this set every 30 minutes.
If the ephemeris tape is unavailable (unreadable), it substitutes the GSE coor-
dinates from the instrument data telemetry tape for the corresponding ephemeris
coordinates, choosing these to be as closely as possible on the half hour, and
fills the remaining positions with dummy numbers.

10.1 File Format

The EX-file always has 49 lines (records) which have been written with
a formatted sequential FORTRAN WRITE as follows:

```
      MMMM=0
      DO 38 I=1,49
   36 WRITE(7,37) IYYDDD,MMMM,RX,RY,RZ,RT,DZ,IMLAT,TLOCL,RSEY,RSEZ,RL

   37 FORMAT(I6,I5,5F6.1,I4,F5.1,2X,3F6.1)

   38 MMMM=MMMM+30
```

The variable names represent the following quantities:

IYYDDD is the year (two digits) and day of year (three digits).

MMMM   is the universal time in minutes.

RX, RY, RZ, and RT are the GSM X, Y, Z, and radial distance, respectively,
       all in units of "earth radii" ("Re"). RY and RZ are set to 999. if
       GSM coordinates not available (RX same in GSE).

DZ   is the (calculated) distance in "earth radii" from the nominal neutral
       sheet in the geotail according to Fairfield and Ness [J.Geophys. Res.,
       75, 7032, 1970]. This is only displayed for GSM X < -11 Re, otherwise
       set to 999. If no GSM coordinates available, it is set to 0.

IMLAT is the geomagnetic latitude in degrees, rounded to the nearest integer.
       This is set to 0, if no ephemeris tape available.

TLOCL is the geographic local time in hours and 1/10 hours. This is set to 0,
       if no ephemeris tape available.

RSEY and RSEZ are the GSE Y and Z in "earth radii" (may have values even when
       no ephemeris tape available; same with RX and RT).

RL   is McIlwain's L value. This is only defined in the inner magnetosphere,
       otherwise set to 0. (also when no ephemeris tape available).

11. GRAPHIC REPRESENTATION

A subset of the data in the ED- and MD-files is available in graphical form in a series of booklets, one booklet for each month of data. There are two pages of graphs for each day, each page covering 12 hours of universal time. Each page consists of a vertical stack of 7 panels. These panels show the following data items:

Panel 1 (top) shows the "total" ion density from the ED-file (EDDNS) and the partial densities of He++, He+, and O+ from the MD-file (DNS8). Note: the labels He+ and O+ may not be appropriate in the magnetosheath and solar wind, where heavier ions in high charge states may dominate weak count rates near those M/Q values, especially near M/Q= 4.

Panel 2 shows the He++/H+ density ratio from the MD-file (DNS8[He++]/DNS8[H+]). This panel and the top one are the only ones with MD-data, the ones below all have data from the ED-file only.

Panel 3 shows the ion "thermal" energy from the ED-file (EDEMN).

Panel 4 shows the "thermal" energy density from the ED-file multiplied by 2/3 (EDDNS*EDEMN*2./3.) along with the magnetic pressure and field strength based on the ED-averages. Note: the magnetic pressure and field strength are based on the square root of BXED**2 + BYED**2 + BZED**2 (not on BTED) in order to show more clearly those (rare) times when the magnetic field is flawed. Those times are mostly characterized by a sudden and/or strong reduction in the magnetic pressure/field strength which is not associated with a corresponding increase in the "thermal" energy density of the ions (total pressure not preserved). The brief (one data point) error in the magnetic field gain factor on many inbound passes is also clearly seen in this panel (errors discussed in connection with the ED- and MD-files above).

Panel 5 shows the ion drift speed (in GSE X-Y plane) from the ED-file (EDVEL).

Panel 6 shows the magnetic field elevation angle (relative GSE X-Y plane) from the ED-file (ITHETB).

Panel 7 (bottom) shows the ion drift angle (IEDANG) and magnetic longitude angle (IPHIB) in the GSE X-Y plane from the ED-file.

Below the bottom panel are the UT and assorted ephemeris. When ephemeris tape has not been available (very rare) only the geocentric distance (R) will show.

APPENDIX A

(continued)

Sample printouts of data files

A1. Magnetosphere /Geomagnetically Quiet Day

(Low O+/H+ density ratio)

	ID																	
78064	94	-0.9	4.7	5.9	7.7	51	101	1.65E+00	2.08E+00	1.56E+01	33	92.00	0.00	0.1	16.1	-12.3	-11.3	-0.8
78064	242	-2.2	4.6	7.3	8.9	55	115	1.80E+00	2.13E+00	7.95E+00	73	168.00	0.00	0.1	16.1	-12.3	-11.3	-0.8
78064	374	-2.4	4.2	8.2	9.6	60	120	1.64E+00	2.23E+00	7.20E+00	88	60.00	0.00	0.1	16.1	-12.3	-11.3	-0.8
78064	438	-2.0	3.7	7.9	9.0	62	119	1.67E+00	2.23E+00	3.48E+00	-97	60.00	0.00	0.1	16.1	-12.3	-11.3	-0.8
78064	502	-1.2	3.7	6.7	7.8	60	108	1.71E+00	2.24E+00	1.95E+01	-30	60.00	0.00	0.1	16.1	-12.2	-11.3	-0.8
78064	582	0.6	4.9	5.2	7.2	47	83	1.84E+00	2.23E+00	1.79E+01	-7	88.00	0.00	0.1	16.1	-12.2	-11.3	-0.8
78064	666	1.9	6.4	5.4	8.6	39	73	1.68E+00	2.20E+00	1.74E+01	4	68.00	0.00	0.1	16.1	-12.2	-11.3	-0.8
78064	742	1.9	6.7	6.0	9.3	41	74	1.83E+00	2.11E+00	2.10E+01	72	60.00	0.00	0.1	16.1	-12.2	-11.2	-0.8
78064	805	1.6	6.3	6.1	9.0	43	76	1.84E+00	2.12E+00	3.21E+01	56	60.00	0.00	0.1	16.1	-12.2	-11.2	-0.8
78064	869	2.4	6.5	5.1	8.7	36	69	1.84E+00	2.02E+00	3.30E+01	21	60.00	0.00	0.1	16.1	-12.1	-11.2	-0.8
78064	933	4.2	7.8	4.6	10.0	27	62	1.90E+00	1.89E+00	2.57E+01	-28	60.00	0.00	0.1	16.1	-12.1	-11.2	-0.8
78064	1021	4.8	7.3	5.8	10.5	34	57	2.02E+00	1.69E+00	2.95E+01	-39	104.00	0.00	0.1	16.1	-12.1	-11.2	-0.8
78064	1177	6.5	12.0	6.0	14.9	24	62	2.47E+00	1.44E+00	4.34E+01	-36	168.00	0.00	0.1	16.1	-12.1	-11.2	-0.8
78064	1309	4.0	9.0	4.1	10.7	23	66	1.65E+00	1.86E+00	2.81E+01	-79	60.00	0.00	0.1	16.1	-12.1	-11.2	-0.8
78064	1373	1.3	7.4	4.2	8.6	29	80	1.76E+00	1.93E+00	2.77E+01	-123	60.00	0.00	0.1	16.1	-12.0	-11.2	-0.8
78064	1437	1.7	8.2	3.7	9.3	24	78	1.77E+00	1.98E+00	2.60E+01	-169	60.00	0.00	0.1	16.1	-12.0	-11.2	-0.8
78064	1517	4.9	11.2	3.2	12.7	15	67	2.03E+00	1.65E+00	2.29E+01	-225	88.00	0.00	0.1	16.1	-12.0	-11.2	-0.8
78064	1601	7.2	13.3	5.4	16.1	20	61	1.76E+00	1.47E+00	2.38E+01	85	68.00	0.00	0.1	16.1	-11.9	-11.2	-0.8
78064	1677	8.9	14.4	5.6	17.9	18	58	2.30E+00	1.12E+00	2.16E+01	26	60.00	0.00	0.1	16.1	-11.9	-11.1	-0.8
78064	1741	11.0	15.0	4.4	19.1	13	54	2.38E+00	1.10E+00	2.97E+01	18	60.00	0.00	0.1	16.1	-11.9	-11.1	-0.8
78064	1805	10.5	15.3	4.2	19.1	13	56	2.60E+00	1.11E+00	3.41E+01	-26	60.00	0.00	0.1	16.1	-11.8	-11.1	-0.8
78064	1869	10.6	13.5	5.3	17.9	17	52	2.46E+00	1.19E+00	1.68E+01	4	60.00	0.00	0.1	16.1	-11.8	-11.1	-0.8
78064	1957	10.2	14.0	4.1	17.8	13	54	2.21E+00	1.34E+00	1.91E+01	-61	104.00	0.00	0.1	16.1	-11.8	-11.1	-0.8
78064	2113	6.4	11.1	5.2	14.3	22	60	2.17E+00	1.62E+00	2.21E+01	-41	168.00	0.00	0.1	16.1	-11.8	-11.1	-0.8
78064	2261	1.2	9.0	7.0	11.5	38	82	1.77E+00	1.81E+00	2.44E+01	-48	87.75	0.00	0.1	16.1	-11.8	-11.1	-0.8
78064	2341	2.3	9.3	5.9	11.2	32	76	1.77E+00	1.79E+00	2.91E+01	-22	60.00	0.00	0.1	16.1	-11.8	-11.1	-0.8
78064	2405	4.3	9.9	5.3	12.0	26	66	1.81E+00	1.77E+00	2.60E+01	-43	60.00	0.00	0.1	16.1	-11.7	-11.1	-0.8
78064	2473	6.1	11.1	4.3	13.4	19	61	1.86E+00	2.15E+00	1.42E+01	-55	68.00	0.00	0.1	16.1	-11.7	-11.1	-0.8
78064	2541	6.2	11.3	3.8	13.4	16	61	1.69E+00	1.74E+00	1.25E+01	-82	60.00	0.00	0.1	16.1	-11.7	-11.1	-0.8
78064	2613	6.2	11.4	3.6	13.5	16	61	1.93E+00	1.57E+00	1.38E+01	-68	60.00	0.00	0.1	16.1	-11.6	-11.1	-0.8
78064	2677	6.4	11.5	3.7	13.7	16	61	1.86E+00	1.55E+00	8.51E+00	-80	60.00	0.00	0.1	16.1	-11.6	-11.1	-0.8
78064	2741	6.5	11.5	3.5	13.7	15	60	1.89E+00	1.56E+00	2.78E+01	-63	60.00	0.00	0.1	16.1	-11.6	-11.1	-0.8
78064	2805	6.1	11.0	3.4	13.0	15	61	1.85E+00	1.55E+00	3.71E+01	-60	60.00	0.00	0.1	16.1	-11.6	-11.1	-0.8
78064	2893	3.2	9.0	3.4	10.2	20	70	1.94E+00	1.54E+00	2.40E+01	-153	104.00	0.00	0.1	16.1	-11.5	-11.1	-0.8
78064	3048	2.0	9.4	5.0	11.0	27	78	1.86E+00	1.66E+00	8.80E+00	-134	168.00	0.00	0.1	16.1	-11.5	-11.1	-0.8
78064	3180	5.0	11.3	2.9	12.7	13	66	1.78E+00	1.68E+00	1.82E+01	-221	60.00	0.00	0.1	16.1	-11.5	-11.0	-0.8
78064	3244	5.5	12.9	3.1	14.3	13	67	1.65E+00	1.66E+00	1.63E+01	81	60.00	0.00	0.1	16.1	-11.5	-11.0	-0.8
78064	3408	6.3	12.7	3.7	14.7	15	64	1.93E+00	2.21E+00	1.38E+01	71	68.00	0.00	0.1	16.1	-11.4	-11.0	-0.8
78064	3476	6.2	12.7	3.6	14.6	14	64	1.66E+00	1.69E+00	1.86E+01	108	60.00	0.00	0.1	16.1	-11.4	-11.0	-0.8
78064	3548	5.8	12.5	3.3	14.2	13	65	1.94E+00	1.53E+00	1.50E+01	168	60.00	0.00	0.1	16.1	-11.4	-11.0	-0.8
78064	3612	5.8	12.1	4.1	14.1	17	64	1.91E+00	1.53E+00	9.34E+00	107	60.00	0.00	0.1	16.1	-11.4	-11.0	-0.8
78064	3676	6.2	11.9	4.2	14.0	17	63	1.92E+00	1.54E+00	1.70E+01	115	104.00	0.00	0.1	16.1	-11.4	-11.0	-0.8
78064	3828	6.9	11.6	5.0	14.4	20	59	1.98E+00	1.49E+00	1.31E+01	172	168.00	0.00	0.1	16.1	-11.4	-11.0	-0.8
78064	3984	5.9	11.8	6.2	14.6	25	64	1.96E+00	1.58E+00	1.19E+01	118	60.00	0.00	0.1	16.1	-11.4	-11.0	-0.8
78064	4116	7.3	13.4	4.1	15.8	15	61	1.77E+00	1.53E+00	2.15E+01	40	60.00	0.00	0.1	16.1	-11.4	-11.0	-0.7
78064	4180	8.0	14.2	4.5	17.0	16	60	1.79E+00	1.42E+00	1.84E+01	25	60.00	0.00	0.1	16.1	-11.4	-11.0	-0.7
78064	4244	7.0	11.9	5.6	15.0	22	60	1.76E+00	1.53E+00	1.62E+01	27	60.00	0.00	0.1	16.1	-11.4	-10.9	-0.7

The following is a dense numeric data dump ("MD-file"). It is reproduced below in reading order (the page is printed rotated 90°). Each group begins with a record line starting `78064 <index>` followed by data rows.

```
78064    2    18 -12.2 -11.3   -0.8 16.6   0.5  5  3.1    0.8  5.7 11  6.3  9.1   1.28E+01           1.58E+00  0   9.22E-01   16.1 1   -9.8  5.6
1.10E-01   5   1.57E+00  0   2.17E+00  0   8.25E+00 22  42   13  4.19E-03 11 124.00 0.00   24 146   5.52E-02  1   1.46E+00   16.1 1    7.17E-01  0
8.07E-04  65   5.66E-02  2   6.72E+00  2   1.56E+01 40 -19   19  3.94E-03 11 124.00 0.00   39 137   7.77E-03 10   4.39E+00   16.1 1    2.39E+00  2
0.00E+00  -1   7.86E-03 12   3.03E+00 18   5.29E+01 42 -41   23  5.11E-03 11 124.00 0.00   23 151   1.82E-02 13   2.26E+00   16.1 1    9.36E-01 17
3.85E-03  74   1.85E-02 14   5.79E+00 11   4.81E+00260  21   76  1.45E-02 11 124.00 0.00   24 147                3.94E+00   16.1 1    2.08E+00  9

78064   18    33 -12.0 -11.2   -0.8 16.4   0.6  5  3.1    7.1 12.2 11  4.7 15.1   3.46E+00           1.65E+00  0   9.10E-01   16.1 1   -9.8  5.5
3.18E-01   4   1.73E+00  0   1.43E+00  0   2.90E+01  4  12    2  4.13E-03 11 124.00 0.00    7 165   6.48E-02  2   8.98E-01   16.1 1    5.25E-01  0
5.03E-04  97   6.60E-02  2   5.14E+00  2   1.15E+01 46 -20   20  3.89E-03 11 124.00 0.00    6 165   5.90E-03 15   3.38E+00   16.1 1    1.71E+00  2
1.50E-03  35   5.78E-03 16   2.32E+00 33   2.92E+01 97 -126  95  5.04E-03 11 124.00 0.00    8 165   2.69E-02 10   1.55E+00   16.1 1    5.82E-01 45
2.13E-03 129   2.97E-02  9   3.92E+00 10   2.34E+01 36  66   16  1.43E-02 11 124.00 0.00    4 165                2.32E+00   16.1 1    1.54E+00  9

78064   33    49 -11.8 -11.1   -0.8 16.2   0.7  6  3.1    4.9 10.4 11  4.5 12.6   5.37E+00           1.59E+00  0   8.87E-01   16.1 1   -9.7  5.4
2.02E-01   4   1.67E+00  0   1.67E+00  0   1.34E+01  9 -15    4  4.03E-03 11 123.75 0.00    8 161   5.79E-02  2   1.07E+00   16.1 1    6.04E-01  0
0.00E+00  -1  -6.09E-02  2   5.52E+00  2   1.63E+01 35 -19   16  3.79E-03 11 124.00 0.00   11 161   5.57E-03 15   3.52E+00   16.1 1    2.05E+00  2
5.32E-04  70   5.45E-03 16   1.61E+00 56   4.55E+01 63 -112  31  4.91E-03 11 124.00 0.00    8 162   1.36E-02 17   1.22E+00   16.1 1    7.02E-01 39
-1.13E-03 156  1.20E-02 21   5.08E+00 17  -1.00E+00 -1   0   -1  1.40E-02 11 124.00 0.00    5 166                4.38E+00   16.1 1    1.26E+00 19

78064   49    65 -11.5 -11.0   -0.8 16.0   0.9  6  3.1    6.4 12.1 17  4.1 14.3   4.10E+00           1.70E+00  0   7.62E-01   16.1 1   -9.7  5.3
0.00E+00  -1   1.75E+00  0   1.53E+00  0   1.44E+01 12 102    7  2.86E-03 17  60.00 0.00    8 161   5.97E-02  3   9.30E-01   16.1 1    5.78E-01  0
0.00E+00  -1   6.23E-02  3   5.80E+00  3   3.16E+01 27 119   20  3.22E-03 17  60.00 0.00   11 160   5.62E-03 20   3.78E+00   16.1 1    1.99E+00  2
0.00E+00  -1   5.71E-03 21   2.29E+00 37  -1.00E+00 -1   0   -1  4.22E-03 17  68.00 0.00   11 161   2.32E-02 12   1.64E+00   16.1 1    9.21E-01 29
3.68E-03  73   2.21E-02 13   4.58E+00 11   2.28E+01 47 -145  29  1.20E-02 17 124.00 0.00    5 162                3.75E+00   16.1 1    1.26E+00 11

78064   65    80 -11.4 -10.9   -0.7 15.8   1.0  7  3.1    2.2  8.7 11  7.6 13.2   4.70E+00           1.68E+00  0   9.57E-01   16.1 1   -9.6  5.2
2.87E-01   3   1.67E+00  0   1.58E+00  0   1.40E+01  9  43    5  4.35E-03 11 124.00 0.00   10 158   6.04E-02  2   1.03E+00   16.1 1    5.35E-01  0
1.01E-03  63   5.84E-02  2   4.92E+00  3   2.37E+01 25 -62   24  4.10E-03 11 124.00 0.00    5 164   5.40E-03 15   3.35E+00   16.1 1    1.65E+00  3
2.66E-03  26   4.78E-03 19   1.69E+00 62   4.53E+01 73 -144 181  5.30E-03 11 124.00 0.00   19 155   1.99E-02 11   1.40E+00   16.1 1    4.19E-01 69
8.46E-03  45   1.99E-02 14   4.78E+00 12   1.01E+01121 -148 116  1.51E-02 11 124.00 0.00   19 152                3.16E+00   16.1 1    1.83E+00  9

78064   80    96 -11.2 -10.9   -0.7 15.6   1.1  7  3.2   -0.2  5.8 11  5.6  8.4   1.20E+01           1.86E+00  0   8.28E-01   16.1 1   -9.6  5.1
2.27E-01   4   1.84E+00  0   1.47E+00  0   1.18E+01 10 -23    5  3.76E-03 11 124.00 0.00   28 144   6.15E-02  2   9.71E-01   16.1 1    4.81E-01  0
1.15E-03  50   6.23E-02  2   5.17E+00  2   1.14E+01 50  65   28  3.55E-03 11 124.00 0.00   29 142   7.62E-03 11   3.37E+00   16.1 1    1.79E+00  2
1.23E-03  48   8.08E-03 12   1.56E+00 37   2.42E+01 80 149   77  4.59E-03 11 124.00 0.00   28 144   2.15E-02 11   1.43E+00   16.1 1    5.20E-01 35
6.98E-03  47   2.50E-02 11   4.41E+00 11   1.39E+01 68  34   23  1.31E-02 11 124.00 0.00   19 153                3.10E+00   16.1 1    1.73E+00  8

78064   96   111 -11.0 -10.8   -0.6 15.4  999.0 8  3.2   -2.0  5.6 12  7.5 10.5   7.78E+00           1.76E+00  0   7.35E-01   16.1 1   -9.5  5.0
3.47E-01   3   1.76E+00  0   1.55E+00  0   1.58E+01  8  34    6  3.34E-03 12 124.00 0.00   21 148   6.17E-02  2   1.01E+00   16.1 1    5.40E-01  0
1.06E-03  55   6.25E-02  2   5.02E+00  2   6.27E+00 91  80   29  3.15E-03 12 124.00 0.00   21 150   5.77E-03 12   3.28E+00   16.1 1    1.80E+00  2
8.55E-04  50   6.20E-03 14   2.71E+00 25   1.04E+01240 165   87  4.08E-03 12 124.00 0.00   32 138   2.48E-02  8   1.82E+00   16.1 1    6.84E-01 30
-3.84E-04 439  2.43E-02 10   5.07E+00  9   2.27E+01 44   3   25  1.16E-02 12 124.00 0.00   33 141                3.34E+00   16.1 1    1.43E+00  8

78064  111   127 -10.7 -10.7   -0.6 15.1  999.0 8  3.2    2.7  8.5 12  7.7 12.5   5.41E+00           1.54E+00  0   8.05E-01   16.1 1   -9.5  4.9
2.32E-01   4   1.57E+00  0   1.68E+00  0   2.00E+01  6  11    3  3.66E-03 12 124.00 0.00   17 152   6.00E-02  2   1.11E+00   16.1 1    5.88E-01  0
1.13E-03  53   6.36E-02  2   5.68E+00  2   1.89E+01 31   4   15  3.45E-03 12 124.00 0.00   21 151   7.73E-03 11   3.91E+00   16.1 1    1.86E+00  2
1.74E-03  37   7.14E-03 13   3.59E+00 15   1.26E+01180  58  159  4.46E-03 12 124.00 0.00   19 151   2.58E-02  9   2.49E+00   16.1 1    6.94E-01 25
6.06E-03  59   2.65E-02 10   4.32E+00 11   2.65E+01 33 -63   28  1.27E-02 12 114.50 0.00   24 148                3.03E+00   16.1 1    1.28E+00 11

78064  127   142 -10.5 -10.6   -0.5 14.9  999.0 9  3.2   -0.1  7.4 12  7.6 10.8   7.43E+00           1.69E+00  0   7.47E-01   16.1 1   -9.4  4.9
2.81E-01   3   1.68E+00  0   1.65E+00  0   1.38E+01 12  28    7  3.39E-03 12 124.00 0.00   26 144   6.41E-02  1   1.07E+00   16.1 1    5.78E-01  0
2.04E-03  35   6.56E-02  2   5.69E+00  2   2.12E+01 27 121   32  3.20E-03 12 124.00 0.00   26 144   7.90E-03  9   3.84E+00   16.1 1    1.98E+00  2
2.35E-03  31   8.16E-03 11   2.72E+00 18   3.17E+01 65 240   25  4.14E-03 12 124.00 0.00   25 144   1.72E-02 12   1.98E+00   16.1 1    8.10E-01 18
4.56E-03  72   1.61E-02 15   5.46E+00 12   3.58E+01 40 -60   20  1.18E-02 12 124.00 0.00   26 144                3.99E+00   16.1 1    1.53E+00 10

78064  142   158 -10.3 -10.5   -0.5 14.7  999.0 9  3.3    2.1  8.8 11  5.3 10.8   8.58E+00           1.86E+00  0   8.75E-01   16.1 1   -9.3  4.7
1.62E-01   4   1.88E+00  0   1.73E+00  0   1.33E+01 11 -116   7  3.98E-03 11 124.00 0.00   19 151                1.17E+00   16.1 1    5.62E-01  0
78064  158
```

```
1
78064    158  1093 -12.2 -11.3   -0.8 16.6   -9.8 5.6    0.5 5    3.1 0.8    5.7 6.3    9.1 1.28E+01   0 2.02E-01 11 32  4
 21.19   5  42  189 185 360   0.56 33  2   255 352 360   0.25 50  1   381 184 360   0.44 37  2   509 252 360   0.31 44  1   448 228 360
 99.63   2 133  580  50 360   2.81 14  6   645 158 207   0.81 27  3   773 257 207   0.44 37  3   903 113 360   0.31 44  1   446  21 360
 62.50   3  75  194 328 360   2.50 15  5   257 288 266   0.81 27  2   384 268 157   0.13 70  2   515 243  30   0.25 50  1   452 342 360
101.00   2 123  584 164 360   3.63 13  6   649 243 360   0.88 26  4   777  10 182   0.88 26  4   907 286 360   0.13 70  1   440   1 360
167.50   1 189  184 253 360   4.56 11  7   248 302 360   0.81 27  2   376  11 360   0.31 44  2   504  79 360   0.38 40  1   456  66 360
139.25   2 165  578 173 360   5.00 11  9   642 193 360   0.88 26  4   771 350  54   0.56 33  2   896   4 360   0.13 70  1   439 242 360
111.13   2 141  199 200 360   4.94 11  8   260 283 360   0.81 27  4   388  22  69   0.25 50  1   517  90 360   0.25 50  1   460 268 360
 97.00   2 115  590 155 360   5.31 10 10   652 297 266   0.81 27  4   780 336 123   0.56 33  1   908 345 360   0.44 37  2   433 222 360
 76.31   2  95  180 140 360   4.69 11  8   245 277 296   0.63 31  3   375 223 207   0.25 50  1   500 266 360   0.25 50  1   464 293 360
 78.94   2  99  572 153 360   3.31 13  7   637 350 182   0.56 33  3   767 237  94   0.31 44  2   894 127 360   0.06100  1   431  15 360
 62.06   3  79  204  72 360   3.69 13  8   264   7 187   0.56 33  3   393 165 360   0.31 44  1   520  85 360   0.06100  1   470 343 360
 71.94   2  83  595 327 360   3.00 14  7   659  17 360   0.50 35  2   784  31 182   0.44 37  2   913 247 360   0.25 50  1   425  24 360
 74.38   2  99  176  85 360   3.38 13  6   242 253 296   1.06 24  2   369 232 360   0.69 30  2   498  89 360   0.13 70  1   473 279 360
 70.56   2  99  571   5 360   3.56 13  6   632  29 296   0.44 37  2   761 246 360   0.44 37  1   888 107 360   0.25 50  2   421 271 148
 75.88   2  87  205 279 360   3.63 13  7   270  28 266   0.56 33  1   397 308 360   0.19 57  1   524 229 360   0.06100  1   477  62 360
 80.56   2  95  597 234 360   3.56 13 10   663 101 207   0.31 44  1   788 174 360   0.38 40  2   919 238 360   0.25 50  1   416   9 360
 78.88   2  99  175 297 360   3.88 12  8   237  50 266   0.44 37  1   364 330 157   0.31 44  1   492  98 360   0.13 70  1   840 242 360
 70.38   2  87  567 340 360   4.38 11  8   631 271 360   0.25 50  2   756  14 360   0.50 35  2   887  78 360   0.13 70  1   836 158 360
 62.75   3  79  211 240 360   3.19 14  9   273 324 153   0.56 33  1   400 274 182   0.63 31  2   528  12 360   0.13 70  1   845  84 360
 45.25   3  75  601 348 360   3.19 14  7   666  96 207   0.31 44  2   792 317 182   0.31 44  2   922 203 360   0.38 40  2   832  14 360
 40.63   3  58  170  94 360   2.50 15  5   232 207 360   0.25 49  2   360 276 360   0.56 33  2   488 256 360   0.25 50  1   848  50 360
 26.00   4  38  562  19 360   2.25 16  6   627 187  94   0.38 40  1   752 231 360   0.63 31  1   880 329 360   0.19 57  1   828 261 360
 19.31   5  24  213  88 360   2.50 15  6   279 344 123   0.25 50  1   405 146 360   0.88 26  3   532  96  69   0.25 50  1   852 223 360
 12.81   6  22  607   8 360   1.19 22  4   668  62 182   0.31 44  1   796  12 360   0.50 35  2   924 139 148   0.19 57  2   824 117 157
  8.81   8  14  167  40 360   1.13 23  3   229 242 296   0.31 44  2   359 158 360   0.94 25  3   484 172 360   0.19 57  1   856 307 360
  8.13   8  11  558 266 360   0.94 25  3   623 103 360   0.31 44  2   750  23 360   0.63 31  2   876 156 157   0.19 57  1   821 181 207
  5.44  10  10  216 142 193   0.50 35  2   409 319 360   0.25 50  1   539 205 360   0.69 30  3   821 181 207   0.31 44  3   860  61 360
  5.75  10   9  612 350 360   0.50 35  2   677  48 360   0.50 35  1   804 298 360   0.50 35  2   935   2  -1   0.06100  1   816 279 360
  3.44  13   6  160 350 360   0.38 40  2   225  98 360   0.44 37  2   355  44 360   0.31 44  2   480 117 360   0.31 44  1   864 145 360
  2.25  16   7  611  92  94   0.13 70  1   674 353 360   0.19 57  1   800 185 360   0.56 33  4   929 312 118   0.31 44  1   812 107 360
  2.00  17   4  220 197 178   0.31 44  1   285 335 360   0.25 50  2   415 280 360   0.44 37  1   540 324 360   0.19 57  1   868 318 360
  1.18  19   3  554 211 266   0.22 44  1    10 196 360   0.33 70  1     7 201 360   0.36 24  2   810 289 360   0.28 44  1   744   3 360
1
78064   1093 2029 -12.0 -11.2   -0.8 16.4   -9.8 5.5    0.6 5    3.1 0.8    7.1 4.7   15.1 3.46E+00   0 1.99E-01 11 32  4
 51.75   3 213  191 272 178   0.38 40  1   253  55 360   1.31 21  9   384  89 360   0.38 40  2   508 103  94   0.25 50  1   449 257 360
278.50   1 345  581  20 360   6.88  9 11   648  64 360   1.00 24  4   772  19 182   0.56 33  2   901 206 237   0.06100  1   445  84 360
 72.94   2  99  194 268 360   2.63 15  6   259  46 237   0.88 26  2   387  55 360   0.44 37  2   514  35 360   0.25 50  2   454  99 360
148.75   2 221  587  40 360  10.44  7 19   651  59 360   0.94 25  5   779  69 123   0.25 50  2   906 349 153   0.31 44  2   443 266 360
177.75   1 265  186  40 360   4.19 12  9   251 178 326   0.88 26  2   378  69 360   0.50 35  2   505  49 360   0.13 70  1   457 154 360
137.25   2 237  578  24 360   8.81  8 14   641  14 326   0.56 33  2   771 231 360   0.88 26  3   899 299 118   0.19 57  1   438 335 360
121.25   2 141  197 263 360   4.38 11 10   260 223 153   0.50 35  2   392 287 360   1.19 22  4   517  30 148   0.19 57  1   461 179 360
 89.69   2 221  590  65 266   6.50  9 11   652 207 242   0.81 27  3   782 153 178   1.19 22  4   910 103 153   0.25 50  1   434 221 360
 85.38   2 141  183  45 360   4.94 11 10   245 217 246   0.63 31  2   375 103 360   1.31 21 13   502  53  45   0.06100  1   466 140 360
 59.69   3 119  575  29 360   5.19 10 11   638 349 360   0.38 40  2   764 151 182   1.13 23  3   896 274 262   0.06100  1   429  19 360
 70.56   2  87  203 254 360   4.00 12  8   267 273 296   0.38 40  2   395 341 360   0.63 31  3   520  84 178   0.31 44  2   470 194 148
```

```
78064    2   18 -12.2 -11.3   -0.8  16.6  -9.8    5.6    0.5    5  3.1
       0.8        5.7        6.3        9.1  1.28E+01   0 2.02E-01 11 25   4
                 0              0              0              0
         0   1      1    4         0    2         0    2
         0   1      1    4         1    2         0    2
         0   1      0    4         2    2         0    2
         0   1      2    4         0    2         0    2
         3   1      0    4         0    2         0    2
         0   1      0    4         2    2         0    2
         0   1      0    4         0    2         0    2
         1   1      2    4         0    2         0    2
         0   1      0    4         0    2         0    2
         1   1      0    4         0    2         0    2
         2   1      1    4         0    2         0    2
         0   1      2    4         0    2         0    2
         0   1      2    4         0    2         0    2
         0   1      0    4         1    2         0    2
         0   1      3    4         0    2         2    2
         0   1      2    4         0    2         3    2
         0   1      0    4         1    2         2    2
         0   1      1    4         1    2         1    2
         0   1      0    4         1    2         1    2
         0   1      1    4         0    2         0    2
         1   1      0    4         1    2         1    2
         0   1      0    4         0    2         1    2
         0   1      0    4         0    2         0    2
         1   1      1    4         1    2         0    2
         0   1      0    4         0    2         0    2
         0   1      1    4         1    2         0    2
         0   1      2    4         0    2         0    2
         1   1      1    4         3    2         0    2
         0   1      3    4         1    2         0    2
         2   1      1    4         0    2         1    2
         0   1      0    4         0    2         2    2
         0   1      0    4         1    2         1    2
         1   1      0    4         0    2         0    2
         0   1      1    4         0    2         1    2
         0   1      0    4         2    2         2    2
         0   1      4    4         0    2         0    2
         0   1      0    4         0    2         1    2
         0   1      0    4         2    2         2    2
         3   1     10    4        11    2         3    2
         0   1     14    4         9    2         5    2
         0   1      4    4         4    2         3    2
         0   1      0    4         1    2         3    2
         0   1      0    4         1    2         0    2
         0   1      0    4         1    2         0    2
         0   1      0    4         1    2         0    2
         0   1      0    4         0    2         1    2
         0   1      0    4         0    2         0    2
         0   1      2    4         0    2         4    2
         0   1      1    4         1    2         0    2
         0   1      2    4         0    2         0    2
         0   1      2    4         1    2         0    2
         0   1      4    4         0    2         2    2
         8   1     36    4        16    2        25    2
        24   1    422    4       166    2        75    2
        38   1    860    4       292    2       113    2
        26   1    442    4       155    2        93    2
         5   1     37    4        18    2        36    2
         1   1      4    4         0    2         0    2
         0   1      0    4         0    2         0    2
         0   1      0    4         0    2         0    2
         0   1      1    4         0    2         0    2
         0   1      1    4         0    2         1    2
         0   1      0    4         0    2         1    2
         0   1      2    4         0    2         1    2
```

```
78064      0 -12.3 -11.3  -0.8  16.8   0.4   4  3.1   -9.8   5.6   0.0
78064     30 -12.0 -11.2  -0.8  16.4   0.6   5  3.1   -9.8   5.5   0.0
78064     60 -11.6 -11.0  -0.8  16.0   0.9   6  3.1   -9.7   5.3   0.0
78064     90 -11.2 -10.8  -0.7  15.6   1.1   7  3.2   -9.6   5.1   0.0
78064    120 -10.7 -10.7  -0.6  15.1 999.0   8  3.2   -9.5   4.9   0.0
78064    150 -10.3 -10.5  -0.5  14.7 999.0   9  3.3   -9.3   4.8   0.0
78064    180  -9.8 -10.3  -0.3  14.2 999.0  10  3.3   -9.2   4.6   0.0
78064    210  -9.3 -10.0  -0.2  13.7 999.0  11  3.4   -9.1   4.3   0.0
78064    240  -8.9  -9.8   0.0  13.2 999.0  12  3.4   -8.9   4.1   0.0
78064    270  -8.3  -9.5   0.1  12.7 999.0  12  3.5   -8.7   3.9   0.0
78064    300  -7.8  -9.2   0.2  12.1 999.0  13  3.5   -8.5   3.7   0.0
78064    330  -7.3  -8.9   0.3  11.5 999.0  13  3.6   -8.3   3.4   0.0
78064    360  -6.7  -8.6   0.4  10.9 999.0  13  3.7   -8.0   3.2   0.0
78064    390  -6.1  -8.2   0.5  10.2 999.0  12  3.8   -7.7   2.9   0.0
78064    420  -5.4  -7.8   0.5   9.5 999.0  12  3.9   -7.4   2.6   0.0
78064    450  -4.8  -7.4   0.5   8.8 999.0  11  4.0   -7.0   2.3   0.0
78064    480  -4.1  -6.9   0.4   8.0 999.0  10  4.1   -6.6   2.0   0.0
78064    510  -3.3  -6.3   0.3   7.2 999.0   8  4.3   -6.1   1.7   7.7
78064    540  -2.5  -5.7   0.1   6.2 999.0   6  4.5   -5.5   1.3   6.6
78064    570  -1.7  -4.9   0.0   5.2 999.0   3  4.8   -4.9   0.9   5.4
78064    600  -0.8  -4.0  -0.3   4.1 999.0  -2  5.3   -4.0   0.5   4.2
78064    630   0.2  -2.8  -0.5   2.8 999.0 -10  6.3   -2.8   0.1   3.0
78064    660   1.0  -0.9  -0.5   1.5 999.0 -26  9.5   -1.0  -0.4   2.0
78064    690   0.1   1.5   0.2   1.5 999.0   7 17.8    1.5  -0.1   1.4
78064    720  -1.7   2.1   1.0   2.9 999.0  23 20.8    2.2   0.6   3.4
78064    750  -3.1   2.1   1.7   4.1 999.0  25 22.1    2.4   1.2   5.1
78064    780  -4.3   2.0   2.2   5.2 999.0  24 22.8    2.4   1.7   6.6
78064    810  -5.4   1.8   2.6   6.2 999.0  23 23.2    2.3   2.1   8.0
78064    840  -6.3   1.5   3.0   7.2 999.0  22 23.5    2.2   2.5   9.4
78064    870  -7.2   1.2   3.4   8.0 999.0  21 23.8    2.0   2.9  11.0
78064    900  -8.0   0.8   3.6   8.8 999.0  20 24.0    1.9   3.2   0.0
78064    930  -8.7   0.4   3.9   9.5 999.0  19  0.1    1.7   3.6   0.0
78064    960  -9.4   0.0   4.1  10.2 999.0  18  0.3    1.5   3.8   0.0
78064    990 -10.0  -0.4   4.3  10.9 999.0  17  0.4    1.2   4.1   0.0
78064   1020 -10.6  -0.8   4.4  11.5 999.0  17  0.5    1.0   4.4   0.0
78064   1050 -11.2  -1.2   4.5  12.1   3.5  16  0.6    0.8   4.6   0.0
78064   1080 -11.7  -1.6   4.6  12.7   3.6  16  0.6    0.6   4.9   0.0
78064   1110 -12.2  -2.0   4.7  13.2   3.8  16  0.7    0.4   5.1   0.0
78064   1140 -12.7  -2.5   4.7  13.7   3.9  16  0.8    0.1   5.3   0.0
78064   1170 -13.1  -2.8   4.7  14.2   4.1  16  0.9   -0.1   5.5   0.0
78064   1200 -13.6  -3.2   4.7  14.7   4.3  17  0.9   -0.3   5.7   0.0
78064   1230 -14.0  -3.6   4.6  15.1   4.5  17  1.0   -0.5   5.8   0.0
78064   1260 -14.3  -3.9   4.6  15.6   4.7  18  1.0   -0.8   6.0   0.0
78064   1290 -14.7  -4.2   4.6  16.0   4.9  19  1.1   -1.0   6.2   0.0
78064   1320 -15.1  -4.6   4.6  16.4   5.2  19  1.1   -1.2   6.3   0.0
78064   1350 -15.4  -4.8   4.5  16.8   5.4  20  1.2   -1.4   6.5   0.0
78064   1380 -15.7  -5.1   4.5  17.1   5.7  21  1.2   -1.6   6.6   0.0
78064   1410 -16.0  -5.3   4.5  17.5   6.0  23  1.2   -1.8   6.8   0.0
78064   1440 -16.4  -5.6   4.6  17.9   6.3  24  1.3   -2.1   6.9   0.0
```

A2. Magnetosphere /Geomagnetically Disturbed Day

(High O+/H+ density ratio)

	ID																	
78124	123	48.6	23.8	-11.4	55.4	-12	26	1.60E-01	5.05E+00	1.91E+02	8	132.00	0.00	0.1	16.1	-10.7	0.1	2.8
78124	256	42.7	29.7	-13.7	53.9	-15	35	2.20E-01	4.69E+00	1.12E+02	6	116.00	0.00	0.1	16.1	-10.7	0.1	2.8
78124	350	39.3	32.7	-10.3	52.2	-11	40	3.28E-01	3.58E+00	9.24E+01	-16	60.00	0.00	0.1	16.1	-10.7	0.0	2.8
78124	418	40.3	32.6	-9.8	52.8	-11	39	2.53E-01	4.94E+00	6.24E+01	-13	56.00	0.00	0.1	16.1	-10.6	0.0	2.8
78124	544	40.5	31.6	-6.9	51.9	-8	38	2.09E-01	4.94E+00	4.29E+01	24	154.00	0.00	0.1	16.1	-10.6	0.0	2.8
78124	671	39.7	30.0	-9.3	50.6	-11	37	1.60E-01	5.68E+00	1.10E+02	27	64.00	0.00	0.1	16.1	-10.5	0.0	2.7
78124	757	34.4	28.0	-8.3	45.2	-11	39	2.34E-01	4.19E+00	1.29E+02	34	96.00	0.00	0.1	16.1	-10.5	0.0	2.7
78124	844	33.8	26.7	-10.1	44.3	-13	38	2.12E-01	4.51E+00	5.37E+01	18	66.00	0.00	0.1	16.1	-10.5	0.0	2.7
78124	933	37.1	25.8	-11.7	46.7	-15	35	1.85E-01	4.72E+00	1.12E+02	18	96.00	0.00	0.1	16.1	-10.4	0.0	2.7
78124	1047	40.1	25.3	-11.8	48.9	-14	32	1.80E-01	5.13E+00	1.36E+02	19	116.00	0.00	0.1	16.1	-10.4	0.0	2.7
78124	1141	45.7	23.7	-9.0	52.3	-10	27	2.09E-01	4.74E+00	8.66E+01	21	60.00	0.00	0.1	16.1	-10.4	0.0	2.6
78124	1209	47.2	22.7	-7.3	53.0	-8	26	2.12E-01	4.74E+00	1.85E+02	17	56.00	0.00	0.1	16.1	-10.4	0.0	2.6
78124	1305	52.3	23.4	-9.3	58.1	-9	24	3.33E-01	4.18E+00	1.78E+02	-1	116.00	0.00	0.1	16.1	-10.3	0.0	2.6
78124	1427	61.9	19.7	-10.4	65.9	-9	18	4.00E-01	4.13E+00	1.65E+02	-25	116.00	0.00	0.1	16.1	-10.3	0.0	2.6
78124	1544	58.1	19.9	-16.6	63.7	-15	19	3.06E-01	3.95E+00	2.07E+02	-5	102.00	0.00	0.1	16.1	-10.3	-0.1	2.5
78124	1636	53.6	17.0	-17.6	59.0	-17	18	3.18E-01	4.38E+00	1.24E+02	-8	66.00	0.00	0.1	16.1	-10.2	-0.1	2.5
78124	1725	55.6	17.7	-18.5	61.3	-18	18	2.97E-01	4.50E+00	1.45E+02	-7	96.00	0.00	0.1	16.1	-10.2	-0.1	2.5
78124	1839	61.4	15.9	-17.5	65.9	-15	15	5.55E-01	3.24E+00	4.09E+01	-70	116.00	0.00	0.1	16.1	-10.1	-0.1	2.5
78124	1933	66.1	18.2	-11.0	69.4	-9	15	3.09E-01	4.66E+00	6.20E+01	6	60.00	0.00	0.1	16.1	-10.1	-0.1	2.5
78124	2001	59.7	17.4	-7.3	62.6	-7	16	3.14E-01	4.09E+00	1.87E+02	21	56.00	0.00	0.1	16.1	-10.1	-0.1	2.5
78124	2097	65.7	13.4	-5.2	67.3	-4	11	3.29E-01	3.75E+00	5.83E+01	-7	116.00	0.00	0.1	16.1	-10.0	-0.1	2.4
78124	2219	67.6	11.0	-5.0	68.8	-4	9	2.86E-01	3.67E+00	6.66E+01	-14	116.00	0.00	0.1	16.1	-10.0	-0.1	2.4
78124	2336	63.3	9.3	-2.8	64.1	-3	8	3.16E-01	3.83E+00	2.69E+01	-11	102.00	0.00	0.1	16.1	-10.0	-0.1	2.4
78124	2428	54.2	10.7	-0.5	55.3	-1	11	5.90E-01	3.93E+00	1.48E+01	-57	66.00	0.00	0.1	16.1	-9.9	-0.1	2.4
78124	2517	47.4	10.9	0.0	48.7	0	13	3.66E-01	4.36E+00	3.61E+01	-132	96.00	0.00	0.1	16.1	-9.9	-0.1	2.3
78124	2630	54.8	5.6	-2.6	55.3	-3	6	6.74E-01	4.35E+00	9.85E+01	-61	104.00	0.00	0.1	16.1	-9.9	-0.1	2.3
78124	2724	61.9	3.2	-3.7	62.1	-3	3	5.17E-01	5.63E+00	4.72E+01	-71	60.00	0.00	0.1	16.1	-9.8	-0.2	2.3
78124	2792	62.2	3.5	-5.0	62.6	-5	3	2.93E-01	4.41E+00	4.09E+01	-78	56.00	0.00	0.1	16.1	-9.8	-0.2	2.3
78124	2888	60.6	4.8	-6.0	61.2	-6	5	3.12E-01	4.37E+00	1.65E+02	-11	116.00	0.00	0.1	16.1	-9.8	-0.2	2.3
78124	3010	57.5	2.8	-8.9	58.4	-9	3	2.68E-01	4.71E+00	1.67E+02	-13	116.00	0.00	0.1	16.1	-9.7	-0.2	2.2
78124	3127	57.9	1.3	-9.1	58.7	-9	1	2.80E-01	5.11E+00	1.61E+02	-6	102.00	0.00	0.1	16.1	-9.7	-0.2	2.2
78124	3219	59.6	1.4	-9.6	60.4	-9	1	2.66E-01	5.17E+00	6.58E+01	-9	66.00	0.00	0.1	16.1	-9.6	-0.2	2.2
78124	3308	61.3	3.7	-10.7	62.4	-10	3	3.29E-01	5.72E+00	1.22E+02	-19	96.00	0.00	0.1	16.1	-9.6	-0.2	2.2
78124	3422	61.0	3.6	-10.8	62.0	-10	3	3.35E-01	5.21E+00	1.22E+02	-16	116.00	0.00	0.1	16.1	-9.6	-0.2	2.2
78124	3516	61.8	5.9	-12.4	63.3	-11	5	4.13E-01	5.81E+00	6.19E+01	-18	60.00	0.00	0.1	16.1	-9.5	-0.2	2.1
78124	3605	63.8	7.0	-12.0	65.4	-11	6	4.02E-01	5.02E+00	3.00E+01	-44	56.00	0.00	0.1	16.1	-9.5	-0.2	2.1
78124	3701	67.6	8.4	-12.8	69.3	-11	7	2.90E-01	5.17E+00	3.75E+01	-61	82.00	0.00	0.1	16.1	-9.5	-0.2	2.1
78124	3802	69.5	11.8	-17.6	72.7	-14	10	1.88E-01	4.63E+00	7.01E+01	-65	74.00	0.00	0.1	16.1	-9.4	-0.3	2.1
78124	3919	70.8	10.8	-20.3	74.5	-16	9	1.80E-01	4.60E+00	5.79E+01	-47	116.00	0.00	0.1	16.1	-9.4	-0.3	2.1
78124	4012	69.5	12.3	-19.2	73.1	-15	10	1.37E-01	4.64E+00	9.54E+00	-82	102.00	0.00	0.1	16.1	-9.4	-0.3	2.0
78124	4101	71.0	10.6	-18.5	74.2	-14	9	1.65E-01	5.29E+00	2.62E+01	-38	65.81	0.00	0.1	16.1	-9.4	-0.3	2.0
78124	4214	68.9	10.4	-16.4	71.6	-13	9	1.86E-01	4.37E+00	6.44E+01	-108	94.00	0.00	0.1	16.1	-9.3	-0.3	2.0
78124	4308	67.4	10.9	-14.9	69.9	-12	9	1.80E-01	4.48E+00	1.44E+01	-138	116.00	0.00	0.1	16.1	-9.3	-0.3	2.0
78124	4376	66.2	9.9	-13.8	68.4	-12	8	1.65E-01	4.49E+00	5.23E+01	-158	60.00	0.00	0.1	16.1	-9.3	-0.3	2.0
78124	4472	67.2	9.1	-12.1	68.9	-10	8	1.80E-01	4.50E+00	1.11E+01	-167	56.00	0.00	0.1	16.1	-9.3	-0.3	1.9
78124	4594	67.2	3.6	-9.0	68.0	-8	3	2.29E-01	3.71E+00	8.97E+01	-97	116.00	0.00	0.1	16.1	-9.2	-0.3	1.9
78124	4728	71.6	5.4	-7.9	74.0	-6	4	9.49E-02	5.25E+00	1.70E+02	-173	116.00	0.00	0.1	16.1	-9.2	-0.4	1.9

```
78124   0          13 -10.6   0.0   2.8  11.0 999.0     4 23.7      41.5           29.1       -9.9                51.9   2.82E-01   1  4.62E-01  1   1.4   2.4
0.00E+00 -1   1.41E-01   1  3.86E+00  1  5.71E+01 10 242       3  1.38E-03 16 120.00  0.00  10 180  1.06E-01  1  1.90E+00  2  2.14E+00  1
-8.06E-0534B  8.65E-04 62  2.10E+01 43  1.31E+02172   -1      60  2.00E-03 16 100.00  0.00  11 179  4.81E-04104  0.00E+00 -1  1.18E+01 62
 3.57E-04 84  7.30E-03 10  5.45E+00  9  2.92E+01 83 -133      10  2.62E-03 16 120.00  0.00  15 176  6.86E-03 10  3.07E+00 14  2.73E+00  6
 3.64E-03 60  4.17E-01  1  5.40E+00  1  2.60E+01  7  -70       6  7.39E-03 16 120.00  0.00  15 175  2.37E-01  1  2.79E+00  2  2.98E+00  1
78124  13          26 -10.4   0.0   2.6  10.7 999.0     4 23.8      48.4           23.0      -11.3                55.3   2.48E-01   1  6.40E-01  1   1.2   2.3
0.00E+00 -1   1.63E-01   1  4.33E+00  1  6.23E+01  7 -121       3  1.91E-03 13 120.00  0.00  11 178  1.29E-01  1  2.07E+00  2  2.24E+00  1
 3.28E-04129  4.21E-04135  0.00E+00 -1 -1.00E+00 -1    0      -1  2.77E-03 13 120.00  0.00  12 178 -2.35E-05999  0.00E+00 -1  0.00E+00 -1
 2.61E-04120  6.52E-03 12  4.63E+00 11  7.32E+01 50 -146      12  3.62E-03 13 120.00  0.00  14 176  7.91E-03 10  1.41E+00 25  3.01E+00  7
 2.46E-03100  4.89E-01  1  4.44E+00  1  4.49E+01  3  -17       1  1.02E-02 13 120.00  0.00  11 179  4.91E-01  1  1.80E+00  2  2.09E+00  1
78124  26          40 -10.1  -0.1   2.5  10.4 999.0     4 23.8      62.1           14.4      -10.1                65.0   1.83E-01   1  7.23E-01  1   1.1   2.2
0.00E+00 -1   2.03E-01   1  3.89E+00  1  3.62E+01 12 -133       4  2.16E-03 12 120.00  0.00   7 179  1.55E-01  1  1.76E+00  2  2.07E+00  1
-2.92E-04100  2.99E-04196  1.32E+01140 -1.00E+00 -1    0      -1  3.13E-03 12 120.00  0.00   7 180  5.97E-04 96  6.60E+00 91  0.00E+00 -1
-2.59E-04 98  2.10E-02  5  3.64E+00  6  1.10E+01 90 -104      73  4.09E-03 12 120.00  0.00   9 180  1.07E-02  8  1.52E+00 18  2.17E+00  6
 6.70E-04310  5.16E-01  1  3.94E+00  1  1.04E+01 16   45      56.8  1.16E-02 12 120.00  0.00   6 179  3.94E-01  1  1.66E+00  2  2.13E+00  1
78124  40          53  -9.9  -0.2   2.3  10.1 999.0     4 23.9      56.8            5.1       -5.0                57.5   2.54E-01   1  5.21E-01  1   0.9   2.1
0.00E+00 -1   1.81E-01   1  3.64E+00  1  2.84E+01 17  -12       4  1.56E-03 15 120.00  0.00   2 180  1.51E-01  1  1.47E+00  2  2.15E+00  1
-5.88E-05461  0.00E+00 -1  0.00E+00 -1 -1.00E+00 -1    0      -1  2.26E-03 15 120.00  0.00   4 180  0.00E+00 -1  0.00E+00 -1  0.00E+00 -1
 0.00E+00 -1   1.13E-02  8  3.54E+00 10  3.61E+01 50  -11       8  2.95E-03 15 104.00  0.00   6 179  1.11E-02  8  1.25E+00 21  2.30E+00  6
 6.63E-03 49  4.76E-01  1  5.25E+00  1  4.30E+01  5  -19       1  8.34E-03 15 120.00  0.00   6 180  4.29E-01  1  2.45E+00  3  3.07E+00  1
78124  53          66  -9.6  -0.2   2.1   9.8 999.0     4 23.9      64.9            7.1      -13.8               -66.9   1.77E-01   1  5.21E-01  1   0.7   2.0
0.00E+00 -1   2.67E-01   0  4.76E+00  1  2.49E+01 12 -101      12  1.56E-03 15 120.00  0.00  14 176  1.61E-01  1  2.27E+00  2  2.46E+00  1
-2.17E-05999  0.00E+00 -1  0.00E+00 -1 -1.00E+00 -1    0      -1  2.26E-03 15 120.00  0.00  14 176  0.00E+00 -1  0.00E+00 -1  0.00E+00 -1
 2.36E-04126  1.23E-02  7  4.09E+00  8  2.11E+01 78  -59      26  2.95E-03 15 120.00  0.00  14 176  9.12E-03  8  2.58E+00 11  1.81E+00  8
 2.36E-03 90  3.73E-01  1  4.44E+00  2  1.99E+01  8  -88       7  8.31E-03 15 104.00  0.00  14 176  2.70E-01  2  3.00E+00  2  2.03E+00  2
78124  66          79  -9.3  -0.3   1.9   9.5 999.0     4 24.0      68.9            8.3      -13.4                71.0   5.72E-02   2  4.86E-01  2   0.6   1.9
0.00E+00 -1   8.72E-02   1  4.30E+00  1  2.86E+01 22 -158      10  1.45E-03 15 120.00  0.00  14 176  8.53E-02  1  2.52E+00  2  1.79E+00  1
 2.81E-04146 -4.11E-05999  0.00E+00 -1 -1.00E+00 -1    0      -1  2.11E-03 15 120.00  0.00  14 176 -2.98E-05999  0.00E+00 -1  0.00E+00 -1
 4.32E-04 94  4.54E-03 16  2.32E+00 33  6.06E+01 51 -151      16  2.75E-03 15 120.00  0.00   8 179  4.49E-03 16  1.41E+00 44  1.29E+00 21
 3.21E-03 71  2.05E-01  2  3.87E+00  2  8.00E+01  3 -166       1  7.77E-03 15 104.00  0.00   9 180  2.03E-01  2  2.23E+00  2  1.77E+00  2
78124  79          92  -9.0  -0.4   1.8   9.2 999.0     4 24.0      43.6           15.5       10.5                54.9   8.09E-02   3  7.70E-01  3   0.4   1.8
0.00E+00 -1   6.10E-02   1  6.17E+00  1  1.18E+02  7 -130       4  2.30E-03 12 120.00  0.00   8 180  5.57E-02  1  4.29E+00  2  1.94E+00  2
-1.38E-04231  1.03E-03 59  1.38E+01 38  2.72E+02 73  -21      29  3.34E-03 12 120.00  0.00  12 178  1.37E-03 42  7.28E+00 32  1.51E+00 82
-2.67E-04 95  2.65E-03 31  6.96E+00 20  4.61E+01150 -108      38  4.36E-03 12 120.00  0.00   1 178  2.99E-03 24  5.41E+00 15  2.63E+00 16
 7.35E-03 53  7.39E-02  4  6.87E+00  3  5.22E-019999 -248      19  1.23E-02 12 120.00  0.00   0 178  7.58E-02  3  4.48E+00  3  2.60E+00  3
78124  92         106  -8.7  -0.5   1.6   8.9 999.0     3  0.0      10.1           14.2       33.2                37.8   2.54E-01   2  2.18E+00  2   0.3   1.7
0.00E+00 -1   9.76E-02   1  5.61E+00  1  2.10E+01 31 -128      21  6.52E-03  7 120.00  0.00  44 127  9.89E-02  1  3.68E+00  1  1.80E+00  1
-3.84E-04140  2.01E-03 49  1.30E+01 36  1.88E+02 65  -86      44  9.45E-03  7 120.00  0.00  44 125  2.55E-03 31  7.41E+00 20  4.25E+00 18
 9.46E-04 69  2.18E-03 59  8.79E+00 37  3.96E+02 50   47      31  1.24E-02  7 120.00  0.00  46 124  2.31E-03 45  4.63E+00 24  2.55E+00 21
 9.26E-03 43  9.06E-02  4  8.55E+00  3  2.48E+01 24   24       7  3.49E-02  7 120.00  0.00  46 126  1.22E-01  3  4.35E+00  2  2.36E+00  2
78124 106         119  -8.4  -0.6   1.4   8.5 999.0     3  0.1      16.2           11.6       28.9                35.4   3.56E-01   2  2.22E+00  2   0.1   1.5
0.00E+00 -1   8.78E-02   1  4.90E+00  2  8.50E+01  7   -1       5  6.63E-03  7 117.75  0.00  45 125  8.82E-02  1  3.22E+00  1  1.68E+00  1
0.00E+00 -1   5.45E-04194  2.32E+01147  1.34E+022285 -167      57  9.58E-03  7 104.00  0.00  46 125  0.00E+00 -1  0.00E+00 -1  0.00E+00 -1
 3.67E-04146  3.77E-03 35  2.90E+00 59  1.17E+02 61   42      34  1.26E-02  7 117.75  0.00  44 127  3.82E-03 30  1.75E+00 58  1.84E+00 22
 4.79E-03 72  1.96E-01  3  6.22E+00  2  1.94E+01 16   12      10  3.54E-02  7 103.75  0.00  42 128  2.02E-01  2  3.86E+00  2  2.14E+00  2
78124 119         122  -8.2  -0.6   1.3   8.3 999.0     3  0.1      23.9           12.3       34.1                43.5   5.61E-02   6  3.17E+00  2   0.0   1.5
0.00E+00 -1   8.11E-02   2  5.08E+00  2  6.52E+00155 -171      26  9.46E-03 10  50.00  0.00  43 128  8.70E-02  2  3.25E+00  2  1.79E+00  1
```

```
1
78124  30
       821 -10.6  0.0  11.0  2.8   0.0  10.6  2.4  999.0   4  23.7  41.5   29.1  -9.9  51.9   2.82E-01  1  2.53E-02  16 32 16

0.86  13 10  71 175  11  1 0.02100  11  132 204 360  1  254 254 360  3  0.11 37 37  378 181  76  0.05 57 1  320 184 360
10.05  3 64 448 225 190  1 0.05 57      512 197 360  1  634 343 360  7  0.88 13 29  759  29 145  0.06 50 1  318 315 360
3.91   6 23  74 215 360  1 0.02100      137 106 360  2  260 326 360  1  0.03 70     384 186 360  0.05 57 2  327 256 360
4.92   5 75 454 223 185  1 0.02100      516 347 360  4  639 223   8  9  1.42 10     764 231 155  0.09 40 1  312   2 360
1.66   9  9  65 207 360  1 0.02100      129 238 360  2  250 222 360  3  0.25 24     375 230 360  0.06 50 1  328  29 360
4.63   5 95 445 222  11  0 0.00999      509 305 360  4  630 222   8  9  1.48 10     753  38 158  0.02100 1  308 241 360
1.30  10  8  77 210 181  1 0.05 57      140  71 360  2  262 203 180 12  0.44 18     387 248 360  0.02100 1  335 212 360
2.80   7 22 457 225 192  1 0.05 57      518 209 360  2  642 196 360 15  2.52  7     766  34 170  0.02100 1  305 164 360
2.06   8 11  63  15 178  1 0.03 70      123 196 360  2  247 227 360 18  1.38 10     373  16  20  0.06 50 1  336 234 360
2.72   7 16 442 227 192  1 0.03 70      502 160 360  1  626  28 360 16  2.08  8     750  50 175  0.05 57 1  300 344 360
2.33   8 14  83 208 197  1 0.03 70      142  37 360  2  267  67 360  7  0.77 14     392  24 182  0.02100 1  343  35 360
3.14   7 15 463 230 192  1 0.09 57      522 330 360  2  647  38 360 11  1.22 11     770 221  20  0.06 50 1  297 349 360
2.00   8  8  56 207 192  1 0.02100      121  48 360  2  244 232 360  5  0.86 13     366 223 155  0.08 44 1  344 168 360
3.36   6 18 436 230 185  1 0.02100      500 275 360  2  623  40 360  5  1.02 12     746 230 360  0.05 57 1  293 243 360
2.38   8 12  85  18 180  0 0.00999      150 167 360  2  272 240 360  8  0.95 12     396 241 141  0.00999 0  350  84 360
2.48   7 11 465  26 197 -1 -1.00 -1  -1  -1 -1  -1   1  653  28 360 10  1.13 11     776 234  37  0.06 50 1  289  78 360
2.59   7 15  54  22 360  1 0.05 57      114 255 360  1  238 219 360 12  1.13 11     363 220 360  0.05 57 1  700 207 360
1.84   9 11 433 227 192  1 0.02100      496 199 360  3  621 215  37  8  0.63 15     743 228 360  0.03 70 1  697 227 360
2.20   8  9  91  16 215  1 0.03 70      150 256 360  4  275 228   8 42  3.47  6     399 221  26  0.06 50 2  704 276 360
3.66   6 16 468  36 200 -1 -1.00 -1  -1  -1 -1  -1   3  655 213 360  7  1.41 10     778  44 182  0.03 70 1  695   5 360
3.17   7 16  48  24 192  1 0.05 57      110 134 360  1  234  83 360 17  2.28  8     360 225 192  0.08 44 1  708  52 360
3.20   6 15 428  32 360  1 0.02100      493 204 360  2  615 224 360  8  1.31 10     741  28 293  0.06 50 1  688 175 360
3.44   6 18  92 208 171  1 0.02100      157 298 360  1  278 223 360  5  1.28 11     403 357 190  0.08 44 1  712 225 360
2.72   7 10 474  33 207 -1 -1.00 -1  -1  -1 -1  -1   1  658 201 360  6  1.23 11     785 197 219  0.06 50 1  687 138 360
1.86   9  9  45   7 200  0 0.00999      110 112 360  1  231  44 360  8  1.44 10     355   0 160  0.00999 0  716 249 360
2.19   8 11 425  37 185  1 0.03 70      488 288 360  2  613 288 360 11  1.31 10     735  38 185  0.03 70 1  680  36 360
2.30   8 12  98 191 207  1 0.11 37      158 123 360  2  284 228   8  5  1.39 10     407  22 182  0.08 44 2  723  35 360
3.50   9 11 481 201 185 -1 -1.00 -1  -1  -1 -1  -1   1  667 231 360  4  1.19 16     790  39  -1  0.09 40 2  677  26 155
2.14   8  9  43 197 200  1 0.06 50      103 356 360  2  226 216 360  3  0.61 16     352 328 200  0.30 22 3  726  30 178
2.14   8  8 477  36 207 -1 -1.00 -1  -1  -1 -1  -1   1  662  28 360  6  1.30 10     787  15 212  0.33 21 3  674  46  19
1.88  12  5 100  53 197  1 0.09 57      162 207 360  1  286 105 360 21  0.66 21     410 354 185  0.52 17 9  729  40  89
2.29   7 10 420 202 187  1 0.04 57      482 245 360  0  0.00999  2  316 360 16  1.01  8  671  36  13  0.42 18 4  608  42 168
1
78124  821
       1613 -10.4  0.0  10.7  2.6   0.0  1.2  2.3  999.0   4  23.8  48.4   23.0  -11.3  55.3   2.48E-01  1  3.50E-02  13 32 16

2.81  7 13  70 179 185  1 0.08 44  130 134 360  1  255  76 360 40  0.09 40 1  379 114 360  0.02100 1  322 110 360
8.84  4 28 450 246 197  1 0.06 50  511 179 360  5  636 231  11  7  3.09  7 25  758 318 360  0.00999 0  320 292 360
3.77  5 46  73 226  30  1 0.06 50  134 262 360  2  259 234 360 20  0.38 20 2  383 161 360  0.08 44 1  324  60 360
5.06  9 34 455  14 207  1 0.00999  518 332 360  2  642 222 360  7  2.89  7 26  764 309  67  0.08 44 1  312 102 360
1.67  6 23  67 221  81  1 0.02100  130  97 360  2  254  16 360 10  1.30 10  7  377 222  44  0.06 50 1  329 248 360
3.77  7 20 447 214  37  1 0.03 70  508 250 360  2  633 221 360  4  7.17  4 60  755   0 126  0.06 50 1  308 341 360
2.69  6 16  79 224  10  1 0.05 57  139  53 360  2  265 209 360 15  0.63 15  7  388   3 178  0.00999 0  336  26 360
3.64  7 14 459 209  52  1 0.03 70  520 142 360  1  642 288 360 38  4.58  5 38  767 348 126  0.05 57 1  306  97 360
2.52  7 22  61 216 182  1 0.03 70  122 274 360  3  246 201 360  4  0.58 16  4  372 335 163  0.00999 0  340 140 360
3.19  7  9 444 211 197  1 0.03 70  504  63 360  2  628 357 360 50  6.47  4 50  752   5 141  0.08 44 2  303  20 360
2.13  8    83 226 192  1 0.06 50  143 166 360  2  269  44 360  9  1.14 11  9  391  13 360  0.05 57 1  341 273 360
```

```
78124     0    13 -10.6    0.0    2.8   11.0    1.4    2.4  999.0    4  23.7
          41.5      29.1      -9.9      51.9   2.82E-01   1  2.53E-02  16  25  16
                     0              0                          0
          0    1       0    4         0    2         1    2
          0    1       0    4         1    2         0    2
          0    1       2    4         0    2         0    2
          0    1       0    4         1    2         0    2
          0    1       0    4         0    2         0    2
          1    1       0    4         0    2         0    2
          1    1       0    4         0    2         0    2
          0    1       1    4         0    2         0    2
          1    1       1    4         0    2         0    2
          1    1       0    4         0    2         0    2
          0    1       0    4         0    2         1    2
          0    1       0    4         0    2         3    2
          0    1       0    4         0    2         1    2
          0    1       1    4         0    2         9    2
          0    1       1    4         1    2         3    2
          0    1       0    4         4    2         2    2
          0    1       0    4         1    2         0    2
          0    1       1    4         1    2         1    2
          0    1       0    4         0    2         0    2
          0    1       0    4         0    2         0    2
          0    1       0    4         0    2         0    2
          0    1       0    4         0    2         0    2
          0    1       0    4         0    2         0    2
          0    1       0    4         1    2         0    2
          0    1       1    4         0    2         0    2
          0    1       0    4         0    2         0    2
          0    1       0    4         0    2         0    2
          0    1       1    4         0    2         0    2
          0    1       0    4         0    2         0    2
          0    1       0    4         1    2         0    2
          0    1       0    4         0    2         0    2
          0    1       0    4         0    2         0    2
          0    1       0    4         0    2         0    2
          0    1       0    4         0    2         0    2
          0    1       0    4         0    2         0    2
          0    1       0    4         0    2         0    2
          0    1       0    4         0    2         0    2
          0    1       0    4         0    2         0    2
          0    1       0    4         0    2         0    2
          0    1       0    4         0    2         0    2
          0    1       0    4         0    2         0    2
          0    1       0    4         0    2         0    2
          0    1       0    4         0    2         0    2
          0    1       2    4         0    2         0    2
          0    1       0    4         0    2         0    2
          0    1       0    4         0    2         0    2
          0    1       0    4         0    2         2    2
          0    1       6    4         0    2         0    2
          2    1      13    4         1    2         7    2
          0    1      10    4         1    2         2    2
          1    1       2    4         0    2         2    2
          0    1       0    4         0    2         1    2
          0    1       0    4         0    2         1    2
          0    1       0    4         0    2         0    2
          0    1       0    4         0    2         1    2
          0    1       0    4         0    2         0    2
          0    1       1    4         0    2         0    2
          0    1       0    4         0    2         1    2
```

78124	0	-10.8	0.1	2.9	11.1	999.0	4	23.7	1.4	2.5	0.0
78124	30	-10.2	-0.1	2.5	10.5	999.0	4	23.8	1.1	2.2	0.0
78124	60	-9.6	-0.2	2.1	9.8	999.0	4	23.9	0.7	2.0	0.0
78124	90	-8.9	-0.4	1.7	9.1	999.0	3	0.0	0.4	1.7	0.0
78124	120	-8.2	-0.6	1.3	8.3	999.0	3	0.1	0.0	1.5	0.0
78124	150	-7.4	-0.8	0.9	7.5	999.0	2	0.3	-0.3	1.2	0.0
78124	180	-6.5	-1.0	0.6	6.6	999.0	0	0.5	-0.7	0.9	7.2
78124	210	-5.5	-1.2	0.2	5.7	999.0	-3	0.8	-1.1	0.6	6.0
78124	240	-4.4	-1.4	-0.2	4.6	999.0	-7	1.2	-1.4	0.2	4.9
78124	270	-3.0	-1.5	-0.6	3.4	999.0	-13	1.9	-1.6	-0.1	3.8
78124	300	-1.2	-1.4	-0.8	2.1	999.0	-27	3.7	-1.6	-0.4	2.8
78124	330	0.9	-0.4	-0.5	1.1	999.0	-20	10.7	-0.5	-0.4	1.2
78124	360	1.3	1.6	0.9	2.2	999.0	26	15.8	1.8	0.5	2.7
78124	390	0.7	3.0	1.8	3.6	999.0	32	17.8	3.3	1.2	4.9
78124	420	0.1	4.0	2.5	4.7	999.0	31	18.7	4.4	1.7	6.7
78124	450	-0.6	4.9	3.0	5.8	999.0	30	19.2	5.3	2.2	8.1
78124	480	-1.2	5.7	3.4	6.7	999.0	29	19.6	6.1	2.6	9.5
78124	510	-1.8	6.3	3.8	7.6	999.0	27	19.9	6.8	3.0	10.9
78124	540	-2.4	6.9	4.1	8.4	999.0	25	20.1	7.4	3.3	12.4
78124	570	-3.0	7.5	4.4	9.2	999.0	23	20.3	7.9	3.6	0.0
78124	600	-3.6	8.0	4.7	9.9	999.0	22	20.4	8.4	3.9	0.0
78124	630	-4.1	8.4	4.9	10.6	999.0	20	20.5	8.8	4.2	0.0
78124	660	-4.6	8.8	5.2	11.2	999.0	19	20.6	9.2	4.4	0.0
78124	690	-5.1	9.1	5.5	11.8	999.0	18	20.7	9.6	4.6	0.0
78124	720	-5.6	9.4	5.8	12.4	999.0	17	20.8	9.9	4.9	0.0
78124	750	-6.1	9.6	6.2	12.9	999.0	16	20.9	10.2	5.1	0.0
78124	780	-6.6	9.8	6.5	13.5	999.0	15	21.0	10.5	5.3	0.0
78124	810	-7.0	9.9	6.9	14.0	999.0	14	21.0	10.8	5.4	0.0
78124	840	-7.4	10.0	7.3	14.4	999.0	14	21.1	11.0	5.6	0.0
78124	870	-7.9	10.0	7.8	14.9	999.0	14	21.1	11.3	5.8	0.0
78124	900	-8.3	10.0	8.2	15.3	999.0	14	21.2	11.5	5.9	0.0
78124	930	-8.7	9.9	8.7	15.8	999.0	14	21.2	11.7	6.1	0.0
78124	960	-9.1	9.8	9.2	16.2	999.0	14	21.3	11.9	6.2	0.0
78124	990	-9.4	9.6	9.6	16.6	999.0	14	21.3	12.0	6.3	0.0
78124	1020	-9.8	9.4	10.1	16.9	999.0	15	21.4	12.2	6.5	0.0
78124	1050	-10.2	9.2	10.5	17.3	999.0	16	21.4	12.3	6.6	0.0
78124	1080	-10.5	9.0	10.9	17.6	999.0	16	21.4	12.5	6.7	0.0
78124	1110	-10.8	8.8	11.3	17.9	999.0	17	21.5	12.6	6.8	0.0
78124	1140	-11.2	8.6	11.6	18.3	7.8	18	21.5	12.7	6.9	0.0
78124	1170	-11.5	8.4	11.9	18.6	8.2	19	21.5	12.8	7.0	0.0
78124	1200	-11.8	8.2	12.2	18.8	8.6	21	21.6	12.9	7.1	0.0
78124	1230	-12.1	8.0	12.4	19.1	9.0	22	21.6	13.0	7.2	0.0
78124	1260	-12.4	7.9	12.6	19.4	9.4	23	21.6	13.0	7.2	0.0
78124	1290	-12.7	7.8	12.8	19.6	9.8	24	21.7	13.1	7.3	0.0
78124	1320	-12.9	7.8	12.9	19.9	10.1	25	21.7	13.2	7.4	0.0
78124	1350	-13.2	7.8	13.0	20.1	10.4	26	21.7	13.2	7.4	0.0
78124	1380	-13.5	7.9	13.0	20.3	10.7	27	21.7	13.3	7.5	0.0
78124	1410	-13.7	8.0	13.0	20.5	11.0	28	21.8	13.3	7.6	0.0
78124	1440	-14.0	8.1	13.0	20.8	11.2	29	21.8	13.3	7.6	0.0

APPENDIX A

(continued)

Sample graphs of data files

0.1-16 keV/e IONS   8-APR-91,11:42:09
ISEE-1, DAY 64, 1978
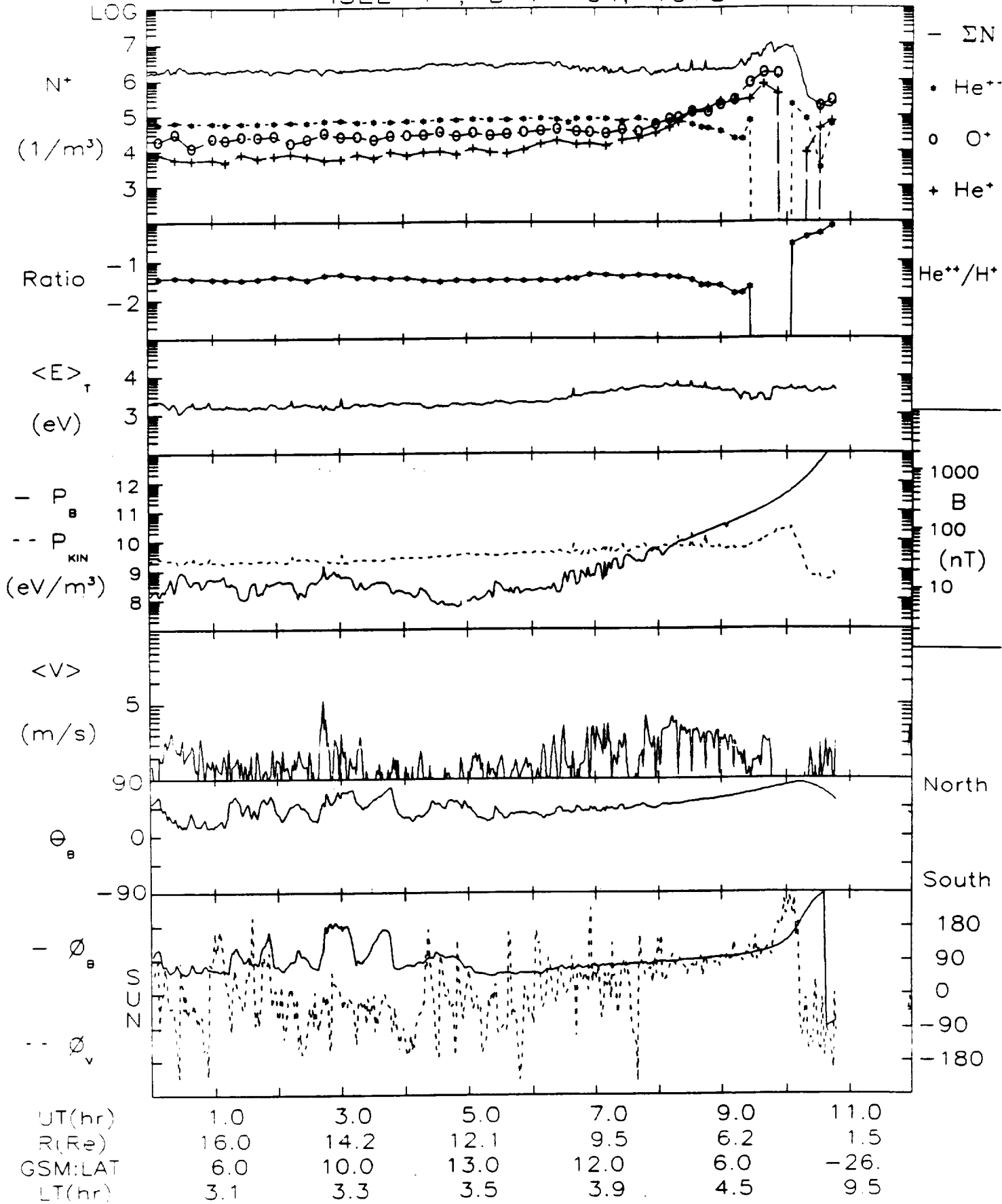
0.1–16 keV/e IONS   27-APR-91,15:02:13
ISEE-1 , DAY 124, 1978
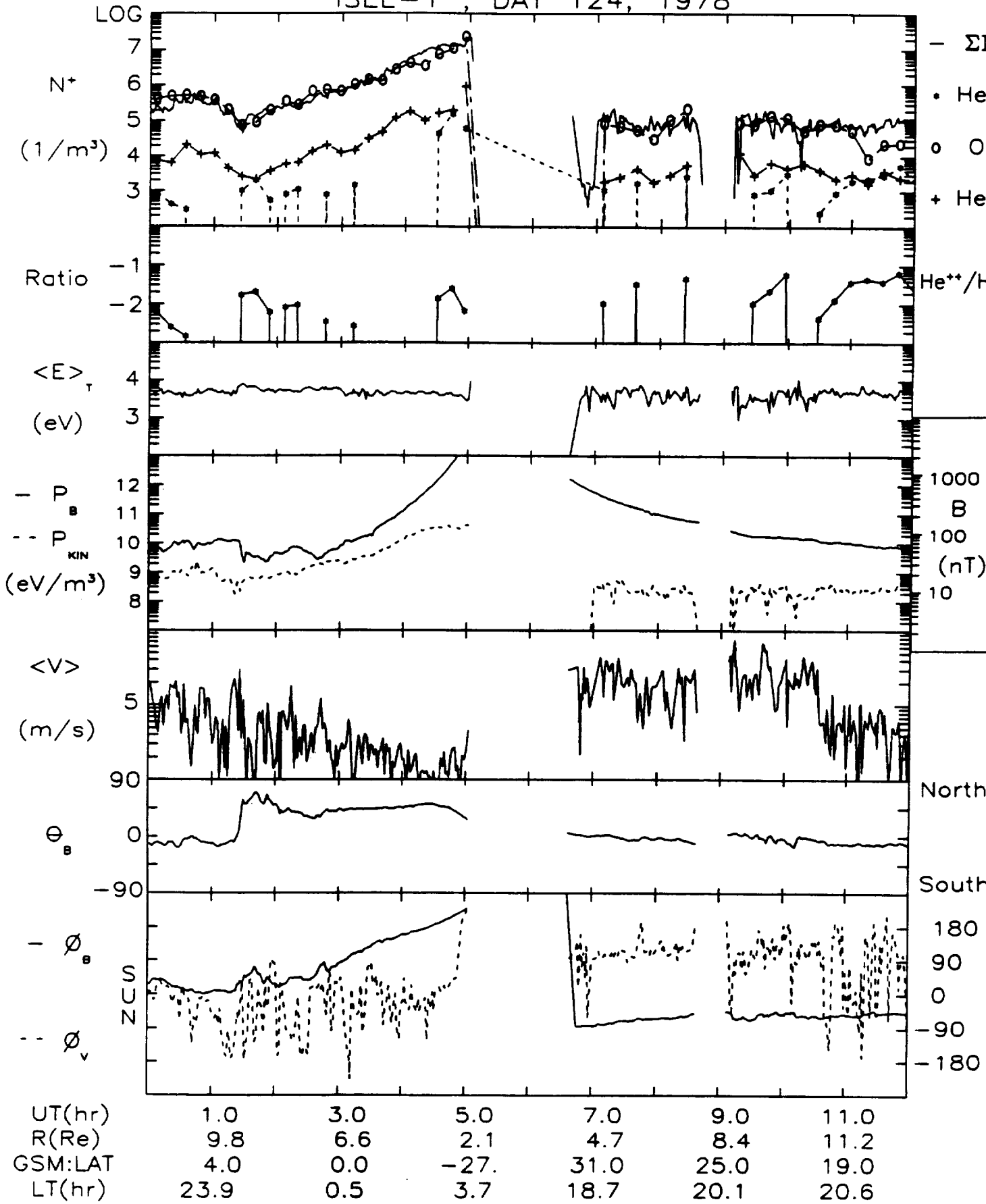
APPENDIX A

(continued)

VAX/VMS command files

```
From:    LPARL1::LENN          2-DEC-1991 11:54:48.54
To:      NCF::SUMANT
CC:      LENN
Subj:    ISEE Data Archiving/ Command file #1


$!************** LOCKHEED PLASMA COMPOSITION EXPERIMENT ON ISEE-1 **************
$!                     ****** COPY_ISEEMS.COM ******
$!
$! Interactive command file for copying data from archival tapes (label: ISEEMS)
$!               using the VAX/VMS Backup Utility
$!
$!                          by O. W. Lennartsson
$!               Lockheed Missiles & Space Company, Inc.
$!                     Research and Development
$!                       Dept. 91-20, Bldg. 255
$!                        3251 Hanover Street
$!                        Palo Alto, CA 94304
$!
$! Telephone (415) 424-3259
$!
$! Developed under NASA Contract NAS5-33047
$!
$! The command language is that of VAX/VMS Version 5.4
$!
$! To execute this file, simply enter @COPY_ISEEMS, if the file resides in the
$! same directory used for the data files, otherwise specify directory name in
$! the command: @directory_nameCOPY_ISEEMS (your default directory should be the
$! one used for data files).
$!*****************************************************************************
$WRITE SYS$OUTPUT " "
$DEFAULT_DIR = F$LOGICAL("SYS$DISK")+F$DIRECTORY()
$WRITE SYS$OUTPUT "Your default directory is: ",''DEFAULT_DIR'
$WRITE SYS$OUTPUT "Is this where you want the files?"
$WRITE SYS$OUTPUT "If not, Ctrl/Y, reset default and reenter command."
$WRITE SYS$OUTPUT " "
$INQUIRE DUM "If directory OK, then press return"
$SET NOON
$WRITE SYS$OUTPUT " "
$INQUIRE NAME "Which tape drive? (enter name of device)"
$DRIVE= F$STRING(NAME)
$ALLOCATE 'DRIVE' TAPE
$IF $SEVERITY .EQ. 1 THEN GOTO DRIVE_OK
$WRITE SYS$OUTPUT "EXIT"
$WRITE SYS$OUTPUT "Reenter command if trying another drive."
$SET ON
$EXIT
$DRIVE_OK:
$SET ON
$WRITE SYS$OUTPUT " "
$WRITE SYS$OUTPUT "Mount tape on ''F$LOGICAL("TAPE")'"
$WRITE SYS$OUTPUT " "
$INQUIRE DUM "When tape mounted and on line (!), then press return"
$MOUNT/FOREIGN/DENSITY=6250 TAPE
$WRITE SYS$OUTPUT " "
$WRITE SYS$OUTPUT -
  "If you only want to copy the Data User's Guide, enter Y (yes) here,"
$INQUIRE GUIDE -
```

```
        "otherwise press return again"
$IF GUIDE THEN SET NOON
$IF GUIDE THEN GOTO ONLY_GUIDE
$WRITE SYS$OUTPUT " "
$WRITE SYS$OUTPUT "Data files are copied by date, starting with the ",-
 "first date entered,"
$WRITE SYS$OUTPUT "and ending with the second date (inclusive) ",-
 "-assuming one and the same year."
$WRITE SYS$OUTPUT "If data run into second year, reenter a new set ",-
 "of dates for that second year."
$WRITE SYS$OUTPUT -
 "It is OK to copy one single day also, that is second date = first date."
$IRWND=0
$NYOLD=0
$NEW_YEAR:
$WRITE SYS$OUTPUT " "
$INQUIRE P2 "What YEAR? (two digits)"
$LENGTH_OF_YEAR:
$LP2=F$LENGTH(P2)
$IF(LP2.EQ.2) THEN GOTO CHECK_YEAR
$INQUIRE P2 "Enter two digits for the year: 77 or 78 or 79 or 80"
$GOTO LENGTH_OF_YEAR
$WRONG_YEAR:
$INQUIRE P2 "Enter either of 77 or 78 or 79 or 80"
$CHECK_YEAR:
$NY=F$INTEGER(F$EXTRACT(0,2,P2))
$IF(NY.LT.77.OR.NY.GT.80) THEN GOTO WRONG_YEAR
$IF(NY.EQ.NYOLD) THEN GOTO YEAR_OK
$IF(NY.LT.NYOLD) THEN GOTO WRONG_ORDER_YEARS
$MNDAY=999
$MXDAY=0
$YEAR_OK:
$IRWRS=0
$WRITE SYS$OUTPUT " "
$INQUIRE P3 "First DAY to be copied? (one to three digits)"
$LP3=F$LENGTH(P3)
$IF(LP3.GT.3) THEN GOTO YEAR_OK
$IF(LP3.EQ.2) THEN P3:= "0''P3'"
$IF(LP3.EQ.1) THEN P3:= "00''P3'"
$ND=F$INTEGER(F$EXTRACT(0,3,P3))
$IF(NY.EQ.80) .AND. (ND.LT.1.OR.ND.GT.366) .OR. -
    (NY.NE.80) .AND. (ND.LT.1.OR.ND.GT.365) THEN GOTO YEAR_OK
$IF(ND.LE.MXDAY) THEN IRWRS=1
$IF(IRWRS.EQ.1) THEN GOTO OVERLAP1
$NO_OVERLAP1:
$ISTART=ND
$YEAR_STILL_OK:
$WRITE SYS$OUTPUT " "
$INQUIRE P3 "Last DAY to be copied? (in that same segment)"
$LP3=F$LENGTH(P3)
$IF(LP3.GT.3) THEN GOTO YEAR_STILL_OK
$IF(LP3.EQ.2) THEN P3:= "0''P3'"
$IF(LP3.EQ.1) THEN P3:= "00''P3'"
$ND=F$INTEGER(F$EXTRACT(0,3,P3))
$IF(NY.EQ.80) .AND. (ND.LT.1.OR.ND.GT.366) .OR. -
    (NY.NE.80) .AND. (ND.LT.1.OR.ND.GT.365) THEN GOTO YEAR_STILL_OK
$IF(ND.LT.ISTART) THEN GOTO WRONG_ORDER_DAYS
```

```
$IF (ND.GE.MNDAY) .AND. (IRWRS.EQ.1) THEN GOTO OVERLAP2
$NO_OVERLAP2:
$IRWRS=0
$ISTOP=ND
$IDAY=ISTART
$SET NOON
$BACKUP_TO_DISK:
$IF (IDAY.LT.MNDAY) THEN MNDAY=IDAY
$IF (IDAY.GT.MXDAY) THEN MXDAY=IDAY
$IF (IDAY.LE.9) THEN YYDDD= F$STRING(NY) + "00" + F$STRING(IDAY)
$IF (IDAY.GT.9) .AND. (IDAY.LE.99) THEN -
 YYDDD= F$STRING(NY) + "0" + F$STRING(IDAY)
$IF (IDAY.GT.99) THEN YYDDD= F$STRING(NY) + F$STRING(IDAY)
$IF (IDAY.EQ.ISTART) THEN YYDDD1=YYDDD
$IF (IRWND.EQ.0) THEN BACKUP/LOG TAPE:'YYDDD'.BCK 'DEFAULT_DIR'
$IF (IRWND.EQ.1) THEN BACKUP/REWIND/LOG TAPE:'YYDDD'.BCK 'DEFAULT_DIR'
$IRWND=0
$IDAY=IDAY+1
$IF (IDAY.LE.ISTOP) THEN GOTO BACKUP_TO_DISK
$NYOLD=NY
$WRITE SYS$OUTPUT " "
$IF (ISTOP.EQ.ISTART) THEN WRITE SYS$OUTPUT -
 "Last segment copied: a single day ",'YYDDD'
$IF (ISTOP.GT.ISTART) THEN WRITE SYS$OUTPUT -
 "Last segment copied: days ",'YYDDD1'," through ",'YYDDD'
$WRITE SYS$OUTPUT " "
$INQUIRE MORE -
 "Are there more data files to be copied from this tape? [Y/N]"
$IF MORE THEN GOTO NEW_YEAR
$WRITE SYS$OUTPUT " "
$INQUIRE GUIDE -
 "Do you want to copy the User's Guide? (last file on the tape) [Y/N]"
$ONLY_GUIDE:
$IF GUIDE THEN -
 BACKUP/LOG TAPE:GUIDE.BCK 'DEFAULT_DIR'
$IF $SEVERITY .EQ. 1 THEN GOTO REMOVE_TAPE
$DIR 'DEFAULT_DIR'GUIDE.
$IF $SEVERITY .EQ. 1 THEN GOTO REMOVE_TAPE
$IF GUIDE THEN WRITE SYS$OUTPUT " "
$IF GUIDE THEN WRITE SYS$OUTPUT "Tape already at end, must be rewound."
$IF GUIDE THEN -
 BACKUP/REWIND/LOG TAPE:GUIDE.BCK 'DEFAULT_DIR'
$GOTO REMOVE_TAPE
$WRONG_ORDER_DAYS:
$WRITE SYS$OUTPUT " "
$WRITE SYS$OUTPUT "First and last days in wrong order!"
$INQUIRE REDO "Want to reenter dates? [Y/N]"
$IF REDO THEN GOTO NEW_YEAR
$GOTO REMOVE_TAPE
$WRONG_ORDER_YEARS:
$WRITE SYS$OUTPUT " "
$WRITE SYS$OUTPUT "Going backwards in years (rewinding tape)?"
$INQUIRE SURE "Is this really the year you want? [Y/N]"
$IF SURE THEN IRWND=1
$IF SURE THEN NYOLD=0
$IF SURE THEN MNDAY=999
$IF SURE THEN MXDAY=0
```

```
$IF SURE THEN GOTO YEAR_OK
$INQUIRE REDO "Want to correct year? [Y/N]"
$IF REDO THEN GOTO NEW_YEAR
$GOTO REMOVE_TAPE
$OVERLAP1:
$WRITE SYS$OUTPUT " "
$WRITE SYS$OUTPUT "Caution:"
$IF(ND.LT.MXDAY) THEN WRITE SYS$OUTPUT -
 "First day precedes days already copied!"
$IF(ND.EQ.MXDAY) THEN WRITE SYS$OUTPUT -
 "First day has already been copied once!"
$!IF(ND.EQ.MXDAY) THEN GOTO NEW_YEAR
$WRITE SYS$OUTPUT "Tape will have to be rewound."
$WRITE SYS$OUTPUT " "
$INQUIRE SURE "Is that what you want? [Y/N]"
$IF SURE THEN IRWND=1
$IF SURE THEN GOTO NO_OVERLAP1
$INQUIRE REDO "Want to correct dates? [Y/N]"
$IF REDO THEN GOTO NEW_YEAR
$GOTO REMOVE_TAPE
$OVERLAP2:
$WRITE SYS$OUTPUT " "
$WRITE SYS$OUTPUT "Caution:"
$IF(ND.GT.MNDAY) THEN WRITE SYS$OUTPUT -
 "Check your Last day entry!"
$IF(ND.EQ.MNDAY) THEN WRITE SYS$OUTPUT -
 "Last day has already been copied once!"
$!IF(ND.EQ.MNDAY) THEN GOTO YEAR_STILL_OK
$WRITE SYS$OUTPUT " "
$INQUIRE SURE "Are you satisfied with your dates? [Y/N]"
$IF SURE THEN GOTO NO_OVERLAP2
$INQUIRE REDO "Want to reenter both dates? [Y/N]"
$IF REDO THEN GOTO NEW_YEAR
$INQUIRE REDO "Want to reenter last day? [Y/N]"
$IF REDO THEN GOTO YEAR_STILL_OK
$REMOVE_TAPE:
$SET ON
$DISMOUNT 'DRIVE'
$DEALLOCATE 'DRIVE'
$WRITE SYS$OUTPUT " "
$WRITE SYS$OUTPUT "EXIT"
$WRITE SYS$OUTPUT "That's the end of this run."
$WRITE SYS$OUTPUT -
 "Tape is dismounted and ''F$LOGICAL("TAPE")' is deallocated."
$EXIT
```

```
$!************** LOCKHEED PLASMA COMPOSITION EXPERIMENT ON ISEE-1 **************
$!                    ****** USER_TAPE.COM ******
$!
$! Interactive command file for copying ISEEMS data files from disk to a new
$!          magnetic tape using the VAX/VMS Copy Utility
$!
$!                         by O. W. Lennartsson
$!               Lockheed Missiles & Space Company, Inc.
$!                        Research and Development
$!                         Dept. 91-20, Bldg. 255
$!                          3251 Hanover Street
$!                          Palo Alto, CA 94304
$!
$! Telephone (415) 424-3259
$!
$! Developed under NASA Contract NAS5-33047
$!
$! The command language is that of VAX/VMS Version 5.4
$!
$! To execute this file, simply enter @USER_TAPE, if the file resides in the
$! same directory used for the data files, otherwise specify directory name in
$! the command: @directory_nameUSER_TAPE (your default directory should be the
$! one used for data files).  The new tape will be labeled IONS and will be
$! written at a density of 1600 bpi.
$!**************************************************************************************
$WRITE SYS$OUTPUT " "
$DEFAULT_DIR = F$LOGICAL("SYS$DISK")+F$DIRECTORY()
$WRITE SYS$OUTPUT "Your default directory is: ",''DEFAULT_DIR'
$WRITE SYS$OUTPUT "Is this where the ISEEMS files are?"
$WRITE SYS$OUTPUT "If not, Ctrl/Y, reset default and reenter command."
$WRITE SYS$OUTPUT " "
$INQUIRE DUM "If directory OK, then press return"
$SET NOON
$WRITE SYS$OUTPUT " "
$INQUIRE NAME "Which tape drive? (enter name of device)"
$DRIVE= F$STRING(NAME)
$ALLOCATE 'DRIVE' TAPE
$IF $SEVERITY .EQ. 1 THEN GOTO DRIVE_OK
$WRITE SYS$OUTPUT "EXIT"
$WRITE SYS$OUTPUT "Reenter command if trying another drive."
$SET ON
$EXIT
$DRIVE_OK:
$SET ON
$WRITE SYS$OUTPUT " "
$WRITE SYS$OUTPUT "Mount tape on ''F$LOGICAL("TAPE")'"
$WRITE SYS$OUTPUT " "
$WRITE SYS$OUTPUT "Make sure tape is on line."
$WRITE SYS$OUTPUT " "
$INQUIRE INIZLD -
 "Has tape already been initialized at 1600 bpi and labeled IONS? [Y/N]"
$IF INIZLD THEN GOTO INITIALIZED
```

```
$INITIALIZE/OVERRIDE=EXPIRATION/DENS=1600/PROT=(G:RW,W:RW) -
 'DRIVE' IONS
$INITIALIZED:
$MOUNT/DENSITY=1600 'DRIVE' IONS TAPE
$WRITE SYS$OUTPUT " "
$INQUIRE GUIDE -
 "Do you want to copy the Data User's Guide at this point? [Y/N]"
$IF .NOT. GUIDE THEN GOTO DATA_NEXT
$SET NOON
$COPY/LOG 'DEFAULT_DIR'GUIDE. TAPE
$IF $SEVERITY .EQ. 1 THEN GOTO DATA_FILES
$WRITE SYS$OUTPUT " "
$INQUIRE DATA "Do you want to copy data files anyway? [Y/N]"
$IF .NOT. DATA THEN GOTO TAPEDIR_LIS
$SET ON
$GOTO DATA_NEXT
$DATA_FILES:
$WRITE SYS$OUTPUT " "
$INQUIRE DATA "And you also want to copy data files? [Y/N]"
$IF .NOT. DATA THEN GOTO TAPEDIR_LIS
$SET ON
$DATA_NEXT:
$WRITE SYS$OUTPUT " "
$WRITE SYS$OUTPUT "Data files are copied by date, starting with the ",-
 "first date entered,"
$WRITE SYS$OUTPUT "and ending with the second date (inclusive) ",-
 "-assuming one and the same year."
$WRITE SYS$OUTPUT "If data run into second year, reenter a new set ",-
 "of dates for that second year."
$WRITE SYS$OUTPUT " "
$WRITE SYS$OUTPUT -
 "If you are copying one single day, then make last date = first date."
$NYOLD=0
$NEW_YEAR:
$WRITE SYS$OUTPUT " "
$INQUIRE P2 "What YEAR? (two digits)"
$LENGTH_OF_YEAR:
$LP2=F$LENGTH(P2)
$IF(LP2.EQ.2) THEN GOTO CHECK_YEAR
$INQUIRE P2 "Enter two digits for the year: 77 or 78 or 79 or 80"
$GOTO LENGTH_OF_YEAR
$WRONG_YEAR:
$INQUIRE P2 "Enter either of 77 or 78 or 79 or 80"
$CHECK_YEAR:
$NY=F$INTEGER(F$EXTRACT(0,2,P2))
$IF(NY.LT.77.OR.NY.GT.80) THEN GOTO WRONG_YEAR
$IF(NY.EQ.NYOLD) THEN GOTO YEAR_OK
$YY= F$STRING(NY)
$DIR/OUTPUT=DRECTRY.TMP 'DEFAULT_DIR'EX'YY'*.DAT
$IF $SEVERITY .EQ. 1 THEN GOTO YEAR_POSSIBLE
$DELETE DRECTRY.TMP;*
$WRITE SYS$OUTPUT " "
$WRITE SYS$OUTPUT "No files found from year ",'YY',"!"
$INQUIRE REDO "Want to reenter year? [Y/N]"
$IF REDO THEN GOTO NEW_YEAR
$GOTO REMOVE_TAPE
$YEAR_POSSIBLE:
```

```
$DELETE DRECTRY.TMP;*
$IF(NY.LT.NYOLD) THEN GOTO WRONG_ORDER_YEARS
$MNDAY=999
$MXDAY=0
$YEAR_OK:
$IRWRS=0
$WRITE SYS$OUTPUT " "
$INQUIRE P3 "First DAY to be copied? (one to three digits)"
$LP3=F$LENGTH(P3)
$IF(LP3.GT.3) THEN GOTO YEAR_OK
$IF(LP3.EQ.2) THEN P3:= "0''P3'"
$IF(LP3.EQ.1) THEN P3:= "00''P3'"
$ND=F$INTEGER(F$EXTRACT(0,3,P3))
$IF(NY.EQ.80) .AND. (ND.LT.1.OR.ND.GT.366) .OR. -
    (NY.NE.80) .AND. (ND.LT.1.OR.ND.GT.365) THEN GOTO YEAR_OK
$IF(ND.LE.MXDAY) THEN IRWRS=1
$IF(IRWRS.EQ.1) THEN GOTO OVERLAP1
$NO_OVERLAP1:
$YYDDD= F$EXTRACT(0,2,P2) + F$EXTRACT(0,3,P3)
$DIR/OUTPUT=DRECTRY.TMP 'DEFAULT_DIR'*'YYDDD'.DAT
$IF $SEVERITY .EQ. 1 THEN GOTO GOOD_START
$DELETE DRECTRY.TMP;*
$WRITE SYS$OUTPUT " "
$WRITE SYS$OUTPUT "No files found with date ",'YYDDD',"!"
$INQUIRE REDO "Want to reenter dates? [Y/N]"
$IF REDO THEN GOTO NEW_YEAR
$GOTO REMOVE_TAPE
$GOOD_START:
$DELETE DRECTRY.TMP;*
$ISTART=ND
$WRITE SYS$OUTPUT " "
$WRITE SYS$OUTPUT -
 "If it is doubtful that all days will fit on this tape,"
$WRITE SYS$OUTPUT "then try successive pairs of first and last days,"
$WRITE SYS$OUTPUT "and put remaining days on a new tape."
$WRITE SYS$OUTPUT -
 "(It is OK to copy one day at a time, that is last day = first day.)"
$YEAR_STILL_OK:
$WRITE SYS$OUTPUT " "
$INQUIRE P3 "Last DAY to be copied? (in that same segment)"
$LP3=F$LENGTH(P3)
$IF(LP3.GT.3) THEN GOTO YEAR_STILL_OK
$IF(LP3.EQ.2) THEN P3:= "0''P3'"
$IF(LP3.EQ.1) THEN P3:= "00''P3'"
$ND=F$INTEGER(F$EXTRACT(0,3,P3))
$IF(NY.EQ.80) .AND. (ND.LT.1.OR.ND.GT.366) .OR. -
    (NY.NE.80) .AND. (ND.LT.1.OR.ND.GT.365) THEN GOTO YEAR_STILL_OK
$IF(ND.LT.ISTART) THEN GOTO WRONG_ORDER_DAYS
$IF(ND.GE.MNDAY) .AND. (IRWRS.EQ.1) THEN GOTO OVERLAP2
$NO_OVERLAP2:
$IRWRS=0
$IF(ND.EQ.ISTART) THEN GOTO SINGLE_DAY
$YYDDD= F$EXTRACT(0,2,P2) + F$EXTRACT(0,3,P3)
$DIR/OUTPUT=DRECTRY.TMP 'DEFAULT_DIR'*'YYDDD'.DAT
$IF $SEVERITY .EQ. 1 THEN GOTO GOOD_STOP
$DELETE DRECTRY.TMP;*
$WRITE SYS$OUTPUT " "
```

```
$WRITE SYS$OUTPUT "No files found with date ",'YYDDD',"!"
$INQUIRE REDO "Want to reenter both dates? [Y/N]"
$IF REDO THEN GOTO NEW_YEAR
$INQUIRE REDO "Want to reenter last day? [Y/N]"
$IF REDO THEN GOTO YEAR_STILL_OK
$GOTO REMOVE_TAPE
$GOOD_STOP:
$DELETE DRECTRY.TMP;*
$SINGLE_DAY:
$ISTOP=ND
$IDAY=ISTART
$SET NOON
$COPY_TO_TAPE:
$IF(IDAY.LT.MNDAY) THEN MNDAY=IDAY
$IF(IDAY.GT.MXDAY) THEN MXDAY=IDAY
$IF(IDAY.LE.9) THEN YYDDD= F$STRING(NY) + "00" + F$STRING(IDAY)
$IF(IDAY.GT.9) .AND. (IDAY.LE.99) THEN -
 YYDDD= F$STRING(NY) + "0" + F$STRING(IDAY)
$IF(IDAY.GT.99) THEN YYDDD= F$STRING(NY) + F$STRING(IDAY)
$IF(IDAY.EQ.ISTART) THEN YYDDD1=YYDDD
$COPY/LOG 'DEFAULT_DIR'*'YYDDD'.DAT TAPE
$IDAY=IDAY+1
$IF(IDAY.LE.ISTOP) THEN GOTO COPY_TO_TAPE
$NYOLD=NY
$WRITE SYS$OUTPUT " "
$IF(ISTOP.EQ.ISTART) THEN WRITE SYS$OUTPUT -
 "Last segment copied: a single day ",'YYDDD'
$IF(ISTOP.GT.ISTART) THEN WRITE SYS$OUTPUT -
 "Last segment copied: days ",'YYDDD1'," through ",'YYDDD'
$WRITE SYS$OUTPUT " "
$INQUIRE MORE -
 "Are there more data files to be copied to this tape? [Y/N]"
$IF MORE THEN GOTO NEW_YEAR
$WRITE SYS$OUTPUT " "
$INQUIRE GUIDE -
 "Do you want to add the Data User's Guide at the end? [Y/N]"
$IF GUIDE THEN -
 COPY/LOG 'DEFAULT_DIR'GUIDE. TAPE
$TAPEDIR_LIS:
$WRITE SYS$OUTPUT " "
$INQUIRE LISTING "Do you want a tape directory file (TAPEDIR.LIS)? [Y/N]"
$IF .NOT. LISTING THEN GOTO REMOVE_TAPE
$DIR/SIZE/DATE/OUTPUT='DEFAULT_DIR'TAPEDIR.LIS TAPE
$SET PROT=(G:RWED,W:RWED) TAPEDIR.LIS
$GOTO REMOVE_TAPE
$WRONG_ORDER_DAYS:
$WRITE SYS$OUTPUT " "
$WRITE SYS$OUTPUT "First and last days in wrong order!"
$INQUIRE REDO "Want to reenter dates? [Y/N]"
$IF REDO THEN GOTO NEW_YEAR
$GOTO REMOVE_TAPE
$WRONG_ORDER_YEARS:
$WRITE SYS$OUTPUT " "
$WRITE SYS$OUTPUT "Going backwards in years?"
$INQUIRE SURE "Is this really the year you want? [Y/N]"
$IF SURE THEN NYOLD=0
$IF SURE THEN MNDAY=999
```

```
$IF SURE THEN MXDAY=0
$IF SURE THEN GOTO YEAR_OK
$INQUIRE REDO "Want to correct year? [Y/N]"
$IF REDO THEN GOTO NEW_YEAR
$GOTO REMOVE_TAPE
$OVERLAP1:
$WRITE SYS$OUTPUT " "
$WRITE SYS$OUTPUT "Caution:"
$IF(ND.LT.MXDAY) THEN WRITE SYS$OUTPUT -
 "First day precedes days already copied!"
$IF(ND.EQ.MXDAY) THEN WRITE SYS$OUTPUT -
 "This day has already been copied!"
$!IF(ND.EQ.MXDAY) THEN GOTO NEW_YEAR
$WRITE SYS$OUTPUT " "
$INQUIRE SURE "Are you sure there will be no duplication? [Y/N]"
$IF SURE THEN GOTO NO_OVERLAP1
$INQUIRE REDO "Want to correct dates? [Y/N]"
$IF REDO THEN GOTO NEW_YEAR
$GOTO REMOVE_TAPE
$OVERLAP2:
$WRITE SYS$OUTPUT " "
$WRITE SYS$OUTPUT "Caution:"
$IF(ND.GT.MNDAY) THEN WRITE SYS$OUTPUT -
 "Last day may be out of order!"
$IF(ND.EQ.MNDAY) THEN WRITE SYS$OUTPUT -
 "Last day has already been copied!"
$!IF(ND.EQ.MNDAY) THEN GOTO YEAR_STILL_OK
$WRITE SYS$OUTPUT " "
$INQUIRE SURE "Are you sure there will be no duplication? [Y/N]"
$IF SURE THEN GOTO NO_OVERLAP2
$INQUIRE REDO "Want to reenter both dates? [Y/N]"
$IF REDO THEN GOTO NEW_YEAR
$INQUIRE REDO "Want to reenter last day? [Y/N]"
$IF REDO THEN GOTO YEAR_STILL_OK
$REMOVE_TAPE:
$SET ON
$DISMOUNT 'DRIVE'
$DEALLOCATE 'DRIVE'
$!DELETE DRECTRY.TMP;*
$WRITE SYS$OUTPUT " "
$WRITE SYS$OUTPUT "EXIT"
$WRITE SYS$OUTPUT "That's the end of this run."
$WRITE SYS$OUTPUT -
 "Tape is dismounted and ''F$LOGICAL("TAPE")' is deallocated."
$EXIT
```

```
$!************** LOCKHEED PLASMA COMPOSITION EXPERIMENT ON ISEE-1 **************
$!                    ****** DELETE_ISEEMS.COM ******
$!
$!   Interactive command file for deleting ISEEMS archival files from disk
$!   (can transfer the deleting to a batch job via REMOVE_ISEEMS_FILES.COM)
$!
$!                           by O. W. Lennartsson
$!                  Lockheed Missiles & Space Company, Inc.
$!                        Research and Development
$!                          Dept. 91-20, Bldg. 255
$!                           3251 Hanover Street
$!                           Palo Alto, CA 94304
$!
$! Telephone (415) 424-3259
$!
$! Developed under NASA Contract NAS5-33047
$!
$! The command language is that of VAX/VMS Version 5.4
$!
$! To execute this file, simply enter @DELETE_ISEEMS, if the file resides in the
$! same directory used for the data files, otherwise specify directory name in
$! the command: @directory_nameDELETE_ISEEMS (your default directory should be
$! the one used for data files).
$!*****************************************************************************
$WRITE SYS$OUTPUT " "
$DEFAULT_DIR = F$LOGICAL("SYS$DISK")+F$DIRECTORY()
$!
$!This directory may or may not be used for the command files.
$!If not, change next command line to appropriate directory:
$COMMAND_DIR = DEFAULT_DIR
$!
$WRITE SYS$OUTPUT "Your default directory is: ",''DEFAULT_DIR'
$WRITE SYS$OUTPUT "Is this where the ISEEMS data files are?"
$WRITE SYS$OUTPUT "If not, Ctrl/Y and reset."
$WRITE SYS$OUTPUT " "
$WRITE SYS$OUTPUT "Files are deleted by date, starting with the ",-
 "first day entered,"
$WRITE SYS$OUTPUT "and ending with the second day ",-
 "-assuming one and the same year."
$WRITE SYS$OUTPUT " "
$WRITE SYS$OUTPUT "If files run into second year, ",-
 "repeat this operation for that year's days."
$WRITE SYS$OUTPUT " "
$INQUIRE P2 "What YEAR? (two digits)"
$LENGTH_OF_YEAR:
$LP2=F$LENGTH(P2)
$IF(LP2.EQ.2) THEN GOTO CHECK_YEAR
$INQUIRE P2 "Enter two digits for the year: 77 or 78 or 79 or 80"
$GOTO LENGTH_OF_YEAR
$WRONG_YEAR:
$INQUIRE P2 "Enter either of 77 or 78 or 79 or 80"
$CHECK_YEAR:
```

```
$NY=F$INTEGER(F$EXTRACT(0,2,P2))
$IF(NY.LT.77.OR.NY.GT.80) THEN GOTO WRONG_YEAR
$YEAR_OK:
$WRITE SYS$OUTPUT " "
$INQUIRE P3 "First DAY? (one to three digits)"
$LP3=F$LENGTH(P3)
$IF(LP3.GT.3) THEN GOTO YEAR_OK
$IF(LP3.EQ.2) THEN P3:= "0''P3'"
$IF(LP3.EQ.1) THEN P3:= "00''P3'"
$ND=F$INTEGER(F$EXTRACT(0,3,P3))
$IF(NY.EQ.80) .AND. (ND.LT.1.OR.ND.GT.366) .OR. -
   (NY.NE.80) .AND. (ND.LT.1.OR.ND.GT.365) THEN GOTO YEAR_OK
$YYDDD= F$EXTRACT(0,2,P2) + F$EXTRACT(0,3,P3)
$DIR/OUTPUT=DRECTRY.TMP 'DEFAULT_DIR'*'YYDDD'.DAT
$IF $SEVERITY .EQ. 0 THEN GOTO NO_FILE
$DELETE DRECTRY.TMP;*
$ISTART=ND
$YEAR_STILL_OK:
$WRITE SYS$OUTPUT " "
$INQUIRE P3 "Second DAY? (last day of same year to be deleted)"
$LP3=F$LENGTH(P3)
$IF(LP3.GT.3) THEN GOTO YEAR_STILL_OK
$IF(LP3.EQ.2) THEN P3:= "0''P3'"
$IF(LP3.EQ.1) THEN P3:= "00''P3'"
$ND=F$INTEGER(F$EXTRACT(0,3,P3))
$IF(NY.EQ.80) .AND. (ND.LT.1.OR.ND.GT.366) .OR. -
   (NY.NE.80) .AND. (ND.LT.1.OR.ND.GT.365) THEN GOTO YEAR_STILL_OK
$YYDDD= F$EXTRACT(0,2,P2) + F$EXTRACT(0,3,P3)
$DIR/OUTPUT=DRECTRY.TMP 'DEFAULT_DIR'*'YYDDD'.DAT
$IF $SEVERITY .EQ. 0 THEN GOTO NO_FILE
$DELETE DRECTRY.TMP;*
$ISTOP=ND
$WRITE SYS$OUTPUT " "
$WRITE SYS$OUTPUT "If you are deleting a large number of files it may ",-
"take a few minutes."
$WRITE SYS$OUTPUT "In the meantime this terminal will be tied up, ",-
"unless you transfer this job"
$WRITE SYS$OUTPUT "to a batch queue."
$WRITE SYS$OUTPUT " "
$INQUIRE BAT "Would you rather delete in BATCH? [Y/N]"
$IF .NOT. BAT THEN GOTO NO_BAT
$INQUIRE BATQU "Enter name of batch queue"
$SUBMIT/QUEUE='BATQU'/LOG_FILE='DEFAULT_DIR'/NOPRINT-
/PARAM=('DEFAULT_DIR,'NY,'ISTART,'ISTOP) -
'COMMAND_DIR'REMOVE_ISEEMS_FILES
$WRITE SYS$OUTPUT " "
$WRITE SYS$OUTPUT "This terminal is yours again"
$WRITE SYS$OUTPUT " "
$EXIT
$NO_BAT:
$WRITE SYS$OUTPUT " "
$WRITE SYS$OUTPUT "As you wish!"
$WRITE SYS$OUTPUT " "
$IDAY=ISTART
$DATA_DELETE:
$IF(IDAY.LE.9) THEN YYDDD= F$STRING(NY) + "00" + F$STRING(IDAY)
$IF(IDAY.GT.9) .AND. (IDAY.LE.99) THEN -
```

```
 YYDDD= F$STRING(NY) + "0" + F$STRING(IDAY)
$IF(IDAY.GT.99) THEN YYDDD= F$STRING(NY) + F$STRING(IDAY)
$DELETE 'DEFAULT_DIR'*'YYDDD'.DAT;*
$IDAY=IDAY+1
$IF(IDAY.GT.ISTOP) THEN GOTO FILES_LEFT
$GOTO DATA_DELETE
$FILES_LEFT:
$WRITE SYS$OUTPUT " "
$WRITE SYS$OUTPUT "Files left:"
$WRITE SYS$OUTPUT " "
$DIR/SIZE=ALL/DATE/PROT ED*,EX*,MC*,MD*,MS*
$EXIT
$NO_FILE:
$WRITE SYS$OUTPUT " "
$WRITE SYS$OUTPUT "Files missing: No ED",'YYDDD',".DAT, etc."
$WRITE SYS$OUTPUT "Check dates and reenter command."
$DELETE DRECTRY.TMP;*
$EXIT
```

```
$!************** LOCKHEED PLASMA COMPOSITION EXPERIMENT ON ISEE-1 **************
$!                  ****** REMOVE_ISEEMS_FILES.COM ******
$!
$!       Batch command file for deleting ISEEMS archival files from disk
$!          (must be submitted from the interactive DELETE_ISEEMS.COM)
$!
$!                          by O. W. Lennartsson
$!                  Lockheed Missiles & Space Company, Inc.
$!                        Research and Development
$!                          Dept. 91-20, Bldg. 255
$!                           3251 Hanover Street
$!                           Palo Alto, CA 94304
$!
$! Telephone (415) 424-3259
$!
$! Developed under NASA Contract NAS5-33047
$!
$! The command language is that of VAX/VMS Version 5.4
$!*****************************************************************************
$DEFAULT_DIR=P1
$SET DEFAULT 'DEFAULT_DIR'
$NY=F$INTEGER(P2)
$ISTART=F$INTEGER(P3)
$ISTOP=F$INTEGER(P4)
$SET NOON
$SET NOVERIFY
$IDAY=ISTART
$DATA_DELETE:
$IF(IDAY.LE.9) THEN YYDDD= F$STRING(NY) + "00" + F$STRING(IDAY)
$IF(IDAY.GT.9) .AND. (IDAY.LE.99) THEN -
 YYDDD= F$STRING(NY) + "0" + F$STRING(IDAY)
$IF(IDAY.GT.99) THEN YYDDD= F$STRING(NY) + F$STRING(IDAY)
$DELETE *'YYDDD'.DAT;*
$IDAY=IDAY+1
$IF(IDAY.LE.ISTOP) THEN GOTO DATA_DELETE
$SET VERIFY
$EXIT
```

APPENDIX B

Publications
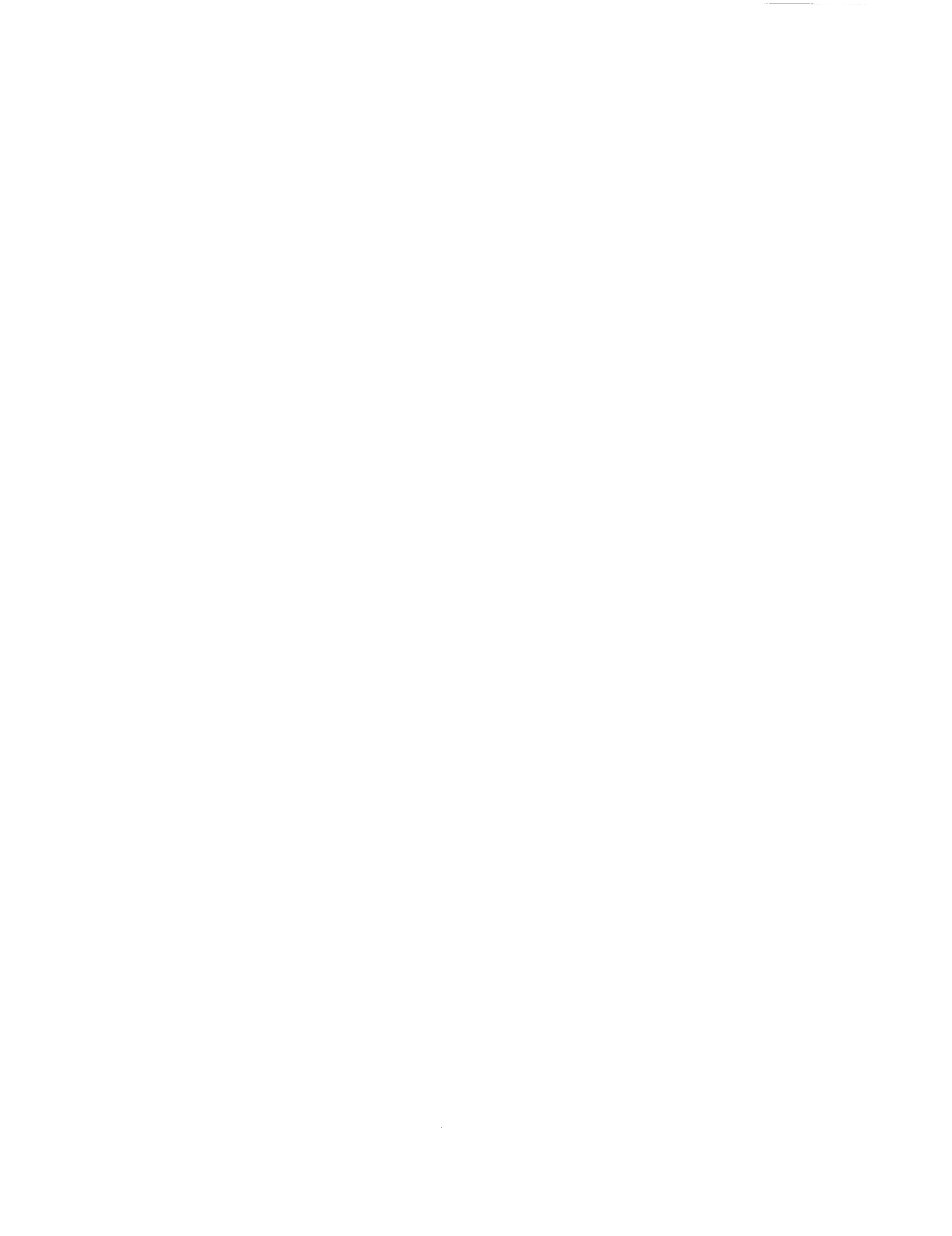
ISEE 1 Observations of Electrostatic Ion Cyclotron Waves in Association With Ion Beams on Auroral Field Lines From ~2.5 to 4.5 R_E

C. A. Cattell,[1] F. S. Mozer,[1,2] I. Roth,[1] R. R. Anderson,[3]
R. C. Elphic,[4,5] W. Lennartsson,[6] and E. Ungstrup[7]

Quasi-monochromatic waves at ~1.2 f_{cH}, where f_{cH} is the hydrogen cyclotron frequency, were observed as the ISEE 1 satellite traversed auroral field lines at radial distances of ~2.5-4.5 R_E near midnight on June 19, 1981. The waves were polarized perpendicular to the magnetic field ($k_\parallel/k_\perp \leq 0.2$). In addition, there were waves at slightly above both the helium and the oxygen cyclotron frequencies. The waves occurred within a region of reduced density (~0.1-0.2/cm^3) with the electron temperature greater than the ion temperature, upflowing hydrogen and oxygen beams, and weak field-aligned currents bounded by electrostatic shocks. The wave characteristics and associations were similar to those observed at lower altitudes by the S3-3 satellite. Comparisons were made between the observed H$^+$ and O$^+$ beams, field-aligned currents, densities and temperatures, and linear theories of electrostatic ion cyclotron waves and H$^+$-O$^+$ two-stream instabilities. The features of the observed waves are most consistent with the current-driven mode. In addition, numerical studies of the linear dispersion relation, using parameters based on the observations, showed that both the parallel and oblique two-stream modes and the ion-beam driven modes were stable while oblique current driven modes were unstable. The O$^+$ and H$^+$ distributions provide evidence for interactions with local electrostatic ion cyclotron waves and for the H$^+$-O$^+$ two-stream instability at altitudes below the satellite.

1. INTRODUCTION

Since the suggestion of *Kindel and Kennel* [1971] that field-aligned currents should drive electrostatic ion cyclotron waves (EIC) in the auroral zone, the occurrence of this wave mode, its source of free energy, its effects on both ions and electrons, and its importance in auroral phenomenology have been studied extensively using rocket, satellite, and laboratory experiments, theoretical analysis, and computer simulations. Observational data on EIC waves were obtained by the S3-3 satellite, and to date, only electrostatic hydrogen cyclotron waves (EHC) have been identified in that data set. Characteristics of the waves, including frequency, wave number, and waveform [*Kintner et al.*, 1978, 1979; *Temerin et al.*, 1979; *Kintner*, 1980], and the association of the waves with ion beams [*Kintner et al.*, 1979], field-aligned currents [*Cattell*, 1981], and other auroral phenomena [*Cattell*, 1984; *Temerin and Mozer*, 1984] have all been described. Similar associations of ion beams and hydrogen cyclotron waves have been observed at higher altitudes by DE 1 [*Kintner et al.*, 1983] and Viking [*André et al.*, 1987]. In contrast, both hydrogen and oxygen cyclotron waves have been reported in rocket data [*Bering et al.*, 1975; *Kelley et al.*, 1975; *Bering*, 1984; *Kintner et al.*, 1989, and references therein]. Two possible sources of free energy for EIC waves have been identified: ion beams and field-aligned currents. Analytical and simulation studies of both beam- and current-driven modes have

been made [*Kindel and Kennel*, 1971; *Ashour-Abdalla and Thorne*, 1978; *Kaufmann and Kintner*, 1982, 1984; *Miura et al.*, 1983; *Bergmann*, 1984; *André*, 1985], including the effects of the waves on both electrons and ions [*Hudson et al.*, 1978; *Ungstrup et al.*, 1979; *Lysak et al.*, 1980; *Dusenbery and Lyons*, 1981; *Ashour-Abdalla et al.*, 1981; *Ashour-Abdalla and Okuda*, 1984]. In addition, there are nonlinear methods for exciting EIC waves such as three-wave decay [*Bergmann*, 1986] and radiation by ion holes [*Tetreault*, 1991]. Laboratory plasma studies have also addressed these phenomena [*Böhmer et al.*, 1976; *Hauck et al.*, 1978; and references therein]. The free energy source and the complex relationship between EIC waves and auroral zone dynamics, however, are still not understood.

More recently, attention has focused on the interaction of oxygen and hydrogen beams drifting relative to one another (rather than a single ion beam drifting relative to the electrons or background ions) [*Bergmann and Lotko*, 1986; *Kaufmann et al.*, 1986; *Bergmann et al.*, 1988; *Dusenbery et al.*, 1988; *Roth et al.*, 1989]. Waves in the same frequency range and with similar wave vectors to EIC waves can be produced by the ion two-stream interaction in certain parameter regimes.

In this paper we focus on one event where quasi-monochromatic waves at approximately the hydrogen cyclotron frequency were observed as ISEE 1 traveled down along auroral field lines from ~4.5 to ~2.5 R_E. The satellite track and a schematic representation of selected data quantities are shown in Figure 1. Waves at both lower (around the hydrogen gyrofrequency) and higher (above the hydrogen gyrofrequency) frequencies were observed at higher altitudes, and possible electrostatic helium cyclotron and oxygen cyclotron waves occurred at lower altitudes. Upflowing hydrogen and oxygen beams and field-aligned currents occurred simultaneously. Using data from the small burst memory of the spherical double-probe experiment (which sampled the electric field at frequencies below 128 Hz), the ion mass spectrometer data, the dc electric and magnetic fields, the high-frequency ($10^2-4 \times 10^5$ Hz) electric field from the swept frequency receiver, the electric spectrum analyzer (5.6 Hz to 311 kHz), and the electron spectrometer, the following topics will be examined: (1) the large-scale morphol-

[1]Space Sciences Laboratory, University of California at Berkeley.

[2]Also at Physics Department, University of California at Berkeley.

[3]Department of Physics and Astronomy, University of Iowa, Iowa City.

[4]Now at Los Alamos National Laboratory, Los Alamos, New Mexico.

[5]Institute of Geophysics and Planetary Physics, University of California, Los Angeles.

[6]Lockheed Palo Alto Research Laboratory, Palo Alto, California.

[7]Danish Space Research Institute, Lyngby.

PRECEDING PAGE BLANK NOT FILMED
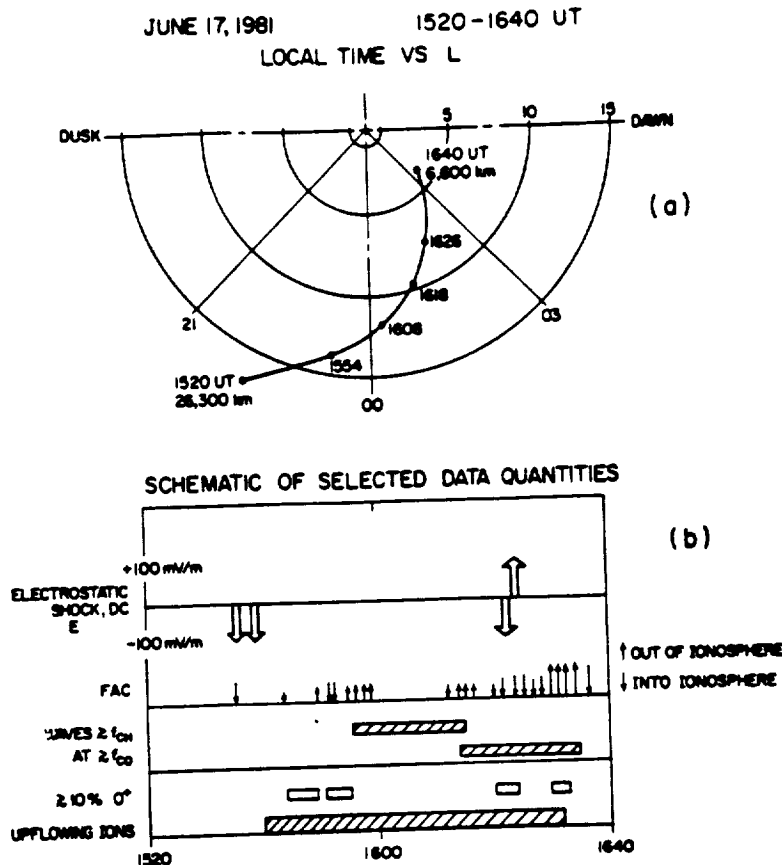
Fig. 1. (a) The satellite track in L-LT coordinates for the event. (b) A schematic model of some important data quantities. The overall structure of the event is very similar to the electrostatic shock events observed at lower altitudes by the S3-3 satellite.

ogy of the event; (2) the characteristics of the EIC waves; (3) wave/particle interactions; (4) free energy sources; and (5) the relationship to higher-frequency waves.

The instrumentation and data sets are described in section 2, the large-scale morphology is presented in section 3 and the low frequency waves in section 4, free energy sources are examined in section 5, the effects of the waves on ions are discussed in section 6, and discussion and conclusions are in section 7.

2. INSTRUMENTATION AND DATA SETS

The dc and low-frequency ac electric field data were obtained from the University of California, Berkeley, double-probe experiment on ISEE 1 [Mozer et al., 1978]. This study concentrates on the electric field from 2 to 128 Hz measured by the burst mode of the instrument which made 128 samples of the electric field along the spinning booms in 0.5 s every 128 s. In addition, the dc 3-s spin period averages of the GSE x and y components of the field, the spacecraft potential (which is indicative of the plasma density), and the outputs of three broad filters will be described. Verification of instrument operation in low-density plasmas and error sources in the electric field measurement are discussed in Mozer et al. [1983] and Pedersen et al. [1984].

The ion data were obtained by the Lockheed energetic ion mass spectrometer on ISEE 1 [Shelley et al., 1978]. During this period the instrument was operated in a special mode, designed to study the auroral acceleration region, in which pitch angle scans of both H^+ and O^+ were obtained at eight energies (0.21–17.4 keV) every 64 s (see Sharp et al. [1983] for details).

The electron data are from the ISEE 1 electron spectrometer [Ogilvie et al., 1978] which was operating in a mode which measured electrons from 105 to 7050 eV. Nine-second averages of the density and temperature and distribution functions will be shown. During this period, detector 1, the poleward detector, was not operating. This has minimal effect on the density and temperature moments; however, velocity moments and therefore the current carried by the electrons could not be calculated accurately.

The magnetic field data are from the University of California, Los Angeles, flux gate magnetometers on ISEE 1 [Russell, 1978]. High time resolution data (4 points per second) will be shown. To determine field-aligned currents, the data were rotated into a dipole coordinate system, and the background field was removed. ISEE 2 data, which were available only during the first part of the event, were used to determine current sheet orientation and thickness.

High-frequency (>100 Hz) ac electric fields were obtained from the swept frequency receiver of the University of Iowa plasma wave experiment on ISEE 1 [Gurnett et al., 1978]. A spectrum from 10^2 to 10^6 Hz was obtained every 32 s. In addition, the data from the electric spectrum analyzer with filters from 5.6 Hz to 311 kHz were examined. Note that it is difficult to see peaks below ~10 Hz in the spectrum analyzer due to solar array noise interference.

3. EVENT OVERVIEW

The large-scale morphology of the time period of interest (1520–1630 on June 19, 1981), which occurred as ISEE moved

in nearly along auroral field lines from an altitude of ~26,300 km to ~6600 km (~5.1-2 R_g geocentric), is presented schematically in Figure 1 (described above), and selected data are shown in Figure 2. During this period, ISEE moved from a dipole L of ~15 and local time of ~2245 to a dipole L of ~4 and local time of ~0300. From ~1535 to ~1630 the duskward (y GSE) component of the 3-s-averaged electric field (Figure 2a) was generally variable and ≤40 mV/m with the maximum field of ~100 mV/m occurring in a narrow spike at ~1623. If, however,

the electric fields observed at ~1535 were mapped, assuming equipotential field lines, to the same altitude as those at ~1623, the magnitudes would be comparable. Examination of the raw electric field data shows that these large fields had a time scale of several spin periods, so that the spin period averaged data provide an accurate determination of the magnitude of the field in the spin plane. The x component (i.e., close to parallel to B) was always much smaller than the y component. Note that comparison with S3-3 data [Mozer et al., 1980] suggests that
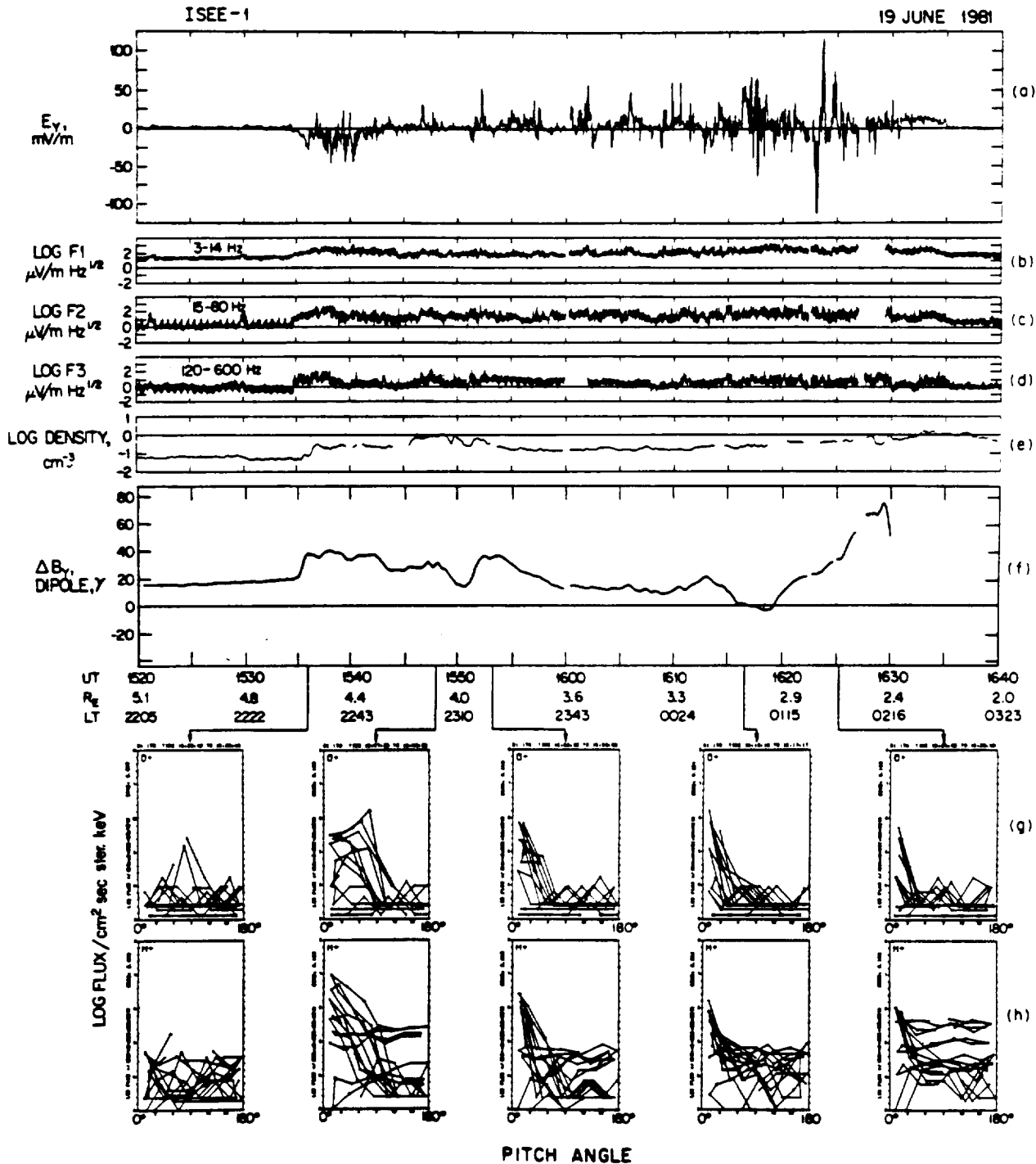
Fig. 2. An overview of the event on June 19, 1981: (a) the dawn-dusk component of the electric field, (b) the negative of the spacecraft potential which is indicative of the thermal plasma density, (c)-(e) the outputs of three broad filters, (f) the azimuthal perturbation in the magnetic field which indicates field-aligned currents, and (g) and (h) selected pitch angle distributions of O+ and H+, respectively.

the largest component of the electric field would be the GSE z component, which is not measured by the ISEE satellite. V_{2S}, the negative of the spacecraft potential (Figure 2b), indicates changes in the plasma density, since $V_{2S} \propto \log n T_e^M$ [Mozer et al., 1983]. Density measurements will be discussed in more detail in section 5. There were two broad density depletions, from ~1535 to ~1545 and from ~1553 to ~1623, with another density increase at ~1630.

Figures 2g and 2h show selected pitch angle distributions of O^+ and H^+, respectively. Upflowing ions are peaked at $0°$ since the satellite was in the southern hemisphere. There were no fluxes above background until 1535:42, when the oxygen fluxes (215 and 400 eV) peaked near 90°. By 1538:54, both oxygen and hydrogen were upflowing (peaked at 10°, which was as close as the detector came to B). At ~1542 the O^+ became conical. The highest fluxes were observed from ~1546 to ~1553, when the O^+ was peaked at angles varying from ~45° to ~70° and the hydrogen peaked along the field. Ion beams with variable fluxes and maximum energies were observed in both oxygen and hydrogen throughout the time ~1552—1633, with a second region of intense fluxes occurring from ~1615 to ~1625. From ~1618 to 1622 and from ~1625 to 1630 the distributions were more complex than simple upflowing beams.

The perturbation in the y component of the 4-s-averaged magnetic field in dipole coordinates (in which $\hat{z}$ is along the model field, $\hat{y}$ is azimuthal eastward, and $\hat{x}$ is in the magnetic meridian plane pointing southward) is shown in Figure 2f. Figure 3 shows both the x and the y components of the high-

ISEE MAGNETIC FIELD   JUNE 19, 1981
FIELD-ALIGNED COORDINATES
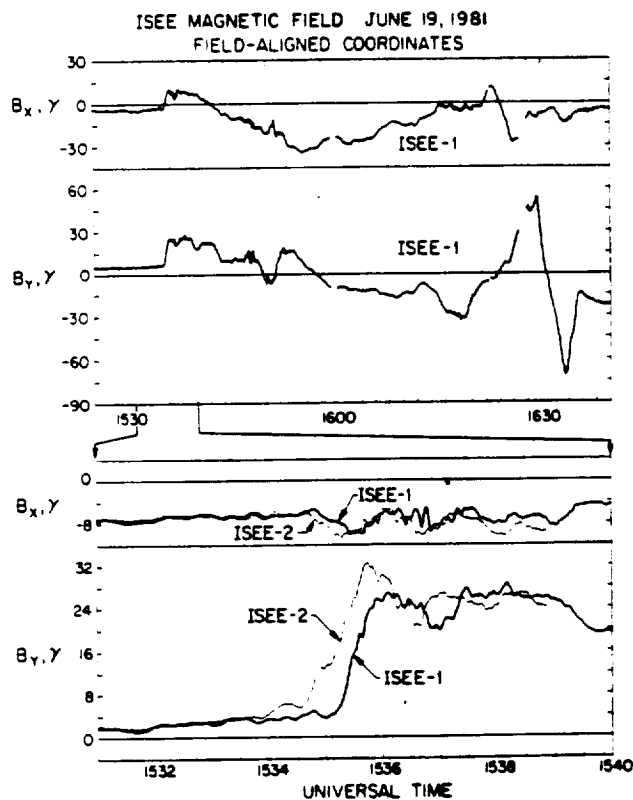
Fig. 3. The magnetic field in field-aligned components (in which the z axis is along the average field direction, and y is azimuthal). The x and y components of the magnetic field measured by ISEE 1 for the entire event are plotted in the top two panels. The bottom two panels show an expanded view of both the ISEE 1 and ISEE 2 magnetic field for the time period when ISEE 2 data were available.

resolution magnetic field in field-aligned coordinates. Field-aligned current sheets extensive in longitude cause perturbations primarily in the y component. For the observed geometry and assumed satellite velocity with respect to the medium, increases (decreases) in B_y correspond to currents flowing toward (away from) the Earth. At ~1536 there was a current toward the Earth (~0.02 A/m), followed by several weaker currents, then an outward sheet of comparable size at ~1543, again followed by weaker currents and, finally, another more intense outward sheet at ~1548. At ~1552 the current was toward the Earth with a magnitude ~0.02 A/m; from ~1554 to ~1619 there was a weak (~0.03 A/m) current generally away from the Earth. The final three currents were the most intense and consisted of an inward current from ~1620 to ~1630 (~0.06 A/m), an outward current from ~1630 to ~1634 (0.09 A/m), and another inward current from ~1634—1636. There may be some inaccuracies in the current determination after ~1610 because the satellite was moving rapidly in local time (i.e., parallel to the assumed current sheet) and the perturbation in the $\hat{z}$ component was becoming large. The fact that the perturbations in the x component were sometimes comparable to the y component perturbations indicates that the observed field-aligned currents are not well modeled by infinite sheet currents aligned along an L shell. ISEE 2 magnetic field data, available until 1539 UT, were used to determine current sheet thickness and current density. The main current at ~1536 had a thickness of ~490–590 km and a maximum current density of 60 nA/m² and was traveling outward (i.e., normal to the L shell) at a velocity of 4–6 km/s. Since the spacecraft are below the magnetic equator, this is a southward motion of the current sheet.

Throughout the region of upflowing ions, density depletion, and large dc electric field, there were enhanced levels of low-frequency noise, as indicated in Figures 2c, 2d, and 2e, which plot the output from three broad filters. This morphology [large spiky electric fields (electrostatic shocks) bounding a region of depleted density, upflowing ion beams, and enhanced plasma waves] is the same as was observed on the S3-3 satellite at lower altitudes (5000–8000 km) [Mozer et al., 1980; Temerin et al., 1981; Mizera et al., 1981; Temerin and Mozer, 1984]. Figure 5 of Mozer et al. [1979], Figure 7 of Mozer et al. [1980], and Figures 2 and 4 of Mizera et al. [1981] all present examples of these associations.

4. WAVE OBSERVATIONS

The low-frequency electric field data which motivated this study are shown in Figures 4a, 4b, and 4c. Each panel contains two consecutive 0.5-s electric field waveforms obtained in the burst mode.

The burst mode data for the initial 30 min of the period in Figure 2 are shown in Figure 4a. Waves above background were not observed until the onset of the field-aligned current, density decrease and large dc electric fields at ~1535. Dominant frequencies varied from $<f_{cH}$ to $~8f_{cH}$ or ~4-74 Hz (which for these samples also corresponded to peaks at $<f_{pi}$, the ion plasma frequency); the spectra were often very flat, and the range of amplitudes was large. One of the two largest amplitude samples occurred during this period, at ~1552, when the dominant frequency was approximately 3 times the hydrogen cyclotron frequency. From ~1600 to 1625 (Figure 4b), quasi-monochromatic waves at approximately f_{cH}, the hydrogen cyclotron frequency, with amplitudes of a few millivolts per meter are apparent in most of the samples in the upper four panels. In addition, waves at $-f_{cH}$ occurred in association with
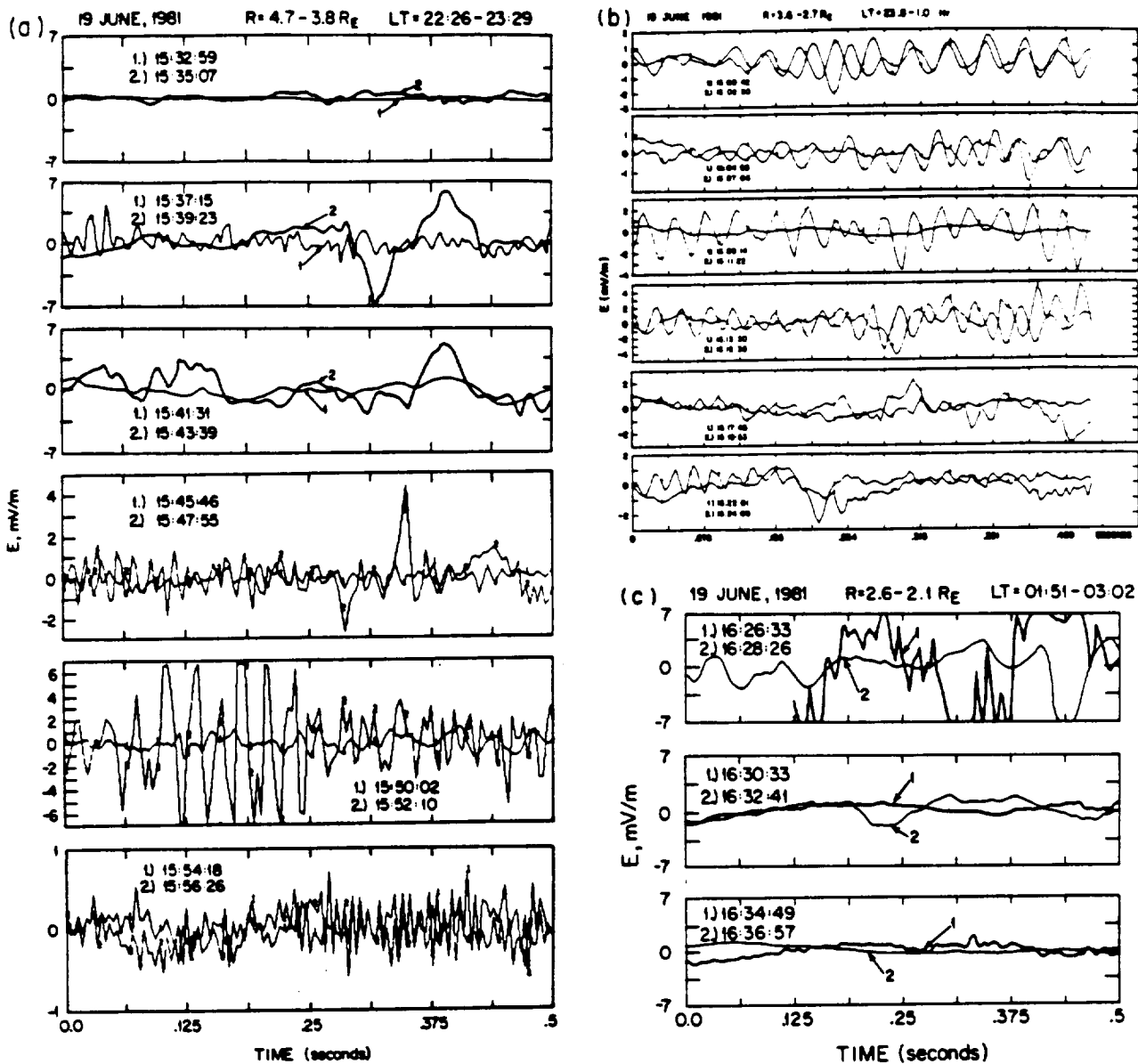
Fig. 4. The 0.5-s snapshots of the electric field along the spinning booms, taken in the burst mode of the instrument, for the period of the event.

waves at lower frequencies during the other samples in this figure. The waves shown in Figure 4c are basically similar to those observed during the preceding samples of Figure 4b. The waves in sample 1 (1626:33) were intense enough to saturate the measured quantity (± 7 mV/m). Since there were missing data points during this burst, a spectrum was not computed, but by examination the dominant frequency was ~5 Hz or ~1.5 f_{cO} with some power occurring near f_{cH} also.

To determine the properties (f, k) of the waves, we have examined various characteristics of the waveforms, the power spectra, and the simultaneous filter data. For all cases when the peak power was $>10^{-2}$ (mV/m)^2 Hz^{-1} (for each sample in Figure 4 for which a Fourier spectrum could be calculated), the frequency at which the peak power was observed has been plotted as a circled dot versus the local hydrogen cyclotron frequency in Figure 5 (the corresponding universal time is also noted). Secondary peaks (power within a factor of 0.5 of the primary peak) have been plotted as crosses. The data from the Univer-

sity of Iowa spectrum analyzer generally agreed well with the peaks observed above -10 Hz.

Before ~1600 the waves occurred over a broad frequency range, as discussed above. It can be seen that after ~1600 the frequencies at the peak power fall into three groups: one associated with the H$^+$ cyclotron frequency, one with the He$^+$ cyclotron frequency f_{cHe} and one with the O$^+$ cyclotron frequency f_{cO}. This suggests that the observed waves may be electrostatic ion cyclotron waves which for brevity will be referred to as EHC, EOC, and EHeC below. Other wave modes, such as ion two-stream instabilities, can also have frequencies in this range. Note that it is difficult to be certain that the waves at $2f_{cHe}$ are electrostatic He$^+$ cyclotron waves for several reasons: (1) the ion mass spectrometer was not in a mode to measure He$^+$, (2) f_{cHe} is also $(f_{cO}f_{cH})^{1/2}$, which is the two-ion hybrid frequency when the O$^+$ and H$^+$ densities are comparable, and (3) there are waves other than EHeC waves that have $f_{cHe} < f < f_{cH}$ such as the Alfvén ion cyclotron waves [Lysak and Temerin, 1983; Temerin
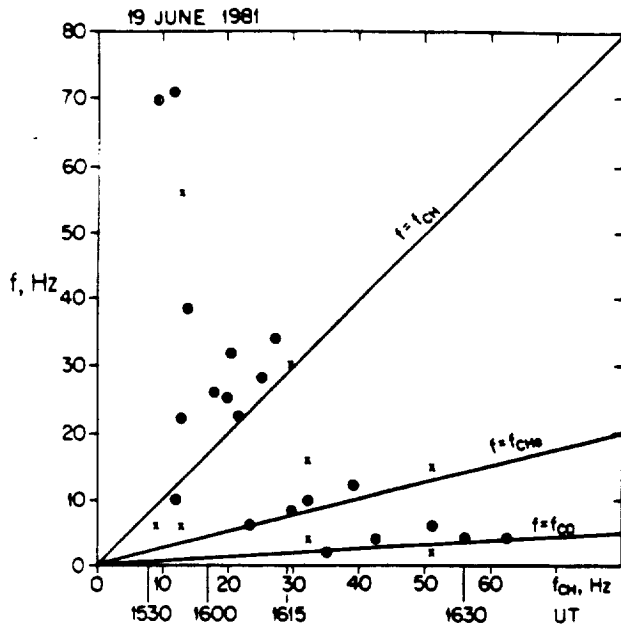
Fig. 5. The frequency at which the peak power (circled dot) occurred for each burst in figure for which a spectrum could be computed. Secondary peaks (with power within a factor of 0.5 of the primary peak) are indicated by a cross.

and Lysak, 1984], and ion two-stream instabilities [*Bergmann et al.*, 1988]. Indirect evidence for the existence of a population of He^+ can be obtained by comparing the density inferred after energy analysis and that after both energy and mass analysis (see Figure 6). At the times where the two are different (for example, at ~1620–1625 and 1543–1546 and other shorter intervals), He^+ may have been present. Ion densities were calculated under the assumption that the fluxes were gyrotropic in the instrument frame and varied linearly with energy between the energy channels sampled.
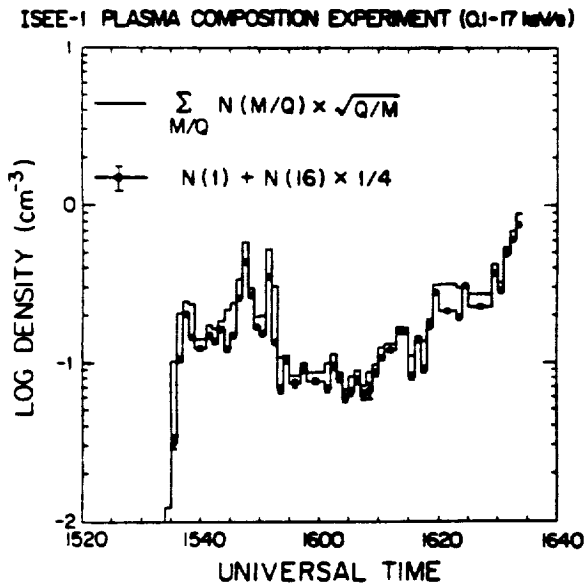
Fig. 6. Comparison of ion densities inferred after energy analysis alone (plain line) and after both energy and mass analysis (line with data points). The error bars on the latter show standard deviations due to counting statistics (about the same as or smaller in the other case). Mass analysis was limited to $M/Q = 1$ (H^+) and $M/Q = 16$ (O^+). Differences between the graphs suggest additional ion species.

The frequency of the EHC waves varies from 1.1 to 1.6 f_{cH+} with the average equal to ~1.25 f_{cH}. Estimates of the magnitude of the wave vector k can be obtained in two ways (see also *Kintner et al.* [1978]). First, the quasi-monochromatic nature of the waves suggests that Doppler shifting must be small. The half width at half maximum had an average value of $\Delta f / f \leq 0.1$. Assuming that the measured width in the peak is due to the Doppler shift, the wave vector can be calculated from

$$\Delta f = f' - f = k \cdot v$$

where f' is the frequency in the spacecraft frame, f is the frequency of the plasma frame, and v is the relative velocity between the plasma and the spacecraft. Although the complete $E \times B/B^2$ velocity could not be calculated during this time period, $(E \times B)_z/B^2$ was usually less than the satellite velocity, so the spacecraft velocity was used in the calculation. The measured Δf therefore yield values of $k = 3-6$ km^{-1}. Since theories of EIC waves yield values of the wave vector comparable to the ion gyroradius, an estimate of the temperature of the ions supporting the wave can be obtained using the magnitude of the wave vector (calculated above) and

$$k \rho_i = \frac{k v_{th,i}}{\Omega_i} - 1.$$

where $v_{th,i}$ is the ion thermal velocity, ρ_i is the ion gyroradius, and Ω_i is the ion cyclotron frequency. The relevant hydrogen temperature T_H would be ~6–21 eV, implying the existence of a cool background ion population. Second, there were several spectra with a double-peaked structure which could be explained by Doppler shifting, assuming $k = k_\perp$, because of the geometry of the booms, magnetic field, and satellite velocity. For these events, $k = 2-4$ km^{-1}, and assuming $k \rho_H - 1$, $T_H - 8 - 30$ eV. These calculations assumed that the observed Doppler shift was not due to the velocity of the ion beams. If we assume that the shift due to the beam velocity is important, we obtain $k - 0.5 - 1.5$ km^{-1} or T_H for the beam of 200–1000 eV. Since the magnetic field is <6° out of the ecliptic plane, $k_\parallel/k_\perp$ can be estimated from the spin modulation of the amplitude of the filter data. Sharp minima in the amplitude of the waves occurred when the booms were aligned with the magnetic field. The shape of the minima is consistent with $0.05 \leq k_\parallel/k_\perp \leq 0.2$. One of the individual burst samples also had a modulation consistent with $0.1 \leq k_\parallel/k_\perp \leq 0.2$; however, time variability in the wave amplitude could also explain the observed variation, and such modulation was not observable in other burst samples.

Because there were fewer samples near f_{cH+} and f_{cO} and because the frequencies are lower and therefore closer to the burst mode resolution, the average properties are not as well determined as for the f_{cH} case. For the samples peaked near the He^+ cyclotron frequency the average was ~1.1 f_{cHe}, with a range from 1 to 1.2 f_{cHe}. The observed half widths of the peaks were almost always within the 2-Hz resolution of the measurement. For the range of spacecraft velocities, therefore, $k \geq 3$ km^{-1}, and assuming $k \rho_{He} - 1$, $T_{He} > 6 - 170$ eV. The one spectrum with a double-peaked structure yielded $T_{He} - 16$ eV. For the events identified as possible electrostatic oxygen cyclotron waves, f_{cO} varied from 2.6 to 4 Hz, and the observed peak frequencies varied from 4 to 6 Hz, with the average dominant frequency approximately equal to 1.4 f_{cO} (this may not be very meaningful, since f_{cO} is so close to the 2-Hz resolution of the spectra). The half width was usually <2 Hz, yielding $T_O \geq 6 - 25$ eV, with the assumption that $k \rho_O - 1$.
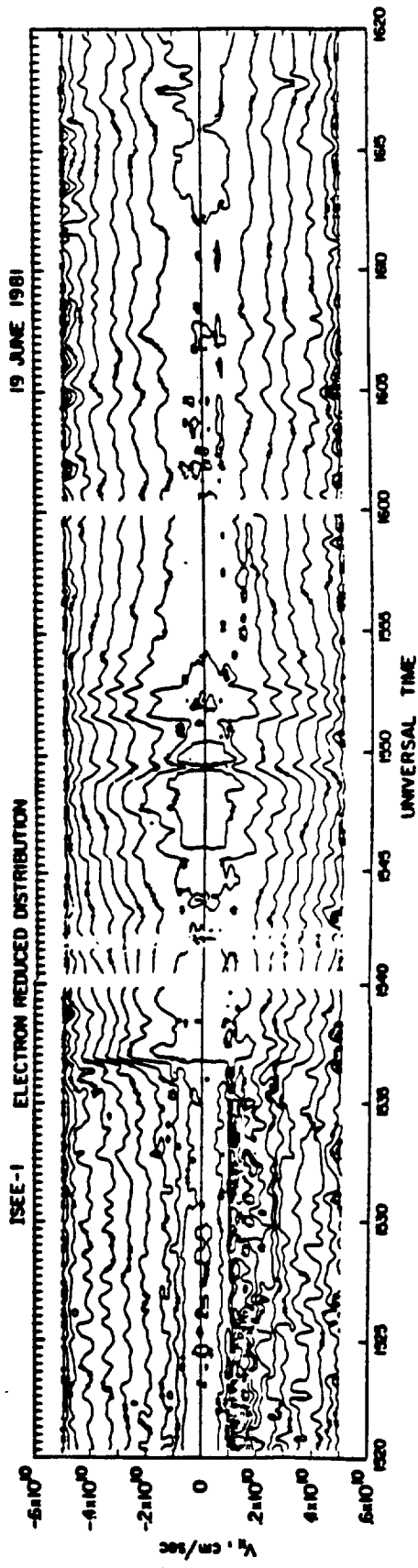
Plate 1. (Note this is a reduction of a fold-out plate that was too large to be copied in one piece. Thus the breaks in the horizontal lines ~1540 UT.)

The frequency and wavelength ranges obtained for the hydrogen cyclotron waves can be compared with previous experimental results from the S3-3 satellite and with various theoretical predictions. The average frequency of the EHC waves observed by the S3-3 satellite is ~1.2 f_{cH} [Bergmann, 1984; M. A. Temerin, private communication, 1984]. Since the S3-3 instrument was a three-axis instrument, $k_\parallel/k_\perp$ was directly measured and found to be usually less than 0.2 [Bergmann, 1984]. These values are consistent with those obtained herein, which suggests that the waves at high altitudes are generated by the same mechanism as those at low altitudes. Bergmann [1984], using linear dispersion relations and a single ion species, concluded that the observed S3-3 wave parameters were most consistent with the current-driven instability.

Wave observations were also obtained at frequencies above 100 Hz by the University of Iowa swept frequency receiver. VLF hiss was very intense in the high-density regions and reduced in both intensity and frequency extent in the low-density regions. Figure 7 presents two representative examples of composite spectra obtained during the period of the EHC waves described above. The first spectrum (at ~1600:40) is generally smoothly falling from the peak above f_{cH} up to the region of z mode and auroral kilometric radiation (AKR). In contrast, the second (at ~1611:20) shows several emission features in the domain between f_{pH} and f_{pe}. The observed AKR in both samples was very intense.

ISEE-1   R ≈ ~3.5 R_E
19 JUNE 1981   LT ≈ ~24 Hr

POWER, V^2/m^2 Hz

UCB 1600:42

UI SFR 1600:40-1601:12

POWER, V^2/m^2 Hz

UCB 1611:22

UI SFR 1611:20-1611:52
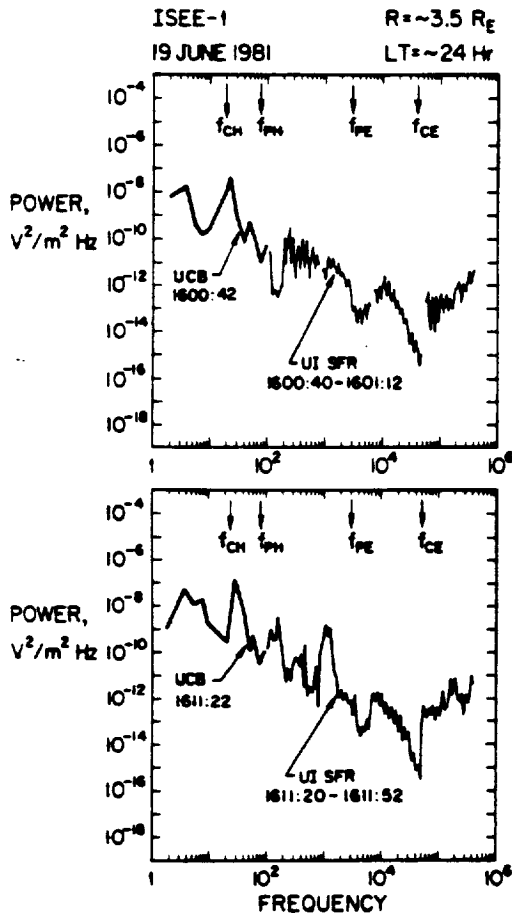
FREQUENCY

Fig. 7. Two composite spectra obtained during the time period when EHC waves were observed. The data below ~120 Hz are from the UCB burst mode; the data above ~100 Hz are from the University of Iowa swept frequency receiver (SFR). Note that there may be some time aliasing since the UCB data are obtained in 0.5 s whereas an SFR spectrum requires 32 s.

5. SOURCES OF FREE ENERGY

Ion beams and field-aligned currents have both been proposed to provide the free energy for growth of the electrostatic ion cyclotron waves which have been observed in the auroral zone. Comparisons of the observational data with theoretical predictions have not yet resolved the question of which is the dominant mechanism [e.g., Kintner et al., 1979; Cattell, 1981; Kaufmann and Kintner, 1982, 1984; Cattell, 1984; Bergmann, 1984; André, 1985; André et al., 1987]. This is in part due to the unmeasured portions of the ion and electron distributions and the low time resolution for current and particle measurements but also to the inescapable problem that when the waves are observed the particle distributions are likely to be marginally stable [e.g., Kaufmann and Kintner, 1982]. During the event described herein, both currents and beams occurred. Another free energy source, the relative streaming of O^+ and H^+ ions, can also produce waves near the ion cyclotron frequency [Bergmann et al., 1988; Kaufmann et al., 1986; Roth et al., 1989]. The very different time resolutions of the wave measurements (0.5 s, repeated every 128 s), the current measurement (~0.25 s), and the ion measurement (~64 s) do not allow for detailed correlations between wave properties (such as amplitude, coherence, etc.) and the magnitude of the current or shape of the ion distribution function; however, the observed relationships provide information on the likely dominant generation mechanism for the measured waves.

Current-driven electrostatic ion cyclotron waves will be considered by comparing the observations described above to the linear dispersion relation and to prior theoretical studies. The first step is to examine wave and particle measurements to determine the density and temperature of various components of the plasma. These will be used with the current measurements to estimate the electron drift velocity. We will show that when waves near the cyclotron frequency were observed, the drift velocity was larger than the critical drift and that EIC waves were suppressed in regions of large field-aligned current when the density and/or temperature were large. Next, we will examine the dependence of the wave frequency on ion composition and conclude that it is consistent with current-driven EIC waves and inconsistent with the two-stream instability. Ion beam-driven modes, including the ion two-stream instability and beam-driven EIC waves with and without a current, will then be examined utilizing previous theoretical studies and numerical solutions to the linear dispersion relation calculated from the observed parameters. We will show that the ion two-stream instability is suppressed for the parameters observed during the time when waves near the cyclotron frequencies occurred. We then solve the dispersion relation, including explicitly the current, the ion beams, and the ion composition, and show that (1) the instability is due to the current, (2) the beams provide damping, and (3) there is a switch in the most unstable mode from f_{cH} to f_{cO} when n_{O}/n_{H} increases. We conclude that our observations are most consistent with the current-driven mode.

First, we will consider field-aligned currents as a source of free energy for the observed waves. The current-driven instability is actually driven by the electron drift which must be above some critical value for marginal linear instability. For example, for an equal temperature plasma (assuming Maxwellian populations) with only a single stationary ion species (hydrogen), the drift of electrons, V_D, must exceed 0.3 times the thermal drift u_e [Kindel and Kennel, 1971]. As the temperature ratio T_e/T_i increases, the critical drift decreases (see, for example, Bergmann [1984], Table 4, which shows values of $V_D/u_e \approx 0.14$ for

$T_e > T_i$ with an additional ion population). In order to determine whether the measured field-aligned currents are above the threshold for linear instability, it is necessary to know (1) whether the current is carried by drifting electrons or by a feature such as a loss cone in the electrons, (2) the electron and ion density and temperatures, and (3) whether there is more than one component for either species. The method we have used to answer these questions is to compare the total density determined by the wave cutoff (measured by the University of Iowa swept frequency receiver) and the densities measured by the particle detectors and to examine the distribution functions for evidence of current-carrying populations.

Figure 8, in which the density determined from each method is plotted, shows that most of the electron density is at energies from 0.1 to 7 keV, except during the period from ~1520 to ~1540 (when there must have been a large population of cold electrons (~0.5 to 1/cm^3)). The measured ion density is also approximately equal to the total density except before ~1540, although there is evidence for an unmeasured cold population with a density of $\leq 0.02/cm^2$ from ~1555 to ~1610. During the period when the EHC waves were observed (~1600--1620), the density was ~0.1-0.2/cm^3, and there was no substantial cold electron population. The field-aligned current was usually $\leq 2 \times 10^{-8}$ A/m^2, with several smaller-scale size sheets with magnitudes up to ~5×10^{-8} A/m^2. Assuming that the current was carried by a drifting Maxwellian with the measured density and temperature, this corresponds to $V_D/v_{the} \approx 0.07-0.15$, which is at
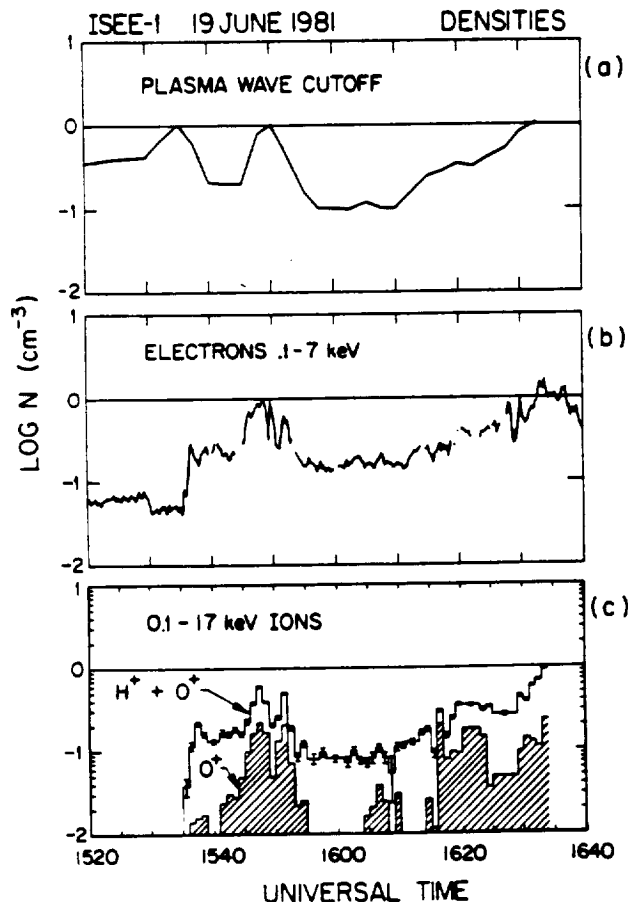
Fig. 8. The plasma density as measured by three different instruments: (a) the density determined from the plasma wave cutoff, (b) the electron density measured between 0.1 and 7 keV, and (c) the ion density measured between 0.1 and 17 keV for O$^+$ ions (hatched) and (O$^+$ + H$^+$) ions.

the low end of the range of critical drifts for $T_e > T_i$ with a single ion beam species present [Bergmann, 1984]. The observed electron distribution, however, was not a drifting Maxwellian when the EIC waves occurred. In fact, the distribution was quite variable in character, as can be seen in Plate 1, in which the reduced electron distribution ($F(v_\parallel) = \int f(v_\perp, v_\parallel) 2\pi dv_\perp$) is plotted versus time. Occasionally, there were beams at ≤ 1 keV. For example, during the downward current sheet at ~1552 there was a low-energy upward electron beam, and in the upward current near 1607-1609 there were downward beams. Unfortunately, an accurate calculation of the current carried by the observed electrons could not be made due to the loss of one detector.

To lend credence to the idea that the waves are current-driven, it is important to understand why EIC waves were not observed in other (often larger) regions of current. For example, one of the largest current densities, at 1536, was flowing into the ionosphere with no simultaneous ion beams. Figure 8 implies that at that time there was a large cold electron population which must have carried the current since the observed hot electrons were almost entirely downgoing. Assuming a temperature of 1-10 eV for the cold electron population with the inferred density of 0.9/cm^3, $V_D/v_{the} \approx 0.003-0.01$ which is much less than the critical value for instability with $T_e = T_i$. There was not a burst sample at this time, but examination of both the University of California at Berkeley and the University of Iowa filters showed no evidence for a peak at or slightly above the hydrogen cyclotron frequency. At ~1543 a large upward current occurred in a region of only hot electrons (if the measured electrons were a drifting Maxwellian, then $V_D/v_{the} = 0.1$) and upflowing ion beams. The burst sample during that current had wave power near f_{cH} but no coherent waves. The largest current during this period ($j ~ 37 \times 10^{-8}$ A/m^2 at ~1632) was also in the region with the highest density ($n \geq 1/cm^3$) and electron temperature and therefore the lowest value of V_D/v_{the}. This observation, that EIC waves were suppressed in regions of large current when the corresponding value of V_D/v_{the} was small, is consistent with theories of current-driven EIC waves.

A second indication that the waves may be current-driven is the dependence of the wave frequencies on the ion composition. Kindel and Kennel [1971] showed that for the current-driven instability, H$^+$ cyclotron waves are linearly more unstable until the density ratio O$^+$/(H$^+$+O$^+$) exceeds ~10-15%, when O$^+$ cyclotron waves become linearly more unstable. The observations presented herein (compare the frequency at which the peak power occurred (Figure 5) with the composition in Figure 6) are consistent with this. When the density ratio was $\leq 10\%$, only EHC waves were observed; from ~10 to 20%, EHC and waves near f_{cH+} and f_{cO} occurred. This dependence of frequency on composition is opposite to that obtained for the ion two-stream instability. As shown in Bergmann et al. [1988], the most unstable oblique mode is above f_{cH} when the percentage of O$^+$ is high and decreases to below f_{cH} when there is less O$^+$. More detailed comparisons with the ion two-stream instability will be described below.

There are also theories which predict the occurrence of EIC waves in a system with a subcritical electron drift (Tetreault, 1991). The EIC waves, in this case, are part of the process by which ion holes evolve into double layers and subsequently decay. No comparisons with this model will be made herein.

Next, we compare the observations quantitatively using a linear dispersion relation solver containing ion beams including composition and either drifting or nondrifting electrons. A car-

toon representation of the particle distributions included is shown in Figure 9. In the presence of two drifting ion populations with a relative drift $\Delta V = V_H - V_O$, the strongest instability can occur when two eigenmodes have a similar dispersion in $\omega - k$ space. In our case the strongest possible candidate for instability occurs for parallel propagation when the slow hydrogen beam acoustic mode with an approximate dispersion relation $\omega \sim k (V_H - c_H)$ couples with a fast oxygen beam acoustic mode $\omega \sim k (V_O + c_O)$, where $c_j^2 = (n_j/n_e)(T_e/m_j)$ are the density weighted sound speeds of species j. The conditions for this interaction are (condition 1)

$$\Delta V / u_e < (1+\delta)(\omega_H/\omega_e)[1+(\omega_O/\omega_H\delta)^2]^{1/2}$$

[Bergmann et al., 1988] and (condition 2) $V_j > u_j$ [Roth et al., 1989], where u_j are the thermal spreads, ω_j are the plasma frequencies, and $\delta = [(n_H/n_O)(m_H/m_O]^{-1/3}$. Condition (1) assures that the drift velocities are close enough together that the slow H^+ and fast O^+ modes can acquire similar phase velocities to enable a fluidlike interaction. Condition (2) assures that the phase velocity of each mode is approximately constant; the contribution of finite ion temperatures modifies each eigenmode dispersion due to additional terms in the expansion of the plasma Z function. For a sufficiently large ion thermal spread the phase velocities of the acoustic modes cannot overlap, and this interaction is stabilized.

(a)

(b)
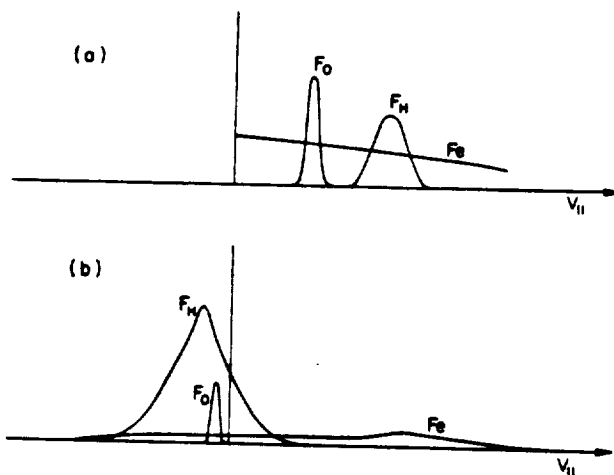
Fig. 9. Schematic representation of the distributions considered in the numerical study of the dispersion relation: (a) without electron drift and (b) with electron drift.

For our benchmark set of parameters, $V_H/u_e - 0.03$, $V_H/V_O - 2$, condition 1 is well satisfied for all ranges of n_O/n_H values. Figure 10 shows the maximum growth rate as obtained from the solution of the dispersion relation for the above parameters with $n_H = n_O$, $V_O/u_O = 5$, and varying the ratio of V_H/u_H. It can be seen that around $V_H/u_H - 2.3$ the parallel ion-ion instability is quenched, with a growth rate $< 3 \times 10^{-4} \omega_H$. The observed contours of hydrogen show relatively warm distributions, and we conclude that the heated hydrogen population is able to quench the parallel ion-ion instability.

The relative drift between each ion species and the electrons can also excite kinetic drift acoustic waves. The growth rate is proportional to the imaginary part of the dielectric function

$$\mathrm{Im}\,\varepsilon \propto \frac{\omega_H^2}{k^2 u_H^2} \frac{\omega - kV_H}{k\,u_H} e^{-(\omega - kV_H)^2/k^2 u_H^2} + \frac{\omega_e^2}{k^2 u_e^2} \frac{\omega}{k\,u_e} e^{-(\omega - k u_e)^2} \quad (1)$$
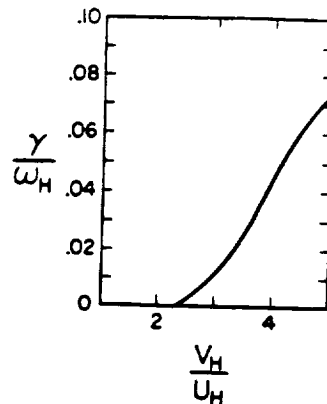
Fig. 10. Plot of the maximum growth rate for the parallel ion two-stream instability versus $V_H = u_H$, the hydrogen drift/thermal speed for $n_H = n_O$, $V_H/u_e = 0.03$, $V_H/V_O = 2$, and $V_O/u_O = 5$.

with a similar expression for the oxygen ions. However, for our parameters the exponent of the electron term in (1) is very small, the damping from the electron term is larger than the ion inverse damping, and the parallel modes which may be excited by ion beams are stable. In our parameter regime where the cold parallel modes could satisfy the instability condition, they dominate the oblique modes [Bergmann et al., 1988]. Quenching of these ion-ion modes also quenches the oblique modes. The kinetic oblique modes are also damped by the electrons. Therefore we will focus on oblique wave excitation due to a nonthermal electron distribution function.

The observed electrons have a nonzero first moment of the distribution function. Because of the insufficient details on the electron distribution function we shall model them as drifting Maxwellians. It was shown by Kindel and Kennel [1971] that the threshold for the oblique ion cyclotron modes is below the parallel acoustic modes which are excited by the electron current.

Figure 11 shows the lowest dispersion curves above the hydrogen gyrofrequency around the largest growth rates for two ion density ratios, $n_O/n_e = 0.1$ and 0.5. In Figure 11 the propagation angle is $83°$, $T_e/T_H = 3.5$, $u_H/u_O = 3$, $\Omega_H/\omega_H = 0.24$, $V_e/u_e = 0.16$, $|V_H/u_H| = 2.1$, and $|V_O/u_O| = 3.1$ ($V_H, V_O < 0$). For the given parameters the maximum growth rate is $\gamma/\omega_H = 0.0041$ (0.0021) at $\omega = 1.1$ (1.0), and $k\rho_H \cong 1.05$ for $n_O/n_e = 0.1$ (0.5), respectively. In the vicinity of the hydrogen gyrofrequency the approximate dispersion relation may be obtained by keeping only the first cyclotron term in the hydrogen Bessel summation and the leading terms in the oxygen and electron susceptibilities. The dispersion relation becomes $\omega - kv_H = \Omega_H/(1 - \alpha(\omega, k))$ where $\alpha = O[\Gamma_1(k^2 \rho_H^2)]$ includes all the nonresonant corrections. Since $V_e/u_e << 1$, we may neglect the electron plasma function contribution which results in

$$\omega \approx -k_{\parallel} |V_H| + \quad (2)$$

$$\Omega_H \{1 + \Gamma_1(k_{\perp}^2 \rho_H^2)/[1 + k^2 \lambda_H^2 + \frac{n_e}{n_H}\frac{T_H}{T_e} + \frac{n_O}{n_H}\frac{T_H}{T_O}]\}$$

which is a Doppler-shifted electrostatic hydrogen cyclotron mode with oxygen corrections. Here $\Gamma(x) = e^{-x} I(x)$ where I is the modified Bessel function. The resonant oxygen contribution to the hydrogen cyclotron term is proportional to

$$\Gamma_{16}(k_{\perp}^2 u_O^2/2\Omega_O^2) Z(\omega - 16\Omega_O - k_{\parallel}V_O/k_{\parallel}u_O)$$

which is negligibly small. One observes from (2) that addition
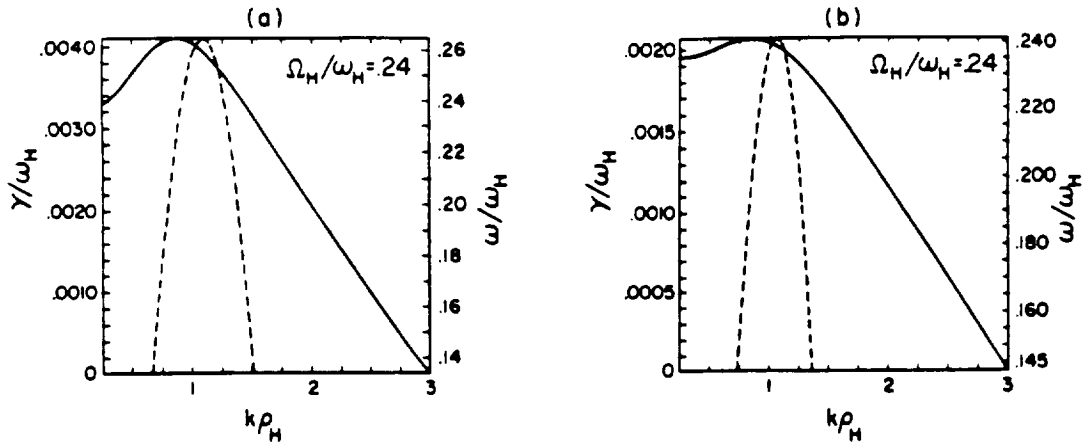
Figure 11. The dispersion curves for growth rate and real frequency near Ω_H for (a) $n_O/n_e = 0.1$, and (b) $n_O/n_e = 0.5$, for $\theta = 83°$, $T_e/T_H = 3.5$, $u_H/u_O = 3$, $V_e/u_e = 0.24$, $V_H/u_H = -2.1$, and $V_O/u_O = -3.1$. The real frequency curve is the same for both cases, on this scale.

of oxygen density decreases slightly the eigenfrequency of the hydrogen cyclotron mode. This brings the frequency closer to the hydrogen gyrofrequency, increasing the damping of the waves, since the growth rate is proportional to

$$\frac{2\omega_e^2}{k^2 u_e^2} \frac{\omega - k_\parallel V_e}{k_\parallel u_e} Z_i \left[\frac{\omega - k_\parallel V_e}{k_\parallel u_e}\right] + \qquad (3)$$

$$\sum_s \frac{2\omega_s^2}{k^2 u_s^2} \frac{\omega + k_\parallel V_s}{k_\parallel u_s} \sum_n \Gamma_n Z_i \left[\frac{\omega - n\Omega_s + k_\parallel V_s}{k_\parallel u_s}\right]$$

where the summation is over the ions and $Z_i(x) - e^{-x^2}$ denotes the imaginary part of the plasma function. Therefore the addition of oxygen makes the hydrogen cyclotron mode more stable, and for a marginally stable interaction an enhanced oxygen flux may stabilize the interaction. For the given parameters, decreasing the electron drift to $V_e/u_e = 0.12$ stabilizes the high-density case (condition 2) while the low-density case is still unstable. This may explain the absence of observed wave power above the hydrogen cyclotron frequency when the oxygen density is enhanced. Addition of cold nondrifting ion population does not affect this instability.

In the low-frequency range the unstable interaction is also due to the destabilizing effect of electrons and damping by the ions. Around the oxygen gyrofrequency the hydrogen ions are not resonant and do not affect the real frequency. The dispersion relation is obtained similarly to equation (2) and is given in the oxygen frame by

$$\omega \cong \Omega_o \left\{1 + \Gamma_1 (k_\perp^2 \rho_o^2) / [1 + k^2 \lambda_o^2 + \frac{n_H}{n_O} \frac{T_O}{T_H} + \frac{n_e}{n_O} \frac{T_O}{T_e}]\right\} \qquad (4)$$

showing that an increase in n_O moves the frequency away from the oxygen gyrofrequency, decreasing the damping. Therefore, close to marginal stability an increase (decrease) in the oxygen density makes the growth rate positive (negative). This behavior is in contrast to that at the higher hydrogen cyclotron frequency. Figure 12 shows the real frequencies and the growth rates in the oxygen reference frame for $V_e/u_e = 0.16$, $|V_H/u_H| = 1.3$, and $\Omega_H/\omega_H = 0.24$ ($\Omega_O/\omega_H = 0.015$) at the propagation angle 88° which maximizes the growth rate. The maximum growth rates are $4 \times 10^{-4} \omega_H$ and $1.2 \times 10^{-4} \omega_H$ at $\omega/\Omega_O \cong 1.3$ and 1.15, and $k\rho_O = 0.9$ for $n_O/n_e = 0.5$, 0.1, respectively. Enhanced density of oxygen decreases (quenches) the modes above the hydrogen gyrofrequency and increases (excites) the modes above the oxygen gyrofrequency.

6. EFFECT OF THE WAVES ON THE IONS

With the assumption that the observed O^+ and H^+ beams were accelerated through the same potential drop, the interaction between the ion species and waves at and below the spacecraft can be addressed. Ion beams of all species would have the same peak energy per charge, and each would have the temperature of its source population. Any differences from such distributions can be attributed to interactions between the various ion species and/or interactions with waves due to other free energy sources. Both theoretical and experimental studies of O^+, He^+, and H^+ ion beams have been made utilizing this assumption by numerous authors [e.g., Collin et al., 1981, 1987; Bergmann and Lotko, 1986; Kaufmann et al., 1986; Reiff et al., 1986, 1988; Dusenbery et al., 1988; Roth et al., 1989; Winglee et al., 1989]. These studies have all shown that the ions are strongly heated and that often there is a transfer of energy from the H^+ ions to the O^+ ions which may be dependent on the composition ratio [see Collin et al., 1987; Reiff et al., 1988]. The studies of Reiff et al. [1988] and Collin et al. [1987] suggested that during solar maximum, O^+ and H^+ have comparable energies in contrast to solar minimum when the O^+ is more energetic. Their explanation was that the O^+-H^+ relative streaming instability was most efficient at transferring energy to the O^+ ions when the O^+/H^+ ratio was low, as occurs on a statistical basis during solar minimum. Note that the event described herein occurred at solar maximum.
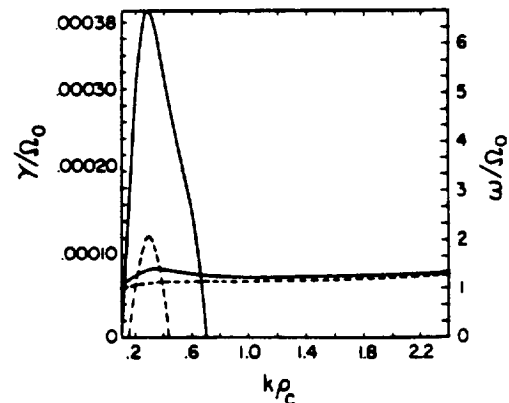
Fig. 12. The dispersion curves near Ω_O for $n_O/n_e = 0.1$ (dashed line) and $n_O/n_e = 0.5$ (solid line).

Distribution functions for O^+ and H^+ are presented in Figure 13 for that portion of the event when waves near the various cyclotron frequencies occurred. The time indicated is at the end of the sample, and the velocities are scaled so that O^+ and H^+ ions with the same energy would occur at the same distance from the center. For most of the time periods shown, there were distinct O^+ beams, whereas the H^+ beams were often obscured by a nearly isotropic component, which may have originated above the spacecraft (compare bottom panels in Figure 1). When both O^+ and H^+ beams are distinct in these contour plots, for instance at 1602:22, 1605:34, 1607:42, and 1618:21, the O^+ beams are generally more energetic. This may not seem to agree with the statistical results for data during solar maximum, but this event does not have O^+/H^+ ratios as high as are typically found then, at least not according to Figure 8. This figure is not directly comparable to the results of *Collin et al.* [1987] and *Reiff et al.* [1988], however, since those were obtained with an isotropic component subtracted. We have tried to emulate that by comparing the energies at peak upward flux

of O^+ and H^+ ions as a function of the ratio of the same two fluxes (not shown), but the ~40 data points available have too much scatter to show a clear trend. The data of *Collin et al.* [1987] also show large scatter, and it is only on a much larger statistical basis that their argument holds.

There is evidence in the distributions for the operation of both the O^+-H^+ two-stream instability and the EIC waves. The tendency of the O^+ beams to have a higher energy than the H^+ beams and the fact that V_H was not 4 times larger than V_o are consistent with the two-stream instability. This occurred throughout most of the time period and provides evidence that the two-stream instability modified the distributions below the satellite at altitudes where that mode was unstable. The broadening of the O^+ distributions during periods when waves near f_{cH} and f_{cO} occurred but not during periods of waves near f_{cH} is consistent with heating by the locally observed EIC waves. Several specific examples can be seen in Figure 14 which presents O^+ and H^+ distributions and simultaneous power spectra. The spectrum in Figure 14(a) has a peak slightly above
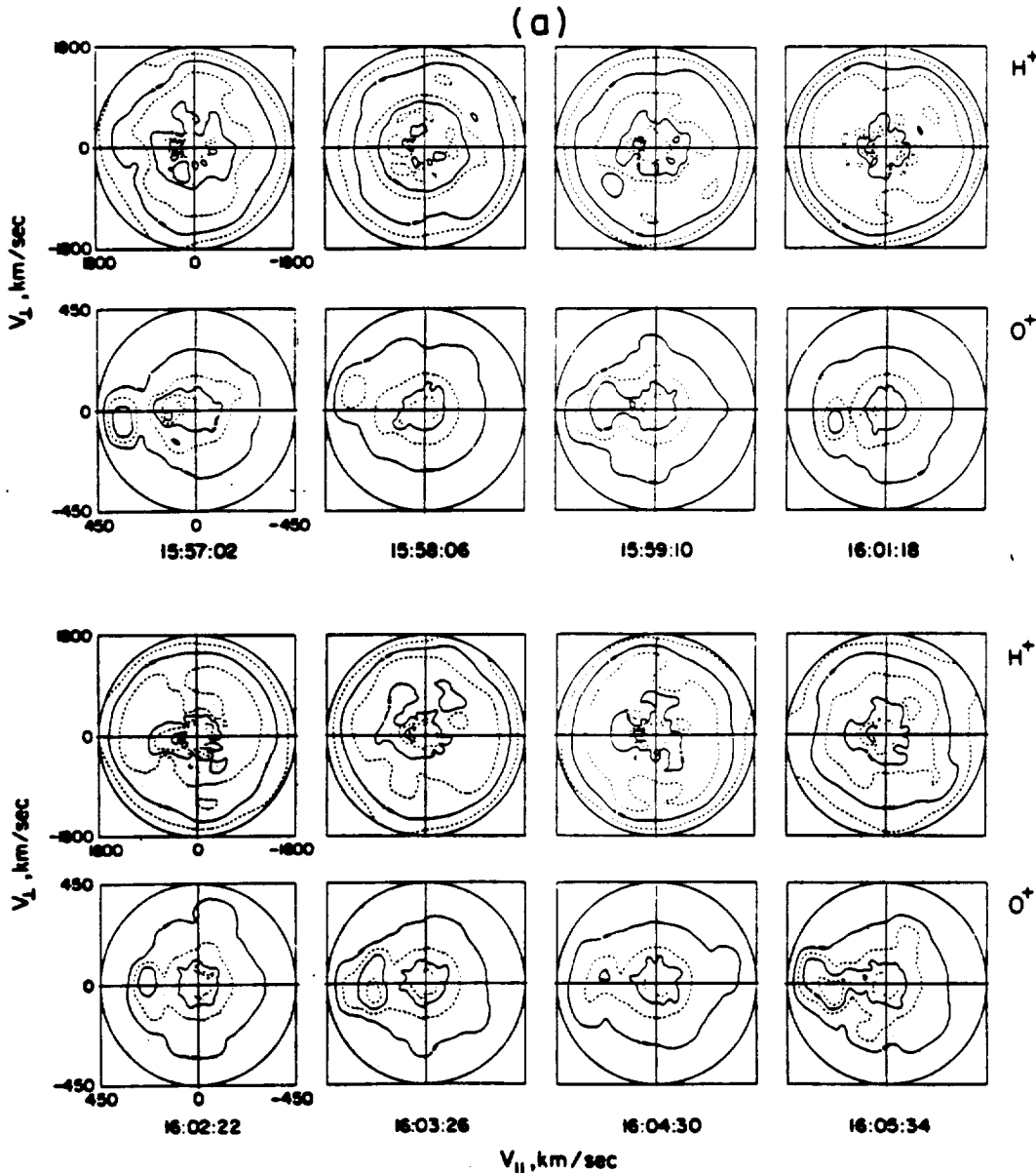
Fig. 13. The distribution function ($f(v_\perp, v_\parallel)$) for H^+ and O^+ for the time period when EIC waves were observed.

(b)
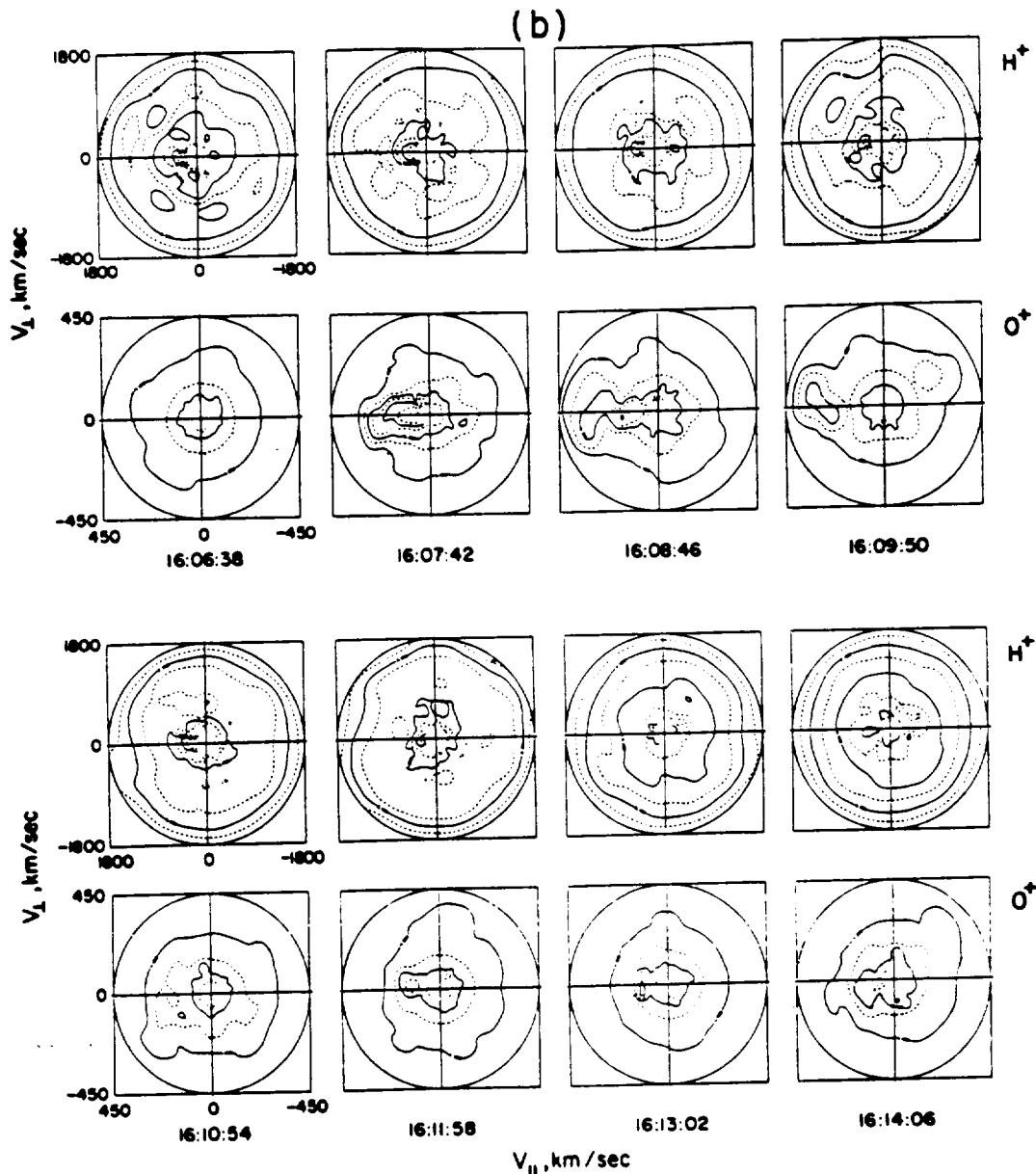
Fig. 13. (continued)

f_{cH}. The H$^+$ distribution shows strong perpendicular heating, while the O$^+$ beam retains beamlike characteristics. The spectrum in Figure 14(b) has power near both f_{cH} and f_{cH^+}, and in this case both distributions show strong heating and modification from a beamlike distribution. The spectrum in Figure 14(c) had a peak at $-2.8 f_{cH}$. These were the most intense waves observed during the event. Both O$^+$ and H$^+$ were upflowing, and both show evidence of strong modification. During the period of the spectrum in Figure 14(d) which peaked near f_{cO}, the O$^+$ distribution shows heating of the background ions at $-90°$ as well as perpendicular heating of the beam.

7. DISCUSSION AND CONCLUSIONS

The low-frequency electric field data presented herein have provided evidence for the existence of electrostatic hydrogen cyclotron waves on auroral field lines at altitudes of $-2.5-4$ R_E. The identification of the observed waves near the cyclotron frequencies as electrostatic ion cyclotron waves is based on the consistency of the observed and deduced properties of the waves with theories of EIC waves. Neither magnetic measurements nor density measurements at the relevant frequencies were available to provide the definitive proof that the waves were electrostatic. The S3-3 satellite did have density fluctuation measurements and did show that the waves observed in the electric field were electrostatic. The average frequency and propagation angle are within the range observed by the S3-3 satellite at lower altitudes. In addition, the waves have the same association with regions of low density, ion beams, and field-aligned currents as was observed at lower altitudes. This implies that the cyclotron frequency waves observed by ISEE were also EHC waves and that the waves are excited by the same free energy source throughout the altitude range $-1.5-4$ R_E. Studies based on the S3-3 data were not able to definitively determine the excitation mechanism. The fact that all the identified EHC
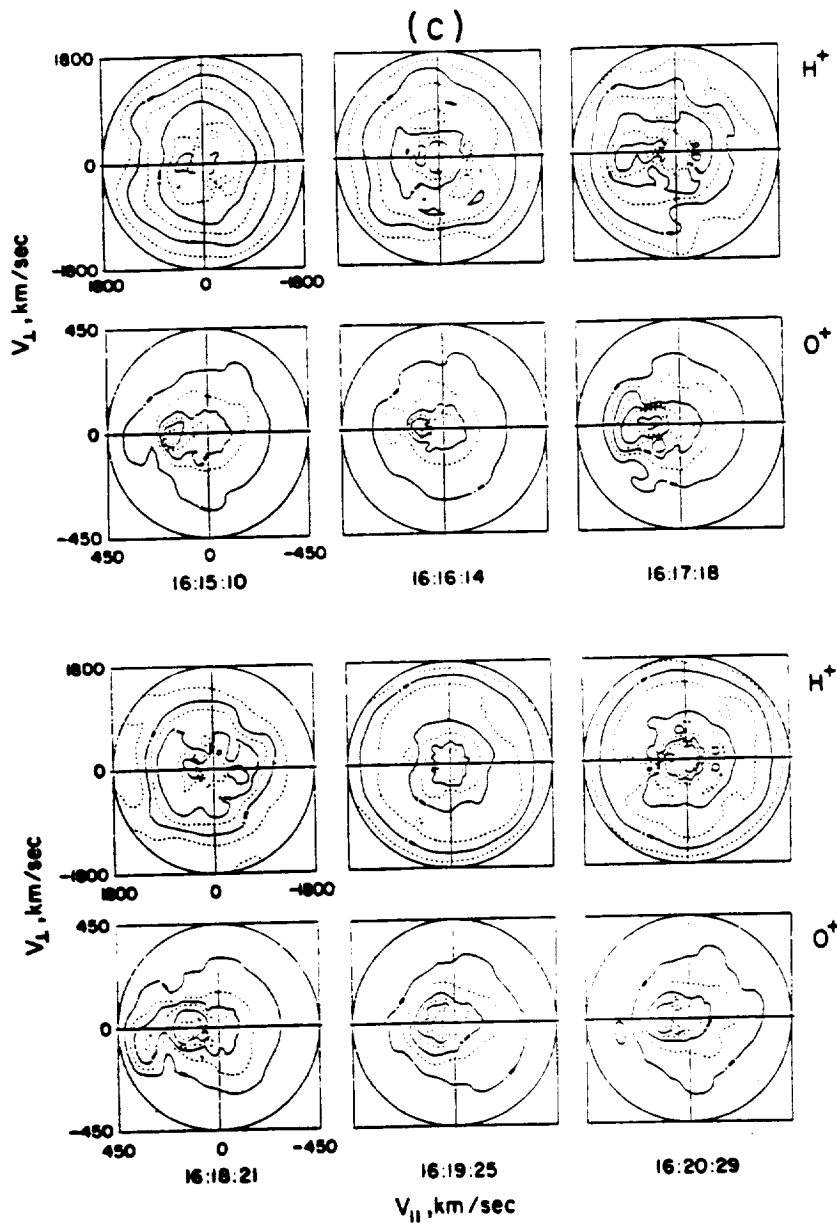
Fig. 13. (continued)

wave events occurred when there were ion beams [Kintner et al., 1979] and a careful numerical study of the linear dispersion relation for one particular event [Kaufmann and Kintner, 1982, 1984] both pointed to ion beams as the most likely free energy source. A linear study of both current- and beam-driven modes based on the average range of observed plasma parameters for S3-3, however, concluded that the observed wave properties were more consistent with current-driven modes [Bergmann, 1984]. Researchers were hampered in their efforts by the lack of information on the cold plasma, poor time resolution in the field-aligned current measurements, and the difficulty involved in properly including all the ion species.

For the event described herein the most complete data set yet assembled has been utilized to address the question of the instability mechanism for the waves at the ion cyclotron frequency. Good estimates of the cold electron and ion densities, ion composition ratios, high-resolution current measurements, electron

distributions, and distributions of both hydrogen and oxygen ions were available. During the period when waves near the gyrofrequencies of H^+, O^+, and He^+ occurred, the available data strongly support the idea that there were no unmeasured cold ions or electrons. The ratio of $n(O^+)/n(H^+)$ varied from ~0 to 1, and there was indirect evidence for the existence of He^+. There were at least four possible sources of free energy for wave growth: (1) field-aligned currents, (2) O^+ beams, (3) H^+ beams, and (4) the relative streaming of the O^+ and H^+. The first three could drive EIC waves, while the fourth could drive the ion two-stream instability which has a similar frequency regime. Qualitative comparisons between the wave characteristics, plasma parameters, and previously published linear theories of EIC waves and two stream instabilities suggest that the observed waves near f_{cH} are current-driven EHC waves. The relationship of the dominant wave frequency to the composition ratio also lends credence to the idea that the waves near f_{cO} and
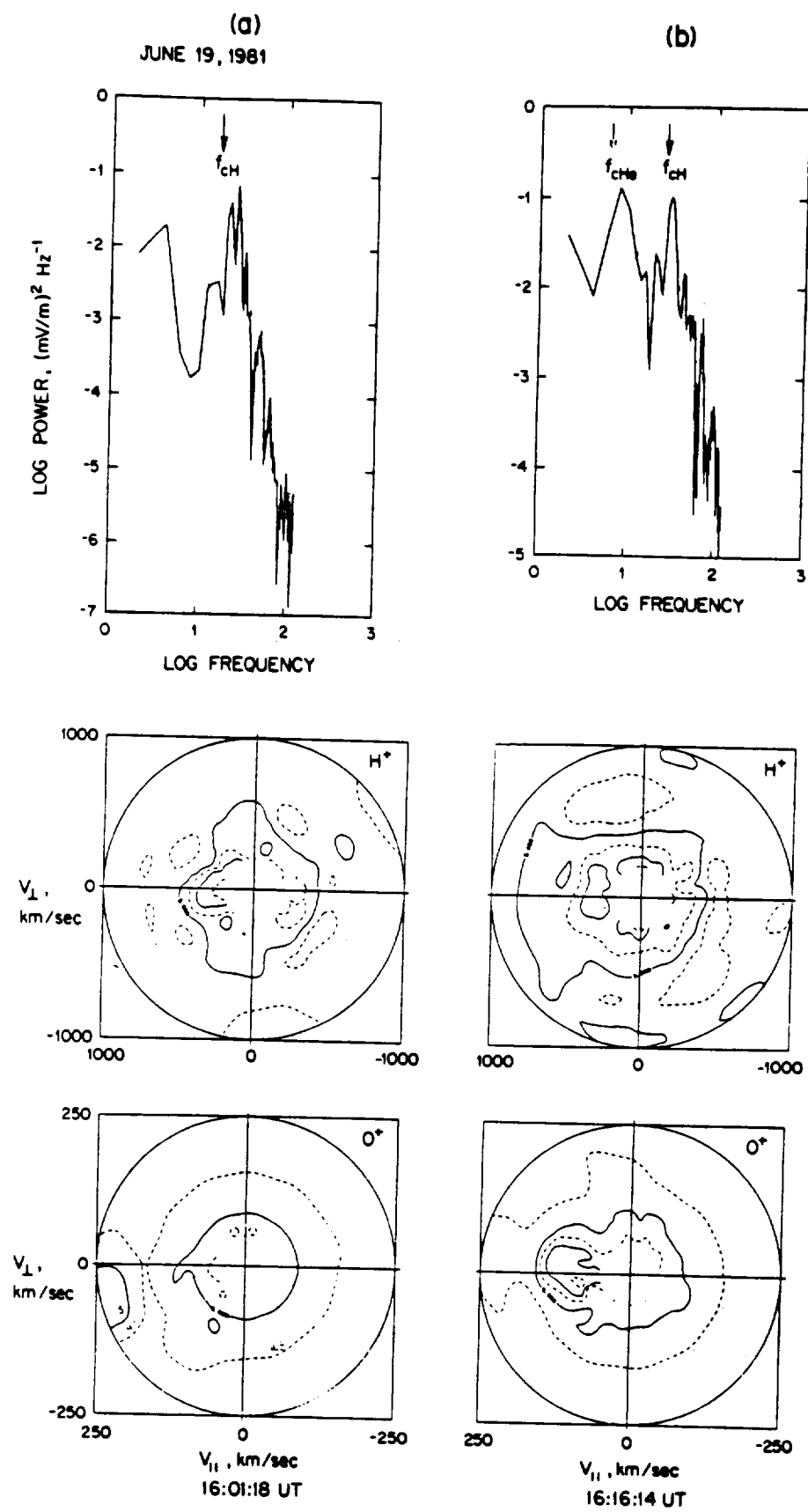
Fig. 14. Four representative examples of the electric field power spectrum and simultaneous ion distribution functions.

C-2

(c)

(d)
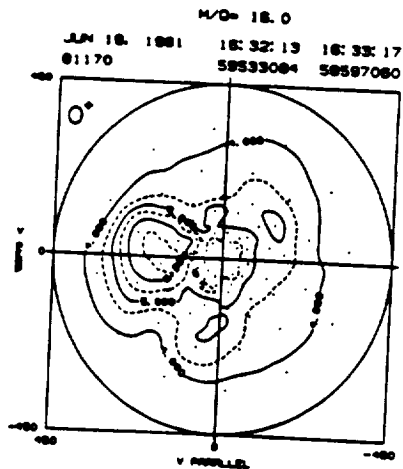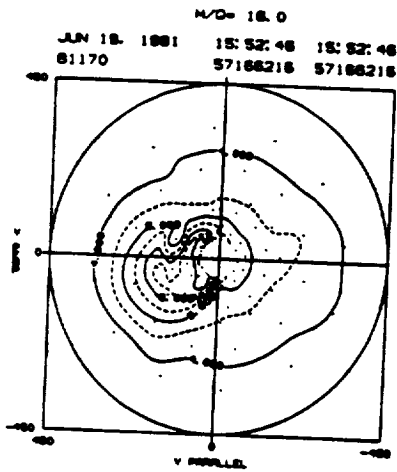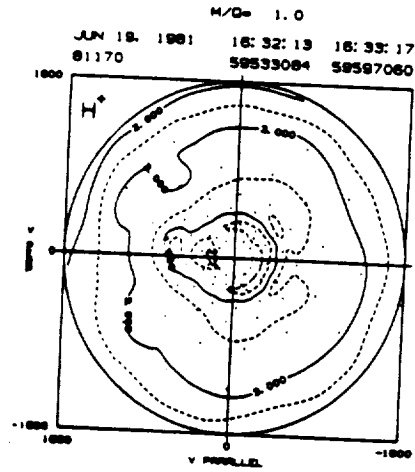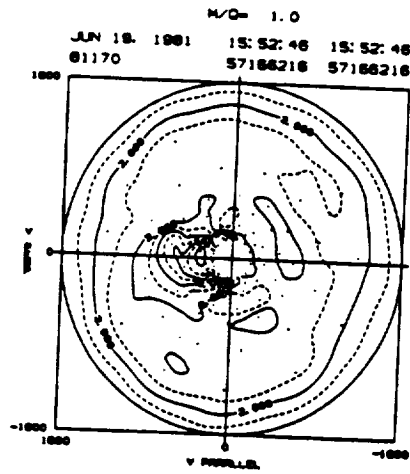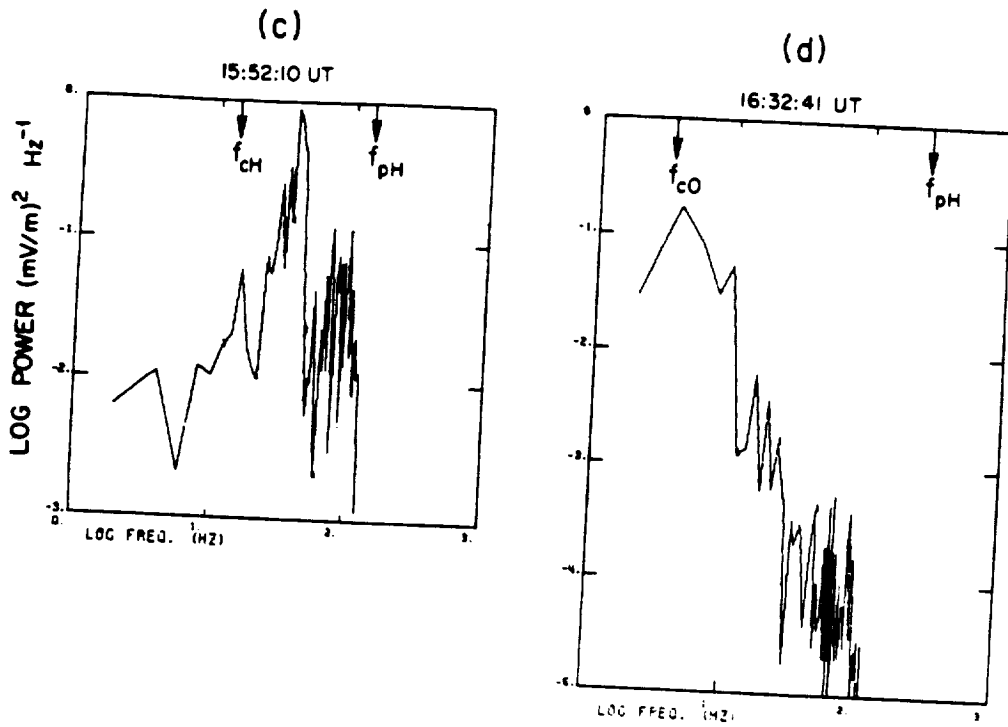
Fig. 14. (continued)

f_{cH_+} are also current-driven EIC waves. Although the observed electron distributions were not drifting Maxwellians as is assumed in standard theoretical studies, there is evidence that the distribution has a nonzero first moment as required for current-driven waves.

Solutions to the linear dispersion relation have also been obtained utilizing the observed plasma parameters to determine whether the ion two-stream instability should be unstable, whether the beams or the current drive the EIC waves, and what the expected relative growth rates are. These studies have shown that the parallel ion two-stream instability is quenched by the observed warm hydrogen distributions. In addition, the parallel modes driven by an ion beam either on the electrons or on background ions are also stable. Since for our parameter regime, parallel propagating waves are more unstable than oblique ones, neither type of instability can explain the observations. Oblique modes driven by the electron current are unstable and have frequencies comparable to those observed.

Examination of the O^+ and H^+ distributions provides evidence that the ion distributions have been strongly modified at altitudes below the spacecraft. In particular, several examples of an O^+ beam having higher energy than the accompanying H^+ beam suggest a transfer of energy from the H^+ to the O^+, as expected from the ion two-stream instability. There is also evidence of further heating of the ions by the locally excited EIC waves.

REFERENCES

André, M., Ion waves generated by streaming particles, *Ann. Geophys., Ser. A, 3*, 73, 1985.

André, M., H. Koskinen, G. Gustafsson, and R. Lundin, Ion waves and upgoing ion beams observed by Viking, *Geophys. Res. Lett., 14*, 463, 1987.

Ashour-Abdalla, M., and H. Okuda, Turbulent heating of heavy ions on auroral field lines, *J. Geophys. Res., 89*, 2235, 1984.

Ashour-Abdalla, M., and R. M. Thorne, Toward a unified view of diffuse auroral precipitation, *J. Geophys. Res., 83*, 4775, 1978.

Ashour-Abdalla, M., H. Okuda, and C. Z. Cheng, Acceleration of heavy ions on auroral field lines, *Geophys. Res. Lett., 8*, 795, 1981.

Bergmann, R., Electrostatic ion (hydrogen) cyclotron and ion acoustic wave instabilities in regions of upward field-aligned current and upward ion beams, *J. Geophys. Res., 89*, 953, 1984.

Bergmann, R., Three-wave coupling coefficients in a drifting bi-Maxwellian plasma, *J. Plasma Phys., 36*, 97, 1986.

Bergmann, R., and W. Lotko, Transition to unstable ion flow in parallel electric fields, *J. Geophys. Res., 91*, 7033, 1986.

Bergmann, R., I. Roth, and M. K. Hudson, Linear stability of the H^+-O^+ two-stream interaction in a magnetized plasma, *J. Geophys. Res., 93*, 4005, 1988.

Bering, E. A., The plasma wave environment of an auroral arc: Electrostatic ion cyclotron waves in the diffuse aurora, *J. Geophys. Res., 89*, 1635, 1984.

Bering, E. A., M. C. Kelley, and F. S. Mozer, Observations of an intense field-aligned ion flow and associated intense narrow band electric field oscillations, *J. Geophys. Res., 80*, 4612, 1975.

Böhmer, H., J. P. Hauck, and N. Rynn, Ion-beam excitation of electrostatic ion-cyclotron waves, *Phys. Fluids, 19*, 340, 1976.

Cattell, C. A., The relationship of field-aligned currents to electrostatic ion cyclotron waves, *J. Geophys. Res., 86*, 3641, 1981.

Cattell, C., The association of field-aligned currents with small-scale auroral phenomena, in *Magnetospheric Currents, Geophys. Monogr. Ser., vol. 28*, edited by T. Potemra, p. 243, AGU, Washington, D. C., 1984.

Collin, H. L., R. D. Sharp, E. G. Shelley, and R. G. Johnson, Some general characteristics of upflowing ion beams over the auroral zone and their relationship to auroral electrons, *J. Geophys. Res., 86*, 6820, 1981.

Collin, H. L., W. K. Peterson, and E. G. Shelley, Solar cycle variation of some mass dependent characteristics of upflowing beams of terrestrial ions, *J. Geophys. Res., 92*, 4757, 1987.

Dusenbery, P. B., and L. R. Lyons, Generation of ion-conic distribution by upgoing ionospheric electrons, *J. Geophys. Res., 86*, 7627, 1981.

Dusenbery, P. B., R. F. Martin, Jr., and R. M. Winglee, Ion-ion waves in the auroral region: Wave excitation and ion heating, *J. Geophys. Res., 93*, 5655, 1988.

Gurnett, D. A., F. L. Scarf, R. W. Fredricks, and E. J. Smith, The ISEE-1 and ISEE-2 plasma wave investigation, *IEEE Trans. Geosci. Electron., GE-16, 225*, 1978.

Hauck, J. P., H. Böhmer, N. Rynn, and G. Benford, Ion beam excitation of ion-cyclotron waves and ion heating in plasmas with drifting electrons, *J. Plasma Phys., 19*, 253, 1978.

Hudson, M. K., R. L. Lysak, and F. S. Mozer, Magnetic field-aligned potential drops due to electrostatic ion cyclotron turbulence, *Geophys. Res. Lett., 5*, 143, 1978.

Kaufmann, R. L., and P. M. Kintner, Upgoing ion beams, 1, Microscopic analysis, *J. Geophys. Res., 87*, 10,487, 1982.

Kaufmann, R. L., and P. M. Kintner, Upgoing ion beams, 2, Fluid analysis and magnetosphere-ionosphere coupling, *J. Geophys. Res., 89*, 2195, 1984.

Kaufmann, R. L., G. R. Ludlow, H. L. Collin, W. K. Peterson, and J. L. Burch, Interaction of auroral H^+ and O^+ beams, *J. Geophys. Res., 91*, 10,080, 1986.

Kelley, M. C., E. A. Bering, and F. S. Mozer, Evidence that the electrostatic ion cyclotron instability is saturated by ion heating, *Phys. Fluids, 18*, 1950, 1975.

Kindel, J. M., and C. F. Kennel, Topside current instabilities, *J. Geophys. Res., 76*, 3055, 1971.

Kintner, P. M., On the distinction between electrostatic ion cyclotron waves and ion cyclotron harmonic waves, *Geophys. Res. Lett., 7*, 585, 1980.

Kintner, P. M., M. C. Kelley, and F. S. Mozer, Electrostatic hydrogen cyclotron waves near one earth radius altitude in the polar magnetosphere, *Geophys. Res. Lett., 5*, 139, 1978.

Kintner, P. M., M. C. Kelley, R. D. Sharp, A. G. Ghielmetti, M. Temerin, C. A. Cattell, and P. Mizera, Simultaneous observations of energetic (keV) upstreaming ions and EHC waves, *J. Geophys. Res., 84*, 7201, 1979.

Kintner, P. M., D. M. Kumpar, and E. G. Shelley, Examples of low frequency waves and energetic ions observed from DE-A, *Eos Trans. AGU, 64*, 811, 1983.

Kintner, P. M., W. Scales, J. Vago, R. Arnoldy, G. Garbe, and T. Moore, Simultaneous observations of electrostatic oxygen cyclotron waves and ion conics, *Geophys. Res. Lett., 16*, 739, 1989.

Lysak, R. L., and M. A. Temerin, Generation of Alfvén-ion cyclotron waves on auroral field lines in the presence of heavy ions, *Geophys. Res. Lett., 10*, 643, 1983.

Lysak, R. L., M. K. Hudson, and M. Temerin, Ion heating by strong electrostatic ion cyclotron turbulence, *J. Geophys. Res., 85*, 678, 1980.

Miura, A., H. Okuda, and M. Ashour-Abdalla, Ion beam driven, electrostatic ion cyclotron waves, *Geophys. Res. Lett., 10*, 353, 1983.

Mizera, P. F., et al., The aurora inferred from S3-3 particles and fields, *J. Geophys. Res., 86*, 2329, 1981.

Mozer, F. S., R. B. Torbert, U. V. Fahleson, C.-G. Fälthammar, A. Gonfalone, and A. Pedersen, Measurements of quasistatic and low frequency electric fields with spherical double probes on the ISEE-1 spacecraft, *IEEE Trans. Geosci. Electron., GE-16*, 258, 1978.

Mozer, F. S., C. A. Cattell, M. Temerin, R. B. Torbert, S. Von Glinski, M. Woldorff, and J. Wygant, The dc and ac electric field, plasma density and temperature, and field-aligned current experiments on S3-3, *J. Geophys. Res., 84*, 5875, 1979.

Mozer, F. S., C. A. Cattell, M. K. Hudson, R. L. Lysak, M. Temerin, and R. B. Torbert, Satellite measurements and theories of low altitude auroral particle acceleration, *Space Sci. Rev., 27*, 155, 1980.

F. S., E. W. Hones, Jr., and J. Birn, Comparison of spherical double probe electric field measurements with plasma bulk flows in plasmas having densities less than 1 cm⁻³, cm^{-3}, Geophys. Res. Lett., 10, 377, 1983.

K. W., J. D. Scudder, and H. Doong, The electron spectrometer experiment on ISEE-1, IEEE Trans. Geosci. Electron., GE-16, 261, 1978.

A., C.-G. Fälthammar, V. Formisano, P.-A. Lindqvist, C. C. Cattell, F. Mozer, and R. Torbert, Quasistatic electric field measurements with spherical double probes on GEOS and ISEE satellites, Space Sci. Rev., 37, 269, 1984.

P. H., H. L. Collin, E. G. Shelley, J. L. Burch, and J. D. Winningham, Heating of upflowing ionospheric ions on auroral field lines, in Ion Acceleration in the Magnetosphere and Ionosphere, Geophys. Monogr. Ser., vol. 38, edited by T. Chang, p. 83, AGU, Washington, D. C., 1986.

P. H., H. L. Collin, J. D. Craven, J. L. Burch, J. D. Winningham, E. G. Shelley, L. A. Frank, and M. A. Friedman, Determination of auroral electrostatic potentials using high- and low-altitude particle distributions, J. Geophys. Res., 93, 7441, 1988.

L. M. K. Hudson, and R. Bergmann, Effects of ion two-stream instability on auroral ion heating, J. Geophys. Res., 94, 348, 1989.

C. T., The ISEE 1 and 2 fluxgate magnetometers, IEEE Trans. Geosci. Electron., GE-16, 239, 1978.

R. D., W. Lennartsson, W. K. Peterson, and E. Ungstrup, The mass dependence of wave particle interactions as observed with the ISEE-1 ion mass spectrometer, Geophys. Res. Lett., 10, 651, 1983.

Shelley, E. G., R. D. Sharp, R. G. Johnson, J. Geiss, P. Eberhardt, H. Balsiger, G. Haerendel, and H. Rosenbauer, Plasma composition experimentation on ISEE-A, IEEE Trans. Geosci. Electron., GE-16, 266, 1978.

Temerin, M. A., and R. L. Lysak, Electromagnetic ion cyclotron mode (ELF) waves generated by auroral electron precipitation, J. Geophys. Res., 89, 2849, 1984.

Temerin, M. A., and F. S. Mozer, Observations of the electric fields that accelerate auroral particles, Proc. Indian Acad. Sci., 93, 227, 1984.

Temerin, M. A., M. Woldorff, and F. S. Mozer, Nonlinear steepening of the electrostatic ion cyclotron wave, Phys. Rev. Lett., 43, 1941, 1979.

Temerin, M. A., C. A. Cattell, R. L. Lysak, M. K. Hudson, R. B. Torbert, F. S. Mozer, R. D. Sharp, and P. M. Kintner, The small-scale structure of electrostatic shocks, J. Geophys. Res., 86, 11,278, 1981.

Tetreault, D., Theory of electric fields in the auroral acceleration region, J. Geophys. Res., 96, 3549, 1991.

Ungstrup, E., D. M. Klumpar, and W. J. Heikkila, Heating of ions to superthermal energies in the topside ionosphere with electrostatic ion cyclotron waves, J. Geophys. Res., 84, 4289, 1979.

Winglee, R. M., P. B. Dusenbery, H. L. Collin, C. S. Lin, and A. M. Persoon, Simulations and observations of heating of auroral ion beams, J. Geophys. Res., 94, 8943, 1989.

R. R. Anderson, Department of Physics and Astronomy, University of Iowa, Iowa City, IA 52242.

C. A. Cattell, F. S. Mozer, and I. Roth, Space Sciences Laboratory, University of California, Berkeley, CA 94720.

R. C. Elphic, Los Alamos National Laboratory, Los Alamos, NM 87545.

W. Lennartsson, Lockheed Palo Alto Research Laboratory, Palo Alto, CA 94304.

E. Ungstrup, Danish Space Research Institute, Lundtoft Vej 7 DK-2800, Lyngby, Denmark.

Effects of Solar Cycle on Auroral Particle Acceleration

C. A. CATTELL, T. NGUYEN[1], AND M. TEMERIN

Space Sciences Laboratory, University of California, Berkeley

W. LENNARTSSON AND W. PETERSON

Lockheed Palo Alto Research Laboratory, Palo Alto, California

We present the results of two studies designed to assess the effect of solar cycle on auroral particle acceleration processes. The first study is of data obtained from the S3-3 satellite at geocentric distances from 1.3 to 2.2 R_e during solar minimum and the rising phase of the solar cycle. The S3-3 study included electrostatic shocks, ion beams and conics, and electron beams, but did not include ion composition. The second study is of data obtained by the ISEE-1 satellite when the ion mass spectrometer was operating in a special mode designed to study auroral ion distributions. This study covers geocentric distances from ~2.5 to 7 R_e during solar maximum and includes O^+ and H^+ beams and conics, and electrostatic shocks and low frequency turbulence. The S3-3 statistics for shocks with ion beams imply that the auroral parallel potential drop usually occurs above ~2.2 R_e at solar maximum, while the ISEE-1 observations suggest the potential drop, at solar maximum, may be located at ~2.5 to 4 R_e. The ISEE-1 beam observations (usually at energies less than or equal to 1 keV) imply that the potential drop is less, on average, for solar maximum than for solar minimum. Both data sets provide evidence for increased perpendicular acceleration of ions during solar maximum, associated with electrostatic shocks and enhanced low frequency turbulence. The ISEE-1 data show that the flux of upflowing O^+ continues to increase as $F_{10.7}$ increases from "low" to "high" solar maximum. These data also provide evidence that the ion two-stream instability is important in modifying the ion distributions. Most of these observations may be understood as being due to increased heating of the atmosphere during solar maximum which results in an increase in the H^+ - O^+ charge exchange altitude and an increase in the ionospheric density and temperature. Some effects, including the $F_{10.7}$ dependence of the local time distribution of electrostatic shocks and the apparent decrease in the magnitude of the auroral potential drop at solar maximum, are still not understood.

1. INTRODUCTION

The effect of solar cycle on ion composition in the magnetosphere was first recognized by Young et al. [1982], who showed that the percentage of oxygen observed near geosynchronous orbit was higher during solar maximum than during solar minimum. Similar increases were observed in auroral particles by the S3-3 and DE spacecraft [Yau et al., 1985; Collin et al., 1987] and in the plasmasheet by ISEE-1 [Lennartsson, 1989]. Possible effects of solar cycle on auroral particle acceleration processes have also been examined. Ghielmetti and Johnson [1983] first presented evidence that the occurrence frequency of ion beams decreased during

the rising phase of the solar cycle. Yau et al. [1985], in a DE-1 study of upflowing H^+ and O^+ ions, showed that at solar maximum: (1) the flux of O^+ was higher than H^+; (2) the occurrence probability of conics increased; and (3) the occurrence probability of O^+ at angles of 160° - 180° (i.e., field aligned) increased at high altitudes. Utilizing ISEE-1 electric field and ion composition data on auroral field lines, Nguyen et al. [1986] showed that ion beams were less common and generally had lower energies during periods of high $F_{10.7}$, and that O^+ ions (both beams and conics) were more common than H^+ ions. Collin et al. [1987, 1988] utilizing S3-3 and DE-1 data, provided evidence that: (1) the average energy of O^+ beams was greater than that of H^+ beams at solar minimum, and comparable during solar maximum; and (2) the flux of O^+ beams was often greater than that of H^+ beams. Both they and Reiff et al. [1988] suggested that the observations were consistent with acceleration of the ions in parallel electric fields followed by modification of the ion distributions via the ion two-stream instability.

In this paper, we review and extend the results of two different studies. The first was a study of electrostatic shocks, ion beams and conics, and electron beams using data from the S3-3 spacecraft

---
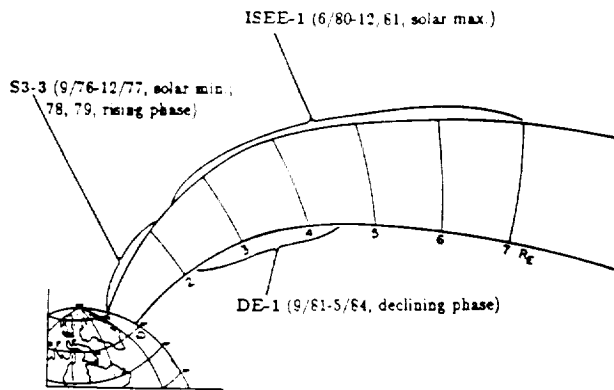
Fig. 1. The radial ranges (geocentric) and time periods of satellite coverage discussed herein. This study uses data from S3-3 and ISEE-1.

[Cattell et al., 1991b]. Composition information was not obtained by the ion detectors utilized for this study. The second study was a study of electrostatic shocks, low frequency turbulence, and O^+ and H^+ beams and conics using data from the University of California at Berkeley electric field detector and the Lockheed Palo Alto Research Laboratory ion composition instrument on ISEE-1 [Nguyen et al., 1986]. The radial ranges of the various data sets utilized herein and in studies referenced above are shown in Figure 1. S3-3 obtained data from 1.3 to 2.2 R_e during solar minimum and the rising phase of the solar cycle. DE-1 covered geocentric distances from ~2.3 to 4.5 R_e. ISEE-1 obtained data on auroral field lines at altitudes from 2.5 to 7 R_e. The coverage in monthly $F_{10.7}$ for different studies is indicated in Figure 2. $F_{10.7}$ was used as an indicator of the solar EUV flux which is correlated with solar cycle. Although daily $F_{10.7}$ was used herein, some studies have suggested that long term averages might correlate better with atmospheric parameters [Hedin, 1984; Gorney, 1990].

The questions to be addressed by the S3-3 study are the following: (1) Is there a difference in the occurrence probability for
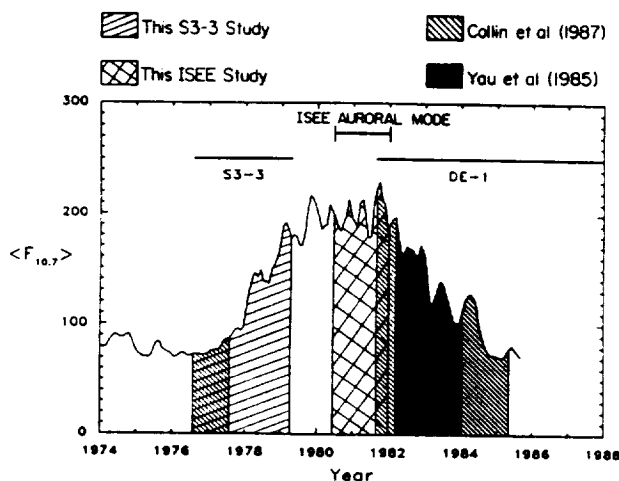
Fig. 2. The coverage in monthly $F_{10.7}$ of various referenced studies.

shocks, shocks with beams, and shocks with conics between periods of high $F_{10.7}$ and periods of low $F_{10.7}$?; (2) Is there evidence for a change in the altitude and/or magnitude of the parallel potential drop which produces auroral ion and electron beams and electrons?; and (3) Is there increased perpendicular acceleration of ions for high $F_{10.7}$? The ISEE-1 study examines the following three questions, viewing the ISEE-1 data set as a solar maximum data set: (1) How do characteristics, i.e., energy, composition and type of upflowing ions at ISEE-1 altitudes compare to previous studies?; (2) How do shocks, beams and conics compare to S3-3 observations at solar minimum and the rising phase of the solar cycle?; and (3) Is there evidence for parallel and/or perpendicular acceleration of ions at these altitudes? In addition, the ISEE-1 data set was divided according to $F_{10.7}$ to determine whether trends in the occurrence of shocks and ions continue to the highest values of $F_{10.7}$ and whether there is evidence for the O^+-H^+ two-stream interaction.

The methodology for the S3-3 study is presented in Section 2.1 and the S3-3 statistical results are shown in 2.2. The ISEE-1 study methodology is described in Section 3.1, including an example of the type of event studied. The statistical results for the ISEE-1 dataset, considered as an example of solar maximum data, are shown and compared to prior studies in Section 3.2. The comparison of high and low $F_{10.7}$ events in the ISEE-1 data is described in Section 3.3. In Section 4, the results of the two studies are combined and conclusions are presented.

2. S3-3 Study of Electrostatic Shocks, Ion Beams and Conics, and Electron Beams

Methodology

The S3-3 study is based on a previous statistical database which was compiled by Redsun et al. [1985] and Bennett et al. [1983]. The database contains 2196 crossings of the auroral zone. Electric fields were obtained by the University of California at Berkeley double probe; electrostatic shocks were defined as the occurrence of a field > 90 mV/m. Ions (0.09 to 3.9 keV) and electrons (0.17 to 9 keV) were measured by the Aerospace Corporation detectors [Mizera and Fennell, 1977]. There was no composition information available from this detector. Daily $F_{10.7}$ was utilized as an indicator of solar activity and solar EUV. Details can be found in the above referenced papers, as well as in Cattell et al. [1991b]. Most of the data was obtained during solar minimum. Good coverage in altitude and magnetic local time was obtained except near noon as can be seen in Figure 3a in which each auroral zone crossing is plotted versus altitude and magnetic local time. The points correspond to a model auroral zone latitude [see Bennett et al., 1983, p. 7108 for details). Points with $F_{10.7}$ < 80 are shown as "x's" and those with $F_{10.7}$ >100 are open squares. Another possible source of bias in the data set is magnetic activity. However, as shown in Figure 3b, both high and low $F_{10.7}$ cases cover almost the complete range of Kp values.

Statistical Results

The occurrence probability of an electrostatic shock for low and high $F_{10.7}$ is shown versus altitude (summed over local time) in

AURORAL ZONE CROSSINGS

AURORAL ZONE CROSSINGS
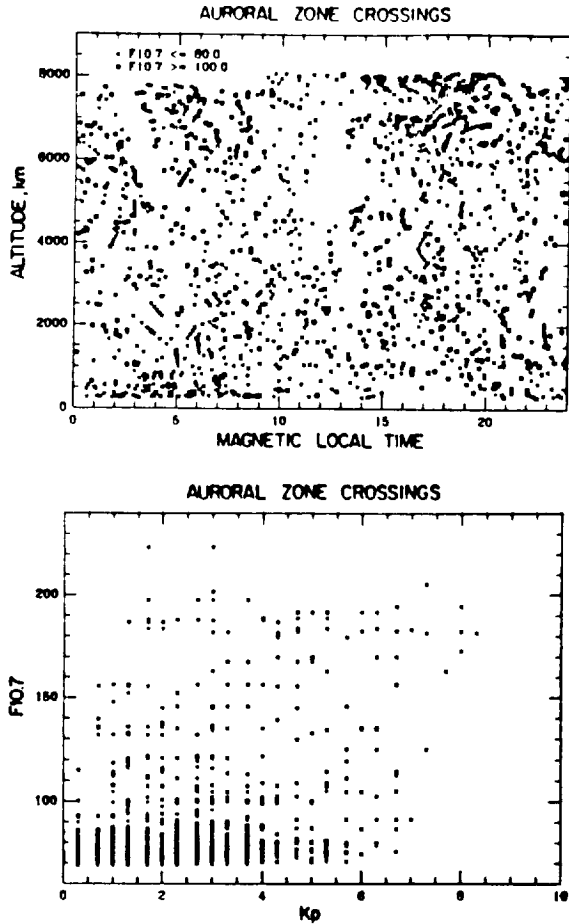
Fig. 3. (a) Scatter plot of S3-3 auroral zone crossings versus altitude and magnetic local time with high (low) $F_{10.7}$ plotted as squares (x's); (b) scatter plot of S3-3 crossings versus $F_{10.7}$ and Kp.

Fig. 4. The occurrence probability of S3-3 electrostatic shocks plotted versus (a) altitude and (b) magnetic local time for high and low $F_{10.7}$.

Figure 4a and versus magnetic local time (summed over altitude) in Figure 4b. In each bin, the total number of shocks observed has been normalized by the number of auroral zone crossings in that bin. Multiple shocks could occur in a given auroral zone crossing [see Bennett et al., 1983]. During periods of low $F_{10.7}$, there was a clear increase with altitude of the probability of observing an electrostatic shock (see Figure 4a). This increase was also observed during periods of high $F_{10.7}$, but there was a leveling off at higher altitudes. The magnetic local time dependence was more complicated. The occurrence frequency of electrostatic shocks was ~2.5-3 times higher for low $F_{10.7}$ than for high $F_{10.7}$ in the postnoon sector. During the prenoon sector, however, shocks had a higher occurrence frequency during high $F_{10.7}$. On average, shocks were more commonly observed during low $F_{10.7}$ than during high $F_{10.7}$.

The distribution of shocks with ion beams is shown in Figure 5. (A shock was defined as having a beam if a beam was observed within one spin period of the shock.) At all altitudes, electrostatic shocks with ion beams are at least twice as likely to occur during low $F_{10.7}$ than during high $F_{10.7}$. Shocks with ion beams were most

common in the evening, ~1600-2200 MLT, during low $F_{10.7}$ (Figure 5b). The occurrence frequency of ion beams was much higher during low $F_{10.7}$ except during the hours of 0000-0400 MLT. Since electrostatic shocks with ion beams were less common during peri-
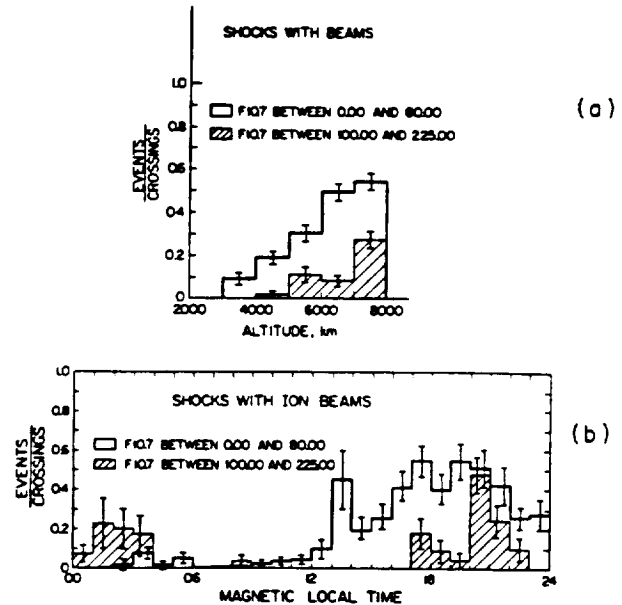
Fig. 5. Same as Figure 4 for electrostatic shocks with ion beams.

ods of high $F_{10.7}$ than during periods of low $F_{10.7}$, it is important to determine whether the remaining shocks were associated with ion conics or with ion distributions which are not indicators of either perpendicular or parallel ion energization. Approximately 18% of the high $F_{10.7}$ shocks were associated with ion beams and ~64% with ion conics. For the periods of low $F_{10.7}$, in contrast, 43% of shocks were observed with ion beams and 43% with conics, while ~14% of the shocks were associated with neither type of distribution.

To examine the question of whether there is a statistically significant difference between the altitude dependence of the magnitude of shocks for solar maximum and solar minimum, we plotted the average magnitude of the shocks in each altitude bin, scaled to the average magnitude at 8000 km. No clear difference was seen. Similarly, the average of the peak energy of the ion beams observed in a given altitude bin increased with altitude for both high and low $F_{10.7}$, but the difference for the two $F_{10.7}$ ranges was not statistically significant.

The main conclusions of the above study are the following: (1) Shocks, in general, are more common during solar minimum than during solar maximum (except from 0 - 5 MLT); (2) Shocks with beams are also more common during solar minimum; and (3) A larger percentage of shocks are associated with conics during solar maximum. It can be inferred that, on average, the auroral parallel potential drop occurs at higher altitudes during solar maximum compared to solar minimum. In addition, there was more perpendicular ion acceleration at altitudes up to 8000 km during solar maximum.

3. ISEE-1 STUDY OF ELECTRIC FIELDS AND IONS

Methodology

The data for this study were obtained from instruments on board the ISEE-1 satellite during 1980 and 1981 as the satellite encountered auroral field lines at distances of 2.5 to 7 R_e. During this period, the Lockheed Ion Mass Spectrometer [Shelley et al., 1978] was operated in a special Auroral Scan Mode [Sharp et al., 1983] which looked at a restricted set of energies and masses so that complete pitch angle spectra could be obtained in approximately 1 minute. In this mode, which was designed for study of auroral phenomena at high altitudes, a complete pitch angle scan for O^+ and H^+ was obtained in 8 energy channels with center energies ranging from 0.21 to 17.4 keV in 52 s (high bit rate) or 64 s (low bit rate). For a sample to be included in this study, the following criteria had to be met: (1) The center angle of the pitch angle bin closest to the magnetic field had to be within 20° of the field direction (~90% of the samples were within 10°, and no qualitative differences in the results were observed between a 10° cutoff and a 20° cutoff); and (2) There was a minimum of 9 counts per sample (corresponding to a flux of 2 to 6 × 10⁴ /cm²-sec-ster-keV for H^+ and 4 to 7 × 10⁴ for O^+ depending only weakly on energy due to pre-acceleration). A beam was defined as the existence of a maximum in the flux along the magnetic field in at least 1 energy channel. A conic was defined as the existence of a maximum in the flux in at least 1 energy channel at an angle between 0° and 90° (or 90° and 180° for the northern hemisphere). Note that a 90° conic at a radial distance

of 2.5 R_e would be observed as a beam within the instrument resolution at a radial distance of ~5-6 R_e, assuming no further energization. It is also possible that some very narrow ion beams would be missed by the detector when the magnetic field is out of the spin plane. Due to the energy dependence of the vertical angular width of the detectors, this would be more likely to occur for energies above ~2 keV. It would also be more likely in low bit rate orbits.

One minute samples (actually 52 s [64 s] for high [low] bit rate orbits) of the raw electric field data from the University of California at Berkeley double probe [Mozer et al., 1978] were utilized. Electric field data were available for ~85% of the ion samples. An electrostatic shock was defined to occur when the average magnitude of the largest 10 points, mapped to 2.0 R_e assuming equipotential field lines, was greater than 100 mV/m. Enhanced low frequency turbulence was defined as the occurrence of one-minute averaged power in 2 out of 3 broadband filters (centered at 4, 32, and 256 Hz) greater than a set value (18, 2, 0.5 $\mu V/mHz^{1/2}$ respectively).

Both ion and electric field data were sorted into 648 three-dimensional bins with nine 0.5-R_e bins by twelve 2-hour bins by six 2-degree bins. The invariant latitude ranged from 64° to 76°. Data were also sorted by $F_{10.7}$ and AE. There were more than 7000 individual samples of ~1 minute each obtained during the ~1 1/2 years of auroral mode operation. Error bars shown in the plots discussed below are statistical and do not reflect systematic errors due to orbital constraints. In particular, there was not much coverage obtained from ~6 to 12 LT for low AE or from 4 to 14 LT for high AE. Since ion beams are not common at those local times [Gorney et al., 1981], this does not strongly influence our conclusions. The distribution of samples in $F_{10.7}$ and AE is presented in Figure 6. For AE ≤ 800, the coverage in $F_{10.7}$ is relatively uniform. The highest values of AE occurred only for the lower values of $F_{10.7}$. Note that all the data were obtained at solar maximum so that the range of $F_{10.7}$ was 140 to 310 in comparison to the S3-3 data which had a range of 60 to 220. For this reason, the ISEE-1 statistical study will be analyzed in two ways: (1) with the data viewed as a

ISEE Auroral Scan Mode Data Set
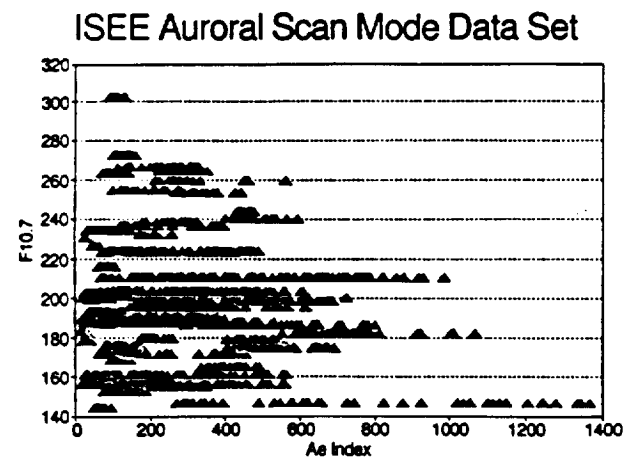
Fig. 6. Scatter plot of ISEE-1 samples, with simultaneous auroral scan mode ion data and electric field data, versus AE and $F_{10.7}$.

whole to study solar maximum effects and (2) with the data divided by $F_{10.7}$ value into two groups (called low maximum and high maximum) to determine whether trends previously observed to occur as $F_{10.7}$ increased continue to the highest values of $F_{10.7}$.

An example of the type of event utilized in this study is shown in Figure 7 in which 70 minutes of data obtained as ISEE-1 moved up along auroral field lines from a radial distance of ~2.5 R_e to ~4.2 R_e near midnight local time. In panel a, the spin-averaged duskward electric field is plotted. Large spiky electric fields, which were identified as electrostatic shocks, occurred around 2120 and 2145 UT. Note that the raw electric field (the component along the spinning boom; not shown) had magnitudes up to ~200 mV/m at those times. The electric field in three filters is shown in panel b. Regions of enhanced power can be seen at ~2110, ~2112-2125, ~2130, ~2141-2155 and ~2200. The negative of the spacecraft potential, panel c, indicates that there was a density depletion in the region between the electrostatic shocks. Selected pitch angle distributions of O+ and H+ show that outside the shocks and density depletion region, there were conical ions, whereas inside there were upflowing ion beams which became broader at higher altitudes. It can be seen that the isotropic H+ background was usually higher than the O+ background. This may have affected selection of events. These data are consistent with observations made on auroral field lines at lower altitudes [see, for example, Mozer et al., 1980]. Another example of the events used in this study can be seen in Figure 2 of Cattell et al. [1991a].
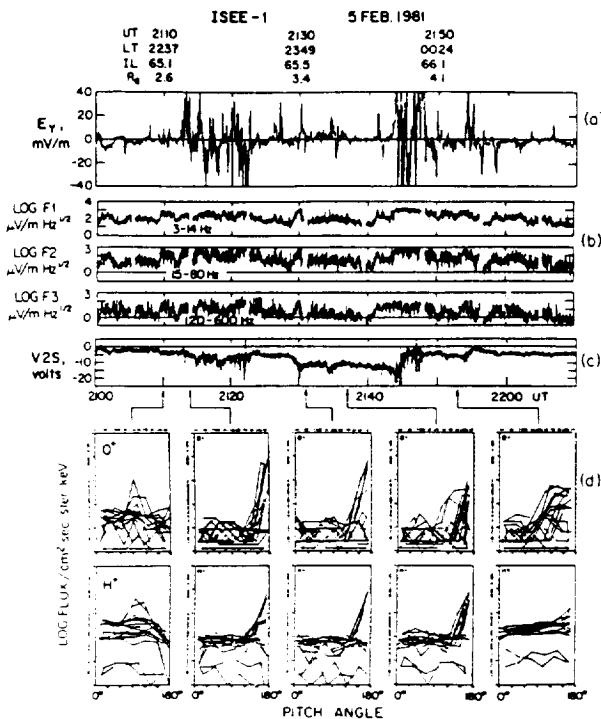
Fig. 7. Electric field and ion data obtained as ISEE-1 moved up along auroral field lines from ~2.5-4.5 R_e. (a) spin-averaged duskward electric field, E_y; (b) electric field in 3 filters; (c) negative of the spacecraft potential, V2S; and (c) selected O+ and H+ pitch angle plots.
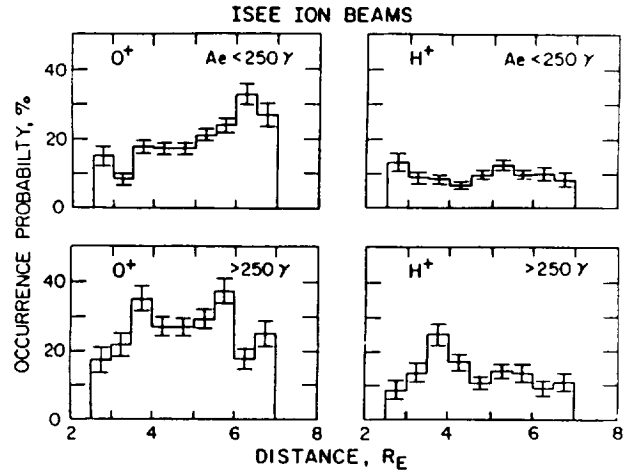
Fig. 8. Occurrence probability of ISEE-1 ion beams for O+ and H+ versus altitude for low and high AE.

Statistical Results for the Study of ISEE-1 Data as a Solar Maximum Data Set

In Figure 8, the occurrence probability of an ion beam at a given radial distance is plotted for both O+ and H+ and for periods of high and low magnetic activity. At these radial distances, both H+ and O+ beams are more common during periods of high magnetic activity than low magnetic activity. The occurrence probability of O+ beams increases with altitude for AE < 250; the probability for H+ does not show a similar increase. This change can be interpreted in the following way: the O+ conics observed at ~3 R_e (see Figure 9) fold up into beams by ~5-6 R_e accounting for the increase in beam occurrence. This would require local acceleration of conics at the higher altitudes to maintain the conic occurrence probability. Very few H+ conics were observed, consistent with the constant occurrence of H+ beams with altitude. During periods of high AE, the probability of observing a beam increases with altitudes up to a radial distance of ~4 R_e. In this case, in order to
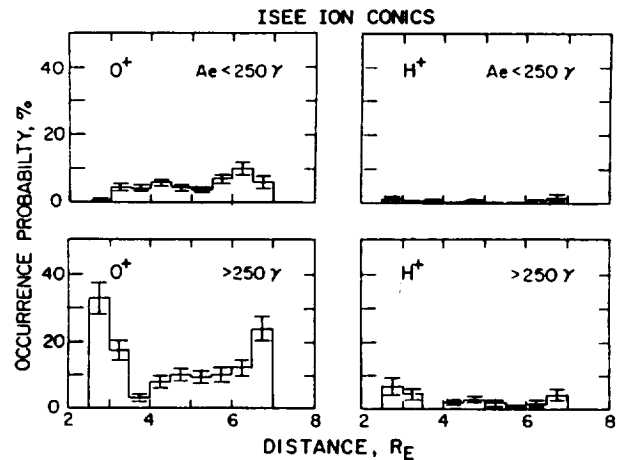
Fig. 9. Same as Figure 8 for ion conics.

ISEE ELECTRIC FIELD
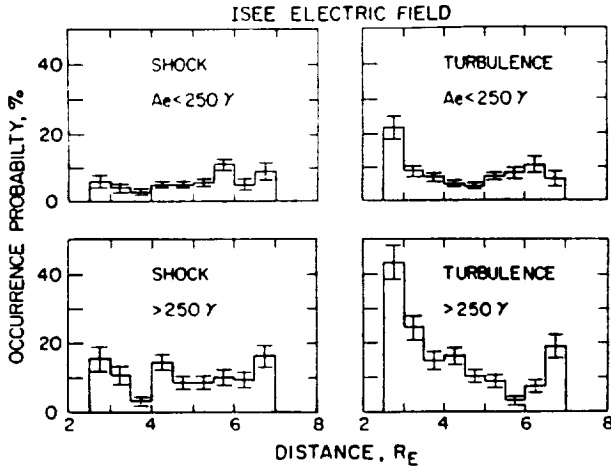
Fig. 10. Same as Figure 8 for electrostatic shocks and samples with enhanced low-frequency wave power.

explain the increased probability of beams at ~3.5 - 4 R_e from the folding up of the conics at ~2.5 - 3 R_e, a parallel potential drop would be required. This suggests that a potential drop exists at these altitudes (~3 - 4 R_e) during active times at solar maximum. The data are consistent with an approximately constant occurrence for O^+ beams between ~4 R_e and 6 R_e. The decrease observed above 6 R_e may be due to: (1) the fact that the LT time coverage above 6 R_e is less uniform; and/or (2) the detector missing very narrow beams, as discussed above. For all AE, O^+ beams are approximately twice as common as H^+ beams. The results for ion conics are shown in Figure 9. O^+ conics are much more common than H^+ conics for all levels of magnetic activity. There is no altitude dependence for quiet times (AE < 250), whereas there is a strong altitude dependence for active times (AE > 250). Note that for high AE the conic probability has an altitude minimum at the same radial distance where the beam probability peaks, consistent with the explanation that the beam peak is due to higher altitude parallel acceleration of the conics. The statistics for electrostatic shocks and enhanced low frequency turbulence are presented in Figure 10. The occurrence probability of shocks is almost constant with altitude for high and low AE. Intense waves are more likely to occur at low altitudes. Both intense waves and electrostatic shocks are approximately twice as likely to occur during high AE than low AE.

The conclusions which can be inferred from the above figures are the following:
(1) For all AE, O^+ dominates upflowing ions (UFI) by a factor of ~3 for conics and ~2 for beams. The distribution in altitude and local time (not shown) is similar for O^+ and H^+. Approximately 85% of the ion beams and 90% of the conics are at energies ≤1 keV. These results confirm the suggestions of Ghielmetti and Johnson [1983] and Yau et al. [1985] about UFI at solar maximum.
(2) A significant number of conics is accelerated at all radial distances. There is evidence for a source of O^+ conics at 2.5 - 3.5 R_e for active times. Conics are strongly correlated with shocks and low frequency turbulence which suggests that the conics are produced by these electric fields.

(3) The radial distribution of beams suggests the possibility of parallel electric field acceleration at radial distances of 2.5 - 4.0 R_e during active times. Comparison with the electrostatic shock data implies that these parallel electric fields are associated with electrostatic shocks, as was found at S3-3 altitudes.
(4) Just as the S3-3 studies have shown, most electrostatic shocks are associated with either ion conics or ion beams. For the rising phase of the solar cycle ($F_{10.7}$ >100), the S3-3 data showed that ~20% (~65%) of the shocks were observed with ion beams (conics). The ISEE-1 data at solar maximum had ~40% (~30%) associated with beams (conics). Note that a percentage of the ion distributions which are identified as beams in upper range of altitudes in the ISEE-1 data set may actually be conics whose opening angle is less than the resolution of the measurement. As discussed above, a 90° conic at 2.5 R_e would fold up and be identified as a beam at ~5 R_e; smaller angle conics would fold up earlier.

$F_{10.7}$ Effects in the ISEE-1 Data Set

Because the range of $F_{10.7}$ values observed in the ISEE-1 auroral scan mode data set was as large as that observed in the S3-3 data set (even though the lowest $F_{10.7}$ was 140 compared to 60 for S3-3), we decided to examine the question of whether previously observed trends, such as the increase in the flux of O^+ and in the occurrence probability of conics and the decrease in the occurrence of beams, continued to the highest values of $F_{10.7}$. In addition, we wished to examine the evidence for the operation of the O^+-H^+ streaming instability at high altitudes. The local time sampling in the ISEE-1 study is not completely uniform; the low $F_{10.7}$ data set has less data at dusk and the high $F_{10.7}$ set has less data postmidnight. Table 1 summarizes the ISEE-1 results for low and high values of $F_{10.7}$. The probability of observing an ion beam decreased with $F_{10.7}$ for both O^+ and H^+. The occurrence frequency of O^+ conics increased with $F_{10.7}$, whereas that of H^+ remains approximately the same. There was no altitude dependence for the O^+ conic events. The ratio of O^+/H^+ conics also increased with $F_{10.7}$, although the ratio for beams remained approximately constant.

Because the methodology used herein and that used by Yau et al. [1985] differed, we have averaged the probability for the 2.2 - 3.2

TABLE 1. ISEE Auroral Scan Mode Data

	(less data at dusk) $F_{10.7} < 180$		(less data post-midnight) $F_{10.7} > 180$	
	$R < 4.5 R_E$	$R > 4.5 R_E$	$R < 4.5 R_E$	$R > 4.5 R_E$
	Ion Data			
H^+ Beams	0.17	0.11	0.1	0.11
O^+ Beams	0.27	0.27	0.17	0.24
O^+/H^+ Beams	1.6	2.5	1.7	2.2
H^+ Conics	0.03	0.01	0.02	0.01
O^+ Conics	0.06	0.06	0.09	0.09
O^+/H^+ Conics	2	6	4.5	9
	Electric Field Data Restricted to 20-04MLT			
Shocks	0.12	0.02	0.2	0.14
Turbulence	0.11	0.02	0.3	0.16

TABLE 2. Yau et al. (1985)

	$100 < F_{10.7} < 170$	$F_{10.7} > 170$
H⁺ Beams	.15	.14
O⁺ Beams	.14	.17
H⁺ Conics	.06	.11
O⁺ Conics	.06	.13

R_e bin and the 4.5 - 4.6 R_e bin from their tables to produce the Yau et al. entry in Table 2. Nevertheless, the numbers in the two tables can not be directly compared because of differences in the $F_{10.7}$ and altitude ranges and instrumentation; instead, trends observed in the two studies can be compared. It can be seen that the number of H⁺ beams decreased slightly with $F_{10.7}$ in the Yau et al. study in agreement with the ISEE study. The number of O⁺ beams, however, increased slightly. This may actually reflect an increase in small angle conics since the Yau et al. study did not distinguish between conics at angles of 160° - 180° and beams. The "conics" entry is for angles from 100° - 160°. It indicates an increase in the occurrence of both H⁺ and O⁺ conics.

Studies of DE-1 and S3-3 data by Reiff et al. [1988] and Collin et al. [1987, 1988] have provided evidence for the occurrence of the H⁺-O⁺ streaming instability which mediates exchange of energy between O⁺ and H⁺ beams. By comparing the energy of simultaneously observed O⁺ and H⁺ beams, they showed that the instability was suppressed when the ratio of O⁺/H⁺ flux increased just as had been theoretically predicted [Bergmann et al., 1988]. In Figure 11, both the ratio of the O⁺/H⁺ average energy and the ratio of the O⁺/H⁺ flux for the ion beam events are plotted versus altitude for the two ranges of $F_{10.7}$ utilized in this section. The ratio of the flux of O⁺ to the flux of H⁺ is larger for the higher $F_{10.7}$ range, whereas the ratio of the average energy of O⁺ to the average energy of H⁺ is smaller. The ratio of the average energy for DE-1 data at solar minimum (maximum) was ~1.4 (1.1). These numbers are in good agreement with the ISEE-1 results (averaged over the altitude range below DE-1 apogee) which were ~1.3 (1.15) for low (high) maximum.

In summary, the trends observed in the occurrence probability of ions from solar minimum to solar maximum (i.e., decrease in beams, increase in conics and increase in O⁺) continue from low to high solar maximum. In addition, ratio of the flux of O⁺ to that of H⁺ was larger for high maximum, whereas the ratio of the average energy of O⁺ was smaller. This is consistent with the operation of the ion two-stream instability and the results of Collin et al. [1987, 1988].

4. DISCUSSION AND CONCLUSIONS

The results of the S3-3 study can be combined with those of the ISEE-1 auroral scan mode study to infer some effects of solar cycle on auroral acceleration processes. The S3-3 observations of electrostatic shocks with ion beams suggest that, at solar maxi-

mum, most of the auroral parallel potential drop occurs above ~2.2 R_e (S3-3 apogee). The ISEE-1 observations of the occurrence probability of ion beams suggest that the parallel potential occurs between ~2.5 and ~4 R_e during solar maximum. In addition, the ISEE-1 study suggests that the magnitude of the parallel potential may be smaller at solar maximum since beams were rarely observed with energies above ~1 keV. The S3-3 data indicate that there is an increase in perpendicular acceleration relative to parallel acceleration from altitudes of ~1.3 to 2.2 R_e from solar maximum to solar minimum. The ISEE-1 data suggest that this trend extends at least to 3.5 or 4 R_e. Both data sets provide evidence that the perpendicular acceleration process is associated with electrostatic shocks and enhanced low-frequency turbulence. The ISEE-1 data indicate that trends (such as the decrease in beams, increase in conics and increase in O⁺, and evidence for the effects of the ion two-stream instability) observed when solar minimum data were compared to solar maximum data are also seen from low solar maximum (as indicated by $F_{10.7}$) to high solar maximum.

Several of these varied effects of solar cycle on auroral acceleration processes may be explained by the effects of solar EUV on the atmosphere and ionosphere. Many researchers have postulated that the heating of the atmosphere due to the increased EUV flux at solar maximum raises the O⁺-H⁺ charge exchange altitude and the O⁺ scale height so that more oxygen can escape [Klumpar, 1979; Young et al., 1982; Moore, 1980; Yau et al., 1985]. Ionospheric temperature and density also increase during solar maximum [Kelley, 1989]. Since many mechanisms which have been proposed to heat ions and to provide the parallel potential drop are current driven, the altitude at which they would become unstable would increase (for a given current density) when the ionospheric temperature and density increased. The increased oxygen density also has an effect on some instabilities including acoustic double layers [Gray et al., 1992], ion cyclotron waves [Cattell et al., 1991a], and ion two-stream waves [Bergmann et al., 1988]. If electrostatic shocks are the nonlinear evolution of a current driven instability [Witt and Lotko, 1983], then the decrease in shock occurrence probability at low altitudes may be understood. If the bulk of the auroral parallel potential drop occurs in shocks, then the $F_{10.7}$ dependence of beams observed by DE-1 and ISEE-1 and
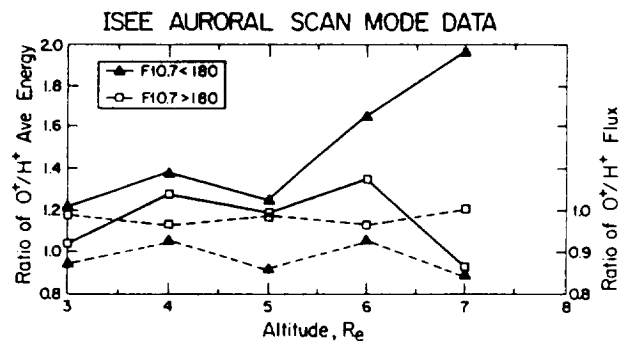
Fig. 11. The ratio of the average energy of O⁺ to that of H⁺ (left-hand scale, solid lines) and the ratio of the average flux of O⁺ to that of H⁺ (right-hand scale, dotted line) versus altitude for low $F_{10.7}$ (triangles) and high $F_{10.7}$ (open boxes).

of shocks with beams observed at S3-3 altitudes may also be explained.

There are several remaining puzzles in the data sets. It is not yet understood why electrostatic shocks are more common post-midnight for high $F_{10.7}$ than for low $F_{10.7}$. It may be due to the local time dependence of both the heating of the atmosphere by solar EUV and the ionization by solar EUV and precipitating particles [Cattell et al., 1991b]. The dependence of conic acceleration on altitude and $F_{10.7}$ is also not fully understood. This study suggests that the acceleration is due to both shocks and waves. If these mechanisms are current driven, then we would not expect enhanced perpendicular acceleration at low altitudes during solar maximum. Some of the enhanced perpendicular acceleration of oxygen at solar maximum may be due to the fact that, when the O^+/H^+ density ratio increases, oxygen cyclotron waves are more linearly unstable than hydrogen cyclotron waves [Kindel and Kennel, 1971; Cattell et al., 1991a]. Finally, the fact that most of the observed ion beams during solar maximum had energies of less than ~1 keV implies a reduction in the total auroral potential drop during solar maximum. Although this conclusion would seem to contradict observations of more intense auroral displays at solar maximum, the fact that the auroral luminosity depends on other factors as well may mitigate this problem.

REFERENCES

Bennet, E. L., M. Temerin, and F. S. Mozer, The distribution of auroral electrostatic shocks below 8000-km altitude, *J. Geophys. Res.*, 88, 710", 1983.

Bergmann, R., I. Roth and M. K. Hudson, Linear stability of the H^+-O^+ two stream interaction in a magnetized plasma, *J. Geophys. Res.*, 93, 4005, 1988.

Cattell, C., F. S. Mozer, I. Roth, R. R. Anderson, R. C. Elphic, W. Lennartsson and E. Ungstrup, ISEE-1 Observations of EIC waves in association with ion beams on auroral field lines from 2.5 - 4.5 R_e, *J. Geophys. Res.* 96, 11421, 1991a.

Cattell, C., S. Chari, and M. Temerin, An S3-3 Satellite Study of the Effects of Solar Cycle on the Auroral Acceleration Process, *J. Geophys. Res.*, 96, 17903, 1991b.

Collin, H. L., W. K. Peterson and E. G. Shelley, Solar cycle variation of some mass dependent characteristic of upflowing beams of terrestrial ions, *J. Geophys. Res.*, 92, 4757, 1987.

Collin, H., W. Peterson, and E. Shelley, The helium components of Energetic Terrestrial ion upflows: Their occurrence, morphology and intensity, *J. Geophys. Res.*, 93, 7558, 1988.

Ghielmetti, A. G., and R. G. Johnson, Variations in the occurrence frequency of UFI events from July 1976 to April 1979 (abstract), *EOS Trans AGU*, 64, 807, 1983.

Gorney, D. J, A. Clarke, D. Croley, J. Fennell, J. Luhmann, and P. Mizera, The Distribution of Ion Beams and Conics Below 8000 km, *J. Geophys. Res.*, 86, 83, 1981.

Gorney, D. J., Solar cycle effects of the near-earth space environment, *Rev Geophys.*, 28, 315, 1990.

Gray, P., M. Hudson, R. Bergmann, and I. Roth, Simulation study of the ion two-stream instability in the auroral acceleration region, *Geophys. Res. Lett.*, 17, 1609, 1990.

Gray, P., M. K. Hudson, and W. Lotko, Acoustic double layers in multi-species plasma, *IEEE Trans. Plasma Sci.*, in press, 1992.

Hedin, A. E., Correlations between thermospheric density and temperature, solar EUV flux and $F_{10.7}$ cm flux variations, *J. Geophys. Res.*, 89, 9828, 1984.

Kelley, M., in *The Earth's Ionosphere—Plasma Physics and Electrodynamics*, Academic Press, Inc., San Diego, 1989.

Kindel, J. M., and C. F. Kennel, Topside current instabilities, *J. Geophys. Res.*, 76, 3055, 1971.

Klumpar, D., Transversely accelerated ions: An ionospheric source of hot magnetospheric ions, *J. Geophys. Res.*, 84, 4229, 1979.

Lennartsson, W., Energetic (0.1- to 16 keV/E) Magnetospheric ion composition at different levels of solar $F_{10.7}$, *J. Geophys. Res.*, 94, 3600, 1989.

Lysak, R. L. and M. K. Hudson, Coherent anomalous resistivity in the region of electrostatic shocks, *Geophys. Res. Lett.*, 6, 661, 1979.

Mizera, P. F., and J. F. Fennell, Signatures of electric fields from high and low altitude particle distributions, *Geophys. Res. Lett.*, 4, 311, 1977.

Moore, T. E., Modulations of terrestrial escape flux composition, *J. Geophys. Res.*, 85, 2011, 1980.

Mozer, F. S., R. Torbert, U. V. Fahleson, C.-G. Falthammar, A. Gonfalone, and A. Pedersen, Measurements of quasistatic and low-frequency electric fields with spherical double probes on ISEE-1 spacecraft, *IEEE Trans. Geosci. Electron.*, GE-16, 258, 1978.

Mozer, F. S., C. A. Cattell, R. L. Lysak, M. K. Hudson, M. Temerin, and R. B. Torbert, *Spac. Sci. Rev.*, 27, 155, 1980.

Nguyen. T., C. A. Cattell, F. S. Mozer, E. Ungstrup, and W. Lennartsson, A statistical study of upflowing ions and electric fields on auroral field lines from ~3 to 7 R_e, *EOS Trans AGU*, 67, 1159, 1986.

Redsun, M. S., M. Temerin, and F. S. Mozer, Classification of auroral electrostatic shocks by their ion and electron associations, *J. Geophys. Res.*, 90, 9615, 1985.

Reiff, P. H., H. L. Collin, J. D. Craven, J. L. Burch, J. D. Winningham, E. G. Shelley, L. A. Frank, and M. A. Friedman, Determination of auroral electrostatic potentials using high and low altitude particle distributions, *J. Geophys. Res.*, 93, 7441, 1988.

Sharp, R., W. Lennartsson, W. Peterson and E. Ungstrup, The Mass Dependence of Wave Particle Interactions as Observed with the ISEE-1 Energetic Ion Mass Spectrometer, *Geophys. Res. Lett.*, 10, 651, 1983.

Shelley, E. G., R. D. Sharp, R. G. Johnson, J. Geiss, P. Eberhardt, H. Balsiger, G. Haerendel and H. Rosenbauer, Plasma Composition Experiment on ISEE-A, *IEEE Geosci. Electron.*, GE-16, 266, 1978.

Witt, E. and W. Lotko, Ion-acoustic solitary waves in a magnetized plasma with arbitrary electron equation of state, *Phys. Fluids*, 26, 2176, 1983.

Yau, A. W., P. H. Beckwith, W. K. Peterson, and E. G. Shelley, Long term (solar cycle) and seasonal variations of upflowing ionospheric ion events at DE-1 altitudes, *J. Geophys. Res.*, 90, 6395, 1985.

Young, D. T., H. Balsinger, and J. Geiss, Correlations of magnetospheric ion composition with geomagnetic and solar activity, *J. Geophys. Res.*, 87, 9077, 1982.

C. Cattell, T. Nguyen, and M. Temerin, Space Sciences Laboratory, University of California, Berkeley, California 94720

W. Lennartsson and W. Peterson, Lockheed Palo Alto Research Laboratory, Palo Alto, California

Specularly Reflected He²⁺ at High Mach Number Quasi-Parallel Shocks

S. A. FUSELIER AND O. W. LENNARTSSON

Lockheed Palo Alto Research Laboratory, Palo Alto, California

M. F. THOMSEN

Los Alamos National Laboratory, Los Alamos, New Mexico

C. T. RUSSELL

Institute for Geophysics and Planetary Physics, University of California, Los Angeles

Upstream from the Earth's quasi-parallel bow shock, the Lockheed Plasma Composition Experiment on ISEE 1 often observes two types of suprathermal He²⁺ distributions. Always present to some degree is an energetic (several keV/e to 17.4 keV/e, the maximum energy of the detector) "diffuse" He²⁺ distribution. Sometimes, apparently when the Alfven Mach number, M_A, is high enough and the spacecraft is near the shock (within a few minutes of a crossing), a second type of suprathermal He²⁺ distribution is also observed. This nongyrotropic, gyrating He²⁺ distribution has velocity components parallel and perpendicular to the magnetic field that are consistent with near-specular reflection of a portion of the incident solar wind He²⁺ distribution off the shock. Specularly reflected and diffuse proton distributions are associated with these gyrating He²⁺ distributions. The presence of these gyrating He²⁺ distributions suggests that specular reflection is controlled primarily by magnetic forces in high Mach number quasi-parallel shocks and that these distributions may be a seed population for more energetic diffuse He²⁺ distributions.

INTRODUCTION

Detailed spacecraft observations and computer simulations of quasi-perpendicular shocks ($\vartheta_{Bn} > 45°$, where ϑ_{Bn} is the angle between the shock normal and the upstream magnetic field) have led to an understanding of the prime energy dissipation process at this type of shock (see *Gosling and Robson* [1985] and *Goodrich* [1985] and references therein). Above a certain Mach number ($M_A = V_{SW} \cdot \hat{n}/V_A \simeq 2.5$-$3$, where V_{SW} is the solar wind velocity, $\hat{n}$ is the shock normal and V_A is the Alfven velocity), a significant fraction (up to approximately 20%) of the incident solar wind proton distribution is reflected off the shock in a near-specular manner (i.e., only the component of the incident velocity parallel to the shock normal changes sign). These specularly reflected protons gyrate into the upstream region and gain energy from the $V \times B$ force in the solar wind. Because their guiding center motion is directed downstream, they return to the shock after approximately one half gyration with significantly more energy than when they left it. The higher energy allows them to penetrate the shock and contribute significantly to the downstream proton heating. This process of reflection, gyration, energization, and return to the shock is self-sustaining as the number of reflected protons is just enough to satisfy the Rankine-Hugoniot conditions for the shock.

Specular ion reflection and its consequences are expected to be qualitatively different at quasi-parallel shocks ($\vartheta_{Bn} < 45°$). Specifically, when $\vartheta_{Bn} \leq 45°$, the guiding center motion of a specularly reflected particle is directed into the upstream re-

gion [*Gosling et al.*, 1982; *Schwartz et al.*, 1983]. Under steady upstream conditions, these ions would not return to the shock and therefore could not contribute to downstream proton heating. Near-specularly reflected protons have in fact been observed at and upstream from the Earth's quasi-parallel bow shock [e.g., *Gosling et al.*, 1982; *Fuselier et al.*, 1986a; *Gosling et al.*, 1989; *Onsager et al.*, 1990].

Whereas the existence of specularly reflected proton distributions at both the quasi-parallel and quasi-perpendicular bow shock is well established observationally, specular reflection of minor solar wind ions (e.g., He²⁺) off the bow shock has received considerably less attention. Nevertheless, there may be reason to expect that specular reflection of He²⁺ does take place at quasi-perpendicular shocks, providing the Mach number is high enough. *Ipavich et al.* [1984] found that the ratio of energetic He²⁺ to proton intensities at equal energy per charge was enhanced by an average factor of 1.6 over the solar wind ratio at high Alfven Mach number quasi-parallel shocks ($M_A > 7$). By comparison, this factor was 0.6 ± 0.3 for quasi-parallel shocks with $M_A < 7$. Ipavich et al. suggested that a specularly reflected He²⁺ population at the quasi-perpendicular shock provided the initial seed population for energetic He²⁺ seen at the high Mach number quasi-parallel shocks. Later, possible evidence for specularly reflected He²⁺ downstream from a high Mach number quasi-perpendicular shock was reported [*Fuselier et al.*, 1988].

In this paper, we present the first observations of near-specularly reflected He²⁺ upstream from high Mach number quasi-parallel shocks. To better compare the results here with observations of more energetic, diffuse He²⁺ distributions [*Ipavich et al.*, 1984], we will use Alfven Mach numbers almost exclusively when discussing Mach number dependence. Although the range of magnetosonic Mach numbers, M_f, in the solar wind is considerably less than that of Alfven Mach numbers, the qualitative results in

this paper based on M_A are also valid for M_f. We compare the He^{2+} observations with simultaneous suprathermal proton observations to determine the density ratio of specularly reflected He^{2+} to protons. The presence of specularly reflected He^{2+} at high Mach number quasi-parallel shocks suggests that it may be a seed population for diffuse He^{2+} seen in the same region.

The He^{2+} observations in this paper are from the Lockheed Plasma Composition Experiment [Shelley et al., 1978]. This set of mass spectrometers measures the velocity distributions of ions from mass/charge $(M/Q) = 1$ to 150 amu/charge in 64 mass steps and in 32 possible energy steps from near the spacecraft potential to 17.4 keV/e. The spectrometer we use in this paper points 5° below the spin (ecliptic) plane and has a field of view ranging from a high of about ±20° at low energies to a low of about ±5° at high energies. Although primarily designed to study the composition of the magnetosphere, during the 1978 and 1979 ISEE solar wind seasons this mass spectrometer was programmed to operate in a variety of modes specifically intended for magnetosheath and solar wind studies. Here, we use data from two specific modes, one at high and one at low data rate. In the high data rate mode, the He^{2+} spectrum from 10 eV/e to 17.4 keV/e is measured in 16 energy steps. Each energy step takes somewhat over 1 spin (=3 s), so that the He^{2+} spectrum with a 7.5° angular resolution in the spacecraft spin plane is completed in 60 s. The time resolution can be improved by reducing the energy coverage. A new He^{2+} spectrum is obtained approximately every 120 s with intervening time spent measuring other mass/charge ions. In the low data rate mode, the He^{2+} spectrum from 10 eV/e to 4.6 keV/e in 8 energy steps is measured in a similar manner to the high data rate

mode except that the angular resolution is 30°. In this low data rate mode, the He^{2+} distribution is measured continuously with a time resolution of about 25 s.

Proton observations in this paper are from the joint Los Alamos Garching Fast Plasma Experiment (FPE) on ISEE 2 [Bame et al., 1978]. In one 3-s spacecraft spin, this electrostatic analyzer measures the two-dimensional velocity distribution of all ions from 70 eV/e to 40 keV/e in 16 energy steps at each of 16 azimuths integrated over ±55° of elevation angle relative to the ecliptic. Full 2-dimensional distributions are repeated every 3 (12) s in high (low) data rate. The FPE spectra displayed in this paper were derived under the assumption that all the observed ions were protons.

Magnetic field measurements in this paper are from the University of California, Los Angeles flux gate magnetometers on ISEE 1 and 2 [Russell, 1978]. These instruments measure the vector magnetic field 16 (4) times a second in high (low) data rate. In this paper, considerably longer averages of these vector measurements will be used.

OBSERVATIONS

July 27, 1979, High Data Rate

The upper left-hand panel in Figure 1 shows the total magnetic field profile (4-s averaged) for a very high Mach number ($M_A \sim 18$, $M_f \sim 5.7$) outbound quasi-parallel shock crossing on this day. The intervals labeled A and B in this panel indicate where, relative to the shock crossing, the He^{2+} spectra in the upper middle and right panels in Figure 1 were measured. Spectrum A was taken just
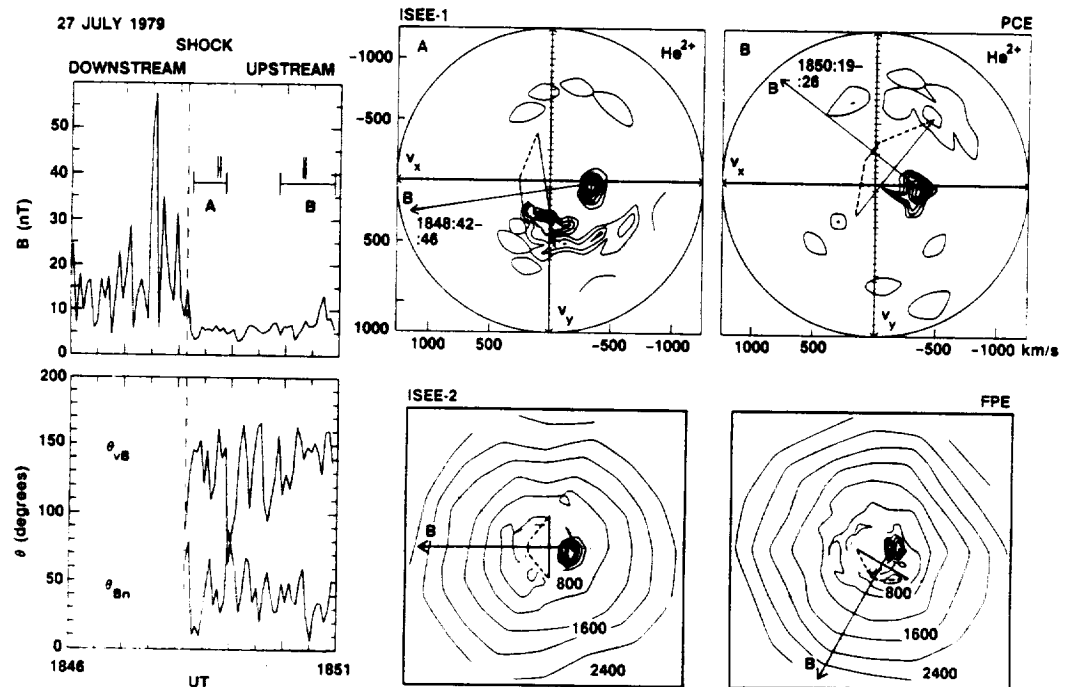
Fig. 1. Upper panels, left to right, total magnetic field profile and two He^{2+} spectra for a high Mach number quasi-parallel shock crossing at 1848:15 UT on July 27, 1979. In both spectra, the cold solar wind He^{2+} distribution is seen at $V_x \approx -325$ km/s. A second nongyrotropic suprathermal distribution is seen in spectrum A with its peak at $V_x = 50$ km/s and $V_y = 325$ km/s and in spectrum B with its peak at $V_x = V_y = -500$ km/s. The vector B in each spectrum shows magnetic field direction projected in the spin plane, averaged over the time required to measure the peak in the suprathermal distribution. These averaging times are listed next to the vector. The dashed line in each spectrum shows the range of possible parallel speed and gyrospeed assuming specular reflection off the bow shock. Lower panels, left to right, ϑ_{Bn} and ϑ_{VB} profiles and two Fast Plasma Experiment ion spectra. The ion spectra clearly show the presence of a diffuse proton distribution extending to the full velocity range.

after the shock crossing, and B was taken somewhat later. The short bars above the A and B intervals identify when the FPE ion spectra in the lower middle and right panels in Figure 1 were measured.

In the He^{2+} spectra in Figure 1, contours of constant phase space density in the spacecraft spin (ecliptic) plane are plotted with two contours per decade. (Geocentric Solar Ecliptic (GSE) coordinates are used throughout.) The small dots in each spectrum show the velocities and the 10° angle bins used to determine the spectrum. Background counts have been removed from these spectra, and only phase space densities corresponding to at least two counts above background are plotted. Because the time required to complete the He^{2+} spectra (~45-60 s) is longer than the characteristic period of the upstream turbulence (~30 s), there is probably considerable time aliasing in the complete He^{2+} spectra in Figure 1. However, measurements at all angles and a fixed speed require only 4 s to complete, and adjacent speeds are measured in only 8 s. These shorter times are more commensurate with the characteristic period of the upstream turbulence. For this reason, the magnetic field direction projected into the spin plane, B in each spectrum, is averaged over the time required to measure the peak of the suprathermal He^{2+} distribution (this distribution is discussed below) and not averaged over the time required to complete the full spectrum. Next to the vector B in each He^{2+} spectrum is the time interval required to measure the peak in the suprathermal distribution.

Clearly evident in both spectra is the cold solar wind He^{2+} distribution at $V_X \approx$ -325 km/s. The angular extent of this distribution is mainly the result of the relatively large 10° angle bins and not the result of a large solar wind He^{2+} temperature. Also evident in the He^{2+} spectra in Figure 1 is a nongyrotropic suprathermal He^{2+} component in spectrum A at $V_X, V_Y \approx$ 50, 325 km/s and in spectrum B at $V_X = V_Y \approx$ -500 km/s. Finally, there are several isolated peaks at all angles and at velocities typically >500 km/s. These do not represent background (which has already been removed from the spectra) but rather are identified as part of a "diffuse" He^{2+} population upstream from the shock. The discontinuous nature of this distribution is a result of its low density and broad angular extent. These diffuse He^{2+} distributions are commonly seen upstream from quasi-parallel shocks with this instrument.

The lower middle and right panels of Figure 1 show the FPE ion spectra. The general format is the same as that for the He^{2+} spectra, but there are some differences. First, the velocity range for the FPE spectra is twice that for the He^{2+} spectra. Second, the ISEE 2 magnetic field direction projected into the ecliptic, B in each FPE ion spectrum, is an average over the time interval required to measure the full FPE spectrum (3 s).

Evident in the FPE ion spectra is the solar wind proton distribution at $V_x \sim$ -325 km/s, which is not well resolved by this instrument. The shoulder on the proton distribution at larger - V_x velocities is the solar wind He^{2+} distribution appearing at $\sqrt{2}$ times the proton velocity because of the assumption that all ions are protons. Clearly evident in the FPE ion spectra is a hot nearly isotropic diffuse proton distribution extending to the full range of the instrument. Diffuse proton distributions are a ubiquitous feature of the region upstream from the quasi-parallel bow shock[see Gosling et al., 1978]. At lower energies (≤ 800 km/s), the diffuse distribution is anisotropic. This lower-energy anisotropy will be discussed below.

For specular reflection off the bow shock, the guiding center motion parallel to the magnetic field, $V_{||}$, and the gyrospeed, v_g of the reflected distribution in the shock frame can be determined

from the shock geometry and the solar wind velocity (see Gosling et al. [1982] for a complete derivation). The derived equations are

$$v_g = | V_{SW} | 2\cos \vartheta_{Vn} \sin \vartheta_{Bn} \qquad (1)$$

$$V_{||} = V_{SW} | \cos \vartheta_{VB} - 2\cos \vartheta_{Bn} \cos \vartheta_{Vn} \qquad (2)$$

Here, ϑ_{Vn} is the angle between the upstream solar wind velocity and the shock normal and ϑ_{VB} is the angle between the magnetic field and the solar wind velocity. By convention, the magnetic field is always assumed to be directed into the upstream region in these formulas, and ϑ_{VB} is therefore always ≥90°. To put these equations in the frame of reference of the solar wind, $V_{SW} \cdot B$ is subtracted from equation (2).

A difficulty with applying (1) and (2) to the observations in Figure 1 is that the instantaneous values of ϑ_{Bn} and ϑ_{VB} at the time an ion is reflected off the shock are not known because the direction of the magnetic field is highly variable. To illustrate this point, the time profiles of the instantaneous values of ϑ_{Bn} and ϑ_{VB} at the spacecraft (from the 4-s average magnetic field data) are plotted in the lower left-hand panel of Figure 1. The large fluctuations in these two parameters are due to large-amplitude MHD-like waves upstream from the quasi-parallel bow shock (see also Greenstadt and Mellott [1985]).

Although the fluctuations of ϑ_{Bn} and ϑ_{VB} are large, there is a quasi-periodicity to them as seen in the lower left-hand panel of Figure 1. To estimate the range of possible values for $V_{||}$ and v_g in (1) and (2), we determined the maximum and minimum values of ϑ_{Bn} and ϑ_{VB} over the intervals A and B in the upper left hand panel of Figure 1. These intervals cover several cycles of the quasi-periodic fluctuations in ϑ_{Bn} and ϑ_{VB}. Because the magnitude of the velocity is unchanged in specular reflection and because the direction of the incident solar wind velocity is assumed to be constant, a maximum in ϑ_{Bn} corresponds to a minimum in ϑ_{VB} and results in a maximum v_g and minimum $V_{||}$ and vice versa. Table 1 lists the maximum and minimum values for ϑ_{Bn} and ϑ_{VB} from Figure 1 and the corresponding maximum and minimum values of v_g and $V_{||}$ computed from equations (1) and (2) and the solar wind parameters on July 27, 1979. The solid bars perpendicular to the magnetic field in each spectrum in Figure 1 are located at the maximum and minimum values of $V_{||}$ from Table 1 and have half length equal to the corresponding minimum and maximum values of v_g from Table 1. Thus, the dashed lines

TABLE 1. Shock Parameters July 27, 1979, 1848 UT (GSE Coordinates)

Parameter	Value	
N_{SW}, cm^{-3}[†]	45	
V_{SW}, km/s[†]	-329, 23, 8	
M_A	18	
n (model)	0.910, 0.353, 0.218	
ISEE 1, 2 separation, km	-691., -1229., -384.	
ϑ_{Vn}, deg	151	

Parameter	1848:42.5-:46 UT	1850:19-:26 UT
$\vartheta_{Bn(max),(min)}$, deg	67, 9	60, 6
$\vartheta_{VB(min),(max)}$, deg	109, 153	140, 145
$v_{g(max),(min)}$, km/s	534, 94	503, 66
$V_{||(min),(max)}$, km/s	224, 571	286, 575

[†]From the Los Alamos Solar Wind Experiment on ISEE 1.

in each spectrum represent the range of possible values for $V_\parallel$ and v_g which specularly reflected particles could have under the observed field conditions.

In both He²⁺ spectra in Figure 1, the suprathermal distribution is nearly consistent with specular reflection off the bow shock. In He²⁺ spectrum A, $V_\parallel$ and v_g for the suprathermal distribution are somewhat less than predicted for specular reflection, and in both spectra A and B the thermal spread of the suprathermal distribution results in a large fraction of He²⁺ at larger and smaller than predicted gyrospeeds.

In the FPE ion spectra, the range of possible $V_\parallel$ and v_g assuming specular reflection is correlated with low-energy anisotropies in the diffuse proton distribution. We therefore suggest that these low-energy anisotropies may be caused by the simultaneous presence of specularly reflected and diffuse proton distributions.

Assuming that the angular extent of the solar wind and suprathermal distributions in He²⁺ spectrum A are the same in the spin plane and perpendicular to the spin plane, the suprathermal distribution is estimated to be about 3% of the solar wind He²⁺ density. This must be considered a rough estimate because the cold solar wind density can be underestimated in this instrument mode and because the extent of the distributions out of the spin plane is not known.

Estimating the density of the presumed specularly reflected protons in the FPE ion spectrum in the lower middle panel of Figure 1 is much more difficult because the specularly reflected distribution, if present, blends continuously into the diffuse distribution. However, the specularly reflected proton distribution is more evident in other FPE spectra (not shown). A rough estimate of the suprathermal distribution below 850 km/s from these spectra is about 0.4% of the solar wind proton density. Because of the lack of a well-defined specularly reflected distribution, this density should only be considered a rough estimate.

September 3, 1978, Low Data Rate

The left-hand panels of Figure 2 show the magnetic field profile and the ϑ_{Bn} and ϑ_{VB} profiles for a high Mach number ($M_A \sim 7$, $M_f \sim 6.3$) quasi-parallel shock crossing on this day. The format is the same as that for the left-hand panels of Figure 1. Although it is not evident in the magnetic field profile in Figure 2, plasma measurements show that the shock was crossed at 1146:45 UT and thereafter the spacecraft were in the upstream region. The maximum and minimum values for $V_\parallel$ and v_g for the shock geometry and solar wind speed on this day are listed in Table 2 in a format identical to that in Table 1.

The right hand panels of Figure 2 show representative He²⁺ and FPE ion spectra upstream from the shock on this day (interval A in Figure 2). The format is identical to that for the middle and right-hand panels of Figure 1. Evident in the He²⁺ spectrum is a suprathermal distribution at $V_x \sim +200$ km/s, $V_y \sim -400$ km/s that is nearly consistent with the range of possible values for $V_\parallel$ and v_g assuming specular reflection. As with He²⁺ spectrum A in Figure 1, the $V_\parallel$ and v_g for the suprathermal distribution are somewhat less than expected for specular reflection. The limited energy range of the instrument mode on this day precludes the identification of a diffuse He²⁺ component.

The FPE ion spectrum in Figure 2 clearly shows a nongyrotropic suprathermal proton distribution that is consistent with specular reflection. Although not clearly distinguishable in this spectrum, longer averages of the FPE data (not shown here) indicate that in addition to the specularly reflected distribution, there is a nearly isotropic diffuse distribution present. Some evidence for this diffuse distribution can be seen in the FPE spectrum in Figure 2 at velocities ≥ 1600 km/s.

In the Plasma Composition Experiment mode used during this day, the He²⁺ spectrum was measured continuously with a time
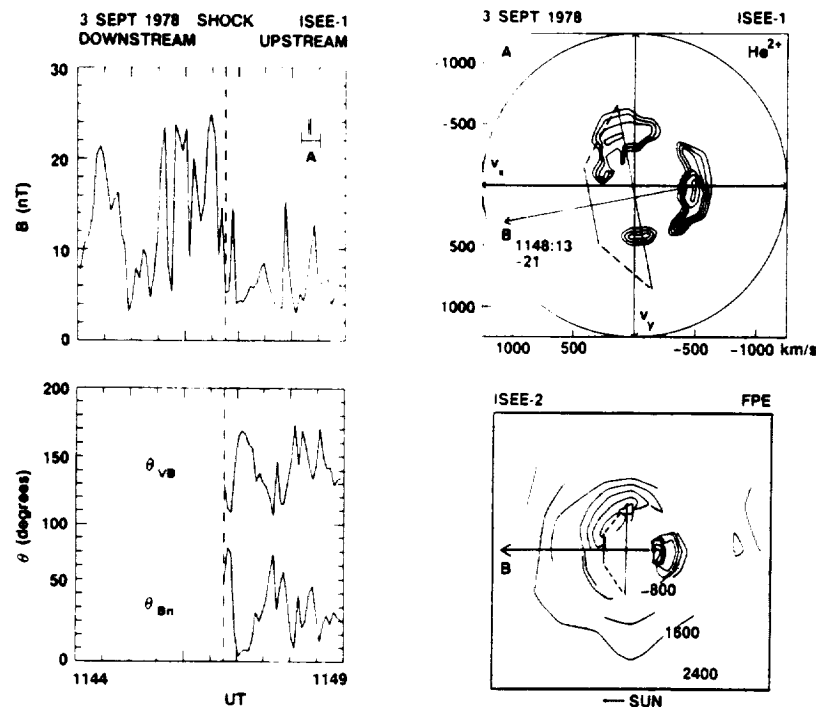
Fig. 2. Magnetic field and ϑ_{Bn} and ϑ_{BV} profiles (left-hand panels) and two representative He²⁺ and FPE ion spectra (right hand panels) from a high Mach number quasi-parallel shock crossing on September 3, 1978. The format is the same as that for Figure 1. Both the He²⁺ and FPE ion spectra show suprathermal distributions consistent with specular reflection.

TABLE 2. Shock Parameters September 3, 1978 1147 UT
(GSE Coordinates)

Parameter	Value
N_{SW}, cm^{-3}†	3
V_{SW}, km/s†	-470, 0, -16
M_A	7
n (model)	0.932, 0.089, 0.254
ISEE 1, 2 separation, km	-731., -407., -297.
ϑ_{Vn}, deg	160

Parameter	1148:13-:21 UT
$\vartheta_{Bn(max),(min)}$, deg	56, 15
$\vartheta_{VB(min),(max)}$, deg	133, 171
$V_{g(max),(min)}$, km/s	754, 228
$V_{\parallel(min),(max)}$, km/s	512, 883

†From the Los Alamos Solar Wind Experiment on ISEE 1.

resolution of about 25 s. Suprathermal He^{2+} distributions consistent with specular reflection were observed continuously from the shock crossing at 1146:45 UT in Figure 2 to about 1149 UT. After this time, it was difficult to distinguish a gyrating distribution in the data. The density of the suprathermal distribution in Figure 2 is estimated to be about 6% of the solar wind He^{2+} density. Again, this should be considered only a rough estimate. The density of the specularly reflected proton distribution is estimated to be about 2% of the solar wind proton density. Thus, specularly reflected He^{2+} and protons appear to be present in roughly solar wind concentrations.

Other Events

We have analyzed several crossings of other high Mach number (M_A=6.3 to 7) quasi-parallel bow shocks and have identified several other examples of near-specularly reflected He^{2+} distributions upstream from these shocks (not shown here). Generally, these other events have the same characteristics as the representative events shown in Figures 1 and 2. In particular, these other events are confined to within a few minutes of the bow shock crossing, and a low-density diffuse He^{2+} is seen with the specularly reflected distribution when the Plasma Composition Experiment is in a mode that can measure this second distribution.

The search for specularly reflected He^{2+} at low Mach number quasi-parallel shocks has been limited to only one shock crossing. We have looked for specularly reflected He^{2+} during the August 15, 1978, specularly reflected proton event [*Gosling et al.*, 1982]. Specularly reflected He^{2+} is absent from this low Mach number (M_A=5.5, M_f=3.3) bow shock crossing despite the presence of a specularly reflected proton distribution with a density of about 3% of the solar wind proton density. Based on the background measurement of the Lockheed Plasma Composition Experiment for this event, an upper limit on the density of all suprathermal He^{2+} is about 0.3% of the solar wind He^{2+} density.

DISCUSSION

In Figures 1 and 2, we present the first observations of near-specularly reflected He^{2+} upstream from quasi-parallel high Mach number shocks. The specularly reflected He^{2+} to proton density ratio upstream from the two quasi-parallel shocks with M_A>7 is roughly the same as the solar wind He^{2+} to proton density ratio.

For the one event with M_A<6, only specularly reflected protons were seen, indicating a specularly reflected He^{2+} to proton density ratio at least a factor of 10 smaller than the solar wind He^{2+} to proton density ratio. While this result suggests that the density of specularly reflected He^{2+} depends on Mach number, an extensive survey of specularly reflected He^{2+} at shocks is needed to confirm this dependence. Other factors such as the solar wind He^{2+} to proton temperature ratio may also affect the relative abundance of specularly reflected He^{2+} [*Burgess*, 1989].

A similar Mach number dependence has been seen for the more energetic diffuse He^{2+} to proton density ratio at quasi-parallel shocks [*Ipavich et al.*, 1984]. Ipavich et al. suggested that He^{2+} specularly reflected off the quasi-perpendicular shock provides the seed population for the observed diffuse He^{2+} distributions in a "nonthermal leakage" process [e.g. *Tanaka et al.*, 1983]. In this process, some solar wind He^{2+} is specularly reflected off the quasi-perpendicular shock. These ions return to the shock after a partial gyration and enter the downstream region. Scattering in the downstream region produces some ions with sufficient velocity parallel to the magnetic field to reenter the upstream region as field-aligned beams. These beams would presumably disrupt to produce diffuse distributions in the upstream region. While this nonthermal leakage process may occur at the bow shock, the observations in this paper suggest that specularly reflected He^{2+} at the high Mach number quasi-parallel shock may also provide a seed population for diffuse He^{2+} distributions.

The close proximity of the specularly reflected He^{2+} distributions to the shock (typically within 1 to 2 min of a shock crossing) presents an interesting problem. How are these near specularly reflected distributions confined to the region near the shock? Is it a temporal confinement or a spatial confinement? (That is, are these distributions disrupted soon after reflecting off the shock to produce diffuse distributions, or do they return to the shock after a short excursion into the upstream region?) The answer is likely some combination of the two possibilities.

The He^{2+} distributions specularly reflected off quasi-parallel shocks propagate into a very turbulent upstream region. The large-amplitude compressive MHD-like waves upstream from these shocks may disrupt the He^{2+} distribution within a few gyroradii of the shock. Once disrupted, these He^{2+} distributions may contribute locally to the diffuse He^{2+} population upstream from quasi-parallel shocks. Also, as the large-amplitude waves convect into the shock, they cause large variations in the instantaneous value of ϑ_{Bn} (see Figures 1 and 2 and *Greenstadt and Mellott* [1985]). It has been suggested that some fraction of specularly reflected protons return to the quasi-parallel shock under these unsteady upstream conditions [*Fuselier et al.*, 1986b; *Gosling et al.*, 1989]. This possibility may not be limited to protons and may also include specularly reflected He^{2+}. Determining the effects of the upstream waves on the He^{2+} distributions will require further study of He^{2+} distributions both upstream and downstream from the shock.

In this paper, we have drawn analogies between the specularly reflected He^{2+} and proton observations. There are also some potentially important differences between these observations. One difference already discussed in detail is the Mach number dependence of the specularly reflected He^{2+}.

Another difference is that predicted values of $V_{\parallel}$ and v_g fit the proton observations better than the He^{2+} observations (see Figure 2). This difference may be the result of projection effects. In all three He^{2+} spectra in this paper, the magnetic field is about 20° out of the ecliptic plane. Since the Plasma Composition Experiment integrates over only ±10° of elevation angle relative to the ecliptic plane, projection effects on the nongyrotropic specularly reflected

distribution may be important. In contrast, the FPE integrates over ±55° of elevation angle relative to the ecliptic plane, and the spectra from this instrument may be less susceptible to projection effects.

Also, we note that the FPE ion spectra for the two events in this paper show obvious differences. One of these is the different absolute densities of the diffuse ion populations in Figures 1 and 2. The absolute density of the diffuse population is much higher in Figure 1 than that in Figure 2 presumably because the solar wind density for that event was much higher than the event in Figure 2 (see Tables 1 and 2). Comparing the relative densities of the diffuse populations in Figures 1 and 2, we find that the diffuse fractions are similar, about 1.4% and 1% of the solar wind proton density for the events in Figures 1 and 2, respectively.

Another difference which may have important implications is the relative densities of the specularly reflected versus proton diffuse distributions for the two events in Figures 1 and 2. Whereas Figure 2 shows a well-resolved specularly reflected distribution, Figure 1 shows little or no evidence for the presence of a specularly reflected distribution. This difference may be related to the rate of disruption of the specularly reflected proton distribution. The rate of disruption depends on the amount of free energy in the specularly reflected distribution and on the level of preexisting turbulence in the upstream region. This efficiency is proportional to the ratio of the effective beam speed to the Alfven speed V_B/V_A [e.g., Gary et al., 1986]. Although the effective beam speed is higher for the event in Figure 2 (because of the higher solar wind velocity), the Alfven speed for the event in Figure 1 is much lower, so that V_B/V_A is a factor of 3 higher for the event in Figure 1 compared to the one in Figure 2. Thus, the larger amount of free energy in the specularly reflected proton distribution in Figure 1 may have caused it to scatter faster than the specularly reflected proton distribution in Figure 2. Note, however, that even if the entire suprathermal proton distribution in Figure 1 is assumed to be originally specularly reflected, the specularly reflected He^{2+} to proton density ratio is still about a factor of 2 above the solar wind He^{2+} to proton density ratio.

An important question which we are not able to answer at present is why He^{2+} specularly reflects off the quasi-parallel bow shock with such large concentrations relative to protons. To answer this question requires a good understanding of specular reflection. Such an understanding does not exist at present.

If the electrostatic potential at the shock is responsible for all ion specular reflection, then, because of the larger mass per charge of He^{2+}, a much smaller fraction of these ions would reflect off the shock as compared to the fraction of reflected protons. However, computer simulations of both quasi-parallel [Quest et al., 1983] and quasi-perpendicular [Leroy et al., 1982] shocks suggest that ion specular reflection occurs through magnetic forces as well. In fact, results from quasi-perpendicular shock simulations show that almost all of the ion reflection can be explained by magnetic forces at high ($M_A > 6$) Mach numbers while electrostatic forces may dominate at low ($M_A < 6$) Mach numbers [Leroy et al., 1982]. Analogous simulation results have not yet been obtained for quasi-parallel shocks, but our observations suggest that the situation is similar for these shocks.

Like electrostatic forces, magnetic forces on the incident ions must be proportional to the charge to mass ratio. However, magnetic forces are also proportional to the ion velocity, and a velocity offset between He^{2+} and protons within the shock might provide the additional force needed to reflect the He^{2+}. Ion velocities in the shock ramp have indeed been found to depend on mass per charge [e.g., Fuselier et al., 1988]. Perhaps future simulations will help

elucidate the relative importance of electric and magnetic forces in the reflection of He^{2+}.

REFERENCES

Bame, S. J., J. R. Asbridge, H. E. Felthauser, J. P. Glore, G. Paschmann, P. Hemmerich, K. Lehmann, and H. Rosenbauer, ISEE-1 and -2 fast plasma experiment and the ISEE-1 solar wind experiment, *IEEE Trans. Geosci. Electron.*, GE-16, 216-220, 1978.

Burgess, D., Alpha particles in field-aligned beams upstream of the bow shock: Simulations, *Geophys. Res. Lett.*, 16, 163-166, 1989.

Fuselier, S. A., M. F. Thomsen, J. T. Gosling, S. J. Bame, and C. T. Russell, Gyrating and intermediate ion distributions upstream from the Earth's bow shock, *J. Geophys. Res.*, 91, 91-99, 1986a.

Fuselier, S. A., J. T. Gosling, and M. F. Thomsen, Motion of ions specularly reflected off a quasi-parallel shock in the presence of large-amplitude monochromatic MHD waves, *J. Geophys. Res.*, 91, 4163-4170, 1986b.

Fuselier, S. A., E. G. Shelley, and D. M. Klumpar, AMPTE/CCE observations of shell-like He^{2+} and O^{6+} distributions in the magnetosheath, *Geophys. Res. Lett.*, 15, 1333-1336, 1988.

Gary, S. P., C. D. Madland, D. Schriver, and D. Winske, Computer simulations of electromagnetic cool ion beam instabilities, *J. Geophys. Res.*, 91, 4188-4200, 1986.

Goodrich, C. C., Numerical simulations of quasi-perpendicular collisionless shocks, in *Collisionless Shocks in the Heliosphere: Reviews of Current Research, Geophys. Monogr. Ser.*, vol. 35, edited by B. T. Tsurutani and R. G. Stone, pp. 153-168, AGU, Washington, D. C., 1985.

Gosling, J. T., and A. E. Robson, Ion reflection, gyration and dissipation at supercritical shocks, in *Collisionless Shocks in the Heliosphere: Reviews of Current Research, Geophys. Monogr. Ser.*, vol. 35, edited by B. T. Tsurutani and R. G. Stone, pp. 141-152, AGU, Washingtion, D. C., 1985.

Gosling, J. T., J. R. Asbridge, S. J. Bame, G. Paschmann, and N. Sckopke, Observations of two distinct populations of bow shock ions in the upstream solar wind, *Geophys. Res. Lett.*, 5, 957-960, 1978.

Gosling, J. T., M. F. Thomsen, S. J. Bame, W. C. Feldman, G. Paschmann, and N. Sckopke, Evidence for specularly reflected ions upstream from the quasi-parallel bow shock, *Geophys. Res. Lett.*, 9, 1333-1336, 1982.

Gosling, J. T., M. F. Thomsen, S. J. Bame, and C. T. Russell, Ion reflection and downstream thermalization at the quasi-parallel bow shock, *J. Geophys. Res.*, 94, 10027-10038, 1989.

Greenstadt, E. W., and M. M. Mellott, Variable field-to-normal angles in the shock foreshock boundary observed by ISEE 1 and 2, *Geophys. Res. Lett.*, 12, 129-132, 1985.

Ipavich, F. M., J. T. Gosling, and M. Scholer, Correlation between the He/H ratios in upstream particle events and in the solar wind, *J. Geophys. Res.*, 89, 1501-1507, 1984.

Leroy, M. M., D. Winske, C. C. Goodrich, C. S. Wu, and K. Papadopoulos, The structure of perpendicular bow shocks, *J. Geophys. Res.*, 87, 5081-5094, 1982.

Onsager, T. G., M. F. Thomsen, J. T. Gosling, S. J. Bame, and C. T. Russell, Survey of coherent ion reflection at the quasi-parallel bow shock, *J. Geophys. Res.*, in press, 1990.

Quest, K. B., D. W. Forslund, J. U. Brackbill, and K. Lee, Collisionless dissipation processes in quasi-parallel shocks, *Geophys. Res. Lett.*, 10, 471-474, 1983.

Russell, C. T., The ISEE-1 and -2 fluxgate magnetometers, *IEEE Trans. Geosci. Electron., GE-16*, 239-242, 1978.

Schwartz, S. J., M. F. Thomsen, and J. T. Gosling, Ions upstream of the Earth's bow shock: A theoretical comparison of alternative source populations, *J. Geophys. Res., 88*, 2039-2047, 1983.

Shelley, E. G., R. D. Sharp, R. G. Johnson, J. Geiss, P. Eberhardt, H. Balsiger, G. Haerendel, and H. Rosenbauer, Plasma composition experiment on ISEE-A, *IEEE Trans. Geosci. Electron., GE-16*, 266-270, 1978.

Tanaka, M., C. C. Goodrich, D. Winske, and K. Papadopoulos, A source of the backstreaming ion beams in the foreshock region, *J. Geophys. Res., 88*, 3046-3054, 1983.

S. A. Fuselier and O. W. Lennartson, Lockheed Palo Alto Research Laboratory, Dept. 91-20 Bldg. 255, 3251 Hanover Street, Palo Alto, CA 94304.

M. F. Thomsen, Los Alamos National Laboratory, ESS-8 MS D438, Los Alamos, NM 87545.

C. T. Russell, Institute for Geophysics ans Planetary Physics, University of California, Los Angeles, CA 90024

He²⁺ Heating at a Quasi-Parallel Shock

S. A. FUSELIER AND O. W. LENNARTSSON

Lockheed Palo Alto Research Laboratory, Palo Alto, California

M. F. THOMSEN

Los Alamos National Laboratory, Los Alamos, New Mexico

C. T. RUSSELL

Institute for Geophysics and Planetary Physics, University of California, Los Angeles, California

We present the first observations of solar wind He²⁺ heating downstream from the Earth's quasi-parallel shock. These observations show that in conjunction with protons, two different regions are observed. In regions where the proton distribution is cooler, more dense, and similar to that observed downstream from quasi-perpendicular shocks, the He²⁺ distribution is shell-like, also similar to that observed downstream from quasi-perpendicular shocks. In regions where the proton distribution is hotter, less dense, and Maxwellianlike, the He²⁺ distribution is also Maxwellianlike without evidence for a shell. These observations support the interpretation that the nearly isotropic proton and He²⁺ distributions are produced through the strong interaction of a very dense specularly reflected proton beam with the incident solar wind, while the cooler proton distributions and shell-like He²⁺ distributions are produced in a manner similar to that at the quasi-perpendicular bow shock.

INTRODUCTION

The study of collisionless shocks in space plasmas has received considerable attention since the early observations of the Earth's bow shock. Most of this attention has been directed toward the understanding of quasi-perpendicular shocks (shocks whose angle between the shock normal and the magnetic field, ϑ_{Bn}, is greater than 45°). Many of the processes at these shocks, including ion dissipation, are well documented [see *Gosling and Robson*, 1985; *Goodrich*, 1985, and references therein]. While this class of shocks is easier to study than quasi-parallel shocks ($\vartheta_{Bn} < 45°$) both from a theoretical and an observational standpoint, significant advances in the understanding of quasi-parallel shocks have also recently been made. Of particular interest here are observations and computer simulations of quasi-parallel shocks which investigate ion thermalization and suggest that these shocks undergo cyclic reformation [*Burgess*, 1989; *Gosling et al.*, 1989; *Scholer and Terasawa*, 1990; *Thomas et al.*, 1990; *Thomsen et al.*, 1990; *Onsager et al.*, 1990].

Recently, cold beams have been detected just upstream from the Earth's quasi-parallel bow shock [*Gosling et al.*, 1989; *Onsager et al.*, 1990]. These beams have velocity space signatures consistent with near-specular reflection off the nearby shock and are similar to those seen just upstream from the quasi-perpendicular bow shock. Downstream from the quasi-parallel shock, the proton distribution is observed to alternate between a hotter, less dense state and a cooler, more dense state [*Gosling et al.*, 1989; *Thomsen et al.*, 1990]. The hot distributions are Maxwellianlike, while the cooler distributions have a core and shoulder also characteristic

of the distributions seen downstream from the quasi-perpendicular bow shock.

From these observations the following model for the quasi-parallel bow shock was developed. This model is supported and strongly influenced by several computer simulations of the quasi-parallel shock [e.g., *Burgess*, 1989; *Scholer and Terasawa*, 1990; *Thomas et al.*, 1990].

Initially, a relatively small fraction (~ few percent) of solar wind H⁺ is reflected off the quasi-parallel shock and propagates into the upstream region. These ions generate large-amplitude waves which convect back into the shock. The waves have a profound effect on the shock, causing large fluctuations of the upstream ϑ_{Bn} [*Greenstadt and Mellott*, 1985] which apparently result in the periodic specular reflection of a larger than normal amount of incident solar wind H⁺. The large fraction of reflected H⁺ propagates into the upstream region and interacts strongly with the solar wind, causing the steepening of the convecting large-amplitude waves and the re-formation of the shock some distance farther upstream.

Downstream from the re-forming quasi-parallel shock, H⁺ distributions alternate between a cooler, denser distribution similar to those observed at quasi-perpendicular shocks and a much hotter, less dense, nearly isotropic distribution. The cooler distribution is believed to be formed much the same way that similar distributions are formed at quasi-perpendicular shocks. That is, a relatively small fraction of ions initially specularly reflect off the shock and gyrate into the upstream region. These ions return to the shock because they reflected off the shock when the instantaneous magnetic field-shock normal orientation was quasi-perpendicular or because they couple rapidly to the incident solar wind. In the downstream region they form the observed shoulder on the transmitted solar wind population. The hotter distributions are believed to be generated by the strong interaction between the solar wind and the large fraction of ions that is periodically reflected off the

shock. The lower densities in these hotter regions may be the result of pressure equalization downstream from the shock.

It has also been suggested that the strongly heated H^+ distributions seen downstream from the quasi-parallel shock and the hot, nearly isotropic distributions seen inside so-called hot diamagnetic cavities or hot flow anomalies (HFAs) are generated by essentially the same strong beam-plasma interaction [*Thomsen et al.*, 1990]. Recent computer simulations of both HFA formation and of the region upstream from the quasi-parallel bow shock suggest that the nonresonant and the resonant ion beam instabilities mediate this strong interaction. For small H^+ beam densities ($\sim$ few percent), simulations show that the solar wind and beam interact through the resonant instability and saturation occurs through pitch angle scattering of the beam, with little effect on the solar wind [*Galvez et al.*, 1990]. For the larger H^+ beam densities ($\geq 10\%$) believed to be responsible for strong ion heating at quasi-parallel shocks and in HFAs, simulations show that the interaction between the solar wind and the beam is through the non-resonant instability and both the solar wind and the beam are heated strongly [*Galvez et al.*, 1990]. These simulations used an infinite, uniform plasma and beam. When the dense beam has finite length in the simulation box, the initial interaction is primarily through the nonresonant instability, but the resonant instability eventually dominates [*Onsager et al.*, 1991]. The end result for the ions is the same: strong heating and scattering of both the solar wind and the H^+ beam.

One of the consequences of strong H^+ interaction through the nonresonant instability is strong scattering and heating of the solar wind He^{2+} distribution. Indeed, observations inside HFAs show this strong He^{2+} heating [*Galvez et al.*, 1990]. In this paper we will take the analogy between the HFAs and the quasi-parallel shocks one step further by presenting He^{2+} distributions downstream from a quasi-parallel shock that also show evidence for strong scattering. These observations support the idea that part of the quasi-parallel shock re-formation process entails the reflection of a large fraction of solar wind H^+, which then interacts strongly with the solar wind H^+, producing waves that scatter and heat the solar wind H^+ and He^{2+} distributions.

The He^{2+} observations in this paper were from the Lockheed Plasma Composition Experiment [*Shelley et al.*, 1978]. This set of mass spectrometers measured the velocity distributions of ions from mass/charge (M/Q) = 1 to 150 amu/charge in 64 mass steps and in 32 possible energy steps from near the spacecraft potential to 17.9 keV/e. The spectrometer used here pointed $5°$ below the spin (ecliptic) plane and had a field of view ranging from a high of about $\pm 20°$ at low energies to a low of about $\pm 5°$ at high energies. During the 1978 and 1979 ISEE solar wind seasons this mass spectrometer was programmed to operate in a variety of modes specifically intended for magnetosheath and solar wind studies. In the high bit rate mode of interest for this paper, the He^{2+} spectrum from 10 eV/e to 17.9 keV/e was sampled in 16 energy steps. Each energy step was maintained for slightly more than 1 spin (for 4 s), so that the He^{2+} spectrum with a $7.5°$ angular resolution in the spacecraft spin plane was completed in 64 s. A new He^{2+} spectrum was obtained approximately every 128 s with intervening time spent measuring other mass/charge ions.

Proton observations in this paper were from the joint Los Alamos /Garching Fast Plasma Experiment (FPE) on ISEE 2 [*Bame et al.*, 1978]. In one 3-s spacecraft spin, this electrostatic analyzer measured the energy-spin angle distribution of the total ion flux from 70 eV/e to 40 keV/e in 16 energy steps at each of 16 azimuths integrated over $\pm 55°$ of elevation angle relative to the ecliptic. Full two dimensional distributions were repeated every 3

s in high data rate. The FPE moments in this paper were derived under the assumption that all ions were protons.

Magnetic field measurements in this paper are from the University of California, Los Angeles, flux gate magnetometer on ISEE 1 [*Russell*, 1978]. This instrument measured the vector magnetic field 16 times a second in high data rate.

OBSERVATIONS

The bottom two panels of Figure 1 show proton and He^{2+} densities and temperatures downstream from a quasi-parallel bow shock on September 1, 1979. The proton observations for this supercritical shock (fast mode Mach number ~ 5.5) were discussed in detail by *Gosling et al.* [1989] and *Thomsen et al.* [1990] and serve as an introduction to the new He^{2+} observations in Figure 1. Although ISEE 1 and 2 were downstream from the quasi-parallel bow shock for the entire interval from 1703 to 1709:30 UT, at least two distinct regions can be identified from the proton moments. From 1703:30 to 1704:20 UT and from 1708:40 to 1709:30 UT the proton density was higher and the temperature was much lower than at other times. In these high-density, low-temperature intervals, the proton distribution had characteristics similar to those observed downstream from quasi-perpendicular shocks. In particular, it consisted of a cold core at low energies (less than ~ 1 keV/e) and a relatively hot shoulder or halo at suprathermal energies ($\sim$ few keV/e) [*Gosling et al.*, 1989; *Thomsen et al.*, 1990]. At higher energies (≥ 10 keV/e), the distribution was different from those observed at quasi-perpendicular shocks because of the presence of the "diffuse" ion population not seen in the quasi-perpendicular geometry. The diffuse ion population is a ubiquitous feature of the regions upstream and downstream from the quasi-parallel shock [e.g., *Thomsen et al.*, 1990]. In the low-density, high-temperature intervals (for example from 1706:30 to 1708:30 UT), the proton distribution was isotropic and Maxwellian-like and did not have the core and halo features seen in the high density, low temperature intervals [*Gosling et al.*, 1989; *Thomsen et al.*, 1990]. However, the hot diffuse ion population was present throughout.

Unlike the proton moments, the He^{2+} moments in the bottom panels of Figure 1 do not exhibit two distinct regions. The He^{2+} temperature was relatively constant throughout the downstream interval, and the He^{2+} density changes did not correlate with those for protons. However, the pitch angle distributions in the upper two panels of Figure 1 clearly show that the He^{2+} distribution was different in the regions of low and high proton temperatures. These distributions were obtained by computing the instantaneous pitch angle distribution in the rest frame of the total proton distribution. The bulk flow velocity from the FPE was used to determine the frame of reference for each spacecraft spin and the instantaneous magnetic field direction for each energy and angle measurement of the He^{2+} distribution was used to determine the instantaneous pitch angle in that frame. Pitch angles not measured by the instrument were interpolated and, in a few cases, extrapolated from measured values. Small dots in the upper panels show the pitch angle and velocity bins used to produce the contour plots, and contours (two per decade) are labeled by the log of the phase space density in cm^{-6} s^3. (Note that the entire energy range for the Plasma Composition Experiment is not displayed in these contour plots.) Although the ISEE 2 proton flow velocities were used for each 3-s spin to determine the frame of reference, no qualitative difference was found by using a bulk flow velocity averaged over the entire ~ 1 minute required to obtain the He^{2+} distribution.
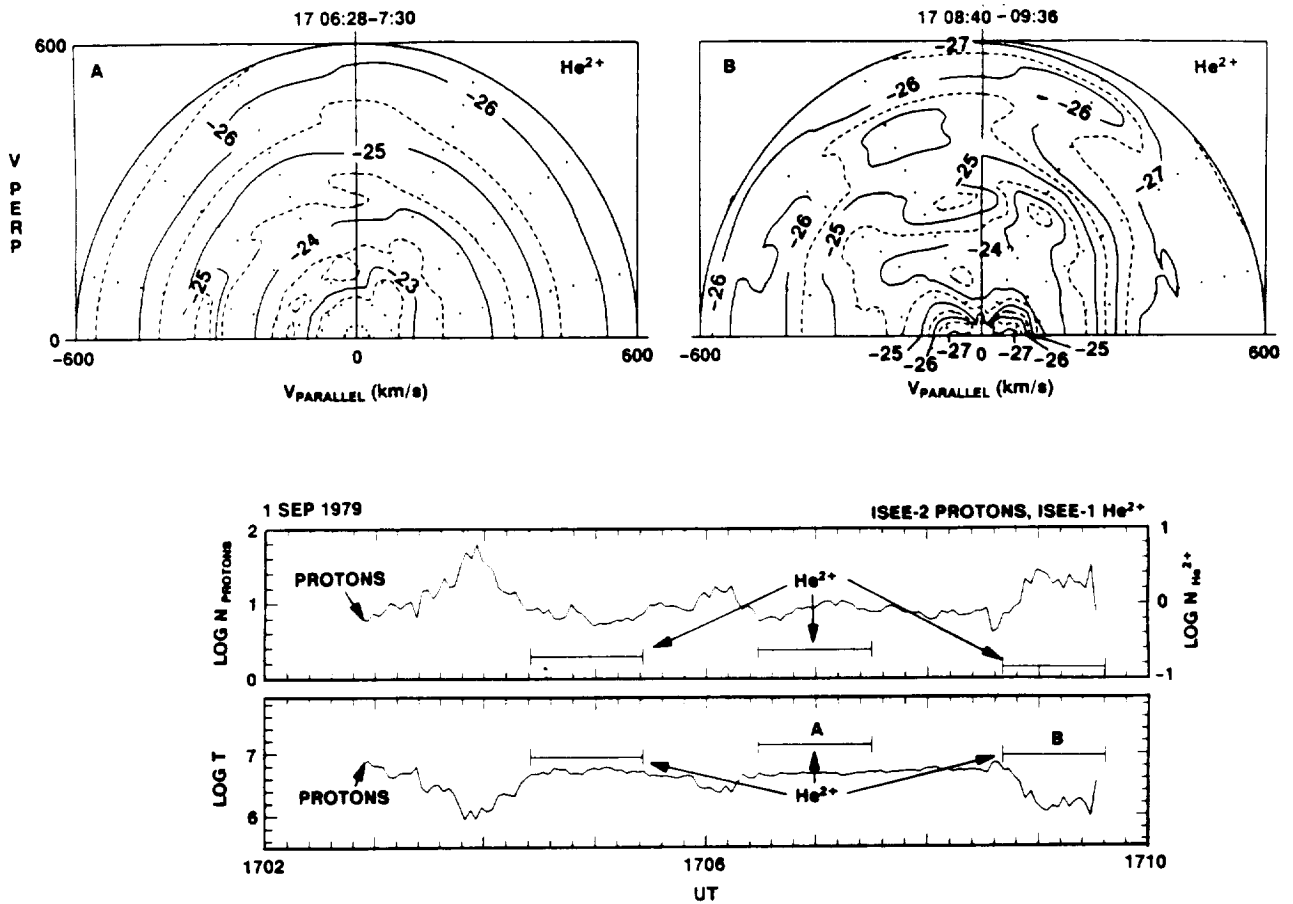
Fig. 1. Proton and He²⁺ moments downstream from a quasi-parallel bow shock on September 1, 1979 (bottom two panels), and He²⁺ pitch angle distributions (in cm⁻⁶ s³) in the rest frame of the proton bulk flow (top two panels). The He²⁺ heating downstream from the shock is independent of the proton heating. However, the distributions associated with the high proton temperatures are Maxwellianlike and isotropic (A), and the distributions associated with low proton temperatures are shell-like and anisotropic (B).

Distribution A in Figure 1 was taken during an extended interval when the proton temperature was high. This He²⁺ distribution is nearly isotropic in the proton frame of reference. The other He²⁺ distribution from the high proton temperature interval (from 1704:24 to 1705:24 UT, not shown) was qualitatively similar to distribution A. Distribution B in Figure 1 was taken during a low proton temperature interval. This He²⁺ distribution is in the form of a partially filled shell centered approximately on the proton flow velocity with shell radius ~200 km/s. Note the "hole" in velocity space centered at zero where the phase space density decreases from 10⁻²⁴ to 10⁻²⁷ cm⁻⁶ s³. This shell distribution is clearly not isotropic and very different from distribution A.

To emphasize further the differences in these two distributions, Figure 2 shows the phase space density summed over all measured pitch angles versus velocity in the proton rest frame for the same two intervals A and B in Figure 1. This time, however, the full energy range of the Plasma Composition Experiment is shown. Dashed curves in this figure show the one count per sample level. The uniform nature of distribution A extends from near zero velocity to about 800 km/s. The shell structure of distribution B is clearly seen in the right-hand panel by the decrease in phase space density below about 50 km/s. In addition, there is a shoulder on distribution B above about 300 km/s and another break at about

500 km/s, where the suprathermal and more energetic parts of the distribution meet.

Although distributions A and B in Figures 1 and 2 are considerably different from one another, they have nearly the same temperature as evidenced by the moments in the bottom panel of Figure 1. By temperature we mean here the average of the parallel and perpendicular temperatures derived from the second moment of the velocity space distribution. Another way to determine the temperature for the nearly isotropic distribution (A in Figure 2) is to fit the velocity distribution below ~800 km/s with a Maxwellian. This will not produce a meaningful result for the shell-like distribution (B in Figure 2) because it is clearly non-Maxwellian. However, the temperature of this distribution can be approximated by assuming that the thermal speed is the radius of the shell (~200 km/s from Figure 2).

Table 1 shows the He²⁺ temperatures computed from the second moment of the distributions as well as those determined from Maxwellian fits and the radius of the shell. Upstream He²⁺ temperatures were determined by fitting the solar wind distribution along the flow direction with a Maxwellian. The upstream proton temperature in Table 1 is from the Los Alamos Solar Wind Experiment [Bame et al., 1978], while the downstream proton temperatures are from the Los Alamos/Garching FPE. The up-
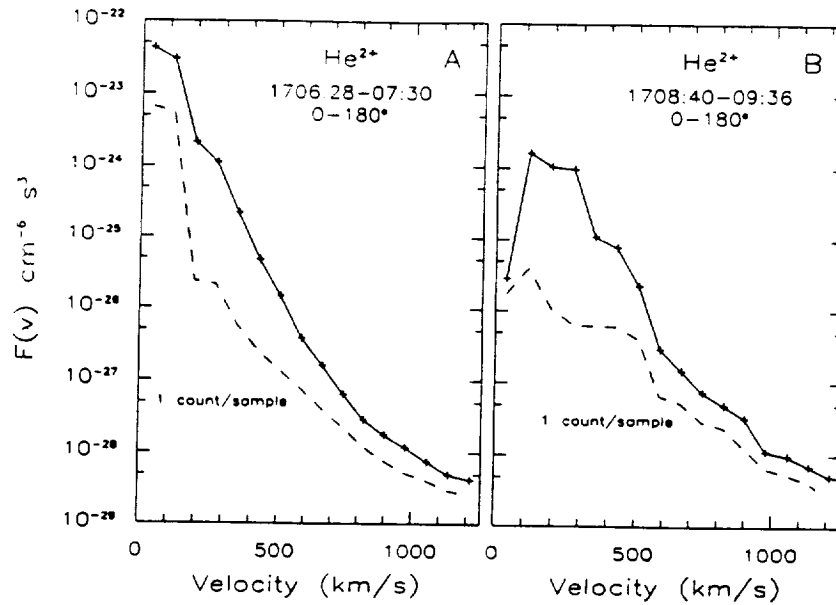
Fig. 2. Velocity distributions for He^{2+} summed over all measured pitch angles for two intervals A and B in Figure 1 downstream from the quasi-parallel shock. Distribution A, associated with high proton temperatures, is Maxwellianlike from near zero to 800 km/s. Distribution B, associated with low proton temperatures, is shell-like with a shell radius of ~200 km/s.

stream temperature ratio in Table 1 is somewhat smaller than the average ratio of 4 in the solar wind [e.g., *Neugebauer*, 1981]. To our knowledge the downstream He^{2+} temperatures and He^{2+} to proton ratios listed in Table 1 are the first reported downstream from the Earth's quasi-parallel shock. For this particular shock the He^{2+} heating appears to be independent of the proton heating. However, the He^{2+} to proton temperature ratio remained roughly constant across the shock if all three measurements are averaged. Table 1 also shows that the moment and fitting methods of determining the He^{2+} temperature produce the same results. This indicates that the hot isotropic distribution A in Figure 1 is well approximated by a Maxwellian from ~0 to ~800 km/s (with correlation coefficient R^2=0.95) and the temperature of the shell distribution B in Figure 1 is essentially determined by the shell radius.

DISCUSSION

In this paper we presented what we believe are the first measurements of the temperature change for He^{2+} across a quasi-parallel bow shock. On average, the He^{2+} distribution and proton distribution maintain their temperature ratio across the quasi-parallel shock.

Although the He^{2+} temperature increase across the shock appears to be roughly constant on average, the He^{2+} distribution observed in the high-density, low-temperature proton region is significantly different from those observed in the low-density, high-temperature proton regions (Figure 1).

In the low-temperature, high-density proton region the He^{2+} distribution (distribution B in Figures 1 and 2) resembles a partially filled shell centered approximately on the proton flow velocity with shell radius ~200 km/s. This shell-like distribution is similar to those observed in the quasi-perpendicular geometry [*Fuselier et al.*, 1988]. In the quasi-perpendicular geometry the formation of a downstream He^{2+} (or other solar wind heavy ion) shell distribution is believed to occur as follows [e.g., *Fuselier et al.*, 1988]: In the solar wind the H^+ and He^{2+} distributions have the same bulk velocity. Across the shock, both distributions are retarded by the same cross-shock electrostatic potential difference. By virtue of its larger M/Q, He^{2+} is decelerated less than H^+ and is initially flowing faster than H^+ in the downstream region. Pitch angle scattering of the He^{2+} distribution by waves in the downstream region eventually produces a shell centered on the H^+ bulk flow velocity with shell radius approximately equal to the initial velocity difference between He^{2+} and H^+ just downstream from the shock.

TABLE 1. Temperatures for September 1, 1979, Quasi-Parallel Shock

Approximate Center Time, UT	T_{He} Moment	T_{He} Fit	T_P Moment	T_{He}/T_P Moment	T_{He}/T_P Fit
1710 (upstream)*	–	2.6×10^5	9.5×10^4	–	2.8
1705 (downstream)	9.0×10^6	9.6×10^6	5.5×10^6	1.6	1.7
1707 (downstream)(A)	1.4×10^7	1.4×10^7	4.8×10^6	2.9	2.9
1709 (downstream)(B)	9.4×10^6	~1×10^7†	2.5×10^6	3.8	3.9

*Upstream proton temperatures are from the Los Alamos Solar Wind Experiment on ISEE 1. He^{2+} temperatures are from the Plasma Composition Experiment.

†Converting a shell radius of 200 km/s into a temperature.

Distribution B in Figures 1 and 2 also shows a shoulder above about 300 km/s. In analogy with a similar shoulder seen on proton distributions taken at the same time [see *Gosling et al.*, 1989, Figure 7] the shoulder on the He^{2+} distribution may be evidence for specularly reflected He^{2+} ions that have returned to the downstream region. Recently, specularly reflected He^{2+} was reported in the region just upstream from some quasi-parallel shocks [*Fuselier et al.*, 1990]. Like their proton counterpart, these ions may return to the shock and be transmitted into the downstream region to form the shoulder seen in Figures 1 and 2. A similar shoulder has also been seen on He^{2+} distributions downstream from quasi-perpendicular shocks [*Shelley et al.*, 1976; *Peterson et al.*, 1979; *Fuselier et al.*, 1988].

The only qualitative difference between distribution B in Figure 2 and the distributions seen downstream from quasi-perpendicular shocks is the presence of He^{2+} from ~800 km/s to 1200 km/s, the full range of the instrument. The presence of this hot He^{2+} distribution is consistent with a recent study of the magnetosheath that showed a good correlation between the hot diffuse proton population seen ubiquitously downstream from the quasi-parallel bow shock and a similar hot He^{2+} population [*Fuselier et al.*, 1991]. Evidence for this hot He^{2+} distribution can also be seen in distribution A in Figure 2.

Below the velocity range corresponding to the diffuse ion distribution the He^{2+} distribution in the low-density, high-temperature proton region (A) is significantly different from that in the high-density, low-temperature proton region (B). In distribution A there is neither evidence for a shoulder at about 300 km/s nor evidence for a shell. The distribution in these high-temperature proton regions is nearly isotropic (see Figure 1, distribution A) and Maxwellianlike out to almost 800 km/s.

Nearly isotropic, Maxwellianlike He^{2+} distributions have been seen inside the so-called HFAs [*Galvez et al.*, 1990]. As discussed in the introduction, the distributions seen there are believed to be produced by strong scattering. The waves that mediate this scattering are believed to be produced by the interaction of a dense H$^+$ beam with the solar wind [*Thomsen et al.*, 1988], through either the nonresonant ion beam instability [*Galvez et al.*, 1990] or some mixture of the nonresonant and resonant instabilities [*Onsager et al.*, 1991]. The end result of this strong interaction is significant scattering of both the solar wind proton and the He^{2+} distributions.

Although the two distributions in Figure 2 are very different, they have the same temperature. In fact, Figure 1 and Table 1 suggest that the He^{2+} temperature increase for this shock is independent of the proton heating. The decoupling of proton and He^{2+} heating at the shock may indicate that the initial velocity difference between the proton and He^{2+} distribution just downstream from the shock determines the final temperature regardless of the level of proton heating. This is probably true for the region of low proton temperature (B in Figures 1 and 2) since the temperature of the He^{2+} distribution is essentially determined by the shell radius (Table 1) which itself is determined by the initial relative drift between the proton and He^{2+} distributions. This might also be the case in the regions of high proton temperature except that the shell is quickly destroyed by strong scattering.

Although we have demonstrated that the He^{2+} distributions are different in the two proton regions downstream from one quasi-parallel shock, we do not have observations downstream from the other shocks recently studied by *Thomsen et al.* [1990]. The main reasons for this are the variety of operating modes of the Plasma Composition Experiment and the time resolution of the instrument. The observations in Figure 1 are a fortuitous occurrence when the Plasma Composition Experiment was in a good mode for He^{2+}

observations and the intervals of low and high proton temperatures lasted for ~1 min. Typically, the cyclic variation between low- and high-temperatures occurs ~1 to a few proton gyroperiods (~10 s) [*Thomsen et al.*, 1990], which is much too fast for the ~1 min composition measurements. This relatively rapid variation, coupled with the fact that not all operating modes sampled He^{2+} often enough, makes a survey of quasi-parallel shocks with this composition instrument very difficult.

In summary, we interpret the new He^{2+} observations in this paper as follows. In the cooler, more dense proton regions downstream from the quasi-parallel shock, the core and shoulder proton distributions and the shell-like and shoulder He^{2+} distributions are most likely formed by essentially the same processes that form these distributions at quasi-perpendicular shocks. Namely, the core proton distribution is directly transmitted solar wind protons, the shell He^{2+} distribution arises from a velocity difference between the He^{2+} and proton distributions in the downstream region followed by pitch angle scattering in the proton rest frame, and the shoulders on both the proton and the He^{2+} distributions are initially reflected solar wind ions that have returned to the shock and entered the downstream region. For the hotter, less dense proton regions, either quite different mechanisms must operate than those in the quasi-perpendicular geometry or both protons and He^{2+} must experience strong scattering and energy diffusion. This scattering may result from waves produced through a strong interaction between the incident solar wind and a relatively dense reflected proton beam. The relative constancy of the downstream He^{2+} temperature suggests that a difference in the level of scattering and energy diffusion may indeed be the principal cause of the differences in the observed He^{2+} distributions.

REFERENCES

Bame, S. J., J. R. Asbridge, H. E. Felthauser, J. P. Glore, G. Paschmann, P. Hemmerich, K. Lehmann, and H. Rosenbauer, ISEE-1 and -2 fast plasma experiment and the ISEE-1 solar wind experiment, *IEEE Trans. Geosci. Electron.*, *GE-16*, 216-220, 1978.

Burgess, D., Cyclic behavior at quasi-parallel collisionless shocks, *Geophys. Res. Lett.*, *16*, 345-348, 1989.

Fuselier, S. A., E. G. Shelley, and D. M. Klumpar, AMPTE/CCE observations of shell-like He^{2+} and O^{6+} distributions in the magnetosheath, *Geophys. Res. Lett.*, *15*, 1333-1336, 1988.

Fuselier, S. A., O. W. Lennartsson, M. F. Thomsen, and C. T. Russell, Specularly reflected He^{2+} at high Mach number quasi-parallel shocks, *J. Geophys. Res.*, *95*, 4319-4325, 1990.

Fuselier, S. A., D. M. Klumpar, and E. G. Shelley, On the origins of energetic ions in the dayside magnetosheath, *J. Geophys. Res.*, *96*, 47-56, 1991.

Galvez, M., S. A. Fuselier, S. P. Gary, M. F. Thomsen, and D. Winske, Alpha particle heating in hot diamagnetic cavities, *J. Geophys. Res.*, *95*, 11,975-11,982, 1990.

Goodrich, C. C., Numerical simulations of quasi-perpendicular collisionless shocks, in *Collisionless Shocks in the Heliosphere: Reviews of Current Research, Geophys. Monogr. Ser.*, vol. 35, edited by B. T. Tsurutani and R. G. Stone, pp. 153-168, AGU, Washington, D. C., 1985.

Gosling, J. T., and A. E. Robson, Ion reflection, gyration and dissipation at supercritical shocks, in *Collisionless Shocks in the Heliosphere: Re-*

views of Current Research, Geophys. Monogr. Ser., vol. 35, edited by B. T. Tsurutani and R. G. Stone, pp. 141-152, AGU, Washington, D. C., 1985.

Gosling, J. T., M. F. Thomsen, S. J. Bame, and C. T. Russell, Ion reflection and downstream thermalization at the quasi-parallel bow shock, *J. Geophys. Res.*, *94*, 10,027-10,038, 1989.

Greenstadt, E. W., and M. M. Mellott, Variable field-to-normal angles in the shock foreshock boundary observed by ISEE 1 and 2, *Geophys. Res. Lett.*, *12*, 129-132, 1985.

Neugebauer, M., Observations of solar-wind helium, *Fundam. of Cosmic Phys.*, *7*, 131-199, 1981.

Onsager, T. G., M. F. Thomsen, J. T. Gosling, S. J. Bame, and C. T. Russell, Survey of coherent ion reflection at the quasi-parallel bow shock, *J. Geophys. Res.*, *95*, 2261-2271, 1990.

Onsager, T. G., D. Winske, and M. F. Thomsen, Interaction of a finite length ion beam with a background plasma: Reflected ions at the quasi-parallel bow shock, *J. Geophys. Res.*, *96*, 1775-1788, 1991.

Peterson, W. K., E. G. Shelley, R. D. Sharp, R. G. Johnson, J. Geiss, and H. Rosenbauer, H^+ and He^{++} in the dawnside magnetosheath, *Geophys. Res. Lett.*, *6*, 667-670, 1979.

Russell, C. T., The ISEE-1 and -2 fluxgate magnetometers, *IEEE Trans. Geosci. Electron.*, *GE-16*, 239-242, 1978.

Scholer, M., and T. Terasawa, Ion reflection and dissipation at quasi-parallel collisionless shocks, *Geophys. Res. Lett.*, *17*, 119-122, 1990.

Shelley, E. G., R. D. Sharp, and R. G. Johnson, He^{2+} and H^+ flux measurements in the dayside cusp: Estimates of convection electric field, *J. Geophys. Res.*, *81*, 2363-2370, 1976.

Shelley, E. G., R. D. Sharp, R. G. Johnson, J. Geiss, P. Eberhardt, H. Balsiger, G. Haerendel, and H. Rosenbauer, Plasma composition experiment on ISEE-A, *IEEE Trans. Geosci. Electron.*, *GE-16*, 266-270, 1978.

Thomas, V., D. Winske, and N. Omidi, Reforming supercritical quasi-parallel shocks, 1, One- and two-dimensional simulations, *J. Geophys. Res.*, *95*, 18,809-18,820, 1990.

Thomsen, M. F., J. T. Gosling, S. J. Bame, K. B. Quest, C. T. Russell, and S. A. Fuselier, On the origin of hot diamagnetic cavities near the Earth's bow shock, *J. Geophys. Res.*, *93*, 11,311-11,325, 1988.

Thomsen, M. F., J. T. Gosling, S. J. Bame, T. G. Onsager, and C. T. Russell, Two-state ion heating at quasi-parallel shocks, *J. Geophys. Res.*, *95*, 6363-6374, 1990.

S. A. Fuselier and O. W. Lennartsson, Lockheed Palo Alto Research Laboratory, Dept. 91-20, Bldg. 255, 3251 Hanover Street, Palo Alto, CA 94304.

C. T. Russell, Institute for Geophysics and Planetary Physics, University of California, Los Angeles, CA 90024.

M. F. Thomsen, Los Alamos National Laboratory, ESS-8 MS D438, Los Alamos, NM 87545.

Alpha Particle Heating in Hot Diamagnetic Cavities

Miguel Galvez

University of New Mexico, Albuquerque

Stephen A. Fuselier

Lockheed Palo Alto Research Laboratory, Palo Alto, California

S. Peter Gary, Michelle F. Thomsen, and Dan Winske

Los Alamos National Laboratory, Los Alamos, New Mexico

The heating of solar wind alpha particles in hot diamagnetic cavities (HDCs) is examined both through data analysis and computer simulation. The Lockheed Plasma Composition Experiment on ISEE 1 shows more than an order of magnitude increase in the alpha temperature between the solar wind and the HDCs, analogous to the strong solar wind proton heating evidenced in the same transition. A one-dimensional electromagnetic hybrid computer simulation is used to study alpha heating by ion/ion instabilities, where the initial condition is a cool field-aligned proton beam streaming relative to the solar wind protons and alpha particles. Low beam densities excite the proton/proton right-hand resonant instability which pitch angle scatters the beam without significantly heating the alphas. At larger beam densities, the proton/proton nonresonant instability saturates by strong trapping of all three ion components; after saturation the large amplitude magnetic fluctuations lead to stochastic scattering and heating of the ions such that the final temperatures of the alphas are typically greater than the final proton temperatures. These results provide further support to the hypothesis of Thomsen et al. (1988) that the nonresonant instability is the primary source of ion heating in hot diamagnetic cavities.

1. Introduction

Hot diamagnetic cavities (HDCs) are local phenomena that occur in the solar wind at and near the Earth's bow shock. They have been identified by *Schwartz et al.* [1985, 1988], *Thomsen et al.* [1986, 1988], *Woolliscroft et al.* [1986], and *Paschmann et al.* [1988] from data obtained from both the International Sun Earth Explorers (ISEE) and the Active Magnetospheric Particle Tracer Explorers (AMPTE) spacecraft. The HDCs are characterized by several intrinsic properties: (1) ion and electron temperatures well above those in the ambient solar wind and internal pressure higher than the solar wind; (2) plasma flow significantly slowed and deflected relative to the solar wind; (3) magnetic field and plasma density which are at or below the ambient solar wind level; and (4) occurrence within the ion foreshock or at the ion foreshock boundary. Further, HDCs tend to occur at transitions between the quasi-perpendicular and quasi-parallel shock geometries and several of them appear to be associated with episodes in which there are reflected solar wind ions.

Thomsen et al. [1988] and *Thomas and Brecht* [1988] have hypothesized that HDCs are formed when the bow shock reflects an abnormally high fraction of incident solar wind ions, perhaps due to a sudden change in the upstream magnetic field direction. The flow of this high-density reflected ion beam through the solar wind ions then gives rise to an

electromagnetic ion/ion instability which, in turn, couples the two ion components and produces the slowed, deflected, hot, expanding plasma of the HDC. *Onsager et al.* [1990] have recently subjected this hypothesis to an observational test and have concluded that the ion/ion relative streaming energy is sufficient to account for the measured proton temperature in most, but not all, of the HDCs surveyed.

A counterstreaming ion configuration can excite several different types of electromagnetic instabilities [*Gary et al.*, 1984]. Linear theory predicts that two relatively cool, Maxwellian-like ion components streaming relative to one another and parallel to a uniform background magnetic field are likely to excite one or both of two electromagnetic ion/ion instabilities: the right-hand resonant instability has the lower threshold and larger growth rate if one ion component is much less dense than the other, whereas the nonresonant instability has both the lower threshold and larger growth rate if the two ion components have densities that differ by less than an order of magnitude [e.g., *Winske and Gary*, 1986]. *Thomas and Brecht* [1988] have modelled the formation of HDCs through simulations of the ion/ion right-hand resonant instability, which primarily pitch-angle scatters the ions of the more tenuous or beam component and usually produces a cold core/hot halo type of ion distribution [*Winske and Leroy*, 1984]. In contrast, *Thomsen et al.* [1988] have argued that the large beam densities needed to produce the large flow deflections and slowing of the HDCs favor the ion/ion nonresonant growing mode. The nonresonant mode is further implicated by the observed strong bulk heating of the ions, implying a more complete coupling of both energy and momentum between the beam and solar wind plasma [Winske and Leroy, 1984].

Alpha particle heating provides another possible discriminant between the two types of instabilities. Typical alpha particle densities in the solar wind are approximately 4% of the proton number density. Because their mass-to-charge ratio is twice as large as that of protons, alphas do not cyclotron resonate with fluctuations of the same wavenumber as the protons. Hence, alpha particles, like other non-resonant components, should be relatively unaffected by a proton-resonant instability [e.g., *Gary et al.*, 1988]. On the other hand, all ion components should respond substantially to enhanced fluctuations from the ion/ion nonresonant instability.

This paper describes two new results concerning alpha particles in hot diamagnetic cavities. First, we report new observations of alphas observed by the ISEE spacecraft which show that, within HDCs, the alpha particles are very hot, adding further support to the hypothesis of *Thomsen et al.* Second, we describe computer simulations of both the ion/ion nonresonant and right-hand resonant instabilities which demonstrate significant differences in the alpha response to the two modes and, in particular, provide still further evidence that the nonresonant instability is the primary coupling mechanism in the formation of HDCs.

The theoretical and computational work of section 3 considers a homogeneous, charge neutral plasma with a uniform magnetic field $\mathbf{B}_o = \hat{z}B_o$ with $B_o > 0$ and no ambient electric field. The following symbols are defined for the jth component: the plasma frequency, $\omega_j \equiv \left(4\pi n_j e_j^2/m_j\right)^{1/2}$; the cyclotron frequency, $\Omega_j \equiv e_j B/m_j c$; the thermal speed $v_j \equiv (T_j/m_j)^{1/2}$; and beta $\beta_j \equiv 8\pi n_e T_j/B_o^2$ where n_o is the total electron density. The Alfvén speed is defined in terms of the total electron density and the proton mass: $v_A = B_o/\sqrt{4\pi n_o m_p}$. The Boltzmann factor k_B is understood to multiply the temperatures T_j throughout this paper, and $\mathbf{V}_{oj}$ represents the average magnetic-field aligned velocity of the jth component. As in Gary et al. [1984] we define the argument of the plasma dispersion function in the linear dispersion equation to be $\zeta_j^{\pm} = (\omega - \mathbf{k} \cdot \mathbf{v}_{oj} \pm \Omega_j)/\sqrt{2}|k_z|v_j$.

2. OBSERVATIONS

The alpha particle observations in this paper are from the Lockheed Plasma Composition Experiment [Shelley et al., 1978]. This set of mass spectrometers measures the velocity distributions of ions from mass/charge $M/Q = 1$ to greater than 150 amu/charge in 64 mass steps and in 32 possible energy steps from near the spacecraft potential to 17.4 keV/e. The data used in this paper are from the spectrometer which points 5° below the spin (ecliptic) plane and has a field of view ranging from a high of about ±20° at low energies to a low of about ±5° at high energies. Although primarily designed to study the composition of the magnetosphere, during the 1978 and 1979 ISEE solar wind seasons this mass spectrometer was programmed to operate in a variety of modes specifically intended for magnetosheath and solar wind studies. However, not all modes provided the time resolution needed to resolve the alpha distribution inside HDCs.

The proton and electron observations used here were obtained with the Los Alamos/Garching Fast Plasma Experiments (FPE's) and the Los Alamos Solar Wind Experiment on ISEE-1 and -2 [Bame et al., 1978]. These observations have previously been described in Thomsen et al. [1986; 1988].

For two of the published HDC events from the ISEE spacecraft, the Plasma Composition Experiment was in a mode that adequately resolved the alpha distribution during these events. These two events occurred on September 3, 1978 (see *Thomsen et al.* [1986], Fig. 2), and September 1, 1979 (see *Thomsen et al.* [1988], Fig. 1).

Figure 1 shows observations from the hot diamagnetic cavity event of September 3, 1978. The electron moments throughout are derived from the ISEE-2 Fast Plasma Experiment, as is the proton temperature within the HDC, while the proton temperature in the solar wind is from the ISEE-1 Solar Wind Experiment. The electron flow speed is shown here in order that we may use continuous data from one instrument (the FPE) to illustrate the relative variation between the solar wind and the HDC; the proton flow speed measured by the FPE in the HDC and by the Solar Wind Experiment in the solar wind shows a similar variation. The hot diamagnetic cavity from 1250:30 to 1253 UT has the low density, very high proton and electron temperatures, and reduced flow speed characteristic of other HDCs (see Thomsen et al. [1986]).

Figure 1 also illustrates the alpha moments derived from the Plasma Composition Experiment on ISEE-1. Comparison of the moments from the two spacecraft is justified because the propagation delay between the spacecraft was only 2.5 s (see Thomsen et al. [1986, Figure 14]), which is much shorter than the 30 s time resolution of the Plasma Composition Experiment. Just before the HDC event (1249:39-1250:28), the solar wind alpha to proton density ratio was 3.6%, the alpha and electron flow speeds were similar, and the alpha to proton temperature ratio was 4.5, all typical values for the solar wind (e.g. Neugebauer [1981]). Inside the diamagnetic cavity, the alpha to proton density ratio ranged between 2% and 4%, the alpha and electron flow speeds were comparable, and the alpha and proton temperatures were nearly equal. Within the HDC all three species exhibited strong heating, and, in particular, the alpha and proton temperatures were approximately equal.

Figure 2 further illustrates this strong alpha particle heating. The solid dots show a cut through the solar wind alpha distribution along the solar wind flow velocity direction, whereas the open circles illustrate a one-dimensional plot of the isotropic alpha distribution within the diamagnetic cavity. The abscissa is the square of the difference in the measured velocity and the bulk flow velocity. The solid line through the HDC data points shows a least squares fit to the distribution at the lowest five measured velocities. Clearly, this temperature is much higher than that for the solar wind distribution. The distribution inside the cavity also a shows a shoulder starting at about $\Delta V^2 = 2.5 \times 10^5$ (km/s)^2, i.e., at about $\Delta V = 500$ km/s. Because of this shoulder on the distribution, the total temperature of the distribution shown in Figure 1 is about 50% higher than the temperature for the lower velocity part of the distribution (or "core"). A similar shoulder at a much higher velocity has been seen on proton distributions from other hot diamagnetic cavity events (see Fig. 10 of Thomsen et al. [1986]) and is a feature seen on other alpha distributions measured inside HDC events.

Figure 3 shows the proton, electron, and alpha moments from the hot diamagnetic cavity event on September 1, 1979. The format is the same as that for Figure 1. In the solar wind, just after the HDC event (1752:39-1753:41 UT), the alpha concentration relative to protons was 3.8%, the alpha and electron flow speeds were nearly equal, and the alpha to

78 Sept 3 ISEE-1,2
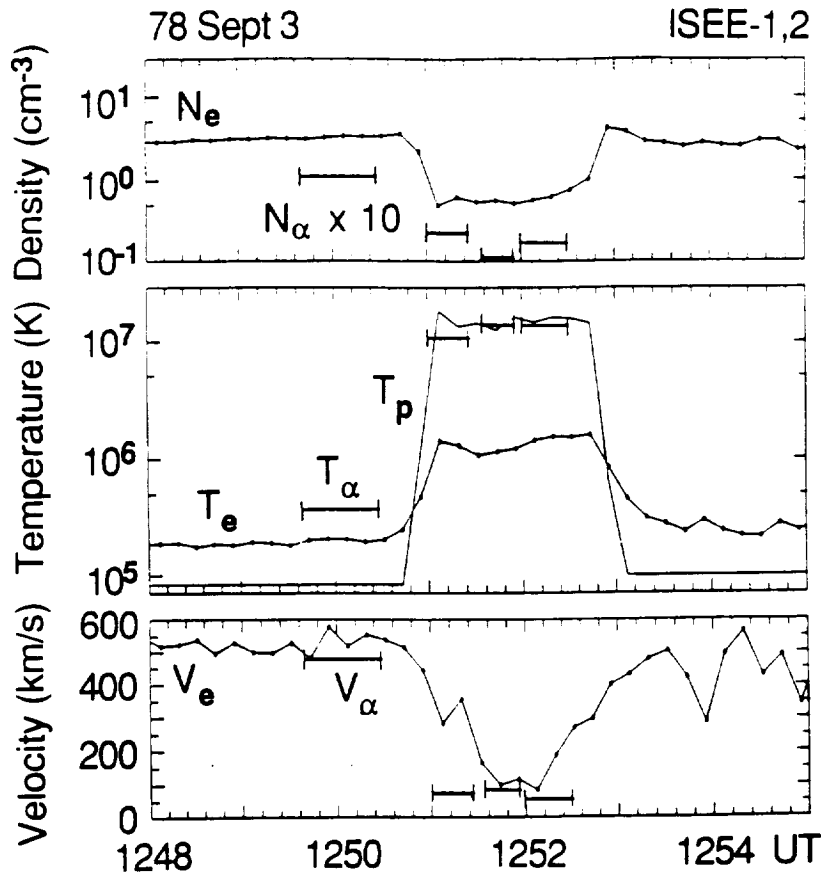
Fig. 1. Densities, temperatures, and velocities of plasma components as observed from ISEE on September 3, 1978. The undotted solid line represents the proton temperature, the dotted solid lines represent electron quantities and the horizontal segments correspond to alpha particle properties.
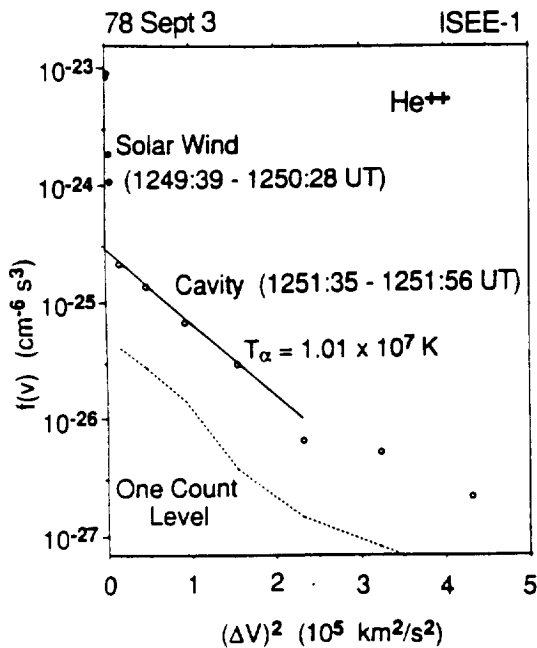
Fig. 2. The alpha particle velocity distribution function at two times on September 3, 1978. The solid dots represent a cut through the solar wind alpha distribution function in the direction of the solar wind velocity, whereas the open circles correspond to a one-dimensional plot of the isotropic alpha distribution within the HDC.

proton temperature ratio was 1.1. With the exception of the temperature ratio, the alpha moments were again typical of the solar wind. Inside the cavity, the alpha concentration decreased, the flow speeds remained similar and the all three components are once again strongly heated. In contrast to Figure 1, however, here the alpha particles have higher temperatures than the protons.

Cuts in the alpha distribution for the September 1, 1979 event (not shown here) show that the alpha heating is largely in the bulk of the distribution. These cuts also show shoulders on the alpha distribution above 2.5×10^5 $(km/s)^2$ similar to the one shown in Figure 2 for the September 3, 1978 event.

Observations in Figures 1, 2, and 3 show that the bulk of the solar wind alpha distribution is strongly heated inside Hot Diamagnetic Cavity events. In both events, the alpha distribution inside the cavity is characterized by a hot Maxwellian-like "core" with a shoulder at $\Delta V=500$ km/s. However, Figures 1 and 3 also show that the amount of alpha heating compared to that of the protons was very different for the two events.

3. COMPUTER SIMULATIONS

This section describes the results of computer simulations which have been run to study the source of alpha particle heating described in section 2. We use the hybrid simulation code of *Winske and Leroy* [1984; 1985], in which the ions are
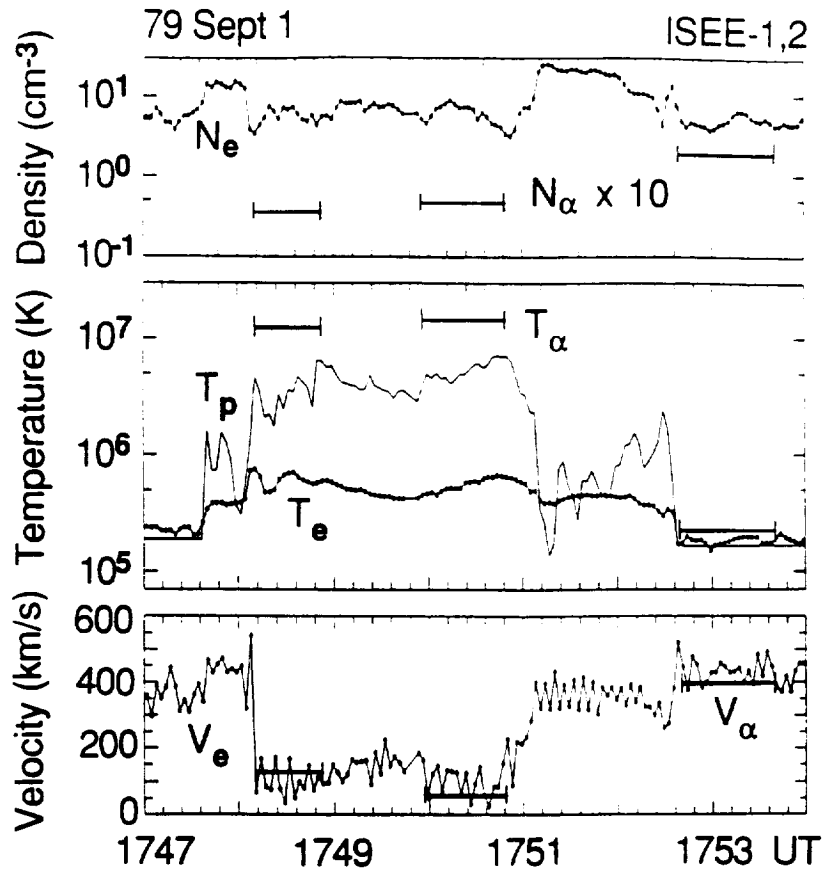
Fig. 3. Densities, temperatures, and velocities of plasma components as observed from ISEE on September 1, 1979. The undotted solid line represents proton temperatures, the dotted solid lines represent electron quantities and the horizontal segments correspond to alpha particle properties.

treated as discrete superparticles and the electrons are taken as a massless, charge-neutralizing fluid. The zero current condition in the direction of B_o, $\sum_j n_j e_j v_{oj} = 0$, holds throughout the simulation. The interactions between the ions and the electric and magnetic fields are calculated self-consistently. The simulation is one-dimensional in space but the particle velocities and electromagnetic fields are three-dimensional vectors. Periodic boundary conditions for both particles and fields are used, consistent with the assumption that the initial conditions of the simulation correspond to the presence of a very long ion beam.

We assume three ion components: the solar wind protons, the reflected proton beam, and the solar wind alpha particles. We designate these components as the core (subscript c), the beam (subscript b), and the alphas (subscript a) respectively. Each ion component has constant density and at $t = 0$ is distributed uniformly in space with a Maxwellian velocity distribution. The average initial velocity of the solar wind protons and alphas is zero in the frame of the simulation; the beam protons have an initial average velocity v_{ob} parallel to the background magnetic field. We use an equal number of simulated particles (typically, 15000) to represent each ion component. The simulations are done in the solar wind rest frame. The time step $\Omega_i \Delta t$, is usually taken to be 0.05, small enough to follow ion gyro motion accurately and keep the speed of the particles along the computation grid much less than one cell per time step. We only consider the case $k \times B_o = 0$, because the maximum growth rate of the

instabilities of interest lies at this angle of propagation [Gary et al., 1984]. Similar simulations with wavevectors oblique to B_o show no important differences with the magnetic-field-aligned simulations described here [e.g., Winske and Quest, 1986].

Table 1 shows two sets of physical (i.e. dimensional) parameters based on the ISEE measurements and given in the spacecraft frame. These parameters represent initial solar wind conditions prior to the formation of the two IIDCs described in section 2; in particular, we assume that the initial beam speed is given by $v_{ob} - v_{oc} = 1.5 v_{sw}$. For both dates we assume that all ion parameters except the beam density are held fixed; we then consider two different beam densities with the electron density and average flow speed adjusted to maintain charge neutrality and the zero current condition. Table 2 then states these parameters as they have been converted to simulation (i.e. dimensionless) parameters. In this table, the parameters are given in the solar wind frame, since this is the frame of the simulations. We here describe in detail the results of our simulations for the September 1, 1979 event; for these parameters we denote the simulation of the tenuous beam as Run 1, and designate the simulation of the relatively large n_b as Run 2.

As prelude to our simulations, we have used an electromagnetic linear Vlasov dispersion code to determine dispersion properties of the instabilities of interest for both events with the two hypothesized beam densities as shown in Table 2. In agreement with Winske and Gary [1986] we have

TABLE 1: Dimensional Parameters

Component Species	c Proton	b Proton	α He^{++}	e Electron
September 1, 1979, 1747 to 1752				
n_j (cm^{-3})	5.5	(0.05,1.0)	0.20	(5.95,6.9)
$T_{\parallel j}$ (eV)	5	5	20	20
$T_{\perp j}$ (eV)	5	5	20	20
v_{oj} (km/s)	−420	210	−420	(−411.7,328.7)
September 3, 1978, 1251 to 1253				
n_j (cm^{-3})	3.0	(0.05,1.0)	0.1	(3.25,4.2)
$T_{\parallel j}$ (eV)	8	8	32	14
$T_{\perp j}$ (eV)	8	8	32	14
v_{oj} (km/sec)	−470	235	−470	(−459.2,−302.1)

$B_o = 5.0 \times 10^{-5}$ G for both dates; $v_A = (45.1, 41.9)$ km/s for September 1, 1979, and $v_A = (61.0,53.7)$ km/s for September 3, 1978. Note that the electron drift speed is chosen so as to satisfy the zero current condition, and all velocities are given in the spacecraft frame.

found that the proton/proton right-hand resonant instability (characterized by $|\zeta_b^+| \lesssim 1$) has the faster growth rate at $n_b \ll n_c$, but that the proton/proton nonresonant mode with $|\zeta_b^-| \gg 1$ develops the larger growth rate as n_b/n_c increases.

For Run 1, linear theory predicts that the wavelength of the most unstable resonant mode ($|\zeta_b^+| \simeq 1$) is $\lambda \omega_i/c \simeq 83$, while for the nonresonant mode ($|\zeta_b^-| \simeq 64$) $\lambda \omega_i/c \simeq 191$. In Run 2, the fastest growing wavelength of the resonant instability is $\lambda \omega_i/c \simeq 56$ and for the nonresonant mode, $\lambda \omega_i/c \simeq 8$. Thus, by choosing the length of the simulation box to be $L\omega_i/c = 120$ for Run 1 and $L\omega_i/c = 32$ for Run 2 we exclude the longer wavelength mode in both cases. So the resonant mode should be simulated in Run 1 while in Run 2 the nonresonant mode can be simulated without ambiguities. A third simulation with the physical parameters of Run 2 was carried out, but with the length of the simulation box increased to include the most unstable waves of the

resonant instability as well as those of the nonresonant instability. The results of this simulation look very similar to those of Run 2, confirming that the resonant instability does not appreciably contribute to the final state of the system under these conditions.

Figure 4 shows the temporal evolution of $|\delta B|^2/B_o^2$ for Run 1 (left frame) and Run 2 (right frame). At early times, the fluctuations are excited by the beam and the wave amplitude grows with time. The instability in Run 2 has a larger growth rate and saturates at relatively short times, $\Omega_i t = 10.2$, compared with Run 1 that saturates at $\Omega_i t = 82$. As shown by this figure, the nonresonant waves reach a larger amplitude, consistent with the idea that a larger wave energy density is needed to disrupt the beam because the efficiency of the nonresonant process is much less.
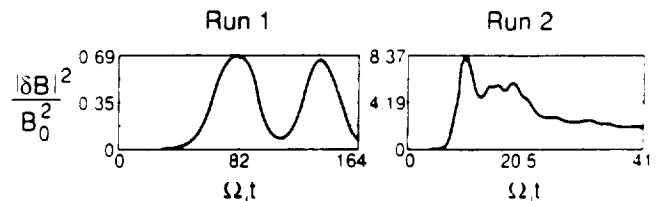
Fig. 4. The temporal evolution of the fluctuating magnetic energy of the system normalized to the initial magnetic energy $|\delta B^2|/B_o^2$. Here, as in Figs. 5 through 7, the left panels depict results from the computer simulation labeled Run 1, whereas the right panels show results from Run 2.

Figure 5 shows the phase of the fluctuating magnetic field $\phi_B = \tan^{-1}(\delta B_y/\delta B_x)$ (solid lines) and the velocity phases of the beam protons $\phi_v = \tan^{-1}(v_y/v_x)$ (dots) as functions of the spatial coordinate z at times when the waves bunch the particles. The left frame, representing Run 1, corresponds to a fluctuation with left-hand sense of spatial rotation with respect to k. The right-hand frame, representing Run 2, shows waves with a right-hand sense of spatial rotation with respect to the wavevector. In our simulations, the magnetic field and the beam drift velocity are parallel,

Table 2: Dimensionless Parameters

Component Species	c Proton	b Proton	α He^{++}	e Electron
September 1, 1979, 1747 to 1752				
n_j/n_e	(0.924,0.797)	(0.008,0.145)	(0.034,0.029)	1.00
$T_{\parallel j}/T_{\parallel 1}$	1.0	1.0	4.0	4.0
$T_{\perp j}/T_{\parallel j}$	1.0	1.0	1.0	1.0
v_{oj}/v_A	0	(14.0,15.0)	0	(0.12,2.18)
September 3, 1978, 1251 to 1253				
n_j/n_e	(0.923,0.714)	(0.015,0.238)	(0.031,0.024)	1.00
$T_{\parallel j}/T_{\parallel 1}$	1.0	1.0	4.0	1.75
$T_{\perp j}/T_{\parallel j}$	1.0	1.0	1.0	1.0
v_{oj}/v_A	0	(11.6,13.1)	0	(0.18,3.12)

$\omega_p/\Omega_p = (6684,7197)$ and $\beta_c = (0.48,0.56)$ for September 1, 1979, and $\omega_p/\Omega_p = (4940,5615)$ and $\beta_c = (0.42,0.54)$ for September 3, 1978. Note that the electron drift speed is chosen so as to satisfy the zero current condition and all velocities are given in the rest frame of the proton core component.
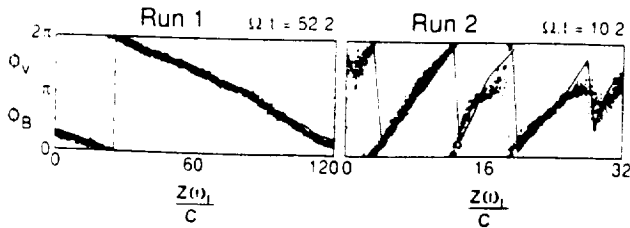
Fig. 5. The phase of the magnetic field ϕ_B (solid line) and the velocity phases ϕ_v of the beam protons (dots) as functions of the spatial coordinate z for Run 1 and Run 2 at the stated times.

so that linear dispersion theory predicts that the right-hand resonant instability has a left-hand sense of rotation and the nonresonant instability has a right-hand rotation. This result confirms that, during growth to saturation, Run 1 and Run 2 correspond to the proton/proton right-hand resonant and proton/proton nonresonant instabilities, respectively.

In both panels of Figure 5, the phases of the beam protons are tightly bunched at each value of z, implying that the fields have phase bunched the beam [Hoshino and Terasawa, 1985]. Furthermore, the particle phases and the phase of the fluctuating fields are similar for all z in both runs, indicating that the phase bunching is due to magnetic trapping and that the fields are near or at saturation [Hoshino and Terasawa, 1985; Gary et al., 1986].

The effects that both instabilities have on the reduced distribution functions of the three ion components are shown in Figure 6. The top panels show the proton distribution function (the core plus the beam) at time $t = 0$. Since $n_b/n_c < 0.01$ in Run 1 the distribution function of the beam can not be resolved and its position has been marked by an arrow. The middle and bottom panels of this figure show the pro-

ton and alpha distributions, respectively, at the end of our simulation runs, where the particles are completely wave-scattered and temperature changes are most evident. This may be the case during the HDC events where the beginning of the wave-particle interaction can not be determined and only the final results are observed.

At post-saturation times, the fluctuating fields maintain relatively large amplitudes and the phase-bunched ion components are stochastically scattered to thermal-like distributions similar to those described in section 2. The fluctuating fields which result from growth of the right-hand resonant instability interact strongly only with the proton beam; neither the proton core (middle left panel) nor the alphas (bottom left panel) show much heating. In contrast, the fields due to growth of the nonresonant instability in Run 2 clearly produce significant heating of both proton components (right middle panel) as well as of the alphas (right bottom panel).

Figure 7 represents the temporal evolution of the ion temperatures for Run 1 and Run 2. The top, middle, and bottom frames show the temperature parallel to B_o of the core, the beam, and the alpha particles respectively. The left frames show that the beam has been preferentially heated in Run 1 because this component is in resonance with the unstable waves. The other two ion components have been only weakly heated to about a factor of 1.6 times their initial temperature; the final value of $T_{\parallel b}/T_{\parallel c}$ is about 72. We recall that the initial temperatures of these two components are equal. At the end of Run 2, all three ion components have been significantly heated, $T_{\parallel b}/T_{\parallel c}$ is approximately 2.3, and $T_{\parallel \alpha}/T_{\parallel b}$ is approximately 4. The factor of two difference in temperature between the two proton components is not large enough to clearly demonstrate a two-temperature distribution in Figure 6.
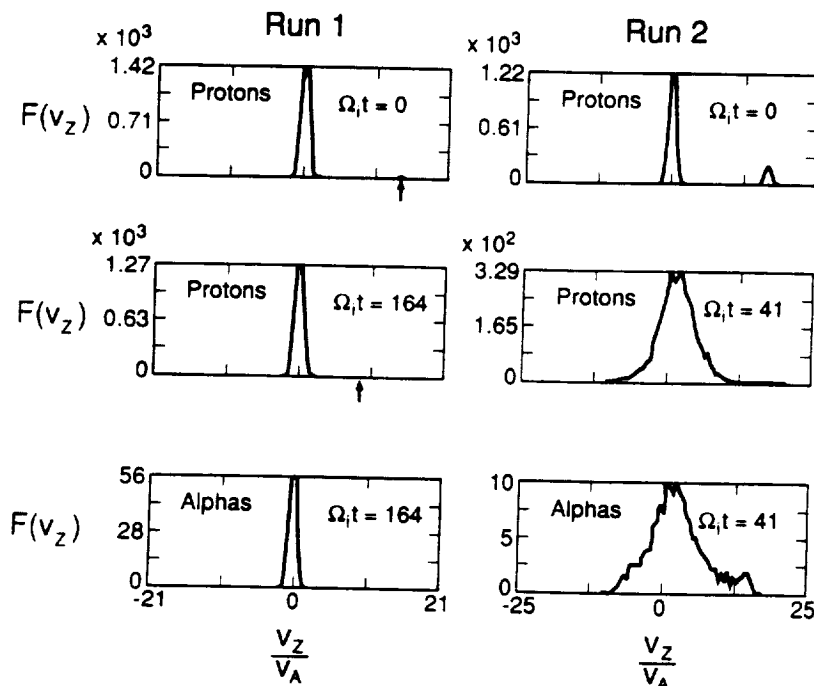
Fig. 6. The reduced proton distribution function (core plus beam) at time $t = 0$ (top panels) and at the end of our simulations (middle panels). The bottom panels show the reduced distribution function of the alpha particles at the end of the simulations.
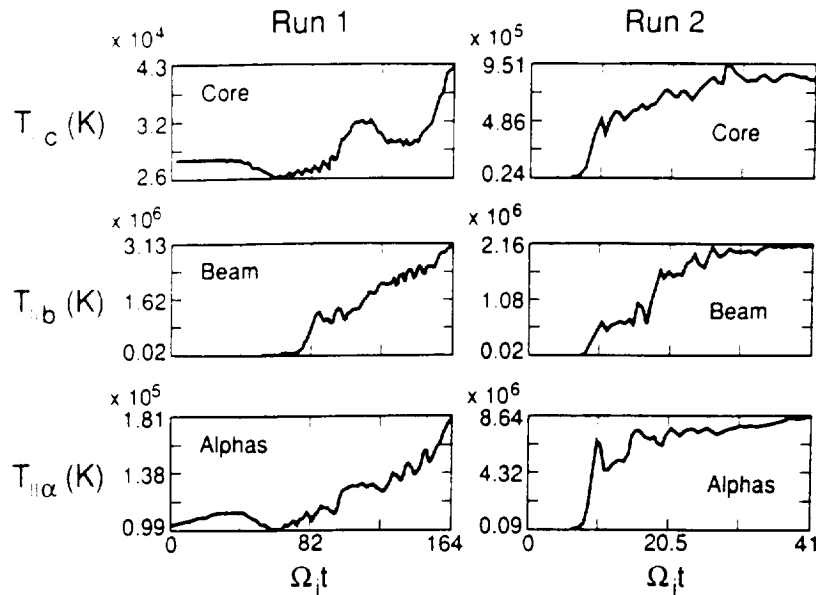
Fig. 7. The temporal evolution of the parallel temperature for the proton core (top panel), the proton beam (middle panel), and the alphas (bottom panel) for Run 1 and Run 2.

We have also carried out another simulation, Run 3, in which most parameters are similar to those of Run 2 except that the density of the beam is increased to be equal to the core density. In this case the temperature evolution for the three ion components is shown by Figure 8. This figure indicates that the ratio of final beam temperatures between this run and Run 2 is about 1.6. This means that for a denser beam the final temperature is higher, as expected, since the free energy that drives the instability is increased.
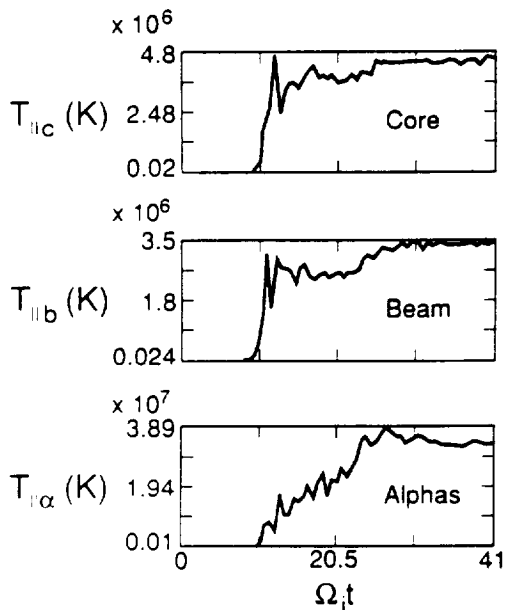
Fig. 8. The temporal evolution of the parallel temperature for the proton core (top panel), the proton beam (middle panel) and the alphas (bottom panel) for Run 3, a simulation in which the density of the beam equals the density of the core of Run 2. Here, as in Run 2, the nonresonant instability is the dominant growing mode.

At the end of Run 3, $T_{\|b}/T_{\|c} = 0.82$ and $T_{\|\alpha}/T_{\|b} = 11.1$, i.e., the core ions are heated more than the beam.

We have carried out several other simulations (not described in detail here) with somewhat different parameters to examine the generality of these results. One finding from such simulations is that the final temperature of the alpha particles is independent of their initial temperature.

The computer simulation results using the September 3, 1978 parameters from Table 2 are essentially the same as those from the September 1, 1979 event; i.e., the nonresonant instability heats the solar wind protons and alpha particles much more than the resonant instability. In this case, the final temperature ratio between the beam and the core is about 1.14, while the final alpha temperature is 0.69 times the final beam temperature.

4. SUMMARY

We have included in this paper two new results related to hot flamagnetic cavities (HDCs). The first uses data obtained from the Lockheed Plasma Composition Experiment on ISEE-1 for the September 3, 1978 and September 1, 1979 events. These new data show that within an HDC alpha particle temperatures are increased more than an order of magnitude over the alpha temperatures in the undisturbed solar wind.

Our second new result has used computer simulations to demonstrate a likely mechanism for the observed alpha heating. We have used a one-dimensional electromagnetic hybrid code to simulate the interaction of an infinitely long proton beam moving through a solar wind plasma of protons and alpha particles for conditions characteristic of the September 1, 1979 and September 3, 1978 ISEE HDC events with different assumed values of the beam density.

The simulations show that the proton/proton right-hand resonant instability, which is dominant at low beam densities, significantly heats only the beam, while the proton core and the alpha particle temperatures remain almost unchanged; i.e., the resonant instability does not heat the so-

lar wind ion components. On the other hand, at higher beam densities the proton/proton nonresonant instability dominates wave growth to saturation; after saturation, the enhanced fluctuating fields strongly heat all three ion components such that their final temperatures are comparable. The simulations also show that the final alpha temperature is independent of the initial alpha temperature and that the final temperatures for all three ion components increase when the beam density increases.

Thus we have used both observations and computer simulations of alpha particle heating to provide strong supporting evidence for the hypothesis that HDCs are the manifestation of the nonresonant ion/ion coupling between the solar wind ions and a relatively dense proton beam reflected at the bow shock. We emphasize, however, that our simulations have studied only infinitely long ion beams. Although *Thomas and Brecht* [1988] have studied the right-hand resonant instability in the presence of a finite length ion beam, a detailed comparison of the resonant and nonresonant instabilities due to a finite beam still needs to be carried out.

REFERENCES

Bame, S. J., J. R. Asbridge, H. E. Felthauser, J. P. Glore, G. Paschmann, P. Hemmerich, K. Lehmann, and H. Rosenbauer, ISEE-1 and ISEE-2 fast plasma experiment and the ISEE-1 solar wind experiment, *IEEE Trans. Geosci. Electron.*, GE-16, 216, 1978.

Gary, S. P., C. W. Smith, M. A. Lee, M. L. Goldstein, and D. W. Forslund, Electromagnetic ion beam instabilities, *Phys. Fluids*, 27, 1852, 1984; Erratum, *ibid.*, 28, 438, 1985.

Gary, S. P., C. D. Madland, D. Schriver, and D. Winske, Computer simulations of electromagnetic cool ion beam instabilities, *J. Geophys. Res.*, 91, 4188, 1986.

Gary, S. P., C. D. Madland, N. Omidi, and D. Winske, Computer simulations of two-pickup-ion instabilities in a cometary environment, *J. Geophys. Res.*, 93, 9584, 1988.

Hoshino, M., and T. Terasawa, Numerical study of the upstream wave excitation mechanism, 1. Nonlinear phase bunching of beam ions, *J. Geophys. Res.*, 90, 57, 1985.

Neugebauer, M., Observations of solar-wind helium, *Fundam. Cosmic Phys.*, 7, 131, 1981.

Onsager, T. G., M. F. Thomsen, J. T. Gosling, and S. J. Bame, Observational test of a hot diamagnetic cavity formation mechanism, *J. Geophys. Res.*, in press, 1990.

Paschmann, G., G. Haerendel, N. Sckopke, E. Möbius, H. Lühr, and C. W. Carlson, Three-dimensional plasma structures with anomalous flow directions near the Earth's bow shock, *J. Geophys. Res.*, 93, 11,279, 1988.

Schwartz, S. J., C. P. Chaloner, P. J. Christiansen, A. J. Coates, D. S. Hall, A. D. Johnstone, M. P. Gough, A. J. Norris, R. P. Rijnbeek, D. J. Southwood, and L. J. C. Woolliscroft, An active current sheet in the solar wind, *Nature*, 318, 269, 1985.

Schwartz, S. J., R. L. Kessel, C. C. Brown, L. J. C. Woolliscroft, M. W. Dunlop, C. J. Farrugia, and D. S. Hall, Active current sheets near the Earth's bow shock, *J. Geophys. Res.*, 93, 11,295, 1988.

Shelley, E. G., R. D. Sharp, R. G. Johnson, J. Geiss, P. Eberhardt, H. Balsiger, G. Haerendel, and H. Rosenbauer, Plasma composition experiment on ISEE-A, *IEEE Trans. Geosci. Electron.*, GE-16, 266, 1978.

Thomas, V. A. and S. H. Brecht, Evolution of diamagnetic cavities in the solar wind, *J. Geophys. Res.*, 93, 11,341, 1988.

Thomsen, M. F., J. T. Gosling, S. A. Fuselier, S. J. Bame, and C. T. Russell, Hot, diamagnetic cavities upstream from the Earth's bow shock, *J. Geophys. Res.*, 91, 2961, 1986.

Thomsen, M. F., J. T. Gosling, S. J. Bame, K. B. Quest, C. T. Russell, and S. A. Fuselier, On the origin of hot diamagnetic cavities near the Earth's bow shock, *J. Geophys. Res.*, 93, 11311, 1988.

Winske, D., and S. P. Gary, Electromagnetic instabilities driven by cool heavy ion beams, *J. Geophys. Res.*, 91, 6825, 1986.

Winske, D., and M. M. Leroy, Diffuse ions produced by electromagnetic ion beam instabilities, *J. Geophys. Res.*, 89, 2673, 1984.

Winske, D., and M. M. Leroy, Hybrid simulation techniques applied to the Earth's bow shock, in *Computer Simulations of Space Plasmas – Selected Lectures at the First ISSS*, edited by H. Matsumoto and T. Sato, p. 568, D. Reidel, Hingham, Mass., 1985.

Winske, D., and K. B. Quest, Electromagnetic ion beam instabilities: comparison of one- and two-dimensional simulations, *J. Geophys. Res.*, 91, 8789, 1986.

Woolliscroft, L. J. C., S. J. Schwartz, C. C. Brown, C. P. Chaloner, P. J. Christiansen, A. J. Coates, A. G. Darbyshire, M. P. Gough, D. S. Hall, A. D. Johnstone, W. A. C. Mier-Jedrzejowicz, A. J. Norris, R. Rijnbeek, and D. J. Southwood, AMPTE-UKS observations of current sheets in the solar wind, *Adv. Space Res.*, 6, 89, 1986.

M. Galvez, University of New Mexico, Albuquerque, New Mexico 87131.

S. A. Fuselier, Lockheed Palo Alto Research Laboratory, Palo Alto, California 94304.

S. P. Gary, M. F. Thomsen, and D. Winske, Los Alamos National Laboratory, Los Alamos, New Mexico 87545.

Solar control of the Earth's emission of energetic O $^+$

W. LENNARTSSON

Lockheed Missiles and Space Company Inc., Research and Development,
Palo Alto, CA 94304, U.S.A.

Abstract—Energetic (0.1–16 keV/e) O $^+$ data obtained in the Earth's plasma sheet (between 10 and 23 R_E) by an ion mass spectrometer on the ISEE-1 spacecraft are compared statistically with published data on the concurrent solar wind and IMF. The most strongly variable parameter of the plasma sheet O $^+$ is its density, which is found to be well correlated with certain solar wind parameters, especially with the solar wind flow speed and the IMF component perpendicular to the flow vector. When those two solar wind parameters are combined to form an electric field ($-\mathbf{v} \times \mathbf{B}$), both the number density and the energy density of the O $^+$ are found to vary in proportion to the square of that electric field, on average, suggesting that the emission of energetic O $^+$ ions from the Earth may be powered by that same field. Based on this and on the previously published correlation with solar activity, it is argued that the emission of O $^+$ is controlled by a combination of high-frequency (ionizing) and quasi-static (accelerating) solar electromagnetic fields.

1. INTRODUCTION

Singly charged oxygen is a variable but usually substantial component of the energetic (keV) plasmas in the magnetosphere. It is typically the dominant ion component at $L < 5$, at least in the 0.1–17 keV/e energy range (e.g. LENNARTSSON and SHARP, 1982), and the second largest one at greater distances, as far out as 23 R_E in the plasma sheet, second only to the omnipresent protons (e.g. LENNARTSSON and SHELLEY, 1986). Possibly the most important aspect of the O $^+$ is its origin: the Earth's atmosphere. The solar wind does have oxygen ions in higher charge states (e.g. BAME et al., 1975), which can charge exchange into O $^+$, but the solar wind concentrations are far too low to account for the prevalence of O $^+$ ions inside the magnetosphere. Moreover, the polar regions of the Earth's exosphere are now known to emit O $^+$ ions, along with H $^+$ and other ions, with energies reaching far into the keV range, and to do that at rates that can account for the O $^+$ concentrations in the equatorial regions of the magnetosphere (e.g YAU et al., 1985, and references therein).

Despite its origin, the O $^+$ component is undoubtedly strongly controlled by the Sun, from the initial ionization of oxygen atoms with energies below 1 eV, all the way through the acceleration by high altitude electric fields to the subsequent transport throughout the magnetosphere. If one considers the magnetospheric O $^+$ ions in the broad context of 'mass, momentum and energy flows through the solar–terrestrial chain', it is fair to say that no solar input of mass *per se* is needed to explain the observations, but some

form of solar energy input is definitely required, and possibly also some input of momentum. This paper examines the potential role of the Sun in that context, using recent data on both the magnetospheric O $^+$ ions and the solar wind plasma and magnetic field. The importance of the Sun's ionizing radiation is noted in passing, in order to address the O $^+$ source, but the emphasis is on the possible effects of the solar wind and its magnetic and electric fields.

2. DATA BASE

The O $^+$ data, unless noted otherwise, are from the Plasma Composition Experiment on the ISEE-1 spacecraft (SHELLEY et al., 1978). These cover energies between 0.1 and 16 keV/e, and have been limited in space to the nightside (GSM $X < 0$) plasma sheet between $R = 10$ R_E and the ISEE-1 apogee at $R = 23$ R_E. These are essentially the same data used by LENNARTSSON and SHELLEY (1986), only slightly reduced in volume by the requirement that concurrent solar wind data be available. The reason for limiting the data to the plasma sheet here is in part to simplify the figures and in part to emphasize data that are the most likely to represent the bulk of the ions. The O $^+$ density is usually higher closer to the Earth, in the equatorial region (LENNARTSSON and SHARP, 1982), but the energy range of these data is inadequate to account for either plasmaspheric ions (below 100 eV/e) or ring current ions (reaching far above 16 keV/e). The tail lobes contain O $^+$ ions as well, but the O $^+$ velocity distributions there are more strongly

collimated (tailward) and narrower in energy (a few hundred eV) than they are in the plasma sheet, and are therefore subject to larger measuring errors (cf. LENNARTSSON, 1989, and references therein). The average densities and energies presented in the following are based on a total of almost 800 individual plasma sheet samples, where each sample is itself an average over time for periods of 1–3 h. The duration of each sample corresponds to about 1 R_E of spacecraft travel along the orbit. All together these samples represent well over 1000 h of measurements in 1978 and 1979.

The solar wind data are a combination of particle and magnetic field (IMF) data from several different instruments and spacecraft and have been obtained from the NSSDC archives (COUZENS and KING, 1986). The original data were either obtained in the close vicinity of the Earth's magnetosphere (within a few tens of R_E) or time shifted to the magnetosphere according to the observed solar wind flow (from ISEE-3). The data used here consist of hourly averages of the proton density and flow vector (GSE) and of the magnetic field vector (GSE and GSM).

In addition, use is also made of the auroral AE index, as recorded by the World Data Center C2 for Geomagnetism (KAMEI and MAEDA, 1981, and subsequent data books).

3. STATISTICAL RESULTS

3.1. Control of O^+ source

The principal ionizing agent is the EUV (extreme ultraviolet) portion of the Sun's electromagnetic radiation, consisting of multiple narrow peaks in the 10–100 nm wavelength range (e.g. BANKS and KOCKARTS, 1973). The intensity of this radiation is known to vary substantially with varying activity on the Sun's surface, that is to vary with the solar 27-day rotation and 11-year sunspot cycle (e.g. LEAN, 1987), so one might expect a corresponding variation in the abundance of energetic O^+ ions in the magnetosphere, even if other conditions were constant. That there is such a correlation is now clear from published data, and is illustrated in Fig. 1 [compiled from YOUNG et al. (1982) and LENNARTSSON (1989)]. The solar activity is measured by the 10.7 cm solar radio emission in this figure, rather than by the EUV itself, because the 10.7 cm indices are considered fairly well correlated with the EUV and are the only ones available for the entire study periods ($F10.7$ obtained by ground observations).

Although the physical link between the ionospheric source and the magnetospheric O^+ may be complex, probably involving heating and expansion of the

neutral atmosphere (YOUNG et al., 1982), it seems rather certain that the solar EUV radiation is the basic controlling medium.

Another ionizing agent is auroral particle precipitation. This is localized in latitude, but its latitudinal extent is comparable to that of the observed outflow of O^+ ions (e.g. GHIELMETTI et al., 1978), and it extends into the nightside atmosphere, so it would seem potentially important. However, there is no obvious reason why this kind of ionization would produce the strong dependence on solar activity shown in Fig. 1. In fact, the studies of YOUNG et al. (1982) and LENNARTSSON (1989) both indicate little or no correlation between auroral and solar activities during solar cycle 21. It is conceivable that the ionizing efficiency of precipitating particles may be indirectly affected by variations in the EUV, via atmospheric variations, but it seems natural to conclude from Fig. 1 that the EUV has direct and dominant control of the O^+ source.

3.2. Control of O^+ acceleration and transportation

Ever since their discovery by spacecraft (SHELLEY et al., 1972) the energetic O^+ ions have been known as a phenomenon related to geomagnetic disturbances. This correlation is evident in all existing data sets, even though the statistical scatter is too large to suggest a simple universal relationship between the O^+ concentration and any particular geomagnetic index. Two examples of published results are illustrated in Fig. 2 [compiled from YOUNG et al. (1982) and LENNARTSSON and SHELLEY (1986)]. Since geomagnetic activity is known to depend on conditions in the solar wind, including the state of magnetization, one has to conclude that the O^+ is also influenced by the solar wind, in one way or another. The question is, in what way?

In a statistical sense the O^+ can be shown to depend on several solar wind parameters, including the proton density, flow speed and ram pressure, and the magnetic field direction and strength. That does not necessarily imply direct physical control of the O^+ by each parameter, however, because those parameters are partially interdependent. An example of that kind of ambiguity is shown in Fig. 3.

At first glance Fig. 3 gives the impression that the plasma sheet O^+ density (solid line) rises with rising solar wind density. This is reasonable, since variations in the solar wind proton density are mainly responsible for variations in the solar wind ram pressure (cf. COUZENS and KING, 1986), and a rising solar wind pressure may compress the geomagnetic tail, including the plasma sheet. The solar wind density used here is a single hourly value, or the average of two or three

(a)

(b)
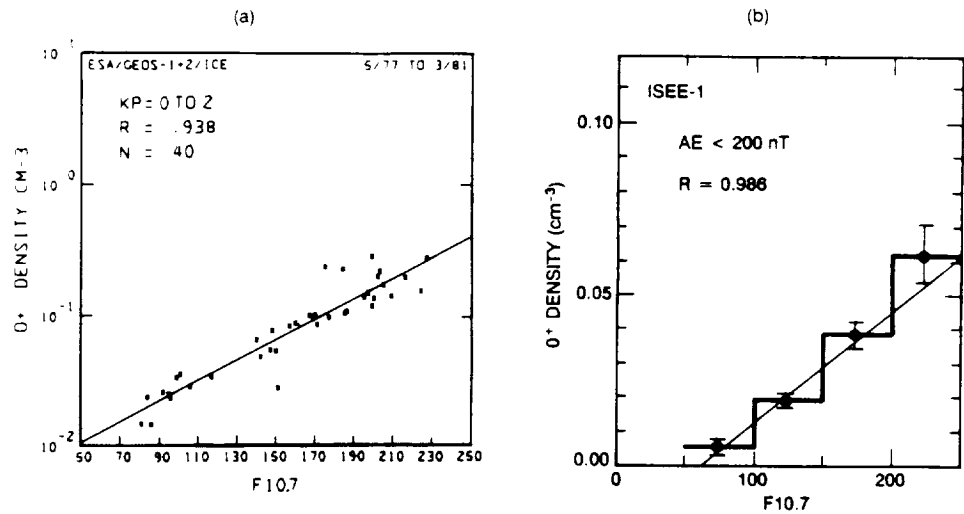
Fig. 1. (a) Monthly averages of the O⁺ density (1–14 keV) near geosynchronous altitude vs the monthly F10.7 solar activity index (YOUNG et al., 1982; GEOS-1 and -2 data). (b) Average O⁺ density (0.1 16 keV) between 10 and 23 R_E in the plasma sheet vs the daily F10.7 index (LENNARTSSON, 1989; ISEE-1 data). Both data sets are limited to fairly quiet geomagnetic conditions ($K_p < 2$ and $AE < 200$ nT, respectively). Straight lines are least-squares fits with correlation coefficient R as shown.

(a)

(b)
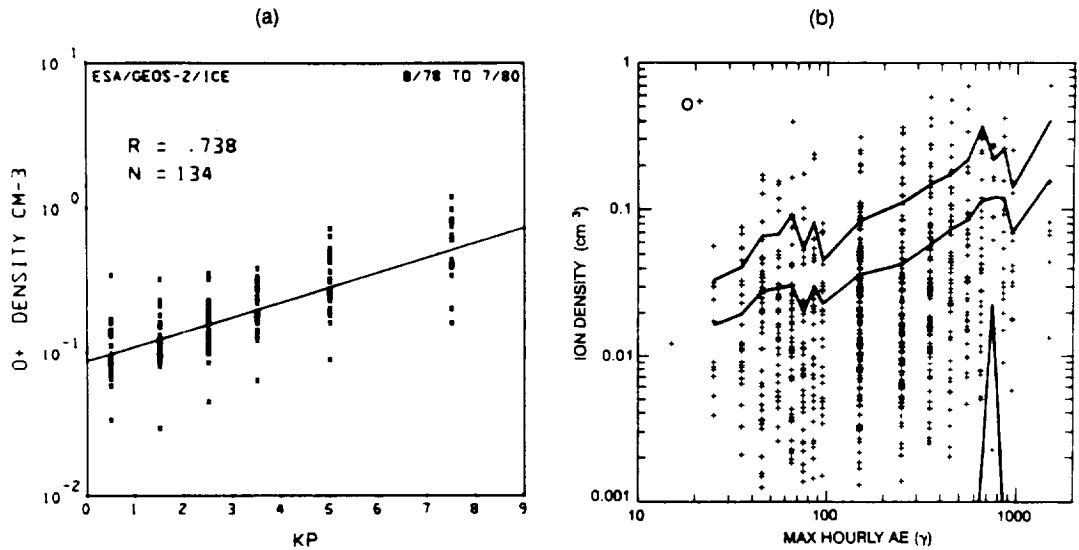
Fig. 2. (a) Monthly averages of the O⁺ density (1–14 keV) near geosynchronous altitude vs the 3-h geomagnetic K_p index. The O⁺ densities have been averaged over 3-h intervals first, then sorted by the corresponding K_p and averaged again at each level of the K_p (YOUNG et al., 1982; GEOS-1 and -2 data). (b) One- to three-hour averages of the O⁺ density (0.1–16 keV) between 10 and 23 R_E in the plasma sheet vs the hourly geomagnetic AE index (maximum AE during O⁺ averaging and preceding hour). The three jagged lines show the mean (middle line) and the mean plus and minus one sample standard deviation (the latter mostly below scale; LENNARTSSON and SHELLEY, 1986; ISEE-1 data).
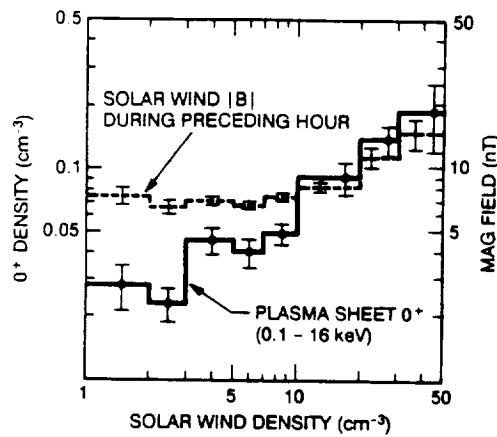
Fig. 3. Average O^+ density in the plasma sheet (10–23 R_E) at different levels of solar wind (proton) density (solid line). The average solar wind magnetic field (IMF) strength preceding the particle samplings is shown for comparison (dashed line, scale on the right). The error bars in this and following figures represent the statistical uncertainty of the average itself (plus and minus one sigma).

hourly values, depending on the length of the concurrent plasma sheet O^+ sampling. However, closer inspection reveals another effect: solar wind densities above 10 cm^{-3} are positively correlated with the strength of the magnetic field (dashed line), so the highest O^+ densities may well result from elevated solar wind magnetic fields. It may even be argued that all significant changes in the O^+ density (judged from the statistical error bars) are correlated with changes in the magnetic field, except perhaps at very low solar wind densities, below 3 cm^{-3}, where the O^+ is also low but the magnetic field is about average. The dependence of the O^+ on solar wind density will be addressed again later.

The justification for using the magnetic field from the hour preceding the O^+ sampling in Fig. 3 is to allow for some time delay between cause and effect. The choice is somewhat arbitrary, because the statistical relationship is essentially the same with a time delay of a couple of hours, or no time delay at all (not shown). This broad time correlation reflects the evolution of each variable: when the magnetic field and the O^+ density are elevated, they usually remain so for many hours. There is nevertheless a clear statistical correlation between the solar wind magnetic field and the magnetospheric O^+ when they are measured within a few hours of each other, a fact that is illustrated more explicitly in Fig. 4. The magnetic field is henceforth called the IMF, for brevity.

Figure 4 shows one important reason, perhaps the

principal reason, why the O^+ density in Fig. 2b, on average, rises with increasing AE index: both rise with increasingly strong IMF. Figure 4 also shows one reason why the scatter of points in Fig. 2b is so great: the AE index strongly favors a southward IMF (solid line), the O^+ does not. This is a rather unexpected difference between the O^+ and the AE and is further examined below. Another reason for the large scatter in Fig. 2b (and other similar figures in the literature) is the nonuniform distribution of the O^+ in space (cf. LENNARTSSON and SHELLEY, 1986).

Although the IMF strength alone orders the O^+ quite well, the direction of the IMF does play an important role. This is illustrated in Fig. 5, where panel a shows that the O^+ (solid line) responds primarily to that component of the IMF which is perpendicular to the GSM X-axis, that is (approximately) perpendicular to the solar wind flow vector. Panel b shows on the other hand that the orientation of that perpendicular IMF component in the GSM Y-Z plane has no significant effect on the O^+ density (within one sigma). By comparison, the AE index (dashed lines) also peaks when the IMF is perpendicular to the solar wind flow (panel a), but it has a strong preference for a southward perpendicular component (panel b, around 180°), in accordance with Fig. 4b.

Considering the fairly wide (30°) angular binning of the IMF in Fig. 5a, chosen so as to allow significant statistics, and considering also the coarse time resolution of the data samplings, both the IMF (1-h averages) and the O^+ (1- to 3-h averages), this figure is compatible with having the O^+ responding only to the perpendicular component of the IMF. It is not possible to prove that case with these data, and probably not with any practical set of data, but it is tempting to assume so. If we do, the next logical step is to assume that the O^+ depends on some other physical quantity that contains the IMF, but only its perpendicular component. One such quantity is the cross-product between the IMF and the solar wind flow vector: $-\mathbf{v} \times \mathbf{B}$. This is the polarization electric field (in MKS) in the solar wind, as seen in the frame of reference of the Earth (e.g. ALFVÉN and FÄLTHAMMAR, 1963). This field lies within a plane perpendicular to the flow vector $\mathbf{v}$, that is approximately (usually to within a few degrees) in the GSM Y-Z plane, but can have a varying direction within this plane due to the varying direction of $\mathbf{B}$. According to Fig. 5b, that degree of freedom is of no consequence to the O^+ density in the plasma sheet. In other words, the O^+ density may depend on the magnitude of the electric field, but not on its direction:

$$n(O^+) = F(E_{SW}) \tag{1}$$
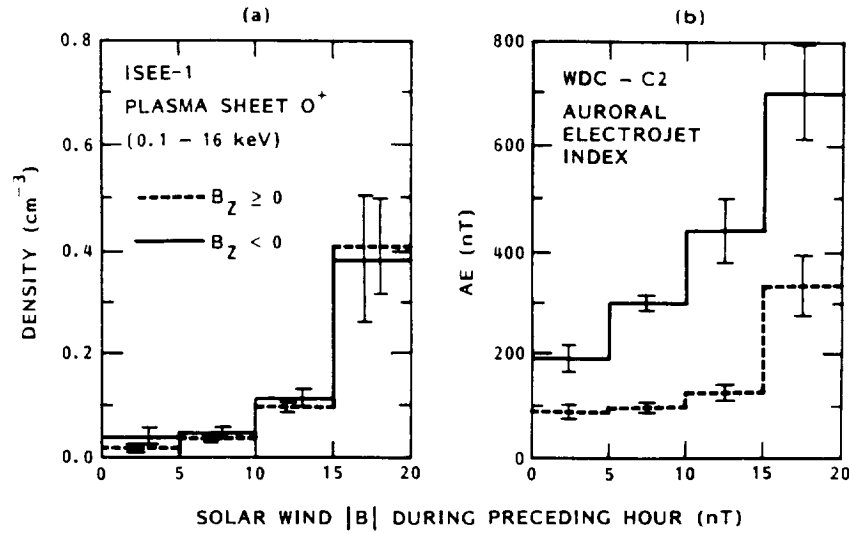
Fig. 4. Average O⁺ density (a) and auroral AE (b), ordered by the IMF strength and GSM Z-direction. The far right bin in each panel includes fields greater than 20 nT.

$$E_{SW} = |-v \times \mathbf{B}|. \qquad (2)$$

Since the flow vector is a factor in (2), and since its magnitude does vary significantly, it is of interest to also order the O⁺ data according to solar wind flow

speed. That has been done in Fig. 6, and it is clear that the O⁺ (solid line) is quite sensitive to this parameter. The O⁺ density increases by about a factor of 20 when the flow speed is only tripled. Part of the explanation is probably again the magnetic field

ISEE - 1: PLASMA SHEET (0.1 - 16 keV/e)
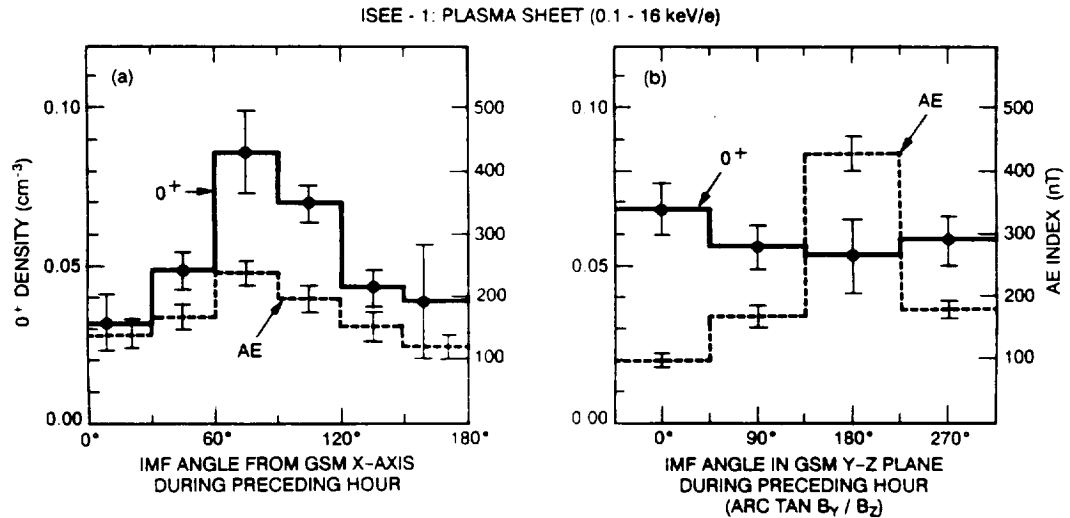
Fig. 5. (a) Average O⁺ density (solid line) ordered by the angle between the Earth–Sun line (X-axis) and the IMF direction. (b) Same density ordered by the rotation angle of the IMF around the Sun–Earth line. The concurrent average AE index is also indicated (dashed lines, scale on the right).
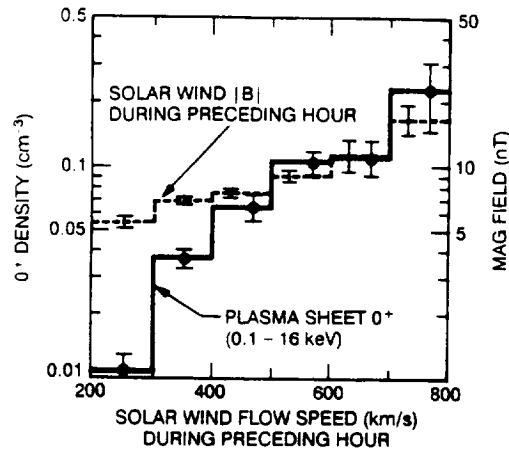
Fig. 6. Average O^+ density (solid line) ordered by the solar wind flow speed. The IMF strength included for comparison (dashed line, scale on the right).

Fig. 7. Average O^+ density (top) and energy (bottom) ordered by the polarization electric field in the solar wind during the preceding hour (solid lines) and during the O^+ sampling (dashed lines). The parabola is a least-squares fit (see text).

(dashed line), since it also tends to increase, on average, thereby pushing the O^+ density still higher (cf. Fig. 4). Even a modest increase in flow speed can thus translate to a rather substantial strengthening of the electric field in (2) and a correspondingly large increase in the O^+ density. The fact that the O^+ is indeed a function of this field is illustrated in Fig. 7.

The electric field values used in Fig. 7 have been derived in two ways, both as single hourly values preceding the O^+ samplings, and as 1- to 3-h averages coincident with the O^+ samplings. The two sets of values order the O^+ data according to the solid and dashed lines, respectively. Either way there is a great deal of statistical variance, but there is no systematic difference between the two sets. The large error bars on the densities (top panel) at fields above 6 mV m are mainly due to undersampling. Fields that high only occur about 3% of the time in these data. Despite these large standard deviations, there is a distinct trend in the O^+ density increase, one that can be fairly well approximated by the thin parabolic line. This line is a linear least-squares fit to all O^+ densities, both solid and dashed, treating the square of the electric field as the independent variable, and weighting the fit by the statistical errors:

$$n(O^+) = (0.020 \pm 0.002) + (0.0047 \pm 0.0003)$$

$$\cdot E_{sw}^2 \quad (cm^{-3}). \quad (3)$$

The correlation coefficient is 0.97.

Since the square of the electric field has the physical dimension of energy density, apart from a normalizing constant, it may seem appropriate to compare it with

the energy density of the O^+ rather than the number density. The relationship (not shown) is in fact rather similar to the one for number density, because the mean energy of the O^+ varies far less than the density, falling only about 30% over the full range of electric fields, as can be seen in Fig. 7 (bottom panel). If the same fitting procedure is applied, then the corresponding least-squares fit to the energy densities is:

$$n \cdot energy(O^+) = (0.078 \pm 0.005) + (0.014 \pm 0.001)$$

$$\cdot E_{sw}^2 \quad (keV\,cm^{-3}). \quad (4)$$

The correlation coefficient is essentially the same, namely 0.96.

4. CONCLUSIONS

The data considered here suggest a simple state of symmetry: the Sun controls the Earth's emission of energetic O^+ ions via electromagnetic fields at extreme ends of the spectrum, one at UV-frequencies (EUV,

FUV) to maintain a source in the ionosphere, the other at almost zero Hz to extract, accelerate and disperse the ions.

The main reason to believe that the original source of the keV O⁻ is controlled via electromagnetic radiation has already been stated in conjunction with Fig. 1, namely the close correlation between this O⁺ and the solar surface activity. This point has been made before in the literature (cf. YOUNG et al., 1982). The second part has no previous endorsement, at least not as a general principle, and may need some elaborating.

Starting from the most basic concepts of solar wind mass, momentum, and energy, it is reasonable to narrow the following discussion to momentum and energy. Treating the solar wind flow of mass as a separate input seems irrelevant, if the O⁺ ions have a terrestrial source, and this source is maintained by electromagnetic (UV) radiation rather than by particle precipitation. It will be argued below that the emission of energetic O⁺ ions is probably not controlled by the solar wind flow of momentum either, but by the energy flow, specifically the flow of solar wind electromagnetic energy.

4.1. Solar wind momentum

The strongest flow of solar wind momentum is in the form of proton ram pressure, that is proton mass density times the square of the flow speed (cf. COUZENS and KING, 1986). This could conceivably affect the O⁻ in different ways, by simply modulating the pressure of O⁻ ions already extracted from the ionosphere, as already mentioned, or by generating electric fields in the Earth's magnetic field, at the magnetopause for instance, which could aid in the extraction, acceleration and dispersion of the O⁺. In either case, by definition, the O⁺ would react to changes in the net solar wind pressure, regardless of whether these were due to changes in proton density or flow speed. By comparing Figs 3 and 6, it appears that the O⁻ density is more sensitive to the flow speed than to the density, however.

In Fig. 3 the O⁺ density (solid line) increases less than a factor of 10 when the solar wind density is increased almost 30-fold (the approximate total range in these data). In Fig. 6, by contrast, the O⁻ density (solid line) increases as much as 20-fold when the flow speed is tripled (the total range here), that is when the square of the flow speed is increased by only a factor of 9. So even though the ram pressure is proportional to both the proton density and the square of the flow speed, a mere 9-fold increase in the latter is sufficient to enhance the O⁺ twice as much as can be accomplished by even a 30-fold increase in the proton

density. It can be added that the lowest solar wind flow speeds, those below 300 km s in Fig. 6, are in fact associated with higher than average solar wind densities (cf. COUZENS and KING, 1986), but still produce the very lowest O⁻ densities. This all suggests that the flow speed by itself is more important than its contribution to the momentum flow.

Furthermore, the O⁺ density is very sensitive to the IMF, according to Fig. 4, even though the magnetic pressure is a small fraction of the total momentum flow—only a few per cent. In fact, some of the variation of the O⁻ density in Fig. 3 can be accounted for by the modest change in the IMF strength (factor of two; dashed line), rather than by the very large change in solar wind density (nearly a factor of 30).

The sorting of O⁻ density by solar wind density can be made more specific by restricting the ranges of the flow speed and the IMF, but that also reduces the statistical material and can only provide a rough estimate. This approach has been tried, and the results (not illustrated) suggest that, given typical values of the flow speed (420–440 km/s) and IMF strength (6.5–7.5 nT), an increase of the solar wind density alone by a factor of 20 may raise the plasma sheet O⁻ density by a factor of 5 or less. Since the flow speed range is restricted in this case, the results also apply to the effect of increasing the ram pressure, or momentum flow, and may simply indicate compression of the geomagnetic tail and a consequent reduction of the volume available to the O⁺. The O⁻ ions are not compressed in an adiabatic sense, however, because their mean energy remains approximately constant in this case (about 4 keV).

4.2. Solar wind energy

Since the O⁺ density is fairly insensitive to changes in the solar wind density alone, and yet responds strongly to an increase in the electric field, as shown in Fig. 7, it would appear that the crucial form of solar energy is electromagnetic rather than kinetic. That is, the kinetic properties of the solar wind affect the emission of O⁺ only indirectly via the embedded fields, specifically the electric field. Accordingly, the flow of energy may be measured by a Poynting vector, at least in a formal sense. The fields are not true radiation fields, since their frequency is virtually zero, but they do have such a vector associated with them: $E \times B \mu_o$ (in MKS). Inserting $-v \times B$ for E gives

$$\text{Poynting vector} = 2 \cdot (\text{magnetic presure}) \cdot v' \quad (5)$$

where v' is the solar wind flow velocity transverse to the IMF vector. This quantity relates numerically to the proton kinetic energy flow in roughly the same

ratio as the magnetic pressure relates to the proton ram pressure, that is it can account for a few per cent of the total solar wind energy flow. That may seem a weak flow, but it does in fact provide ample power for both the O^+ energization and other processes, when integrated over the cross-section of the magnetosphere, or a substantial part thereof, and allowed to act for hours.

Assuming, for example, that the IMF strength is 10 nT and v' is 400 km/s (IMF nearly perpendicular to the solar wind flow), then only about 1% of the Poynting flux in (5) hitting the magnetosphere (circular disk of 25 R_E radius assumed) is required to fill the large plasma sheet segment sampled here with 0.1 cm^{-3} of 4 keV O^+ ions over the course of 1 h [see fig. 2 in Lennartsson and Shelley (1986) for distribution of plasma sheet samplings]. The remaining 99% of the Poynting flux is then available to power other magnetospheric processes. The plasma sheet filling may well be faster, and may be offset by convection losses, but (5) does seem to carry ample power, provided a sufficient fraction of that power is transferred to the ionospheric O^+.

Granted that the solar wind has a sufficient flow of electromagnetic energy to control the extraction, acceleration, and dispersion of the O^+, how is this energy transferred? These data do not answer that question, but they show evidence that the O^+ does indeed respond to the solar wind fields. In particular, the parabolic relationship in equation (4) suggests that the O^+ kinetic energy is produced by dissipation of solar wind electric power. Such dissipation implies time integration, which (4) does not show explicitly, but the data samplings account for that indirectly by averaging over 1 h or more, and (4) is the result of further averaging of many such samplings. In other words, the factor 0.014 contains some kind of implicit average integration time that provides the correct physical dimension ('conductivity·time'). Implicit in equation (4) is also some average loss rate for the O^+ ions, including convection, which may depend on E_w

as well. The fact that the O^+ does not vanish completely when E_w goes to zero may simply mean that the loss rate also goes to zero, or is strongly reduced (reduced convection), leaving behind a residue of O^+ ions.

In view of equation (5), which formally associates the energy flow with the IMF, it might seem that the first step of the energy transfer must involve magnetic merging of the IMF with the geomagnetic field. That may be true in some sense, but the conventional interpretation of merging would then have the O^+ respond the most strongly when the IMF is southward (e.g. Cowley, 1980). That is not evident in these data. On the contrary, Fig. 5b suggests that the O^+ is 'oblivious' to the orientation of the IMF relative to the Earth's dipole. This is a puzzling feature, especially since the concurrent AE index in Fig. 5b does favor a southward IMF. Whatever the role of magnetic merging may be, it is clear from Fig. 5b that the AE index and the plasma sheet O^+ density are measures of different and partially independent elements of auroral activity.

As a final caveat, it must be emphasized that these data are indirect and incomplete measures of the O^+ emission rate. With regard to Fig. 5b, for example, it could be argued that any increase in the emission rate in response to a southward turning of the IMF is offset by a simultaneous increase in the loss rate, due to increased convection, so as to prevent accumulation of O^+ ions in the plasma sheet. That might seem a contrived argument, since the O^+ ions do accumulate in response to the IMF's turning away from the GSM X-axis (Fig. 5a) and to the IMF's increasing in magnitude (Fig. 4a), but it cannot be disproved here. Whether the O^+ emission rate does or does not favor a southward IMF will have to be finally decided by further study of data from polar orbiting spacecraft, studies that take into account the solar wind conditions.

REFERENCES

Alfvén H. and Fälthammar C.-G.   1963   *Cosmical Electrodynamics, Fundamental Principles* (2nd Edn). Oxford University Press, New York.

Bame S. J., Asbridge J. R., Feldman W. C., Montgomery M. D. and Kearney P. D.   1975   *Solar Phys.* **43**, 463.

Banks P. M. and Kockarts G.   1973   *Aeronomy.* Academic, San Diego, California.

Couzens D. A. and King J. H.   1986   *Interplanetary Medium Data Book, Supplement 3, 1977–1985.* NSSDC/WDC-A-R&S, NASA Goddard Space Flight Center, Greenbelt, U.S.A.

Cowley S. W. H.   1980   *Space Sci. Rev.* **26**, 217.

Earth's emission of energetic O[+]

GHIELMETTI A. G., JOHNSON R. G., SHARP R. D. and SHELLEY E. G.	1978	*Geophys. Res. Lett.* **5**, 59.
KAMEI T. and MAEDA H.	1981	*Auroral Electrojet Indices (AE) for January–June 1978.* Data Book 3, World Data Center C2 for Geomagnetism, Kyoto, Japan.
LEAN J.	1987	*J. geophys. Res.* **92**, 839.
LENNARTSSON W.	1989	*J. geophys. Res.* **94**, 3600.
LENNARTSSON W. and SHARP R. D.	1982	*J. geophys. Res.* **87**, 6109.
LENNARTSSON W. and SHELLEY E. G.	1986	*J. geophys. Res.* **91**, 3061.
SHELLEY E. G., JOHNSON R. G. and SHARP R. D.	1972	*J. geophys. Res.* **77**, 6104.
SHELLEY E. G., SHARP R. D., JOHNSON R. G., GEISS J., EBERHARDT P., BALSIGER H., HAERENDEL G. and ROSENBAUER H.	1978	*IEEE Trans. Geosci. Electron. GE* **16**, 266.
YAU A. W., SHELLEY E. G., PETERSON W. K. and LENCHYSHYN L.	1985	*J. geophys. Res.* **90**, 8417.
YOUNG D. T., BALSIGER H. and GEISS J.	1982	*J. geophys. Res.* **87**, 9077.

A Scenario for Solar Wind Penetration of Earth's Magnetic Tail Based on Ion Composition Data From the ISEE 1 Spacecraft

W. LENNARTSSON

Lockheed Missiles and Space Company, Inc., Research and Development, Palo Alto, California

Energetic (0.1-16 keV/e) ion data from the Plasma Composition Experiment on the ISEE 1 spacecraft show that Earth's plasma sheet (inside of 23 R_E) always has a large population of H$^+$ and He^{++} ions. This population is the largest, both in absolute numbers and relative to the terrestrial ions, during periods of extremely weak geomagnetic activity and is then also the most "solar wind like", in the sense that the He^{++}/H$^+$ density ratio is at its peak (about 3% on average in 1978 and 79), and the H$^+$ and He^{++} ions have mean (thermal) energies that are proportional to ionic mass and barely exceed the typical bulk flow energies in the solar wind. These quiet time conditions occur when the IMF is persistently northward and not excessively strong. At more active times the H$^+$ and He^{++} ions are heated in the central plasma sheet, but they can still be found with lower solar wind like energies closer to the tail lobes, at least during plasma sheet thinning. In a number of cases examined here, such low-energy H$^+$ and He^{++} ions are found flowing antisunward close to the lobes, flowing roughly parallel (or antiparallel) to the tail magnetic field at speeds ranging from a few tens to a few hundred kilometers per second, as though they have recently entered the tail earthward of the ISEE 1. In some cases the flow vector appears to contain a significant E × B component directed away from the nearest tail flank. In order to explain these flows, as well as the solar wind like appearance of the plasma sheet as a whole during northward interplanetary magnetic field, it is argued that the solar plasma enters along slots between the tail lobes and the plasma sheet, even quite close to Earth, convected inward along the plasma sheet boundary layer, or adjacent to it, by the electric fringe field of the ever present low-latitude magnetopause boundary layer (LLBL). The main point of the argument is that the required E × B drifts are produced by closing LLBL equipotential surfaces through the plasma sheet.

1. INTRODUCTION

Although it is one of the oldest topics of magnetospheric physics, the entry of solar wind plasma into Earth's magnetic field is still a complex and elusive issue. It has been further complicated by the observations that energetic (hundreds of eV to tends of keV) plasmas inside the magnetosphere can have a terrestrial rather than solar origin [e.g., *Shelley et al.*, 1972; *Ghielmetti et al.*, 1978; *Balsiger et al.*, 1980; *Sharp et al.*, 1981; *Lundin et al.*, 1982; *Hamilton et al.*, 1988]. Based on gross estimates of the total number of charged particles in various parts of the magnetosphere, it can even be argued that the known outflow of terrestrial ions from Earth's polar regions, as measured in a range of energies from less than 1 eV/e to about 20 keV/e, is sufficiently strong to supply the entire positive plasma component, given the proper mechanisms for final adjustment of energies [*Chappell et al.*, 1987].

The traditional view has been that the solar wind plasma does indeed enter, provided it is magnetized and that the embedded magnetic field, the interplanetary magnetic field (IMF), has a proper direction. The conditions for entry have been assumed to be the most favorable when the IMF is pointing southward, opposite the equatorial direction of Earth's magnetic field [e.g., *Cowley*, 1980]. According to this view, the IMF and the geomagnetic field merge on the front of the magnetopause, causing the electric field in the solar wind, that is the field associated with solar wind motion across the IMF (E = −v × B), to be conducted into the high-latitude magnetosphere and into the geomagnetic tail, where it will have a general dawn-to-dusk direction, at least

as long as the IMF has a southward component. Under the influence of this internal electric field, part of the solar wind plasma is thought to convect (E × B drift) into the geotail, across the northern and southern tail lobes, and to converge at the tail midplane beyond some distant location downtail [e.g., *Speiser*, 1965; *Pilipp and Morfill*, 1978; *Cowley*, 1980]. Part of this converging plasma, it is thought, finds itself on closed (newly reconnected) geomagnetic field lines and is subsequently transported earthward (sunward) by a combination of E × B drift and field-aligned jetting [e.g., *Speiser*, 1965] to form the body of the plasma sheet, as well as the near-Earth ring current. The eventual fate of this same plasma is to be partially precipitated into Earth's atmosphere and otherwise ejected through the equatorial magnetopause.

The plasma circulation described by this theory was originally postulated on the basis of observed E × B drifts in the high-latitude regions of Earth's ionosphere [*Axford and Hines*, 1961], and has been corroborated by numerous electric field and plasma drift and plasma dispersion measurements by polar orbiting spacecraft [e.g., *Heppner*, 1972; *Reiff et al.*, 1977; *Heelis et al.*, 1982; *Heppner and Maynard*, 1987], but it has not yet been unambiguously verified by in situ observations in the distant tail. Observations made from the ISEE 3 spacecraft, for instance, show well-defined tail lobes separated by a plasma sheet as far as 225 R_E downtail [*Tsurutani et al.*, 1984; *Zwickl et al.*, 1984]. Judging from measured electron flows, the E × B drift in the plasma sheet appears to be almost exclusively antisunward beyond about 180 R_E [*Zwickl et al.*, 1984], which would be expected where southward pointing IMF field lines have reconnected, but the antisunward motion persists even though the local tail magnetic field between 180 and 225 R_E is northward, and hence the electric field is dawnward, at least half the time [*Tsurutani et al.*, 1984]. Under such conditions it even seems

improbable that the plasma sheet particles have converged through the lobes. On the other hand, the plasma measurements that have been made closer to Earth show that earthward jetting of particles is commonplace [e.g., *DeCoster and Frank*, 1979; *Lyons and Speiser*, 1982; *Eastman et al.*, 1985], whether those particles previously traversed the tail lobes or not.

The purpose of this study is to explore an alternative scenario, one which may not necessarily require that the solar wind plasma be magnetized. This study does not take issue with the notion that Earth's magnetic field merges with the solar wind magnetic field on a regular basis, but it tries to focus on certain other aspects of the interaction between the solar wind particles and Earth's field. It is inspired in part by the simple fact that the geomagnetic tail, as far as we know, always has a plasma sheet, even during times when the physical signs of magnetic merging are weak or absent. In fact, ion composition measurements in the tail have shown that the plasma sheet contains the greatest number of H^+ and He^{++} ions, the principal positive components of the solar wind plasma, during extended periods of extremely weak geomagnetic activity [*Lennartsson and Shelley*, 1986; *Lennartsson*, 1987].

This study is also inspired by other recent plasma observations in the tail, observations that may seem, at least on the surface, to require some modifications of the traditional view of solar plasma circulation. One set of observations in this category consists of the many ISEE measurements of the boundaries between the plasma sheet and the northern and southern tail lobes, boundaries now commonly referred to as the "plasma sheet boundary layer" (PSBL) [e.g., *Parks et al.*, 1984; *Eastman et al.*, 1985]. Among the reported features of the PSBL is its frequently very sharp definition (hundreds of kilometers), as well as its layered structure, which includes layers of low-energy (hundreds of eV) ions and electrons streaming along the magnetic field, both earthward and tailward [*Parks et al.*, 1984]. Such features may suggest that the net plasma motion, including $E \times B$ drifts, is often parallel to the boundary, rather than directed from the lobes into the plasma sheet [cf. *Eastman et al.*, 1985].

Another set of relevant observations pertains to the so called "low-latitude magnetopause boundary layer" (LLBL) [e.g., *Eastman et al.*, 1976; *Mitchell et al.*, 1987], especially to its tailward extension along the dawn and dusk flanks of the magnetopause. The LLBL is known to be at least partially located on closed geomagnetic field lines, and it is believed to always contain solar wind plasma streaming tailward (antisunward) under the influence of a local electric field which is directed from dusk to dawn (tailward $E \times B$ drift). Of particular interest here is the fact that the LLBL appears to exist at all times, even when the IMF is northward [cf. *Mitchell et al.*, 1987], that is when the IMF points in the same direction as the equatorial portion of Earth's magnetic field lines, and is therefore not expected to be merged with Earth's field at the LLBL. The objective of this study is specifically to examine the possible roles of the LLBL and the PSBL in the transport of solar wind plasma from the magnetosheath to the central plasma sheet. In doing so, it will rely heavily on ion composition data from the Lockheed Plasma Composition Experiment on the ISEE 1 spacecraft.

2. INSTRUMENTATION

The ISEE 1 spacecraft (along with the ISEE 2) was launched on October 22, 1977, into an orbit with apogee at almost 23 R_E (geocentric), perigee at about 300 km altitude, an inclination of 29°, and an orbital period of 57 hours. The spacecraft was placed in a spinning mode with the axis nearly perpendicular to the solar ecliptic plane and with a period of approximately 3 s. It reentered almost 10 years later, on September 26, 1987.

The Lockheed Plasma Composition Experiment flown on ISEE 1 is one of a family of instruments using the same type of ion optics and covering nearly the same range of energies (0 eV/e to about 17 keV/e) which have also been flown on GEOS 1 and 2, Dynamics Explorer 1, and Active Magnetospheric Particle Tracer Explorers (AMPTE) CCE [*Shelley et al.*, 1978]. The ISEE 1 instrument consists of two nearly identical mass spectrometers with the respective fields of view centered 5° above and 5° below the spin plane, that is about 5° above and below the solar ecliptic plane. Each field of view is 10° wide along the spin plane and 10°–50° wide transverse to this plane, being the widest at the low-energy end and gradually decreasing to 10° with increasing energy. All data used in this study were obtained with one spectrometer, the one looking below the spin plane. The lowest-energy channel used here, one that extends from about 100 to 300 eV/e, has a field of view that extends from about 10° above the ecliptic plane to 20° below. Information on the instantaneous pitch angles (at center of field of view) is provided by the ISEE 1 fluxgate magnetometer [*Russell*, 1978].

Each spectrometer consists of an electrostatic analyzer to select energy per charge, followed by a combined electrostatic and magnetic analyzer to select mass per charge. Both analyzer sections have particle detectors, so at each energy setting the experiment provides both the total ion flux and the partial flux at a selected mass per charge. Each combination of energy and mass is maintained for at least 1/16 s in high telemetry bit rate and 1/4 in low (normal) bit rate. Different combinations are stepped through in a cyclic fashion according to various patterns controlled by a random access memory which is programmable from the ground. Some patterns, or "modes", may require only a couple of minutes per cycle, others may take 15 to 20 min. The mass selections usually include one that blocks all ions from reaching the second detector, which is a modified Johnston electron multiplier, allowing intermittent measurements of the noise associated with penetrating radiation. These measurements are later used to correct the count rates of mass analyzed ions. The background count rate in the first detector, which is a so-called "spiraltron", is generally negligible and is not corrected for.

The maximum energy range is 0 eV/e (or spacecraft potential) to 17.9 keV/e, divided into 32 contiguous channels, but the lowest channel, from 0 eV/e to about 100 eV/e, is normally limited to energies above 10 eV/e by a retarding potential analyzer (RPA) in the entrance. That same RPA is used to provide "cold plasma" data from 0 to 100 eV/e (retarding within the lowest channel) during part of some measurement cycles. Because of measurement uncertainties associated with spacecraft charging and plasma convection, the lowest-energy channel has not been used in this study. Neither has the highest-energy channel (above 16 keV/e)

been used, because of a slight variation over time of the mass peak locations in that channel. The energy range of these data is therefore generally 100 eV/e to 16 keV/e, unless further limited by a particular instrument mode (see below).

The mass range is from below 1 amu/e to about 150 amu/e, divided into 64 channels, but the most common measurement cycles only sample four to five channels, corresponding to the principal ions, plus a background channel (below 1 amu/e).

This study also makes use of archived solar wind data, both particle data and magnetic field (IMF) data. The ones used here are from the National Space Science Data Center (NSSDC) OMNI files and consist of hourly averages of the proton density and flow vector (in GSE coordinates) and of the IMF vector components (in GSE and GSM coordinates) and magnitude. These are a combination of data from several instruments and spacecraft. Descriptions of the various instruments are referenced in the data handbook by *Couzens and King* [1986]. These solar wind data were either obtained in the close vicinity of the magnetosphere (within a few tens of R_E) or time shifted to the magnetosphere according to the observed solar wind flow (in the case of ISEE 3 [cf. *Couzens and King*, 1986]).

3. DATA FORMAT

The ion data used here are mainly in the form of velocity moments, calculated as sums over discrete energy-angle matrix elements. To calculate full three-dimensional moments from the ISEE 1 data, the ion fluxes measured within the near-ecliptic field of view have been extrapolated to other angles using either of two sets of assumptions:

1. In the central plasma sheet, where most of the statistical material was obtained, the fluxes are assumed to be gyrotropic (independent of gyration angle) over the sampled range of pitch angles and isotropic outside of this range, maintaining the values measured at the smallest and largest pitch angles, respectively. The pitch angles are measured in terms of five bins, covering 0°–15°, 16°–44°, 45°–135°, 136°–164°, and 165°–180°, respectively. This assumption applies to number densities, mean energies, and energy densities. The two-dimensional bulk flow within the field of view, which is generally small compared to the thermal velocities in the central plasma sheet [cf. *Eastman et al.*, 1985], is derived from the partial flow density and partial number density actually measured, using twelve 30° spin angle bins, without extrapolating the ion fluxes into the third dimension. This set of assumptions is expected to be inaccurate at very low ion energies and is the main reason for not including data from the lowest energy channel (below 100 eV/e).

2. In the outer fringes of the plasma sheet, including the plasma sheet boundary layer, and in the lobes, it is assumed that the principal ion flow is parallel to the solar ecliptic plane and that the ion fluxes have rotational symmetry around the flow vector, rather than around the magnetic field. The direction of the flow vector within this plane is determined by the measured flow within the instrument field of view. The only angular variable in this case is measured in terms of the twelve 30° spin angle bins (the width of these bins equals the inherent angular resolution of the instrument in normal low-bit-rate operation). Since the magnetic field is often parallel to the ecliptic plane in these regions of space and since the ion flow is often parallel to the magnetic field,

this second set of assumptions commonly produces about the same numbers as the first set. However, in cases of substantial ion drift across the magnetic field (substantial when compared to thermal velocities) the second set appears to provide more accurate moments, especially number densities. This has been verified by comparing the ion densities with electron densities derived from ISEE 1 and 2 wave experiments on several occasions (one such comparison is made below).

4. STATISTICAL RESULTS FROM CENTRAL PLASMA SHEET

This section revisits a large set of survey data previously described by *Lennartsson and Shelley* [1986]. Those data were selected from a still larger set of magnetotail data using criteria designed to represent the central plasma sheet. One of those criteria, requiring that the mean energy of the ion population as a whole be at least 1 keV, averaged over H^+, He^{++}, He^+, and O^+ ions, has been dropped here, since it proved essentially redundant. The data were acquired over a 2-year period, 1978–1979 and include about 900 samplings of the plasma sheet, where each sampling consists of a 1- to 3-hour averaging of the ion fluxes, sorted by mass and by energy channel into the various spin and pitch angle bins. The duration of each sampling corresponds to about 1 R_E of spacecraft travel along the orbit. The spatial coverage is fairly uniform and extends from a geocentric distance of 10 R_E to the ISEE 1 apogee near 23 R_E, only including points tailward of the dawn-dusk meridian (GSM $X < 0$). These time-averaged flux samplings have been converted to velocity moments using the first set of assumptions described above (gyrotropy). About 630 of these samplings (70%) are covered by concurrent solar wind and IMF data in the NSSDC OMNI files.

4.1. Evidence of a Solar Plasma Component in the Plasma Sheet

Figure 1 illustrates several features of the principal plasma sheet ions that are relevant to the following discussion. Consider first the He^{++} and the O^+ densities in the left panel. These two species clearly behave differently in response to varying geomagnetic substorm activity, as measured by the auroral AE index in Figure 1 (see *Kamei and Maeda* [1981] and subsequent data books): the He^{++} ions are most numerous during extended periods of low activity, whereas the O^+ ions are by far the most abundant during active times. Since O^+ ions are known to be a major component of the auroral and polar outflow of energetic terrestrial ions [e.g., *Yau et al.*, 1985], but He^{++} ions are not, this comparison alone suggests an extraterrestrial, or solar, source for the He^{++}. If the helium were largely of terrestrial origin, it would probably be mostly singly charged, since He^+ ions are a well-known and often significant component of the ion outflow [*Collin et al.*, 1988]. This is not the case in the plasma sheet, however, since the He^{++} density in Figure 1 is substantially higher than the He^+ density at all but the most strongly disturbed times.

Since the solar wind consists mainly of H^+ ions one would thus expect the plasma sheet to have a large component of such ions behaving in much the same manner as the He^{++} component. That is indeed the case, as Figure 1 shows. The H^+ ions are also the most numerous during extended periods of low substorm activity, and the H^+ ions, like the

ISEE 1 PLASMA SHEET SAMPLING (0.1-16 keV/e); TOTAL ION DENSITY ≥ 0.1 cm⁻³
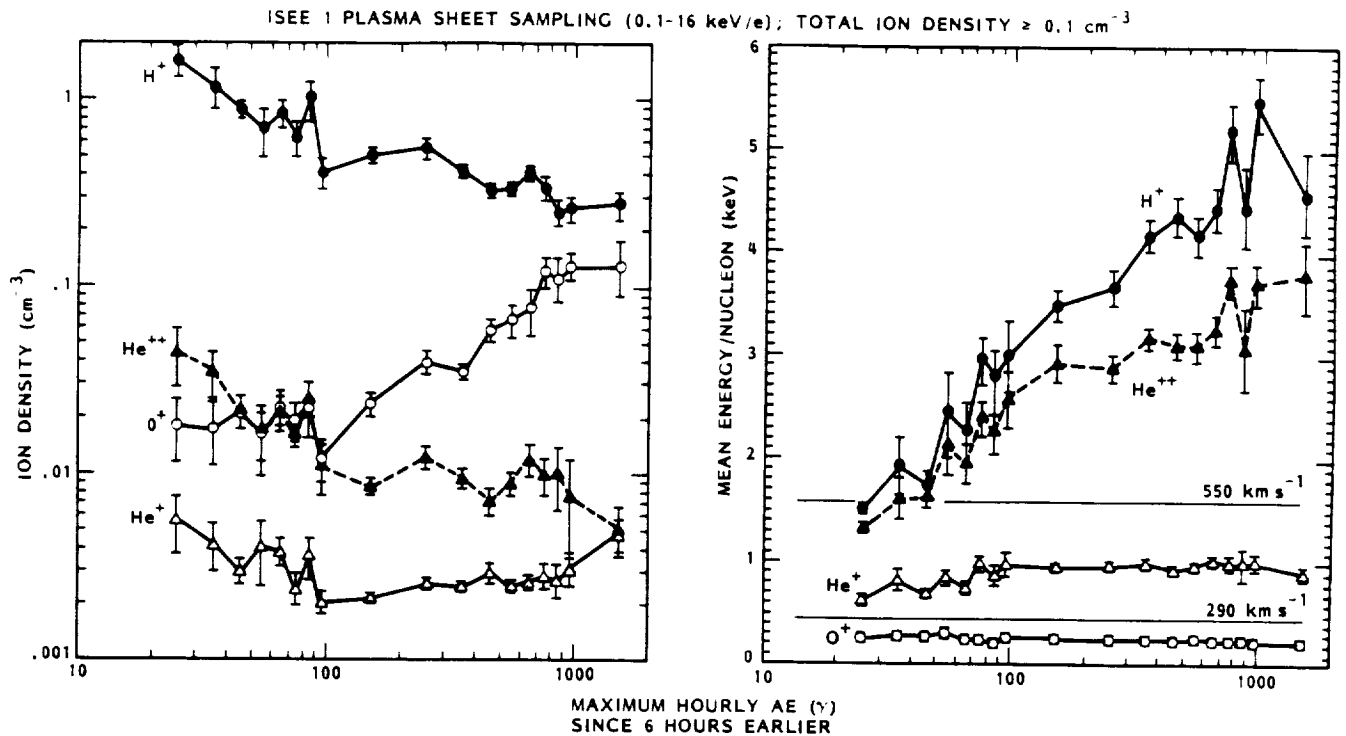
Fig. 1. Central plasma sheet densities (left) and mean energies (right) of the four major ions, averaged over all samples and sorted according to the maximum level of auroral elecrojet (AE) activity during the sampling and the preceding 6 hours. The thin horizontal lines in the right panel indicate the range of energy per nucleon that corresponds to the most common range of solar wind bulk speeds. Error bars in this figure, and in Figures 3–7 and Figure 14 below, show standard deviations of the averages (± one sigma [from *Lennartsson*, 1987]).

He⁺⁺ ions but unlike the O⁺ and He⁺ ions, increase in energy, on average, with increasing activity, as shown in the right panel. If the mean energies are normalized by the number of nucleons specific to each ion species, as done here, then the H⁺ and He⁺⁺ ions clearly show more resemblence to each other than to either of the He⁺ or O⁺ ions.

The similarlity between the normalized energies of H⁺ and He⁺⁺ ions would probably seem greater still if the energy range of the data were extended upward, since the cutoff is measured in energy per charge, not energy per nucleon. For an illustration of that point, see Figure 2. The measured mean energies of the He⁺⁺ and H⁺ ions in this example are about 3.1 and 4.0, respectively, when expressed in units of keV/nucleon. However, if a complete Maxwell-Boltzmann distribution is fitted to the measured portion of each distribution function, as described by *Lennartsson and Shelley* [1986], the resulting thermal energies (kT) are 10.2 and 2.7 keV, respectively, which correspond to mean energies (3 kT/2) that are significantly closer in keV/nucleon (3.8 and 4.1). The distributions in Figure 2 are "typical" in the sense that they are fairly well approximated by Maxwell-Boltzmann distributions within the 0.1 to 16 keV/e energy range, but that same approximation probably does not hold for the high energy tails [cf. *Christon et al.*, 1991]. On the other hand, the high energy tails, above a few tens of keV/e, probably do not follow the same heating trend with increasing activity as the bulk of the distributions [*Christon et al.*, 1991].

As far as the H⁺ population is concerned, there is some inherent ambiguity in the relative importance of the solar and

terrestrial sources. The He⁺⁺/H⁺ density ratio in the central plasma sheet is on average lower than it is in the solar wind, as can be seen from the left panel in Figure 1. The ratio here peaks at about 3% during quiet times and is an average over
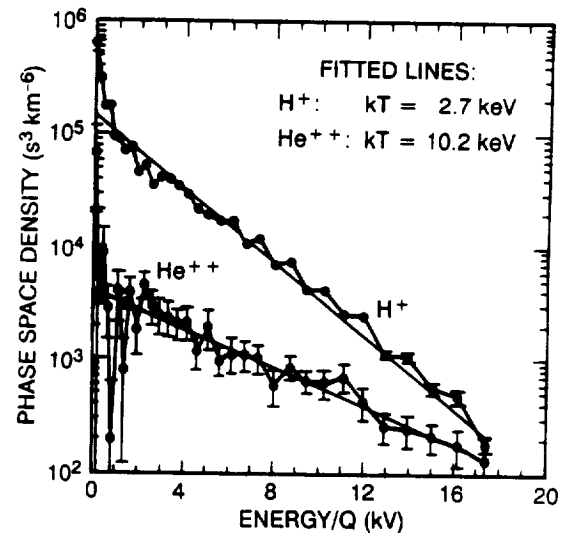
Fig. 2. Typical examples of H⁺ and He⁺⁺ energy distributions (spin averaged) in the central plasma sheet. The error bars here show the Poisson standard deviation of the count rates (±one sigma). The thin straight lines represent Maxwell-Boltzmann distributions fitted as described in *Lennartsson and Shelley* [1986]. (The "zigzag" of the data points is partly due to the sampling procedure, which included separate scans of odd and even energy channels.)

ISEE-1

NO RESTRICTION ON ION DENSITY

---: HOURLY AE < 100γ SINCE 6 HOURS EARLIER

—: HOURLY AE ≥ 500γ AT LEAST ONCE SINCE 6 HOURS EARLIER
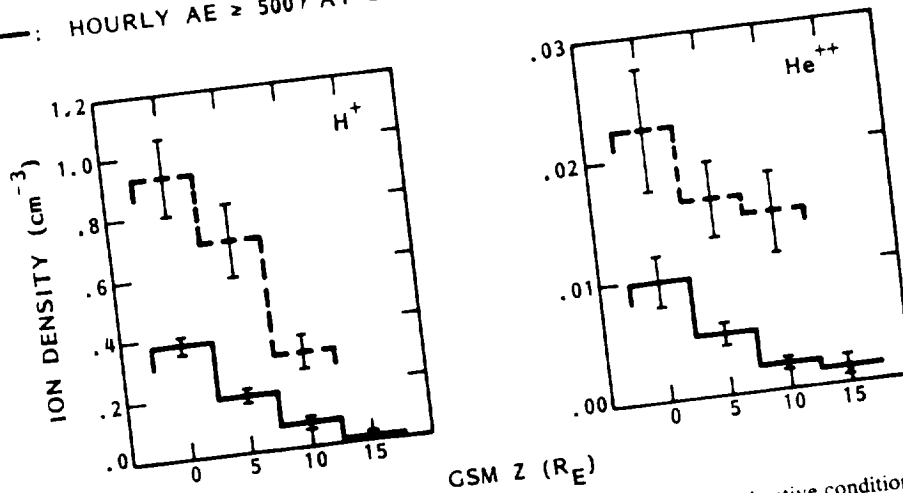
Fig. 3. Densities of the H^+ (left) and the He^{++} (right) during quiet (dashed lines) and active conditions (solid lines), sorted according to the GSM Z coordinate. The averages include samples from the lobe here [from Lennartsson, 1987].

the rising phase of solar cycle 21. The average ratio in the solar wind during the corresponding phase of solar cycle 20 has been reported to rise from about 3.3% to about 4.5% [Feldman et al., 1978], suggesting a value around 4% for the solar component in Figure 1. A value of 3%, however, is sufficiently close to suggest a predominant role of the solar source. Whether the balance can be fully accounted for by a terrestrial H^+ population, even during quiet times, or requires some kind of discrimination against He^{++} ions during their transport to the central plasma sheet, is a question that will be addressed in a future study.

4.2. Some Conditions on a Mechanism for Solar Plasma Entry

According to the right hand panel of Figure 1, those solar wind ions that find their way to the central plasma sheet are heated to energies substantially above their initial bulk flow energy, except during extended periods of low substorm activity, and this heating becomes stronger with increasing activity. Since this process affects the H^+ ions, which are generally the most numerous, the result is a heating of the plasma sheet ion population as a whole when substorm activity is enhanced. This effect is well documented in the literature [e.g., Hones et al., 1971; Huang and Frank, 1986; Baumjohann et al., 1989]. When the H^+ and He^{++} ions are heated, their density is reduced, according to the left panel of Figure 1. This seems to imply that the heating process is associated with an increasing rate of ion loss, perhaps through a combination of injection into the ring current and ejection downtail [e.g., Hones, 1979], and that this loss rate temporarily exceeds the rate of solar ion entry.

Because the H^+ ions are so abundant during quiet times, the reduction in their density during active times translates to a reduction of the plasma sheet ion density as a whole [cf. Lennartsson and Shelley, 1986]. This reduction takes place all across the GSM Z extent ("thickness") of the plasma

sheet, as illustrated in Figure 3, and amounts to a reduction in the total number of particles. This effect is not as well documented in the literature as is the heating [cf. Huang and Frank, 1986; Baumjohann et al., 1989], but it is consistent with the substorm-related effect of "plasma sheet thinning", since that thinning occurs without compression of the pre-existing plasma [Hones et al., 1971]. Furthermore, the two panels of Figure 1 can be seen to complement each other in a physical sense, when these data are compared with avail-able solar wind data (about 70% coverage). In particular, by combining the densities and energies of the four ion species in Figure 1 to form a total ion pressure, this pressure is seen to be related to the proton ram pressure of the solar wind, as shown in Figure 4.

The energies used in Figure 4 are those associated with motion perpendicular to the local magnetic field, but because the ion distributions are fairly isotropic, especially the H^+ and the He^{++} distributions, those energies are approxi-mately equal to 2/3 of the energies in Figure 1 (only 2 degrees of freedom). The solar wind pressures in each bin include both single hourly values, and averages of two or three hourly values, depending on the length of the concurrent plasma sheet samplings. Of the 2- and 3-hour plasma sheet samplings available, only those that were obtained while the GSM Z component of the hourly IMF remained either positive or negative for the duration have been used in Figure 4.

Given the relationship in Figure 4, it seems natural that an increase in the average ion energy of the plasma sheet would be accompanied by a decrease in its ion density, or vice versa, in order that the "right" pressure be maintained. This is not to say that the energy and density variations in the plasma sheet always take place while the solar wind pressure remains constant, but for any given solar wind pressure there is probably a wide range of possible combinations of plasma sheet energy and density, depending on other condi-

ISEE 1 PLASMA SHEET (0.1-16 keV/e)
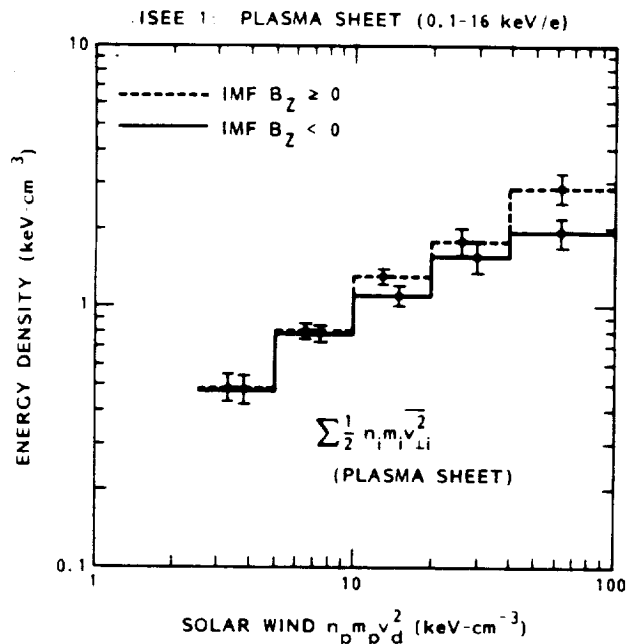
Fig. 4. Average relationship between solar wind (proton) ram pressure and central plasma sheet total ion pressure perpendicular to the tail magnetic field during northward (dashed line) and southward IMF (solid line). The plasma sheet pressure includes the four major ions from Figure 1.

tions. In fact, the heating of the plasma sheet is usually associated with a negative (southward) GSM Z component of the IMF, whereas the solar wind ram pressure is independent of the sign of this IMF component [cf. *Couzens and King*, 1986]. This situation is illustrated in Figure 5.

As Figure 5 shows, the variations of the solar wind ram pressure are mainly due to the large variations of the solar wind density, and the relationship between pressure and density is the same whether the IMF has a positive or a negative B_Z. By contrast, the solar wind ion component in the plasma sheet displays a pronounced asymmetry with respect to the sign of the IMF Z component. The average density is substantially reduced from solar wind values for both polarities, but it stays at the lowest levels for a negative, or southward, B_Z (solid lines). Hence it does not appear that a southward B_Z "opens" the magnetopause to let solar wind plasma enter; it may rather seem as though it shuts out the solar wind. However, another interpretation is that the magnetopause is always open but that a southward B_Z is associated with a higher rate of loss of solar wind plasma from the region between 10 and 23 R_E of the plasma sheet, due to increased earthward and/or tailward convection [cf. *Hones*, 1979].

The positive B_Z case in Figure 5 (dashed lines) is somewhat too coarsely defined to represent the maximum solar ion content in the plasma sheet, with a given solar wind density. By comparing with Figure 1, it is clear that the plasma sheet ion energies in Figure 5 (right panel) remain too high for this case to be limited to AE < 100 nT. One reason is that hourly averages of the IMF components, as used here, do not account for all significant variations of the B_Z; another reason may be that the plasma sheet content depends not only on the concurrent conditions in the solar wind but also on conditions during the preceding hour, or even earlier. In any case, it does appear from these data that

the closer the IMF is to being northward, the weaker the geomagnetic activity is and the larger the plasma sheet H^+ and He^{++} densities are in comparison to the solar wind density. This relationship is further clarified in Figure 6, where the IMF direction within the GSM Y-Z plane is divided into four ranges, but the solar wind pressure has been averaged over. The IMF from the 1 hour preceding the plasma sheet sampling has been used here in order to also allow for some time delay between cause and effect. It is worth remembering that high average H^+ and He^{++} densities are associated with a "thick" (in GSM Z) plasma sheet (Figure 3) and thus with a large total number of particles.

Considering Figure 6, one may ask the question: Does a northward B_Z control the entry process, making it easier for the solar wind plasma to reach Earth's plasma sheet? To address that question, it is necessary to consider the magnitude of the IMF as well. Clearly, a vanishingly small IMF can be of little physical consequence, regardless of its direction, so the effect of the B_Z on the entry process, if any, must increase with increasing field strength, at least increase over some range of field strength. This is examined in Figure 7, which shows the ion densities sorted by four ranges of the IMF strength, under the condition that B_Z be positive. Two sets of IMF values have been used, namely, the hourly value obtained immediately preceding the plasma sheet sampling (solid lines) and the maximum hourly value obtained while the plasma sheet was being sampled (for up to 3 hours at a time; dashed lines).

According to Figure 7, the plasma sheet H^+ and He^{++} densities (top panels) do show some increase with increasing IMF, at least for $|B| < 15$ nT, but so does the solar wind density as well (bottom left panel). The solar wind densities refer to the same hours as the IMF measurements here, and only the hours preceding the plasma sheet samplings are covered by the solid line. The dotted lines show, for comparison, the averages of all available solar wind samplings in 1978 and 1979 with positive B_Z (the corresponding averages with negative B_Z are identical). As found previously (in Figure 5), the plasma sheet densities are expected to increase with increasing solar wind density for northward B_Z, so the result in Figure 7 is probably negative: an increasing IMF, with a northward Z component, does not cause a larger fraction of the solar wind plasma to enter the plasma sheet. Actually, when $|B|$ exceeds 15 nT, the plasma sheet H^+ density becomes a smaller fraction of the solar wind density, presumably due to enhanced geomagnetic activity and increasing loss rates. It appears that the plasma sheet He^{++} density increases marginally more than does the H^+ density, but that is probably to be expected, since larger values of the IMF tend to be associated with larger solar wind He^{++}/H^+ ratios, as reported by *Borrini et al.* [1983] and illustrated in the bottom right panel.

In view of Figures 5 and 7 it seems logical to conclude that the solar wind plasma would have ready access to Earth's plasma sheet even if the IMF vanished altogether. Given a typical solar wind density of about 8 cm^{-3}, the density of the solar ion component in the plasma sheet would apparently be about 0.5 cm^{-3}, when averaged over the volume sampled here and averaged over solar wind velocities. The hourly averaged IMF is not actually zero before or during any of the plasma sheet samplings, but several values about 1.5-2.5 nT are included, and those are associated with normal plasma sheet densities (as high as 0.9 cm^{-3}). When Figures 1-7 are

PLASMA SHEET (ISEE 1) VERSUS SOLAR WIND (OMNI)
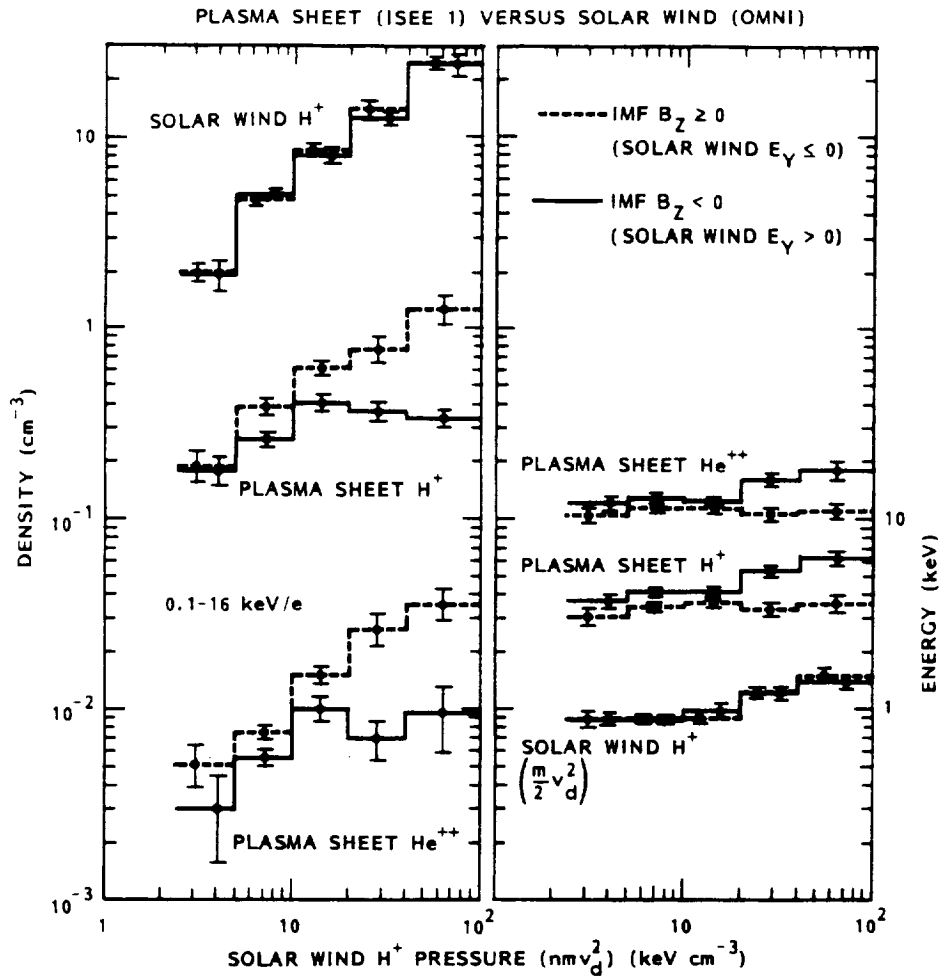
Fig. 5. Densities (left) and mean energies (right) in the central plasma sheet and solar wind, ordered by the solar wind ram pressure and the IMF B_z.

combined, these statistical data thus seem to suggest the following conditions for solar plasma entry into the plasma sheet: (1) It takes place during a wide range of geomagnetic conditions, including times of extreme quiescence (Figures 1 and 3). (2) It can occur without a substantial increase in the mean ion energies (Figure 1; quiet conditions). (3) It occurs even when the solar wind magnetic field (IMF) is extremely weak, and it may not require any such field at all (Figure 7).

PLASMA SHEET H$^+$ AND He^{++} VERSUS IMF DIRECTION

ARC TAN (B_Y/B_Z) DURING PRECEDING HOUR
(IN GSM COORDINATES)
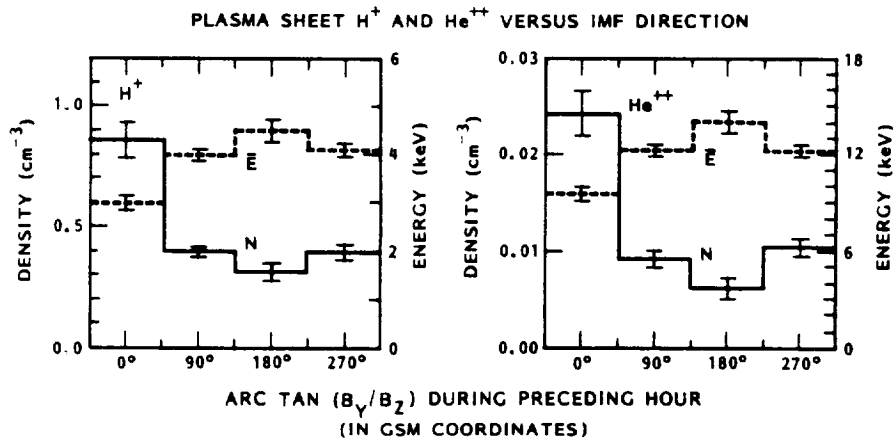
Fig. 6. Densities (solid lines) and mean energies (dashed lines) of the H$^+$ (left) and the He^{++} (right) in the central plasma sheet, ordered by the IMF direction angle in the GSM Y-Z plane (during the hour preceding each plasma sheet sampling).
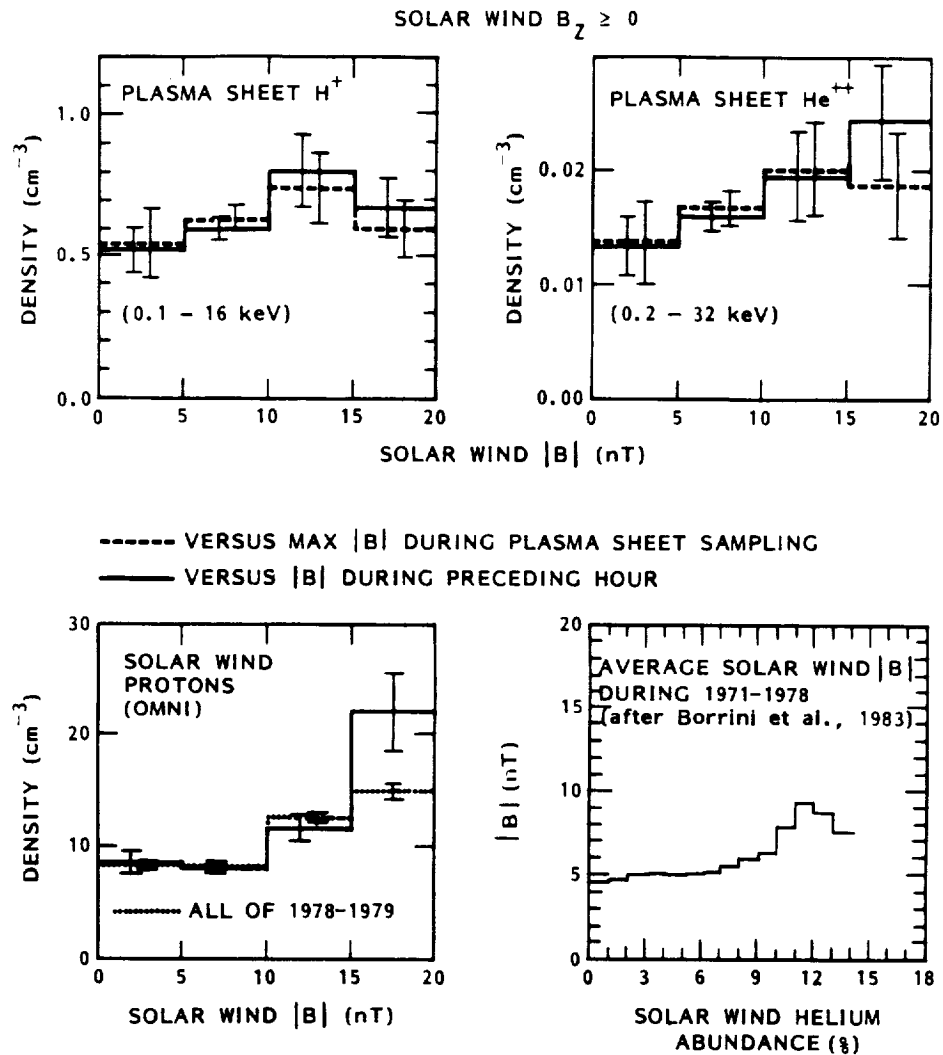
SOLAR WIND $B_Z \geq 0$

Fig. 7. Ion densities in the central plasma sheet (top) and solar wind (bottom left), ordered by the magnitude of the IMF (while $B_Z \geq 0$), and average IMF magnitude ordered by the solar wind helium abundance in percent (bottom right). The far right bin in the top two and bottom left panels includes $|\mathbf{B}| > 20$ nT.

5. ANTISUNWARD FLOW OF H^+ AND He^{++} IONS IN THE TAIL

If one were to trace the solar ions backward in space, from the central plasma sheet to the magnetosheath, one approach would be to look for H^+ and He^{++} ions with increasingly "solar wind like" velocity distributions, assuming that their distributions change gradually along their path. No such tracing has been attempted with these data yet, except that it was found in the statistical studies of the central plasma sheet that the H^+ and He^{++} ions become less energetic away from the center axis of the tail, that is, their mean energies decrease both toward dawn and dusk and toward the northern and southern boundaries of the plasma sheet (e.g., Figure 12 of Lennartsson and Shelley [1986]).

As shown by Figure 1, the entire (spatially averaged) population of H^+ and He^{++} ions in the central plasma sheet becomes solar wind like in energy when substorm activity subsides and the AE goes to zero. The principal remaining difference from the solar wind is that the plasma sheet ions have become isotropized and dispersed in energy during the entry. If some adjacent region of the tail, inside of the

magnetopause boundary layers, can be found to contain such solar wind like ions under more disturbed conditions, or better yet, if it contains H^+ and He^{++} ions that are still flowing antisunward, then it seems logical to assume that this region lies on the path of the solar plasma, and that it is closer to the source. Of particular interest here are the regions forming the boundaries between the plasma sheet and the northern and southern lobes, that is the PSBL. As a case in point, consider Figure 8.

5.1. A Case From the Literature

Figure 8, from about 0930 UT and onward, covers an event that has been discussed previously by Etcheto and Saint-Marc [1985], although the ion composition aspect of this event has not been explored in depth before. The Plasma Composition Experiment on this occasion was being operated in an abbreviated energy-mass scan mode, only scanning energies between 0.1 and 5 keV/e and only sampling four M/Q channels, corresponding to H^+ (open circles), He^{++} (solid circles), O^+ (stars), and background (not
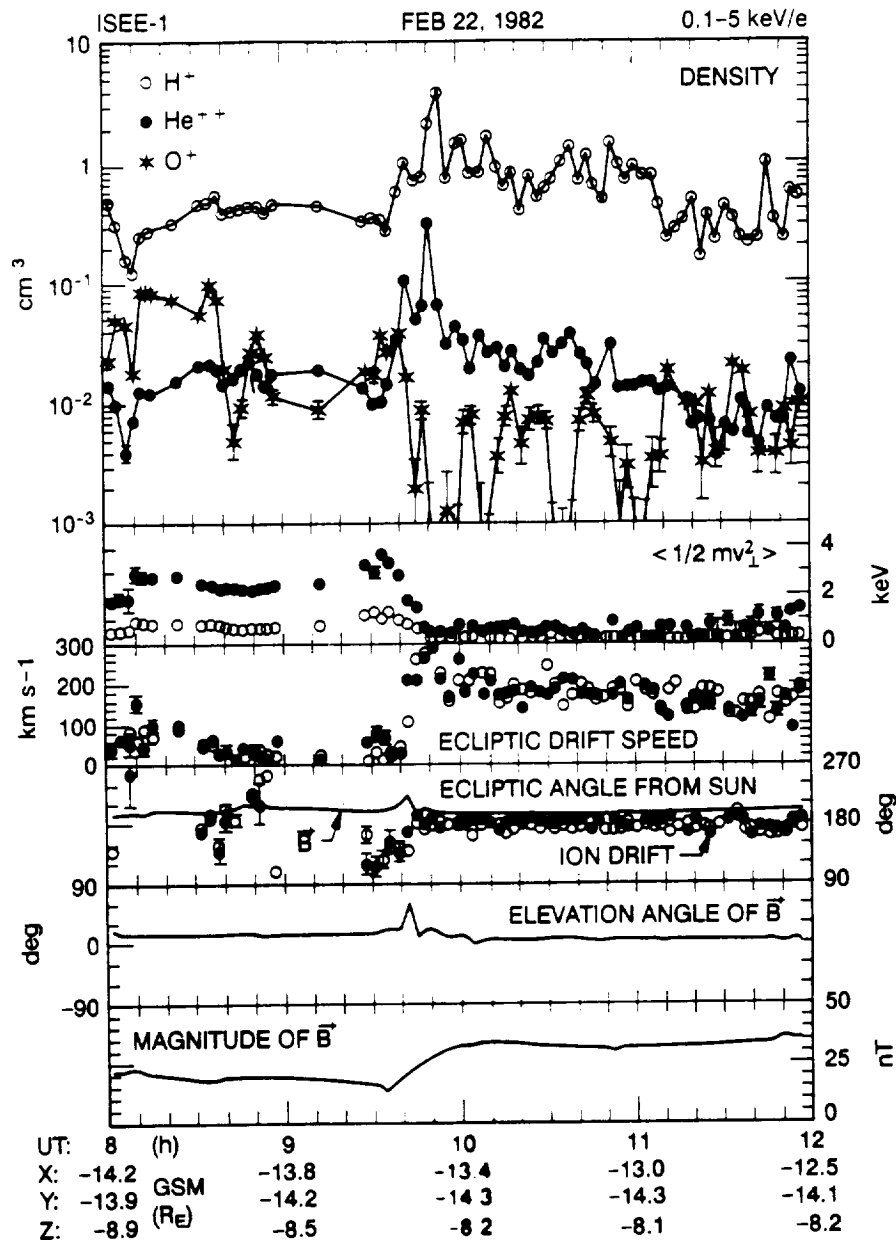
Fig. 8. From top to bottom: number densities; thermal energies associated with motion perpendicular to bulk flow vector (in solar ecliptic plane); bulk flow speeds; longitude angles of bulk flows and of local magnetic field (solid line) counted positive eastward from Sun direction; elevation angle of local magnetic field (above and below ecliptic plane); magnitude of same. Error bars show standard deviations (±one sigma) carried over from counting statistics (mostly smaller than data symbol).

shown). As a result, the time resolution is fairly high here, with each scan cycle requiring about 2.8 min. The coverage is continuous, except for a few data gaps prior to 0930 UT. The ISEE 1 magnetic field data [Russell, 1978] in the bottom three panels have been averaged over the 2.8-min cycle time of the mass spectrometer and are represented by points centered at the middle of each cycle and interconnected by solid lines.

The ion data in Figure 8 are in the form of velocity moments, calculated by the second method described in section 3 above (assuming rotational symmetry around the flow velocity vector). Before discussing the content of Figure 8 it may be of interest to compare the resulting ion

number density with the electron density that Etcheto and Saint-Marc inferred from plasma wave data obtained by the ISEE 1 and 2 relaxation sounder. Such a comparison is shown in Figure 9.

The ion density in Figure 9 is based on the total ion count rate, assuming that it is dominated by H^+ counts. This provides for a more continuous coverage in time than summing the H^+, He^{++}, and O^+ densities. In this case it is also well justified to assume that the H^+ ions are dominant, as is clear from Figure 8 (top panel). In any case, the ion density is in fair agreement with the electron density when they both peak, while it tends to be lower afterward, forming the lower envelope of the many electron density values. One

ISEE FEBRUARY 22, 1982
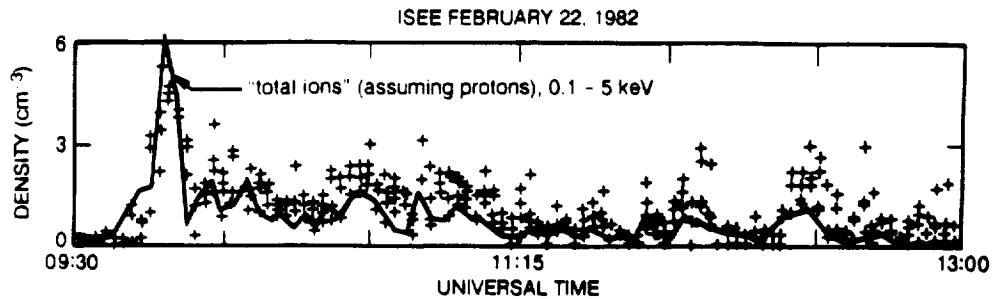
Fig. 9. Comparison between ion density calculated from total ion count rates (solid line; assuming all H⁺) and the electron density inferred from wave data (pluses; the latter from *Etcheto and Saint-Marc* [1985]).

possible explanation for this trend is that the ion bulk flow is sufficiently fast to bring most ions to energies above 0.1 keV/e at the time of the density peak, which is indeed when the flow speeds are at their maximum (Figure 8; third panel down), while it is insufficient later on. Other explanations may involve the different temporal resolutions of the two kinds of measurements.

Returning to Figure 8, it can be seen that the population of H⁺ and He⁺⁺ ions changes character at about 0940 UT. Prior to this time the ISEE 1 spacecraft is within the central plasma sheet, although close to its southern boundary and far toward the dawn flank (fairly low thermal energies in the second panel); after this time it is within the southern PSBL, as inferred by *Etcheto and Saint-Marc* [1985]. While in the central plasma sheet, the instrument measures an essentially isotropic population of H⁺ and He⁺⁺ ions, one that is drifting only slowly (third panel) and in varying directions (fourth panel), having most of its energy in the form of thermal (random) motion (second panel). After 0940 UT, while in the PSBL, the instrument measures a strongly ansotropic population of these ions, one that is flowing rapidly and fairly steadily antisunward, or tailward, and has much lower thermal energies. The latter population appears quite solar wind like, even though the sum of the bulk flow energy and the thermal energy (including thermal motion along the flow vector), observed to vary between 0.3 and 1.2 keV/nucleon, is somewhat low compared to the solar wind energies at this time (1.3 to 1.5 keV/nucleon [cf. *Couzens and King*, 1986]).

It may be noted that this solar wind like ion population is observed on a day which is not extremely quiet but actually somewhat disturbed. The 3-hour *Kp* index during the first half of this day has the values 3+, 5−, 3−, and 4, and the hourly *AE* index ranges between 86 and 660 (being highest between 1000 and 1100 UT). Had the ISEE 1 spacecraft been well within the central plasma sheet at this time, the H⁺ and He⁺⁺ mean energies would probably have been measured to be about 3 to 4 keV/nucleon, according to Figure 1. It may also be noted that the antisunward flow of the H⁺ and He⁺⁺ ions after 0940 UT in the fourth panel of Figure 8 is not exactly along the magnetic field vector, but some 10°–40° to the right, that is toward the interior of the tail. This translates to a cross-*B* drift in the range of 30–100 km s⁻¹ and is consistent with there being duskward **E × B** drift in the PSBL on the dawnside. This particular feature will be dealt with at some length in section 6.

5.2. Some Events Observed at Substorm Onsets

Plasma flows located in a layer of limited extent in GSM *Z*, such as the PSBL, are most readily detected when this layer

moves back and forth across the path of the ISEE 1, which often happens in conjunction with substorm activity [cf. *Eastman et al.*, 1985]. Antisunward flows of the kind illustrated in Figure 8, even if they exist most of the time, may therefore tend to be observed as transient events. An example of such transient flows is illustrated in Figure 10.

Figure 10 has basically the same format as Figure 8, but the data from each accumulation period are displayed as horizontal segments or bars. The instrument energy-mass scan cycle, as indicated by the horizontal bars, is much longer in this case, about 17 min, and consists of multiple scans through every fourth energy channel at various values of M/Q, covering the full energy range for each M/Q by using alternating sets of energy channels. Each energy is maintained for 4 s (1.3 spin revolutions). This cycle time is too long to adequately resolve the substorm dynamics, but by interpolating the total ion count rates in energy and assuming that these are dominated by H⁺ ions, it is possible to calculate "total ion" moments at a higher rate, as shown by the solid lines in the top three panels. The magnetic field data shown by solid lines in the bottom three panels have been averaged over the same time intervals used for the total ion data. Mass analyzed data are shown for H⁺, He⁺⁺, and O⁺, using the same symbols as in Figure 8, as well as densities only for He⁺ ions (crosses; top panel). Due to the rather complex energy-mass scan, it is not practical to display the various ions with their actual sampling times within each scan cycle. It is important to remember, however, that each ion species has been measured intermittently, and that different species have been sampled minutes apart. This probably accounts for most of the differences in flow speed and direction between H⁺ and He⁺⁺ ions, for example (third and fourth panels).

The event of special note here is the density peak near noon (top panel). This peak is similar in magnitude to the peak density in Figure 8, when measured by the total ions, and like the peak in Figure 8 it contains H⁺ and He⁺⁺ ions with very low thermal energies (second panel) and rather fast antisunward flow (third and fourth panels). This particular event is one of about two dozen substorm onset events which were brought to the attention of the author by C. Y. Huang (private communication, 1988) (see also *Huang et al.* [1992]). One probable effect of this substorm [*Huang et al.*, 1992] is the sharp rise in the ion thermal energies after 1200 UT. This was a rather moderate substorm, with the hourly *AE* peaking about 300 nT. Prior to this substorm the *AE* had remained about 50–100 nT for many hours.

The antisunward flows of H⁺ and He⁺⁺ ions in Figure 10, clearly observed during five of the 14 instrument scan cycles
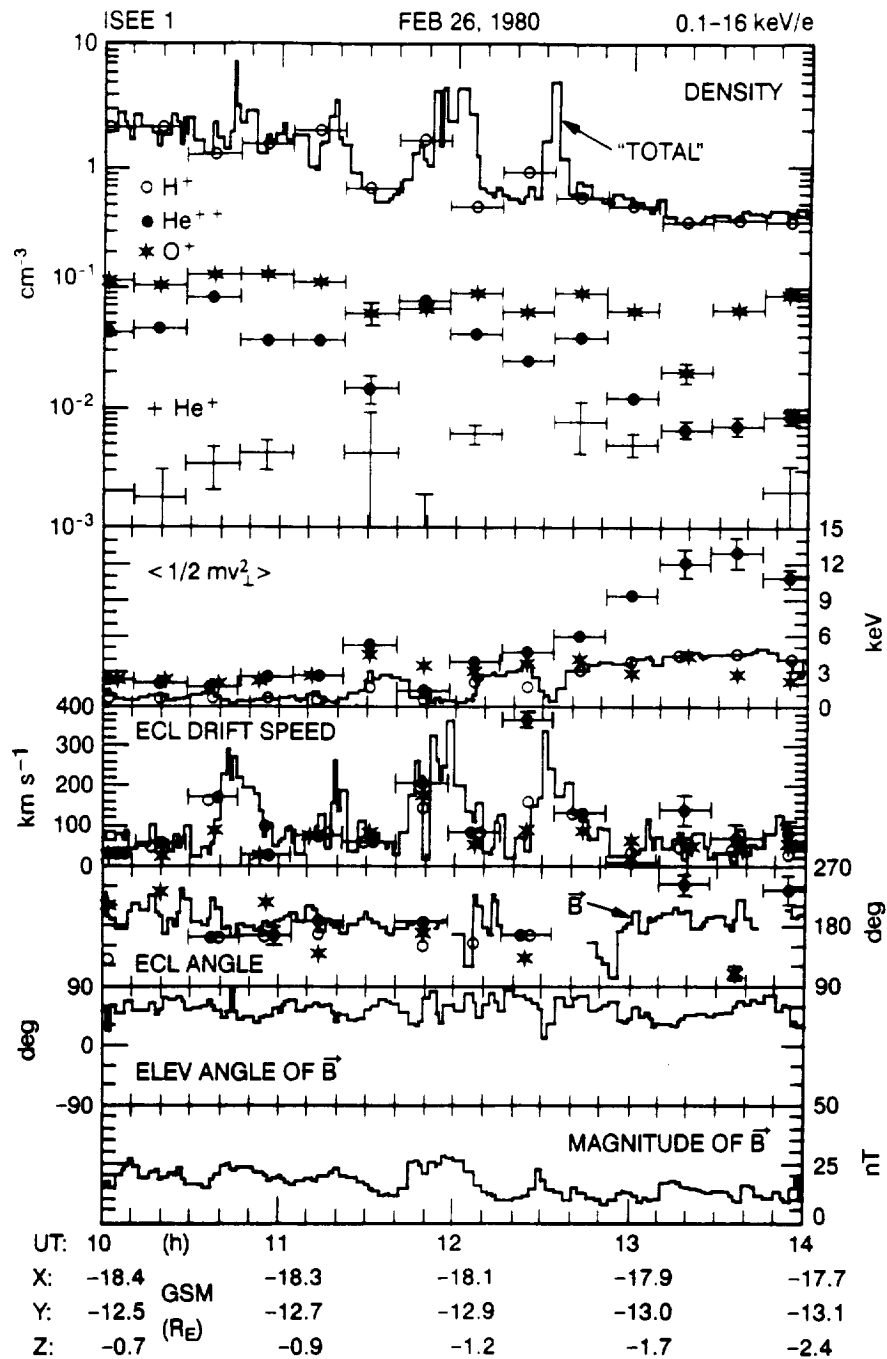
Fig. 10. Same format as Figure 8, except that the mass resolved moments have been averaged over longer intervals (horizontal bars), and the moments based on total count rates (assuming H⁺ and using shorter averaging) have been included in the top three panels, shown by solid lines. Note that in the bottom three panels, solid lines refer again to the local magnetic field.

(fourth panel), are also located far toward the dawn flank, like those in Figure 8. There is, however, a significant difference in the magnetic field between the two figures. In Figure 8, after about 1000 UT, the field is nearly parallel to the ecliptic plane (second panel from bottom) and fairly constant in magnitude (bottom panel), two conditions that are common in the vicinity of the tail lobes and therefore consistent with this region being the PSBL, as inferred by *Etcheto and Saint-Marc* [1985] (compare also *Parks et al.* [1984]), although those same conditions probably apply equally well to the plasma mantle (tail lobe magnetopause

boundary layer [cf. *Rosenbauer et al.*, 1975]). In Figure 10, by contrast, the magnetic field elevation angle is variable and generally greater than 30°, and the field magnitude also varies, and it is weaker than in Figure 8. These conditions are more typical of the central plasma sheet, but they are probably also consistent with the LLBL (low-latitude magnetopause boundary layer [cf. *Eastman et al.*, 1976]).

Based on the in situ data alone, it cannot be excluded that the antisunward flows in Figure 10 are located in the LLBL, rather than in the plasma sheet, although this distinction depends on one's definition of the LLBL. The data in Figure
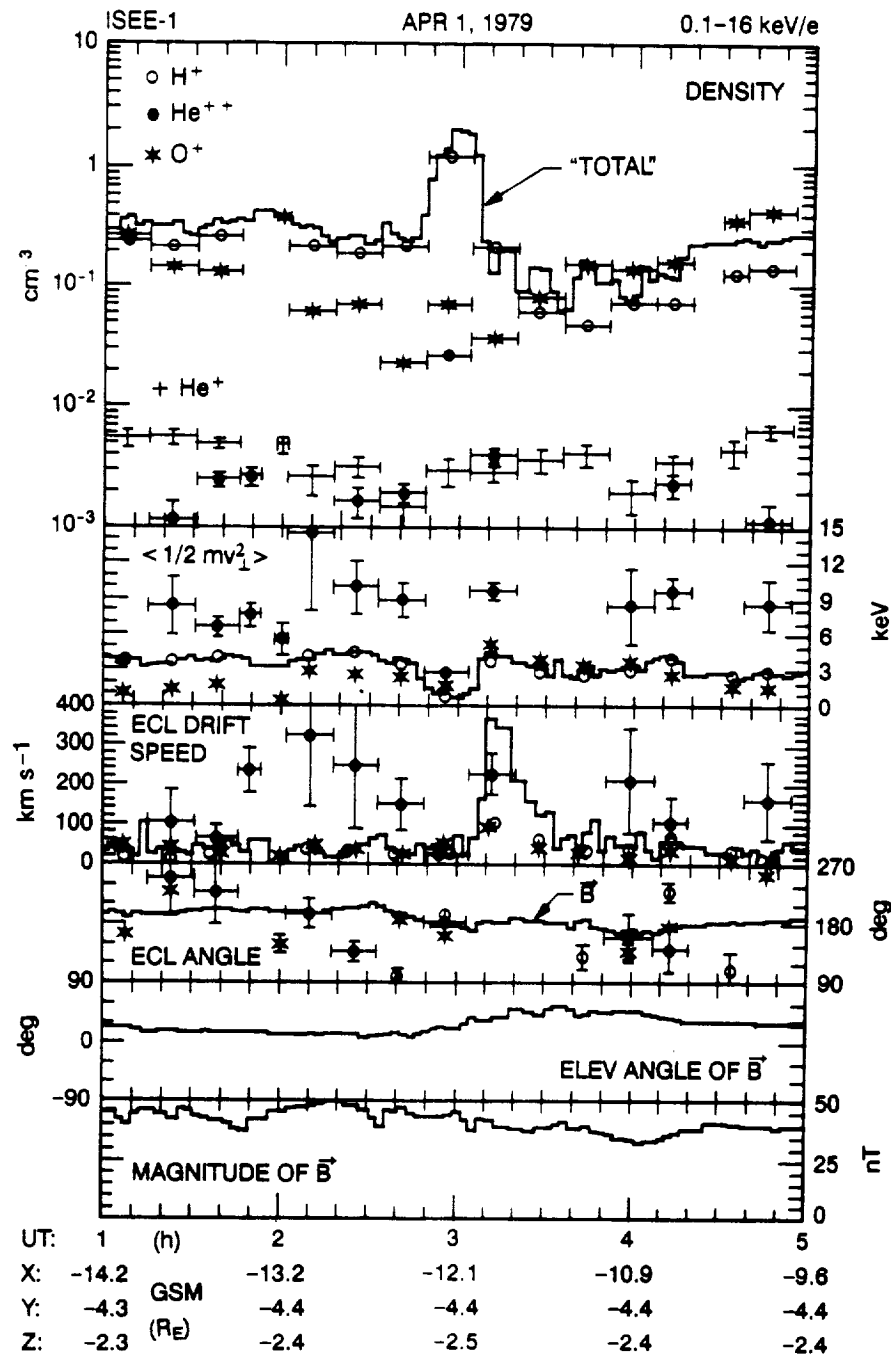
Fig. 11. Same format as Figure 10, except the energy-mass scan cycle is slightly shorter.

10 were obtained at about 13 R_E distance from the GSM X axis (from the Earth-Sun line), near GSM $X = -18\ R_E$, which would seem to be well inside of a nominal magnetopause. Compared to Figure 8, the ISEE 1 is 3–4 R_E closer to the GSM X axis in Figure 10 and 4–5 R_E farther down the tail, so it ought to be several R_E farther away from the magnetopause in Figure 10 (including tail flaring). The magnetopause location does depend on solar wind conditions, but those conditions, according to *Couzens and King* [1986], do not suggest that the magnetopause is more compressed at the time of Figure 10.

Since it may be doubted that the antisunward flows of H$^+$ and He^{++} ions in Figures 8 and 10 are really inside the

magnetotail, it is worth considering Figure 11. Figure 11 has the same identical format as Figure 10, except the energy-mass scan cycle is slightly shorter. Again of special note, the density peak is near the center of Figure 11 (top panel), around 0300 UT. As in Figures 8 and 10, this peak contains H$^+$ and He^{++} ions with reduced thermal energy (second panel), which are flowing antisunward (fourth panel). The most noticeable difference from before is the much lower flow speed, only a few tens of km s^{-1} (third panel). The O$^+$ ions are more abundant here than in either of Figures 8 and 10, but only the H$^+$ and He^{++} ions have a distinct peak in their densities around 0300 UT, which is consistent with the peak being dominated by ions of solar origin. Hence, in this

case a dense population of antisunward flowing solar wind like ions is located only about 5 R_E from the GSM X axis, at GSM $X = -12$ R_E, which surely is far inside of any realistic magnetopause (solar wind conditions fairly normal at this time). Judging from the geomagnetic field magnitude and direction (bottom three panels), this event is very likely in the southern PSBL. This interpretation is further supported by the fact that the ion densities and energies are plasma sheet like both before and after (compare Figure 1).

The antisunward flow near 0300 UT in Figure 11 is yet another event from the aforementioned list of substorm onsets (C. Y. Huang, private communication, 1988). In this case there is not a marked increase in the H^+ and He^{++} thermal energies, when compared to conditions before the flow event, but there is another feature commonly associated with substorms in the ISEE data: the antisunward ion flow at substorm onset is followed by a burst of rapid sunward ion flow [cf. Eastman et al., 1985]. The latter is best seen in the total ion data here by the peak drift speed between 0310 and 0320 UT (third panel). Since the flow direction is sunward at this time, also in the mass resolved H^+ and He^{++} data, it falls outside of the angular range of the fourth panel. As in the case of Figure 10, the substorm is fairly moderate, with a peak hourly AE of 561 nT between 0300 and 0400 UT.

Rather than showing more of these events in the format of Figures 10 and 11, the most relevant parameters of the entire set have been listed in Table 1, and the spatial location of each event has been indicated in a graphical format in Figure 12. The numbering is the same in Table 1 and Figure 12 and is ordered by dates. The events in Figures 10 and 11 have events 14 and 3, respectively. The event in Figure 8 has also been included as event 23.

The times listed in Table 1 are times of persistent antisunward flow, as defined by the total ion count rates, called "all ions" here. The flow during these intervals remains between 90° and 270° from the sunward direction in almost all cases, and it is generally between 150° and 210° when the number density peaks (assuming H^+ ions). A few of the longer intervals include one or two brief (1–3 min each) excursions into the sunward sector. The maximum flow speed during each interval either coincides with the maximum number density or occurs adjacent to it. The mass resolved data, in all but one event, refer to the single energy-mass scan cycle that contains the maximum in the "all ion" number density. The only exception is event 23 (Figure 8), where two adjacent energy-mass scan cycles at the density peak have been averaged in order to give more equal weights to the H^+ and He^{++} ions (only 2.8 min per scan cycle in that case). The mean energies listed in Table 1 are total energies, including the bulk flow energy. The percentage ratios in the rightmost column refers to number densities.

The time intervals in Table 1 generally precede the substorm onset as defined by C. Y. Huang (time of increasing energetic ion fluxes [cf. Huang et al., 1992]), and some of them end as early as 10 min or more prior to onset, as the ISEE 1 moves into a tail lobe with count rates too low to provide reliable moments (plasma sheet thinning). In about half of the 23 events the antisunward flow is observed as the ISEE 1 moves from the plasma sheet and into the southern or northern tail lobe, suggesting that the flow is located in or near the PSBL in those events. In all events, except events 8 and 14, the magnetic field magnitude and direction at least make it probable that the location is adjacent to a tail lobe. This includes a consideration of the ion beta values, which
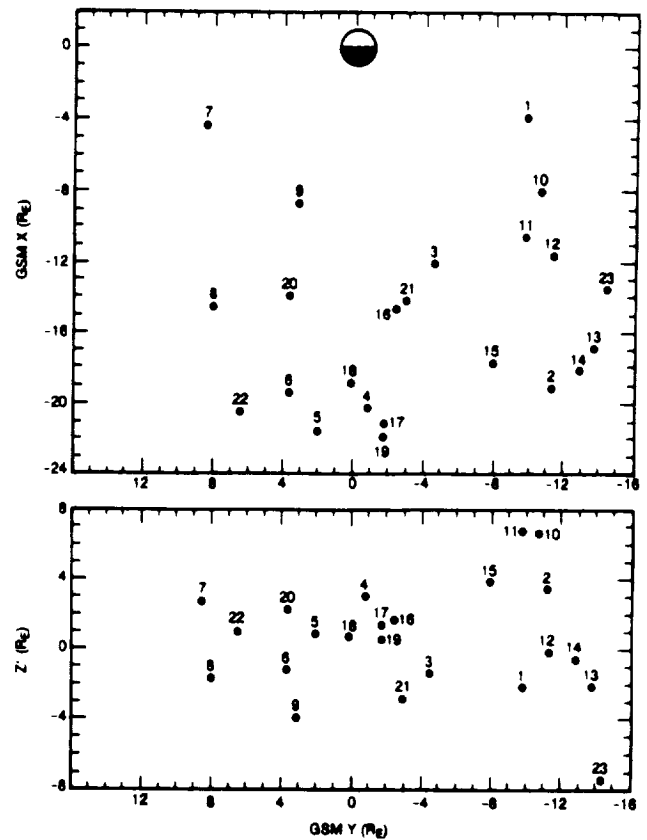
Fig. 12. Location of events of antisunward flowing H^+ and He^{++} ions (at middle of event; see Table 1). Top panel shows location in GSM X versus Y; bottom panel shows distance above and below nominal "neutral sheet", as defined by Fairfield and Ness [1970].

are less or much less than unity in all events but events 8 and 14. Of the latter two, event 14 has already been discussed above (Figure 10). Event 8 may be in the central plasma sheet (compare Figure 12).

In all events listed in Table 1 the H^+ ions are dominant, their density being at least 10 times higher than that of the second most abundant species, which is either the He^{++} or O^+. Considering the energies of the H^+ ions, as listed in the fourth column from the right, it would be reasonable to assume that these ions are of terrestrial origin, having been accelerated upward in the auroral regions [cf. Yau et al., 1985]. This would probably seem the most logical interpretation if only the total ion flux was being measured, without the benefit of mass separation. Even with the ions separated, this interpretation comes to mind, since the H^+ ions are observed together with O^+ ions that are almost certainly of terrestrial origin. However, when the energies of those two species are compared (O^+ energies in the second column from the right), it is seen that the O^+/H^+ energy ratio ranges from a low of 0.16 to a high of 6.7, which is a 42-fold range. This contrasts with the He^{++}/H^+ energy ratio (He^{++} energies in the third column from the right), which only ranges between 2.6 and 5.1. Expressed in a statistical average and a sample standard deviation,

$$O^+\text{-energy}/H^+\text{-energy} = 2.1 \pm 2.1$$

$$He^{++}\text{-energy}/H^+\text{-energy} = 3.7 \pm 0.7$$

TABLE 1. Some Events of Antisunward Flow

| | Event | | All Ions | | Mass Resolved | | | |
| | | | | | Mean Energy, keV | | | |
No.	Date, year/day	Time, UT	V_{max}, km/s	N_{max}, cm^{-3}	H$^+$	He^{++}	O$^+$	He^{++}/H$^+$, %
1	79/050	1351–1400	200	0.45	3.06	10.3	0.49	5.1
2	79/061	1104–1147	130	0.82	1.59	6.56	7.82	3.3
3	79/091	0252–0302	60	2.04	1.17	4.16	1.72	2.2
4	79/100	0441–0528	70	0.49	2.90	10.9	4.49	2.0
5	79/104	1551–1707	220	0.40	3.71	9.55	3.50	5.0
6	79/114	1445–1522	300	0.18	5.11	17.5	6.09	1.7
7	79/127	1150–1221	200	0.25	1.97	9.57	0.81	1.3
8	79/138	1749–1829	30	0.79	3.69	12.1	1.58	1.3
9	79/143	2015–2027	25	0.12	2.15	8.49	3.85	5.6
10	80/018	0754–0831	70	0.20	2.53	9.73	0.97	1.7
11	80/030	0809–0902	45	0.41	1.72	7.38	1.62	1.3
12	80/032	2000–2010	230	0.07	2.75	13.9	2.31	1.6
13	80/050	0357–0410	225	0.18	4.83	12.3	5.11	1.3
14	80/057	1145–1206	365	4.46	1.11	3.11	7.36	4.7
15	80/059	0759–0836	125	0.15	3.48	10.5	5.59	1.6
16	80/068	1509–1600	50	0.47	2.00	7.74	4.45	2.2
17	80/083	1051–1113	100	0.88	0.94	4.18	6.26	3.5
18	80/085	1406–1520	120	1.66	0.50	1.91	3.37	1.7
19	80/091	0235–0309	160	1.60	1.97	7.20	3.70	3.6
20	80/092	1228–1250	35	0.14	1.33	5.04	2.46	4.5
21	80/094	0316–0323	30	0.28	1.49	6.24	1.11	6.4
22	80/107	1026–1055	65	0.39	1.35	5.74	3.53	4.8
23	82/053	0936–1300	290	6.16	0.75	2.35	1.38	6.5

Hence there is virtually no correlation between the H$^+$ and O$^+$ ions in terms of energy (correlation coefficient = 0.1), whereas the H$^+$ ions are fairly well correlated with the He^{++} ions, which are presumably of solar origin (correlation coefficient = 0.9). The modest scatter in the He^{++}/H$^+$ energy ratio may be due in part to a small and variable terrestrial component of the H$^+$ but is probably also due in large part to the fact that different ion species are always sampled at slightly different times (minutes apart). This correlation between the H$^+$ and He^{++} energies, coupled with the fact that the He^{++}/H$^+$ energy ratio is close to the same as in the solar wind (about 4.0), makes it very plausible that the antisunward flows listed in Table 1 are all dominated by ions from the solar wind.

It should also be pointed out that the H$^+$ and He^{++} ions observed during these events resemble the ion component of a plasma region recently described by Zwolakowska and Popielawska [1991]. This region, named the "warm envelope of the plasma sheet" by Zwolakowska and Popielawska is located between the tail lobes and the hotter and more isotropic plasma sheet, and it is characterized by densities greater than 0.1 cm^{-3}, electron temperatures lower than 100 eV, and an ion component dominated by H$^+$ and He^{++} ions with a solar wind like ratio. It has the greatest thickness (in GSM Z) during periods of northward IMF and is the thickest near the flanks of the tail. It is presumably related to the PSBL, which has been defined mostly by ISEE data, but the relationship is unclear, according to the authors, perhaps due in large part to different measuring conditions. Their observations have been made from the Russian spacecraft Prognoz 8, which, like the ISEE 1 and 2 spacecraft, has a strongly elliptical orbit (apogee at 30 R_E) but an orbit of much greater inclination (65°), providing almost perpendic-

ular traversals of the northern lobe. Zwolakowska and Popielawska suggest that this "warm envelope" consists mostly of solar wind plasma originating from the LLBL. Unfortunately, the orientation of the Prognoz 8 spin axis (sunward) precludes a direct verification of the antisunward flows described here.

6. DISCUSSION

Given Table 1 and Figure 12, the natural question to ask is: What mechanism brings solar wind ions to these locations inside the tail, in most cases without substantially increasing their total energy (bulk flow energy plus thermal energy)?

At first glance, it might seem possible that these antisunward flowing ions actually entered much farther down the tail, where they were deflected toward Earth (sunward) by the mechanism discussed by Speiser [1965] and others and subsequently mirrored close to Earth before being intercepted by the ISEE 1. This interpretation does have problems in these cases, however. One is the energies; these ions do not generally have energies quite as large as one would expect from this mechanism, where the initial deflection is caused by the combined action of a dawn-to-dusk electric field, which accelerates the ions, and the Z component of the geomagnetic field [cf. Lyons and Speiser, 1982]. Another problem is the location; the mirrored and antisunward flowing ions would be expected to be closer to the midplane of the plasma sheet than the sunward flowing ions, due to E × B drift in the dawn-to-dusk electric field. In all cases where the ISEE 1 enters either of the lobes, the antisunward flowing ions are found adjacent to the lobe, and there is no evidence of sunward flows in the lobe itself (not illustrated).

Another possibility, which is the one argued here, is that
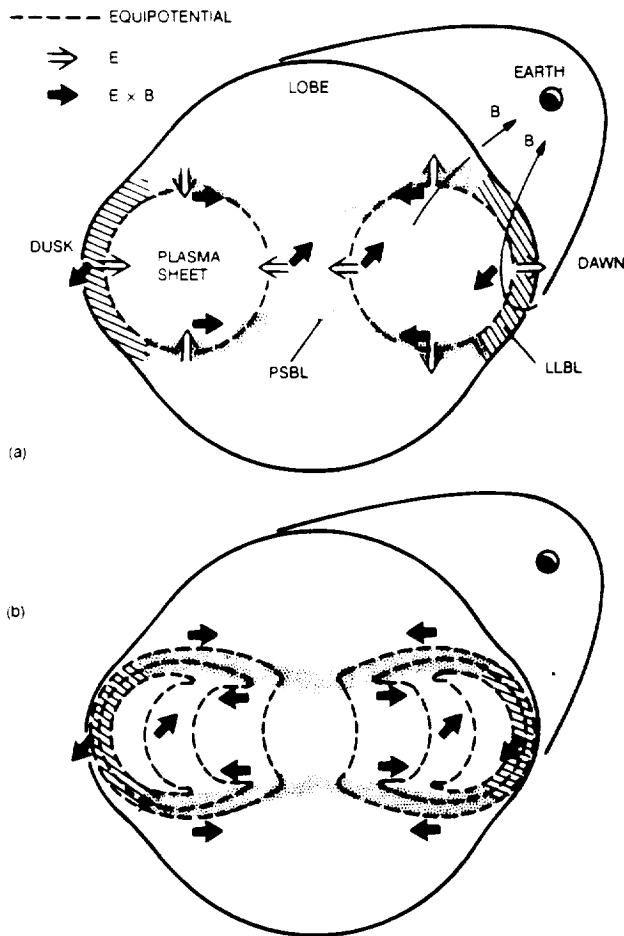
Fig. 13. Cross sections of a geomagnetic tail with internal closure of equipotentials (tubular) associated with electric field in the low latitude magnetopause boundary layer (LLBL). (a) Conceptual geometry showing associated electric field (open arrows) and E × B drift (solid arrows). (b) Equipotentials adjusted to fit observed cross-B drifts in central plasma sheet (see text).

these ions reach their point of observation by duskward or dawnward E × B drift parallel to the PSBL, having entered the tail on the flanks, in the LLBL (on closed field lines [cf. Eastman et al., 1976]), or at the junction of the LLBL and the plasma mantle (on open field lines [cf. Rosenbauer et al., 1975]). A feasible mechanism for this kind of motion is shown schematically in Figure 13.

Figure 13 is based on the fact that the LLBL on either flank is at least partially situated on closed geomagnetic field lines, and is therefore associated with a polarization electric field directed toward dawn [e.g., Eastman et al., 1976; Mitchell et al., 1987]. This field, having the same direction on both the dawn and dusk flanks, allows the boundary layer plasma to flow tailward (antisunward). The mechanism responsible for these boundary layers need not be an issue here; the essential aspects are empirical: the LLBL is virtually always present and appears to contain plasma of mostly solar origin at energies below 10 keV [Mitchell et al., 1987].

Even though the electric field in the LLBL may vary in magnitude over the course of time, it does maintain its dawnward orientation, at least in an average sense, and therefore must have a curl-free component, as assumed in

Figure 13. Another way of stating this is to integrate Faraday's law from time t_1 to time t_2, choosing these times such that the tail magnetic field has identical configurations at both t_1 and t_2:

$$\int_{t_1}^{t_2} (\text{curl } \mathbf{E}) \ dt = \text{curl} \left(\int_{t_1}^{t_2} \mathbf{E} \ dt \right) = -\int_{t_1}^{t_2} \left(\frac{\partial}{\partial t} \mathbf{B} \right) dt = 0$$

In other words, the time-averaged electric field must be curl-free, at least, which means that it must be associated with closed equipotential surfaces. Whether all such surfaces close within the tail, as suggested in Figure 13, may be questionable, but the ones that do will encounter a different magnetic field orientation at different points, as indicated in Figure 13a. Since the electric field is perpendicular to each equipotential surface (open arrows), the associated E × B drift direction will vary as indicated by solid arrows. These arrows have the proper directions, near both dusk and dawn and near both the northern and southern lobes, to transport solar plasma (ions and electrons) from the tail flanks and into the central plasma sheet.

Is this potential configuration supported by data? The electric fields near the midplane, in both the LLBL and the central plasma sheet, have the directions usually associated with those regions in the literature, so the questionable parts are the ones ascribed to the PSBL here. Unfortunately, the spin axis of the ISEE 1 is generally parallel or antiparallel to the expected directions of the electric field in these parts, so the ISEE 1 Double Probe Experiment [Mozer et al., 1978], having booms extended only within the spin plane, is not well suited to prove or disprove this picture.

Of the antisunward flows examined here, event 23 in Table 1 shows the most consistent drift across the magnetic field in a direction that agrees with Figure 13a (compare Figure 8, fourth panel, after 0945 UT). The other events present a more complex picture. If the total ion moments are used (assuming H+ ions are dominant), in order to maximize time resolution (1-3 min), the drift velocity during several events shifts, once or more, from one side of the magnetic field to the other, and in some cases the drift is consistently opposite to the direction prescribed by Figure 13a for that quadrant of the tail. Barely more than half of the events show a clear predominance of drift in the "right" direction. On the other hand, if the equipotential surfaces are folded near the lobes, as outlined in Figure 13b, they can be made consistent with the observed drift directions, assuming that the events with a drift toward the flanks are observed further into the plasma sheet. This is not a mere contrivance; equipotential surfaces of this shape could be produced by a net charge in the PSBL, a charge with the same polarity as the inside of the adjacent LLBL (positive at dawn, negative at dusk).

Some indirect support for Figure 13 may be found in the works of Orsini et al. [1990, and references therein]. They have examined a large number of strongly collimated antisunward flows of ions in or near the PSBL, using the ISEE 2 EGD Positive Ion Experiment [Bonifazi et al., 1978], covering energies between about 50 and 5 keV/e. The ions have been observed during geomagnetically disturbed periods, and have been identified as O+ ions, using concurrent data from the ISEE 1 Plasma Composition Experiment. The EGD instrument, when pointing in a sunward sector, provides a higher angular resolution (5.6° or 2.8°, depending on bit rate) than the Plasma Composition Experiment and is

ISEE-1: CENTRAL PLASMA SHEET
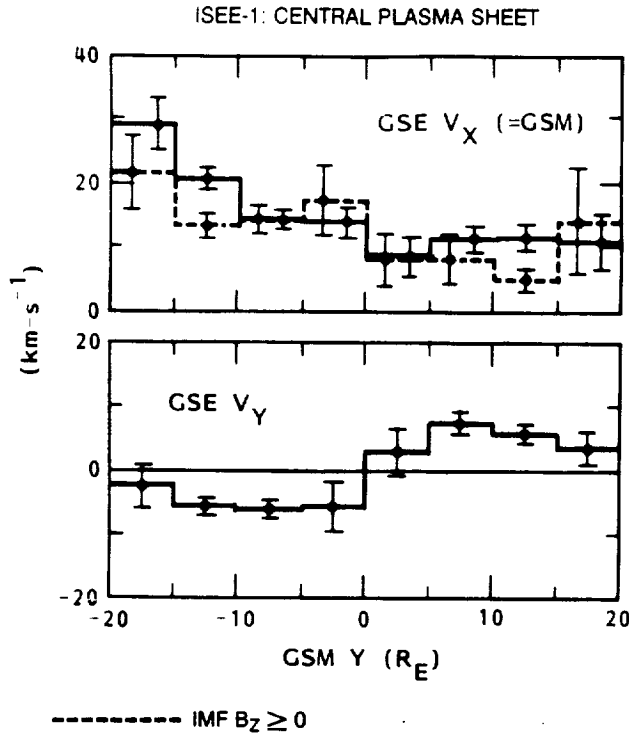
Fig. 14. Average plasma sheet H$^+$ drift velocity perpendicular to B and parallel to solar ecliptic plane (GSE X-Y plane; see text for definition). Solid lines show averages of all samplings, regardless of solar wind conditions; dashed line in upper panel only includes samplings taken while the concurrent hourly IMF B_Z remained northward (for up to 3 hours at a time). The corresponding average of the V_Y component is not significantly different from the one shown in the lower panel and has been omitted. (Error bars show standard deviation of the averages.)

more sensitive to the relative orientation between the ion flow and magnetic field directions. The statistical results of *Orsini et al.* show strong evidence of E × B drift (up to 40 km s^{-1}) from the tail flanks toward the center of the tail on the northern lobe side of the plasma sheet (e.g., Figure 10 of *Orsini et al.* [1990]), in agreement with Figure 13a or 13b. Their results suggest a similar situation on the southern lobe side of the plasma sheet, but the statistics is poor there. Their results also indicate that the E × B drift reverses direction across the PSBL and point toward the flanks immediately inside the plasma sheet. This would again suggest that the equipotential surfaces of Figure 13a be modified as shown in Figure 13b.

Further corroborating evidence for E × B drift toward the flanks inside the plasma sheet can be found among the results of the statistical study discussed in section 4 (among results not previously published). This is illustrated in Figure 14, which shows the average GSE X and Y components (spin plane components) of the H$^+$ bulk velocity in the central plasma sheet, derived under the restriction that only measurements at pitch angles between 45° and 135° be included in the moment calculations. These velocity components are thus rough measures of the average ion drift perpendicular to the measured magnetic field (and in the spin plane). According to this figure, the ion drift inside the plasma sheet is generally sunward, even during periods of northward IMF, and toward the dawn and dusk flanks. This is consistent with

a spatial averaging of the E × B drift produced by the equipotential surfaces in Figure 13b, not including the drift immediately adjacent to the lobes. The lobes and the near-lobe regions of the plasma sheet were intentionally excluded from the statistical material used for Figure 14 (compare criteria used by *Lennartsson and Shelley* [1986]).

It should be mentioned that *Orsini et al.* [1990] interpreted their results in terms of a slightly different electric field model, namely the one constructed by *Rostoker and Bos-tröm* [1976]. One salient feature of that model is charge layers between the lobes and the plasma sheet, positive on the dawn side of midnight, negative on the dusk side, predicting the same kind of dawn-dusk and dusk-dawn drifts as observed by Orsini et al. around the PSBL. This is the only model feature addressed by *Orsini et al.*, so their results can also be seen as indirect support of Figure 13b. The model of Rostoker and Boström differs somewhat from Figure 13b in the treatment of the central plasma sheet (Figure 4 of Rostoker and Boström), and it extends through the tail lobes, which Figure 13b does not address. As far as the central plasma sheet is concerned, it is worth remembering that Figure 13b is consistent with the observed average drifts in Figure 14. Furthermore, Figure 13b is by its definition consistent with the known direction of the electric field in the LLBL [e.g., *Eastman et al.*, 1976]. As far as the tail lobes are concerned, the electric field structure may be largely controlled by the electromagnetic conditions in the solar wind itself. Those same conditions probably influences the electric field in the plasma sheet as well, especially during geomagnetically disturbed times, but Figure 13b may nevertheless represent some kind of "ground state".

7. CONCLUDING REMARKS

Closing equipotential surfaces from the LLBL in accordance with Figure 13 could, in principle, provide access of solar wind plasma along slots between the tail lobes and the plasma sheet by means of E × B drift. That kind of access would explain why solar wind like H$^+$ and He^{++} ions can be observed flowing antisunward, along the tail magnetic field lines, in a region between the lobes and the central plasma sheet (Table 1 and Figure 12). Figure 13 does not necessarily require that these ions maintain an antisunward flow component along the magnetic field once they have crossed the magnetopause, but such a component may remain from the initial inertia of the ions in the magnetosheath. In any case, this component must eventually be converted to thermal motion as the ions enter the central plasma sheet, since in that region the ions are well known to be nearly isotropic [e.g., *Eastman et al.*, 1985; *Orsini et al.*, 1990].

The LLBL acts as a "voltage generator" in Figure 13 [e.g., *Eastman et al.*, 1976]. Since the LLBL is present during times of northward as well as southward IMF [e.g., *Mitchell et al.*, 1987], Figure 13 may provide access of solar plasma to the plasma sheet during a wide range of geomagnetic conditions, including times of extreme quiescence. This would satisfy condition 1 of section 4.2 (end of section; compare also Figures 1 and 3). Since, according to the findings of *Mitchell et al.* [1987], the LLBL may be entirely on closed magnetic field lines for northward IMF, but only partially so for southward IMF, and since the LLBL is also thicker for northward IMF, Figure 13 may even suggest that the solar wind access is the most efficient during times of

northward IMF, that is, during quiet times. That would help explain Figures 5 and 6. However, as mentioned in section 4.2, it is also conceivable that the lower H⁺ and He⁺⁺ densities during times of southward IMF are caused by increased loss in association with substorm activity.

Figure 13 may allow solar ions to enter the central plasma sheet fairly close to the earth (inside of 23 R_E), without requiring that they first visit a thin current layer ("neutral sheet") far downtail in order to be deflected earthward [e.g., Speiser, 1965]. As a consequence, the ions may at times fill the plasma sheet while undergoing little or no net energization. That would satisfy condition 2 in section 4.2. Moreover, having the solar ions enter the near-Earth plasma sheet this way, rather than by earthward jetting from some distant location downtail, may be easier to reconcile with the previous finding by Lennartsson and Shelley [1986] that the He⁺⁺ (and H⁺) ions are significantly less energetic near the northern and southern edges of the central plasma sheet than they are near GSM $Z = 0$ (see Figure 12 of Lennartsson and Shelley). In other words, Figure 13 does not require that the northern and southern boundaries of the plasma sheet be dominated by very fast moving, earthward jetting ions, as might be the case if all solar ions were to arrive from the distant tail under the influence of a dawn-to-dusk electric field.

Finally, there are reasons to believe that the LLBL on the tail flanks would form even if the solar wind itself had no magnetic field [e.g., Coleman, 1971; Eastman et al., 1976; Olson and Pfitzer, 1985]. One feasible mechanism is provided by the gradient B drifts of solar wind particles in the outer fringes of the geomagnetic field, drifts that are in opposite directions for ions and electrons and are capable of generating boundary layer electric fields with the proper polarity [Olson and Pfitzer, 1985]. Closing the associated equipotential surfaces in accordance with Figure 13 could therefore provide access of solar wind plasma to the earth's plasma sheet even in the absence of an interplanetary magnetic field (IMF). That would satisfy condition 3 in section 4.2.

REFERENCES

Axford, W. I., and C. O. Hines, A unifying theory of high-latitude geophysical phenomena and geomagnetic storms, Can. J. Phys., 39, 1433, 1961.
Balsiger, H., P. Eberhardt, J. Geiss, and D. T. Young, Magnetic storm injection of 0.9- to 16-keV/e solar and terrestrial ions into the high altitude magnetosphere, J. Geophys. Res., 85, 1645, 1980.
Baumjohann, W., G. Paschmann, and C. A. Cattell, Average plasma properties in the central plasma sheet, J. Geophys. Res., 94, 6597, 1989.
Bonifazi, C., P. Cerulli-Irelli, A. Egidi, V. Formisano, and G. Moreno, The EGD positive ion experiment on the ISEE B satellite, IEEE Trans. Geosci. Electron., GE-16, 243, 1978.
Borrini, G., J. T. Gosling, S. J. Bame, and W. C. Feldman, Helium abundance variations in the solar wind, Sol. Phys., 83, 367, 1983.

Chappell, C. R., T. E. Moore, and J. H. Waite, Jr., The ionosphere as a fully adequate source of plasma for the Earth's magnetosphere, J. Geophys. Res., 92, 5896, 1987.
Christon, S. P., D. J. Williams, D. G. Mitchell, C. Y. Huang, and L. A. Frank, Spectral characteristics of plasma sheet ion and electron populations during disturbed geomagnetic conditions, J. Geophys. Res., 96, 1, 1991.
Coleman, P. J., Jr., A model of the geomagnetic cavity, Radio Sci., 6, 321, 1971.
Collin, H. L., W. K. Peterson, J. F. Drake, and A. W. Yau, The helium components of energetic terrestrial ion upflows: their occurrence, morphology, and intensity, J. Geophys. Res., 93, 7558, 1988.
Couzens, D. A., and J. H. King, Interplanetary medium data book, supplement 3, 1977–1985, Rep. NSSDC/WDC-A-R&S 86-04, NASA Goddard Space Flight Cent., Greenbelt, Md., 1986.
Cowley, S. W. H., Plasma populations in a simple open model magnetosphere, Space Sci. Rev., 26, 217, 1980.
DeCoster, R. J., and L. A. Frank, Observations pertaining to the dynamics of the plasma sheet, J. Geophys. Res., 84, 5099, 1979.
Eastman, T. E., E. W. Hones, Jr., S. J. Bame, and J. R. Asbridge, The magnetospheric boundary layer: Site of plasma, momentum and energy transfer from the magnetosheath into the magnetosphere, Geophys. Res. Lett., 3, 685, 1976.
Eastman, T. E., L. A. Frank, and C. Y. Huang, The boundary layers as the primary transport regions of the Earth's magnetotail, J. Geophys. Res., 90, 9541, 1985.
Etcheto, J., and A. Saint-Marc, Anomalously high plasma densities in the plasma sheet boundary layer, J. Geophys. Res., 90, 5338, 1985.
Fairfield, D. H., and N. F. Ness, Configuration of the geomagnetic tail during substorms, J. Geophys. Res., 75, 7032, 1970.
Feldman, W. C., J. R. Asbridge, S. J. Bame, and J. T. Gosling, Long-term variations of selected solar wind properties: IMP 6, 7, and 8 results, J. Geophys. Res., 83, 2177, 1978.
Ghielmetti, A. G., R. G. Johnson, R. D. Sharp, and E. G. Shelley, The latitudinal, diurnal, and altitudinal distributions of upward flowing energetic ions of ionospheric origin, Geophys. Res. Lett., 5, 59, 1978.
Hamilton, D. C., G. Gloeckler, F. M. Ipavich, W. Stüdemann, B. Wilken, and G. Kremser, Ring current development during the great geomagnetic storm of February 1986, J. Geophys. Res., 93, 14,343, 1988.
Heelis, R. A., J. K. Lowell, and R. W. Spiro, A model of the high-latitude ionospheric convection pattern, J. Geophys. Res., 87, 6339, 1982.
Heppner, J. P., Polar cap electric field distributions related to the interplanetary magnetic field direction, J. Geophys. Res., 77, 4877, 1972.
Heppner, J. P., and N. C. Maynard, Empirical high-latitude electric field models, J. Geophys. Res., 92, 4467, 1987.
Hones, E. W., Jr., Plasma flow in the magnetotail and its implications for substorm theories, in Dynamics of the Magnetosphere, edited by S. I. Akasofu, p. 545, D. Reidel, Hingham, Mass., 1979.
Hones, E. W., Jr., J. R. Asbridge, and S. J. Bame, Time variations of the magnetotail plasma sheet at 18 R_E determined from concurrent observations by a pair of Vela satellites, J. Geophys. Res., 76, 4402, 1971.
Huang, C. Y., and L. A. Frank, A statistical study of the plasma sheet: Implications for substorm models, Geophys. Res. Lett., 13, 652, 1986.
Huang, C. Y., L. A. Frank, G. Rostoker, J. Fennell, and D. G. Mitchell, Nonadiabatic heating of the central plasma sheet at substorm onset, J. Geophys. Res., 97, 1481, 1992.
Kamei, T., and H. Maeda, Auroral electrojet indices (AE) for January–June 1978, Data Book 3, World Data Cent. C2 for Geomagn., Kyoto Univ., Kyoto, Japan, April 1981.
Lennartsson, W., Plasma sheet ion composition at various levels of geomagnetic and solar activity, Phys. Scripta, 36, 367, 1987.
Lennartsson, W., and E. G. Shelley, Survey of 0.1- to 16-keV/e plasma sheet ion composition, J. Geophys. Res., 91, 3061, 1986.
Lundin, R., B. Hultqvist, N. Pissarenko, and A. Zakharov, The plasma mantle: Composition and other characteristics as observed by means of the Prognoz-7 satellite, Space Sci. Rev., 31, 247, 1982.
Lyons, L. R., and T. W. Speiser, Evidence for current sheet

acceleration in the geomagnetic tail, *J. Geophys. Res.*, *87*, 2276, 1982.

Mitchell, D. G., F. Kutchko, D. J. Williams, T. E. Eastman, L. A. Frank, and C. T. Russell, An extended study of the low-latitude boundary layer on the dawn and dusk flanks of the magnetosphere, *J. Geophys. Res.*, *92*, 7394, 1987.

Mozer, F. S., R. B. Torbert, U. V. Fahleson, C.-G Fälthammar, A. Gonfalone, and A. Pedersen, Measurements of quasistatic and low frequency electric fields with spherical double probes on the ISEE-1 spacecraft, *IEEE Trans. Geosci. Electron.*, *GE-16*, 258, 1978.

Olson, W. P., and K. A. Pfitzer, Magnetospheric responses to the gradient drift entry of solor wind plasma, *J. Geophys. Res.*, *90*, 10,823, 1985.

Orsini, S., M. Candidi, M. Stokholm, and H. Balsiger, Injection of ionospheric ions into the plasma sheet, *J. Geophys. Res.*, *95*, 7915, 1990.

Parks, G. K., et al., Particle and field characteristics of the high-latitude plasma sheet boundary layer, *J. Geophys. Res.*, *89*, 8885, 1984.

Pilipp, W. G., and G. Morfill, The formation of the plasma sheet resulting from plasma mantle dynamics, *J. Geophys. Res.*, *83*, 5670, 1978.

Reiff, P. H., T. W. Hill, and J. L. Burch, Solar wind plasma injection at the dayside magnetospheric cusp, *J. Geophys. Res.*, *82*, 479, 1977.

Rosenbauer, H., H. Grünwaldt, M. D. Montgomery, G. Paschmann, and N. Sckopke, Heos 2 plasma observations in the distant polar magnetosphere: The plasma mantle, *J. Geophys. Res.*, *80*, 2723, 1975.

Rostoker, G., and R. Bostrom, A mechanism for driving the gross Birkeland current configuration in the auroral oval, *J. Geophys. Res.*, *81*, 235, 1976.

Russell, C. T., The ISEE 1 and 2 fluxgate magnetometers, *IEEE Trans. Geosci. Electron.*, *GE-16*, 239, 1978.

Sharp, R. D., D. L. Carr, W. K. Peterson, and E. G. Shelley, Ion streams in the magnetotail, *J. Geophys. Res.*, *86*, 4639, 1981.

Shelley, E. G., R. G. Johnson, and R. D. Sharp, Satellite observations of energetic heavy ions during a geomagnetic storm, *J. Geophys. Res.*, *77*, 6104, 1972.

Shelley, E. G., R. D. Sharp, R. G. Johnson, J. Geiss, P. Eberhardt, H. Balsiger, G. Haerendel, and H. Rosenbauer, Plasma composition experiment on ISEE-A, *IEEE Trans. Geosci. Electron.*, *GE-16*, 266, 1978.

Speiser, T. W., Particle trajectories in model current sheets, 1, Analytical solutions, *J. Geophys. Res.*, *70*, 4219, 1965.

Tsurutani, B. T., J. A. Slavin, E. J. Smith, R. Okida, and D. E. Jones, Magnetic structure of the distant geotail from -60 to -220 R_E: ISEE-3, *Geophys. Res. Lett.*, *11*, 1, 1984.

Yau, A. W., E. G. Shelley, W. K. Peterson, and L. Lenchyshyn, Energetic auroral and polar ion outflow at DE 1 altitudes: Magnitude, composition, magnetic activity dependence, and long-term variations, *J. Geophys. Res.*, *90*, 8417, 1985.

Zwickl, R. D., D. N. Baker, S. J. Bame, W. C. Feldman, J. T. Gosling, E. W. Hones, Jr., D. J. McComas, B. T. Tsurutani, and J. A. Slavin, Evolution of the earth's distant magnetotail: ISEE 3 electron plasma results, *J. Geophys. Res.*, *89*, 11,007, 1984.

Zwolakowska, D., and B. Popielawska, Tail plasma domains and the auroral oval-results of mapping based on the Tsyganenko 1989 magnetosphere model, *Preprint 12*, Polish Acad. of Sci., Space Res. Cent., Warsaw, Poland, Dec. 1991.

W. Lennartsson, Lockheed Missiles and Space Company, Inc., Research and Development, Dep. 91-20, Bldg. 255, 3251 Hanover Street, Palo Alto, CA 94304.

Tail lobe ion composition at energies of 0.1 to 16 keV/e: Evidence for mass-dependent density gradients

O. W. Lennartsson

Lockheed Missiles and Space Company, Incorporated, Research and Development, Palo Alto, California

Abstract. A large set of energetic (0.1- to 16-keV/e) ion composition data from the central magnetotail, obtained by the ISEE 1 spacecraft between 10 and $23R_E$ from Earth, is sorted according to measured total ion beta value, in order to investigate whether bulk properties of different ions vary in different ways between plasma sheet and lobes, as suggested by a comparison of certain experimental and theoretical results in the literature. Despite inevitable difficulties with extracting statistically valid data at very low beta (10^{-2} or lower), the results seem to support a recent theoretical model suggesting that lighter ions have a steeper density gradient than heavier ions, especially when comparing H^+ ions with O^+ ions. The results also indicate that ion velocity distributions are fairly isotropic even at low beta, at least those of H^+ ions, although field-aligned flows are common. The results are evaluated in the context of plasma transport and are found to lend some support to the notion that tail lobe convection may be directed inward from the dawn and dusk flanks.

1. Introduction

As far as plasma measurements are concerned, the tail lobe regions of Earth's magnetosphere are unique in that they are typically not identified by characteristic particle signatures but rather by the disappearance of instrument response, or "plasma dropout" [e.g. *Hones et al.*, 1986]. What is known points to a very low particle density, at least inside of a few tens of Earth radii, where 10^{-2} cm^{-3} may be a typical number [*Akasofu et al.*, 1973; *Zwickl et al.*, 1984], and energies significantly lower than in the plasma sheet [*Akasofu et al.*, 1973; *Hardy et al.*, 1979]. It is also known that the lobes contain narrowly collimated tailward streams of ions, at least part of the time, and that these streams consist not only of H^+ ions but to an even greater extent of O^+ ions, presumably of terrestrial origin [*Sharp et al.*, 1981]. The data on these streams are so far the only information available on the ionic composition of the tail lobe plasma.

This study is an extension of the work by *Sharp et al.* [1981], using a much larger data set from the same experiment (on ISEE 1) and taking a different approach. It is motivated by some apparent discrepancies between different sets of tail ion composition data and between data and theory. The difference in the data refers to the studies by *Sharp et al.* [1981] and *Lennartsson and Shelley* [1986]. As already mentioned, the former study found the O^+ ions to be more abundant than H^+ ions in the tail lobes, at least when the geomagnetic 3-hour range index Kp is above 3+, whereas the latter study found the H^+ ions to be the usually most abundant in the central plasma sheet, even during geomagnetically disturbed conditions. Nevertheless, by sorting data according to the geocentric solar magnetospheric (GSM) Z coordinate (south-north direction), Lennartsson and Shelley found the O^+/H^+ density ratio to peak in a $5R_E$ wide bin centered at $Z = 0$, on average (their

Figure 9b), in apparent disagreement with the greater O^+/H^+ ratio in the lobes. This may imply either that the lobe and plasma sheet ions have substantially different origins, or that the use of a fixed-scale coordinate like the GSM Z can give misleading results. It is certainly possible that a statistical peak in the O^+/H^+ ratio near $Z = 0$ is mainly the result of spatial thinning of the plasma sheet during substorms [*Hones et al.*, 1971], when the O^+/H^+ ratio is typically enhanced in both the lobes and the plasma sheet.

The difference between data and theory refers to the study by *Lennartsson and Shelley* [1986] and a recent theory of tail pressure equilibria by *Kiessling and Ziegler* [1989]. The latter, which uses statistical mechanics rather than MHD, is the first theoretical analysis of tail equilibria with two ion components present, namely H^+ and O^+ ions. Under fairly general assumptions about the relative bulk velocities of the two ion components and the electrons (affecting the cross-tail current) this theory requires that the O^+ ions form a spatially thicker sheet, in GSM Z, than do the H^+ ions (Figures 4 through 7 in that paper). As a consequence, the O^+/H^+ density ratio becomes larger than one in the tail lobes, even if it is much less than one in the central plasma sheet. This may seem to be in agreement with the result of *Sharp et al.* [1981], even though the theoretical velocity distributions are essentially isotropic, not narrow streams, but it is again in apparent disagreement with the statistical Z dependence found by *Lennartsson and Shelley* [1986]. Since the theory assumes that each ion component has identical thermal velocity distributions in the plasma sheet and the lobes, except for the overall amplitudes, it suggests that a variation of the O^+/H^+ ratio with Z can be due to local conditions rather than to the particle sources. The implication is, as stated by Kiessling and Ziegler, that the effect is produced by the different ionic mass of the two components.

This study, like the one by *Lennartsson and Shelley* [1986], treats the ion data in a statistical fashion, but it sorts them according to the calculated ion beta, instead of GSM Z, and follows them well into the lobes. This procedure, as it

happens, removes the aforementioned discrepancies. The approach differs from that of *Sharp et al.* [1981] in that all detector counts are included here (corrected for background noise), not merely isolated counts exceeding three standard deviations of a Poisson distribution (at least 10 counts per unit sampling). The deficiency in individual counts is compensated for by summing them (weighted) into ion velocity moments, while keeping score of the resulting total standard deviations. The objective is to extract the maximum possible information from available data. The rationale may be described by a metaphor: if anything is hidden in a dark place, one is more likely to see it by going there with only a candle at hand than by staying under the bright porch light.

2. Database

The ion data are from the Plasma Composition Experiment on the ISEE 1 spacecraft [*Shelley et al.*, 1978] and cover for the most part the energy range between 100 eV/e and 16 keV/e. This instrument measures ions at various mass per charge (M/Q) in a cyclic fashion, usually by scanning the full range of energy per charge (E/Q) while maintaining a fixed M/Q. Each E/Q setting is typically kept fixed for at least one full spacecraft spin period (3 s). A complete energy-mass scan cycle in the magnetospheric modes of operation usually requires about 8 to 17 min and includes an M/Q setting (<1) which provides direct measurements of detector noise due to penetrating high-energy radiation (mostly MeV electrons). This detector background is subtracted from the other measurements before converting counts to velocity moments. The ion data are supplemented with magnetic field data from the ISEE 1 flux gate magnetometer [*Russell*, 1978]. A more detailed description of the instrument and the data format is given in the appendix.

The data set has been spatially limited to a "central tail" region, defined according to Figure 1 in terms of GSM coordinates. Each point in Figure 1 represents a single energy-mass scan cycle of the instrument, that is a single mass-resolved plasma sample. This region lies at GSM R between 10 and 23R_E, the latter being the ISEE 1 apogee, and at $X < -5R_E$ and $-10R_E < Y < 10R_E$. The bias toward positive Z is a consequence of the ISEE 1 orbit. The data span a total time period from January 2, 1978, to March 1, 1980.

The GSM boundaries are somewhat arbitrary, although they encompass a region where the ISEE 1 spacecraft provides regular sampling of the tail lobes (mostly of the northern lobe). Outside of this region, at $|Y| > 10R_E$, the plasma sheet is often too thick (in the Z direction) to allow that, especially during geomagnetically quiet periods. The ISEE 1 is expected to be well inside of the magnetopause while in this region, but the data have been additionally screened for possible evidence of magnetosheath or solar wind plasmas by the data analysis program. This screening has been based on velocity moments, combining the mass-resolved H^+ and He^{++} moments as well as the "total ion" moments, assuming that the latter are well representative of H^+ ions (see appendix).

Apart from the GSM boundaries in Figure 1, the data have not been ordered explicitly by spatial coordinates here. Instead, they have been ordered by the relative strengths of the measured particle and magnetic field pressures perpen-
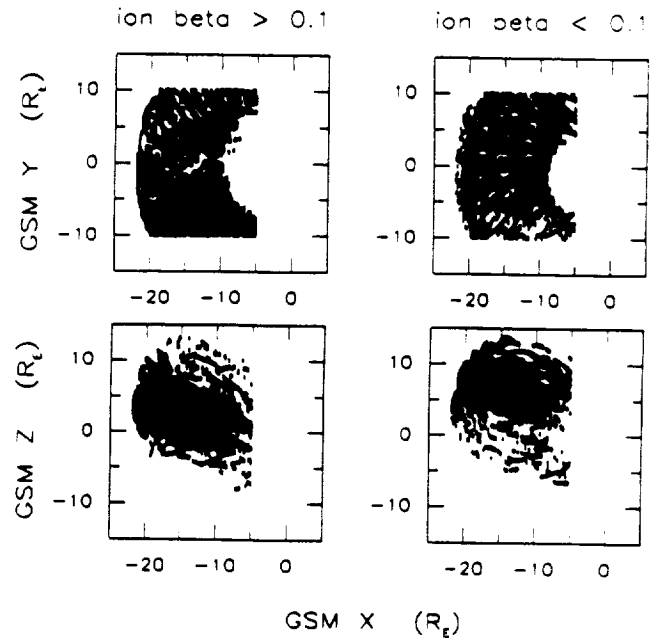
Figure 1. Spatial extent of selected tail data set in geocentric solar magnetospheric (GSM) coordinates, subdivided according to measured ion beta.

dicular to the magnetic field vector, that is by the measured ion beta value in the 0.1- to 16-keV/e energy range, or strictly speaking, by an approximate estimate of the true beta. This estimate has been made with the second set of assumptions listed in the appendix (section A2), and always includes the H^+ pressure, and in most cases the partial pressures of He^{++}, He^+, and O^+ ions as well (all four species usually measured).

This beta value is one obtained in the frame of reference of the spacecraft, rather than the more physically correct value that would be inferred by an observer moving with the local $E \times B$ drift, which is not known. A rough estimate of the resulting error can be made by subtracting, from each partial ion pressure, an energy density corresponding to the trans-B component of the respective drift velocity derived with the first set of assumptions listed in the appendix (section A2). That has been tried and found to have no significant effect on the statistical picture, mainly because that component of the drift energies is relatively small in most cases.

The final size of this data set is further limited by the availability of magnetic tape records of the auroral electrojet (AE) indices, which have been used to divide the data according to geomagnetic activity (see *Kamei and Maeda* [1981] and subsequent data books). As a result, no data from 1977 have been included.

3. Statistical Results

Many aspects of the data are qualitatively similar for different ion species, so in order to save figure space, a single species, namely the H^+, will serve as an example to be referred to later. The H^+ has always been measured here, and it is almost always present in statistically significant numbers.
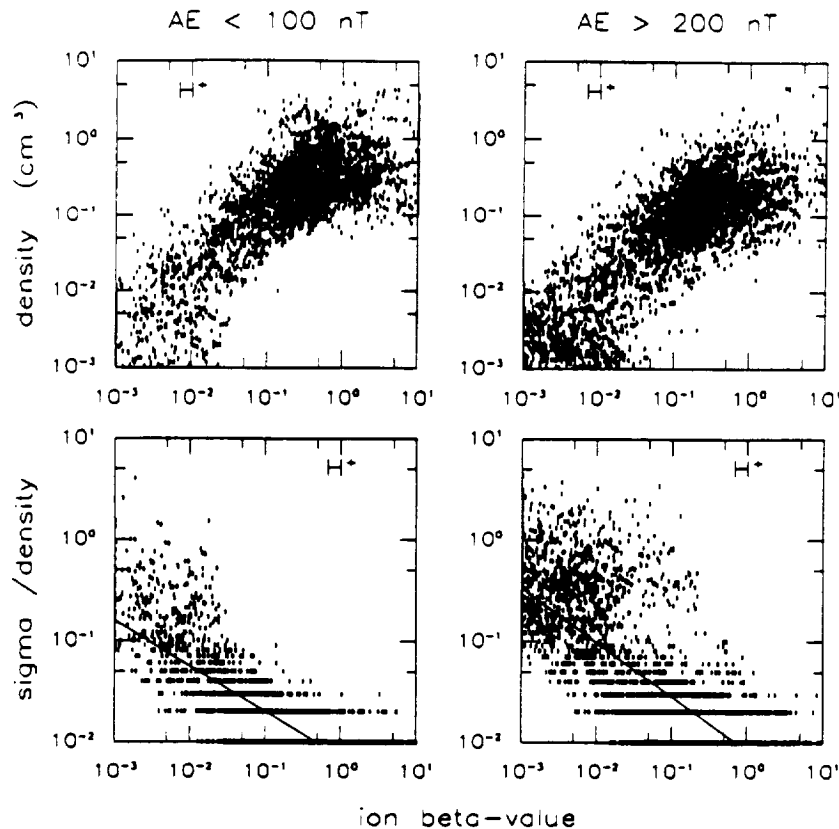
Figure 2. (Top) Density samplings of H^+ ions during (left) quiet and (right) active geomagnetic conditions (see text), and (bottom) statistical uncertainty of each sampling, ordered by corresponding total ion beta. Straight lines intersecting this and following figures are linear least squares fits referred to in the text (all fits are unweighted).

3.1. Proton Density and Energy in Central Tail

Figure 2 shows the H^+ number density (top) in the central tail (Figure 1) and the relative statistical uncertainty (one standard deviation) of this density (bottom), ordered by total ion beta, as defined above, and by geomagnetic activity. The latter has been measured each time by two consecutive hourly AE values, one from the preceding hour and one from the current hour (in universal time). In the left panels are only included those H^+ densities obtained when the two AE values were both below 100 nT, in the right panels are densities obtained when the two AE values were both above 200 nT. This selection does exclude a substantial portion of the data (about 34%), but the differences between quiet and active times are hardly sufficient to justify a third and intermediate group. The reason for using both the preceding and current hours for the AE is to allow for some inertia in the transport of ions, especially of ions from the Earth, although this precaution is somewhat academic in light of the strong autocorrelation of the AE index over many hours (see *Kamei and Maeda* [1981]; see also *Lennartsson and Shelley* [1986]).

The left and right panels of Figure 2 are based, respectively, on 2720 and 3804 independent density numbers, some of which fall below 10^{-3} cm^{-3}, even including some negative ones at beta $<10^{-2}$. Occasional negative "densities" are a normal statistical effect of subtracting a separately measured background count rate from the count rates in the various ion channels, when the signal-to-noise ratio falls

below one. This is reflected in the bottom panels by large statistical uncertainties, or "errors," sometimes exceeding the density itself.

The errors plotted here are the ratio between the calculated standard deviation, which contains the background standard deviation twice (via a sum of variances; see *Lennartsson and Sharp* [1982]) and is positive by definition, and the absolute value of the net density. These numbers have been stored rounded to integers in the data files, representing a percentage, which accounts for the horizontal striations. Values of zero percent have been set to 0.5% when fitting the two straight lines (log-log scale) by the linear (unweighted) least squares method [*Bevington*, 1969, pp. 92–118]. These lines have no other purpose here but to highlight the inherent dependence of data quality on the local beta value. Needless to say, the corresponding correlation coefficients are significant, being $R = -0.77$ on the left and $= -0.79$ on the right [*Bevington*, 1969, pp. 119–127; *Press et al.*, 1986, pp. 484–487].

Figure 2 shows that a density of 10^{-3} cm^{-3} is typically close to the statistical limit of resolution of H^+ ions in these data. The reason is that density numbers used here, like other moments, are all based on essentially random measurements of the accessible velocity space, whether it is filled by mostly noise or mostly signal. It is possible to lower the sensitivity threshold another factor of 10, in terms of ion density, by concentrating on ions that are focused in energy and angle to within a few instrument accumulations [*Sharp*
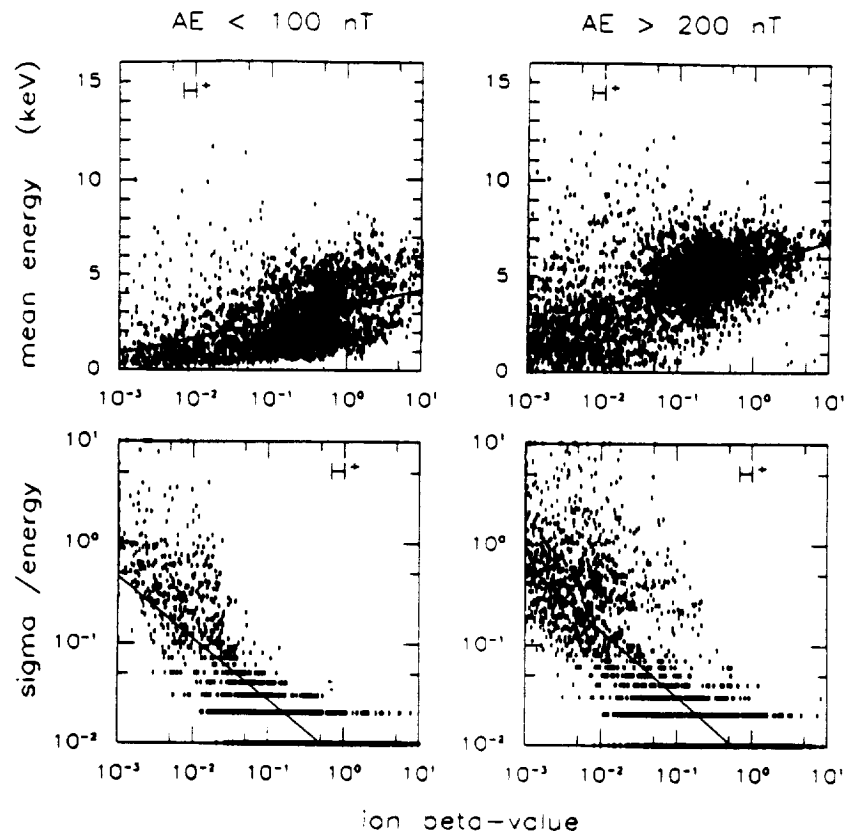
Figure 3. Corresponding (top) mean energies of H $^+$ ions and (bottom) their uncertainties.

et al., 1981], but that is also sure to exclude any hot and near-isotropic ion component that may be present.

To be more specific, an isotropic Maxwell-Boltzmann distribution of H $^+$ ions with a few keV thermal energy and a density of 10^{-3} cm $^{-3}$ generates about one count every 2 to 4 s in this instrument, a rate roughly half as large as the typical background in the lobes, and a total of about 40 counts over the course of a full energy-angle scan of H $^-$ ions. That means 40 net counts after subtraction of an average background rate derived from a sum of 50 to 100 counts in the background channel (about the same total accumulation time). Hence it is practically impossible to discern such a distribution from an energy-angle spectrum of raw counts, but by subtracting an appropriate background and weighting and integrating the counts into number density it becomes possible, albeit with a standard deviation typically between 30% and 40%, because of the background standard deviation. This example illustrates the fact that the signal-to-noise ratio does not have to be greater than one in order for a calculated density to be greater than three standard deviations, but this ratio ought not to be much less than 1/2 with typical lobe background rates.

Figure 3 shows the H $^+$ mean energy (top) and relative uncertainty (bottom) in the same format, except that the top panels have a linear scale on the ordinate and linear regression lines as well ($R = 0.45$ on the left, = 0.57 on the right). Since the mean energy is a ratio between energy density and number density, it has no physical or mathematical meaning if either or both of those densities are negative, so energies have only been calculated for positive values of both densities. The resulting number of points is 2673 (left) and 3510

(right), and the regression lines in the bottom panels have R = -0.84 (left) and = -0.85 (right). It may be noted that energies, at any given beta, are typically higher at $AE > 200$ nT, while densities are lower (Figure 2).

Although the trend is clearly to have lower energies at lower beta, the very highest mean energies have also been sampled at beta <0.1. Except for a few, these extreme values are not, as one might expect, caused by large statistical errors, because most remain when these plots are redrawn including only values with a relative sigma of less than 1/3 (not shown). In some cases they appear to represent beams of H $^+$ ions moving toward the Earth at high speed (up to 1200 km s $^{-1}$; see also *DeCoster and Frank* [1979] and *Eastman et al.* [1985]), in other cases they may be the result of aliasing caused by brief enhancements in the ion flux while the instrument is sampling the higher-energy channels. The relative importance of rapid earthward flows may be judged from Figure 4, which shows the X component of the calculated bulk velocities of H $^+$ ions.

In any case the great majority of H $^+$ energies are quite low at low beta, especially at quiet times, a result that is consistent with many earlier reports of reduced proton energies adjacent to the tail lobes, as measured with regular electrostatic analyzers [e.g., *Akasofu et al.*, 1973]. Taken together, Figures 3 and 4 imply that the H $^+$ energies are generally dominated by random, or "thermal," motion at all beta. This will become even clearer when angular distributions are discussed in section 3.4. It should be mentioned that the regression lines in the top panels of Figure 3 remain almost identical when the plots are limited to points with sigma <1/3 (not shown). This is a good indicator that
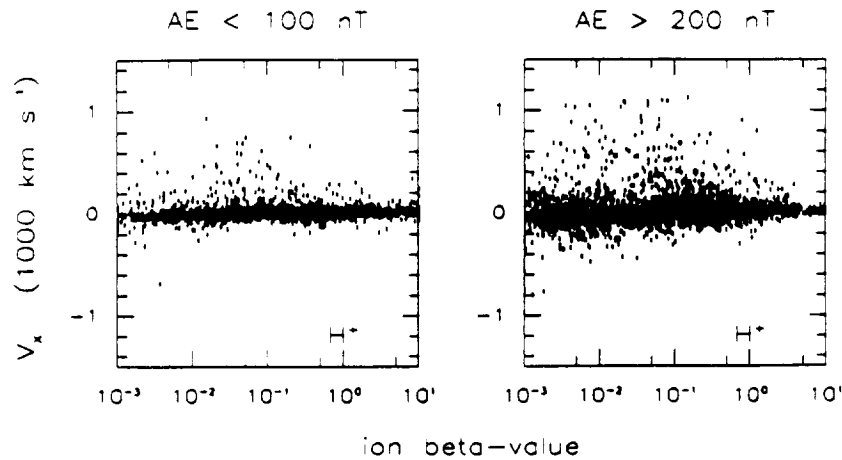
Figure 4. Corresponding drift velocity of H^+ ions along GSM (and GSE) X axis.

background counts have been properly subtracted from all samples, since the background would tend to bias the apparent mean energy toward a rather high value of about 5 keV/e.

3.2. Relative Densities of Other Ions

Figure 5 shows the ratios between the other ion densities and the H^+ density, as a function of the same beta and AE. In forming these ratios, each value of the H^+ density has first been compared with its own standard deviation, or sigma, and in the relatively rare events that it is smaller than one sigma (100% or greater error), including sign, the sigma value has been used to represent the H^+ density in each ratio. The reason for doing this is to avoid large but physically meaningless ratios.

The straight-line segments in each panel are least squares fits (log-log) to points at beta <0.1, only including positive ratios. Rather than enumerating the correlation coefficient and number of samplings for each panel, it may suffice to say that R is about −0.5 to −0.7 and is based on some 425 to 1374 samplings, which means that R is significant in each case. The feature of principal interest here is the consistent increase in the density ratios with decreasing beta. This implies that the H^+ density falls off faster than any of the other densities as one moves into a tail lobe from the plasma sheet.

There are numerous (hundreds of) negative ratios not shown in Figure 5, mostly at beta <0.1 (examples will be shown later). Negative densities are more common with He^{++}, He^+, and O^+ ions than with H^+ ions, for two reasons. One is that the heavier ions must have a larger number density in order to produce a given count rate at a given energy; the other is that the heavier ions generally have a lower count rate to begin with. The result is a lower signal-to-noise ratio and a greater sensitivity to background subtraction. This subject will be discussed in more detail below.

In order to verify the gross trends of the density ratios, Figure 6 shows a subset of the same data, one in which every ratio is based on densities, numerator as well as denominator, with a relative sigma of less than 1/3 (densities greater than 3 sigma). This subset is much smaller, especially at beta <0.01. Nevertheless, the six regression lines remain much the same in each case, and the respective correlation coef-

ficients, ranging from a low of −0.34 (top left) to a high of −0.72 (middle left), are still significant, considering the remaining number of points. In fact, even in the least significant case, the one with the fewest points remaining (middle left; 43 points), the probability of having no actual correlation is less than 10^{-7} [Bevington, 1969, pp. 119–127; Press et al., 1986, pp. 484–487].

It makes no difference whether the 3-sigma criterion used for Figure 6 is applied to the absolute value of each density, or only allows positive densities. At 3 sigma there are no negative ratios left, but there are still 3240 remaining positive ratios (adding all panels). Hence the problem with negative "densities" is eliminated at the 3-sigma level, in this case, although at that level a large portion of valid data is also being discarded. By comparison, there are still some 50 negative ratios left at the 2-sigma level (0.5% of all remaining values).

3.3. Intercomparison of Energies

Figure 7 is analogous to Figure 5, with mean energies substituted for densities. In Figure 7 the ratios have been formed without regard to standard deviations of either numerator or denominator. However, no negative values are involved here, since the mean energies, when calculated, are based on positive energy and number densities (see the explanation of H^+ energies above). The energies of He^{++}, He^+, and O^+ ions appear for the most part to be dominated by thermal motion, like those of the H^+ ions, but the statistics is frequently poor at low beta (see next section).

All ions, except the He^+, tend to become less energetic with decreasing beta, although the wide scatter in Figure 7 may seem to defy any trend. However, as the regression lines suggest, the He^{++} energy typically falls off at about the same rate as the H^+ energy (on a log-log scale), staying about 4 times higher than the H^+ energy, whereas the O^+ energy falls off slightly faster most of the time. The He^+ energy, for some reason, does not show this trend, so the He^+/H^+ energy ratio increases with decreasing beta.

Some of the scatter in Figure 7 is no doubt due to statistical errors, but much of it is real. As far as the He^+/H^+ and O^+/H^+ energy ratios are concerned, the large range of the scatter (two orders of magnitude) is probably real, since it remains about the same at the 3-sigma level, as do the regression lines (not shown). At that level of signifi-
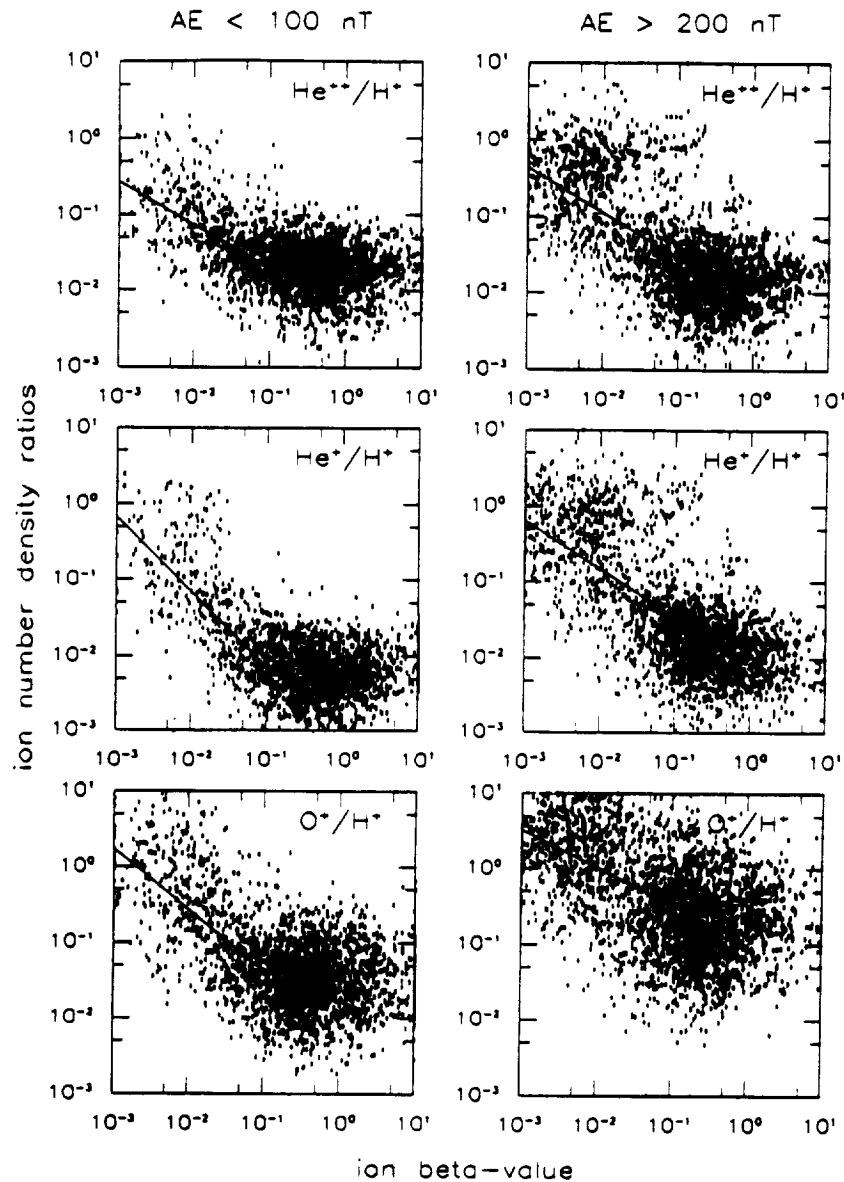
Figure 5. Densities of (top) He^{++}, (middle) He$^+$, and (bottom) O$^+$, normalized by the H$^+$ density measured during same energy-mass scan cycle.

cance the He^{++}/H$^+$ energy ratio is consistently greater than one and more strongly clustered near 4 (not shown).

Despite the scatter, the regression lines still have significant correlation coefficients, at least in the middle (R about -0.25; N about 2000 each) and bottom panels (R about 0.1; N about 2000 and 2700, respectively). The somewhat weaker correlation in the top panels (about -0.08) is of course consistent with a nearly flat regression line (at about 4).

3.4. Angular Distributions

Figure 8 compares the energies parallel and perpendicular to the tail magnetic field for each of H$^+$, He^{++}, and O$^+$ ions under two conditions: (1) At least one of the two magnetic field directions has been sampled by the instrument field of view at all energies (extreme values of center pitch angle less than 5° or greater than 175°). (2) At least one of the two

energies has been calculated with a relative sigma of less than 1/3.

The first condition gives a slight preference to ions flowing tailward along the field lines, because of the spacecraft orbit and the instrument configuration (see Figure 1 and section A1), but both field directions are commonly sampled during the same spin cycle, especially at energies below a few keV/e, where the field of view is rather wide (section A1). Of the two field directions, the tailward is favored by the O$^+$ ions, especially at small beta (not shown), while the earthward is favored by He^{++} and H$^+$ ions with flow speeds well in excess of 100 km s^{-1} (compare Figure 4).

The second condition prevents taking the ratio of two inaccurate numbers and thereby creating artificially large anisotropies. The main reason for not requiring a 3-sigma accuracy on both energies is to allow cases of extreme
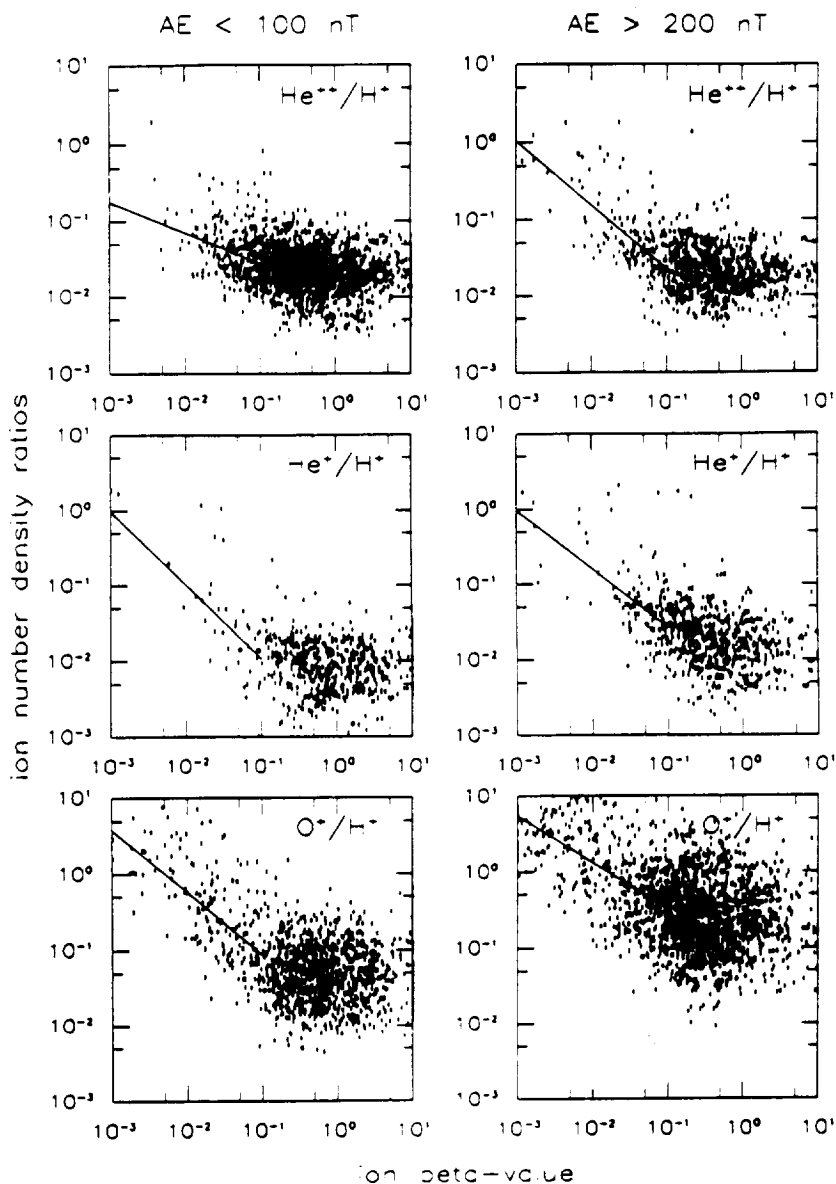
Figure 6. Same as Figure 5, but limited to measurements with less than 33% statistical uncertainty.

field-alignment, where the parallel flux contributes significant counts but the perpendicular flux may be buried in background noise. There is a barrier against very large such anisotropies, because of the 20° binning of the pitch angles during moment calculations (section A2). Even if all counts were confined to a single bin along either field direction, the center of the bin is either at 10° or 170°, so the ratio of parallel to perpendicular energy, when multiplied by two to adjust for the difference in degrees of freedom, could not exceed about 32, assuming no statistical errors in the background subtraction. However, few ratios even come close to 32 in Figure 8; the most common ratio is one, indicating a predominance of isotropic velocity distributions, at least for H^+ ions.

If the conditions on statistical accuracy are removed altogether, the main effects on Figure 8 are to increase both the number and spread of data points at small beta, especially for He^{++} and O^+ ions (about fivefold increase in

number of points at beta <0.1 for O^+), as expected, but the regression lines remain very nearly the same (not shown). In other words, anisotropic ratios become more common, real or not, but they show no greater preference for either large or small values than already indicated in Figure 8. It may also be mentioned that He^+ ions, which are not part of Figure 8, have ratios similar to the O^+ ions, although they have fewer ratios with small sigmas.

A proper comparison of parallel and perpendicular energies should compensate for $E \times B$ drift. Since the latter is unknown here, the next best move is to determine the cross-B component of the measured ion drift velocity in the spacecraft spin plane (approximately the GSE X-Y plane), and subtract the corresponding drift energy from the perpendicular energy, so as to approximate pure gyrational (thermal) energy. In practice, this makes little difference, because the cross-B drift speed is generally small (mostly less than 50 km s^{-1}) compared to thermal velocities in these data.
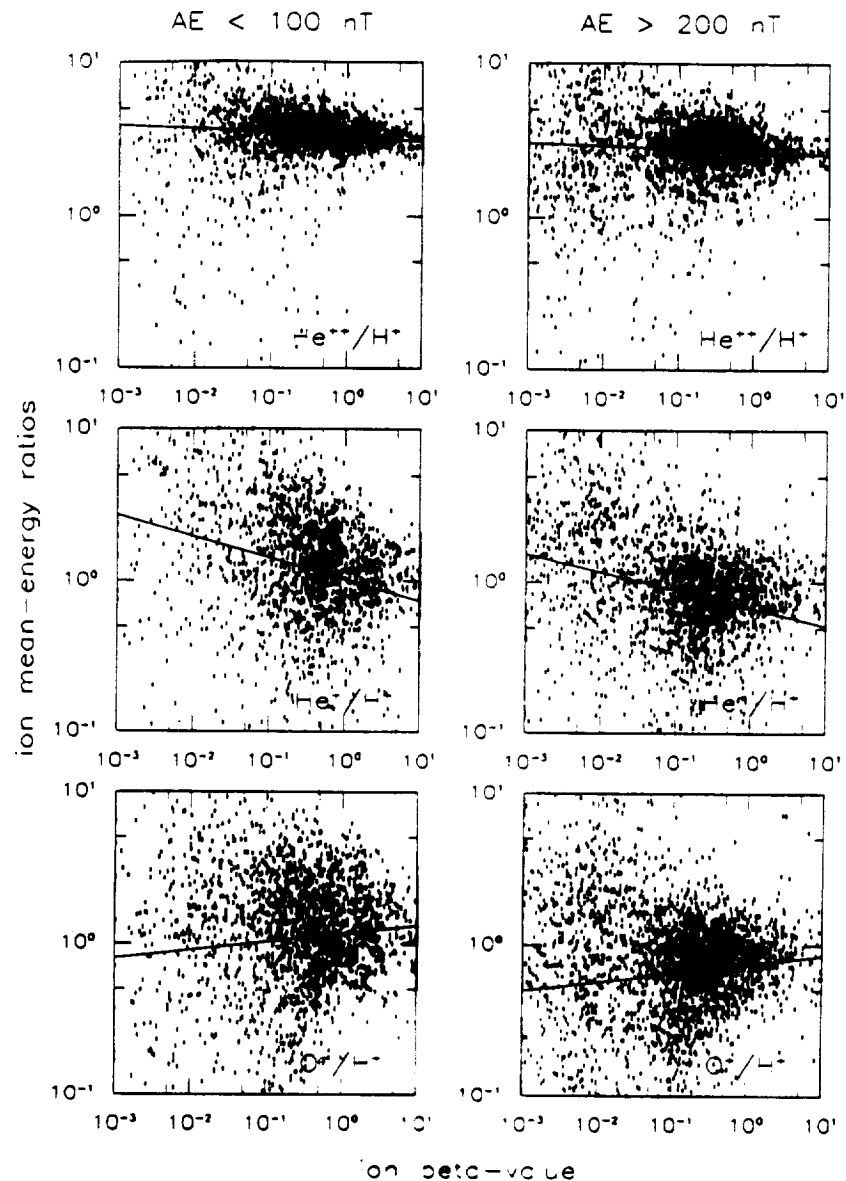
Figure 7. Mean energies of (top) He^{++}, (middle) He^+, and O^+ (bottom), normalized by the H^+ mean energy.

However, the ratios shown in Figure 8 have in fact all been "corrected" this way.

3.5. Extending the Energy Range Downward to 10 eV/e

The lowest-energy channel, from 10 eV/e to about 100 eV/e, not counting the variable RPA settings, has been sampled in about 90% of these data and is represented by a partial number density for each ion species, a quantity that may or may not be an accurate measure, depending on such unknowns as spacecraft potential and $E \times B$ drift direction and speed. This partial density can be added to the normal number density, and by weighting it with a suitable energy (40 eV/e) it can also be used to derive a modified value for the total mean energy.

Adding this low-end density has somewhat different effects at different beta, and the effects also vary with ion species. At beta >0.1, that is including the plasma sheet

proper, the effects are consistently small, especially for H^+ and He^{++} ions, whose density and energy are rarely changed by more than a few percent. The corresponding changes for He^+ and O^+ ions are somewhat larger, often reaching some 10 to 20%. At smaller beta, usually meaning smaller densities as well, the effects are much more variable, sometimes doubling or tripling the density, especially that of O^+ ions. However, if Figures 2 through 8 are redrawn, including this energy channel whenever it has been sampled, the new figures (not shown) are difficult to distinguish from the old ones. There is some increase in the range of scatter, but very little change in the gross trends.

4. Discussion

The most intriguing result of this study is the variation of ion density ratios with beta in Figure 5, that is the increase at
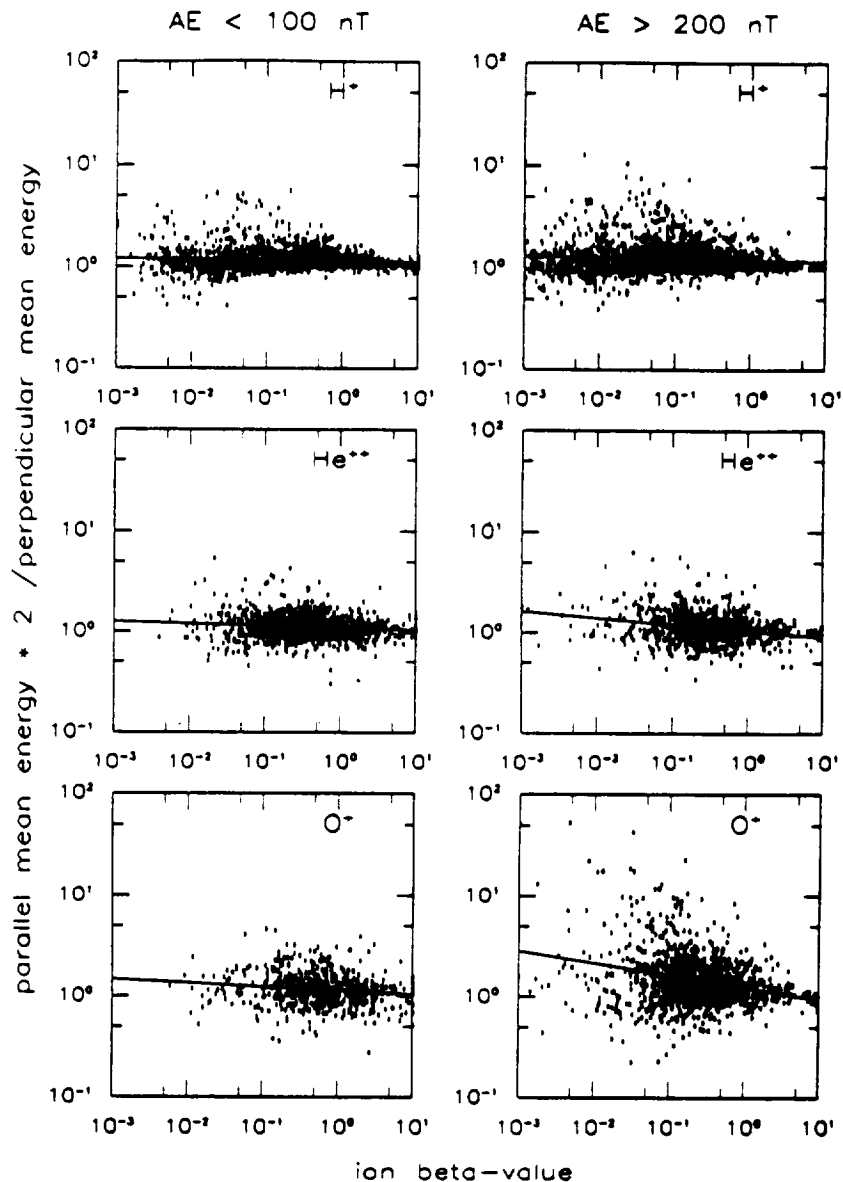
Figure 8. Parallel-to-perpendicular energy ratios for (top) H^+, (middle) He^{++}, and (bottom) O^+, when energies obtained with less than 33% statistical uncertainty (see text for details).

low beta. On one hand, it is in qualitative agreement with the theoretical result of *Kiessling and Ziegler* [1989] regarding the O^+/H^+ ratio, but on the other hand there are instrumental and statistical effects that will conspire to produce a similar result, as shown by the absolute values of negative ratios in Figure 9 (top panels). These effects are due to low count rates, low signal-to-noise ratio, and occasional time aliasing associated with the separate sampling of different ions and of ions and background. The data have been examined very extensively for evidence of these effects, both by imposing various selection criteria in the statistical analysis and by studying many sample events in detail. They are no doubt significant, as Figure 9 proves, but they do not appear to be the sole or even dominant reason.

Figure 10 illustrates some of the ambiguities inherent in low count rates and a low signal-to-noise ratio. Figure 10 actually represents one of the "better" events, in a formal

sense, in that the signal-to-noise ratio is still greater than one, if only marginally, at the times when the He^{++}/H^+ ratio approaches unity. Even so, the low count rates make it fruitless to try to compare the ions in the raw data; it is necessary to sum counts into moments before any kind of pattern can be recognized. In this case the densities of H^+ and He^{++} ions become roughly comparable twice, when the H^+ density is at a local minimum (top panel).

This could still be a time aliasing effect in the background subtraction, since the background measured during the corresponding instrument cycles may have been lower than the actual background during the He^{++} samplings. However, by also comparing the mean energies of the two species in Figure 10, both on an E/Q (middle panel) and E/M basis (bottom panel), it appears that the data are at least consistent with a continuous signal for both H^+ and He^{++} ions. It is clear that the two sets of energies in this case are more
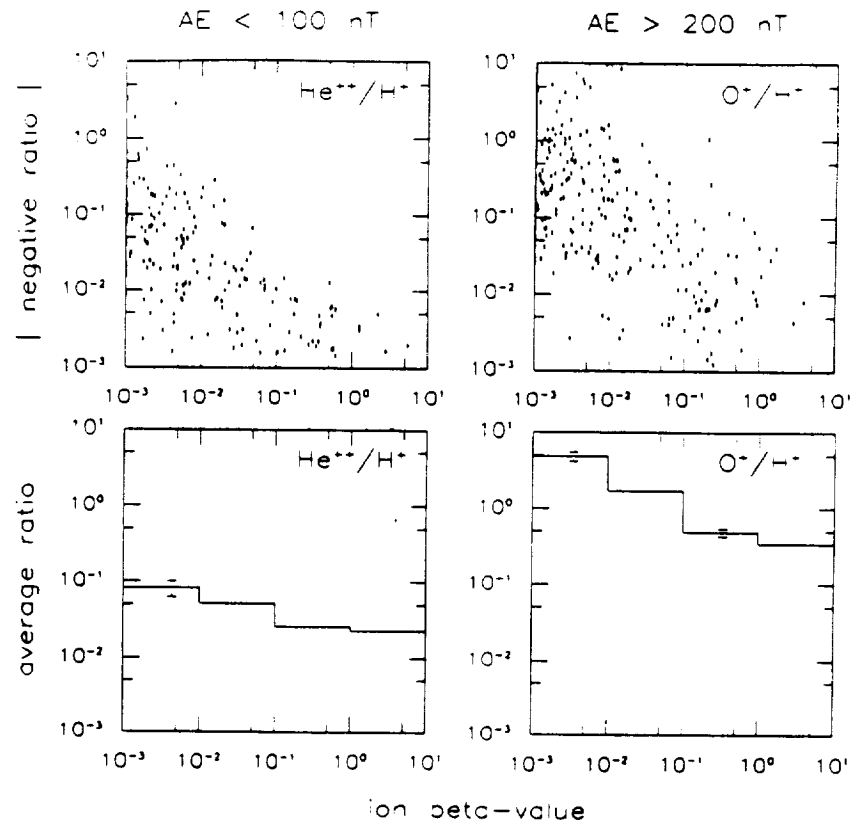
Figure 9. (Top) Examples of negative numbers (modulus) corresponding to the various panels of Figure 5. (Bottom) Corresponding averages (unweighted) when positive and negative numbers are both included (error bars indicate standard deviation of average when larger than line width).

nearly equal on an E/M basis. This would not be expected if background were dominant. In that case the energies would be widely scattered but have a tendency to show equal energy per charge on average, since the total range is measured in E/Q and only positive values are being calculated (the two species sometimes have equal mean E/Q even when their signals are far above background).

In some cases the He^{++}/H^{+} ratio is significantly reduced when the energy range of the data is extended to include the 10- to 100-eV/e channel, but in general the inclusion of this channel only serves to increase the scatter, while the trends remain much the same, as already mentioned in section 3.5. It is worth noting that the H^{+} ions in the 100-eV to 16-keV range usually have a mean energy of at least 500 eV even at low beta (Figure 3), and if these ions are part of a Maxwell-Boltzmann type distribution, their companions at energies below 100 eV have less than 20% of the total density. In those cases where a significantly larger H^{+} density is present below 100 eV, that partial density is probably due to H^{+} ions with a different history than the main population [cf. *Parks et al.*, 1992].

There are three principal reasons why the statistical trends in Figure 5 are probably real, at least qualitatively, even if many of the individual values are not. The first is that the trends in Figure 5 still survive in Figure 6, after all densities (numerator and denominator) with an absolute magnitude smaller than or equal to three sigmas have been discarded. The top and middle panels of Figure 6 have few points left at small beta, but the ones that do remain are consistent with

the same kind of elevated ratios and cannot be easily ascribed to poor counting statistics. At this level of significance the background subtraction should be less critical, and that is confirmed by the elimination of negative ratios altogether, as mentioned above. In order for that to be an artifact, the formulas for density calculations would have to give lower weights to count rates from the background channel than they did to count rates from the ion channels, but those formulas do in fact give identical weight to both, except for the sign.

The second reason is that the same basic trends remain when the H^{+} density is replaced by the "total" density from the energy-analysis section of the instrument (not shown). This density is calculated each time a mass-resolved density is produced (section A2), providing a continuous time reference that helps to eliminate time aliasing as a significant factor. There is only a minor reduction in the ratios using this replacement, consistent with the multiple-ion contribution to the total count rate (proportional to the square root of Q/M at a given energy).

The third reason is that those trends also emerge when the data are binned in beta and averaged within each bin, including all ratios, positive and negative. Two examples are shown in the bottom panels of Figure 9, the left one corresponding to the top left panel of Figure 5, the right one to the bottom right panel of Figure 5. These two examples essentially bracket the slopes of the average ratios corresponding to the other four panels of Figure 5 and are a strong indication that there is an underlying bias toward increased
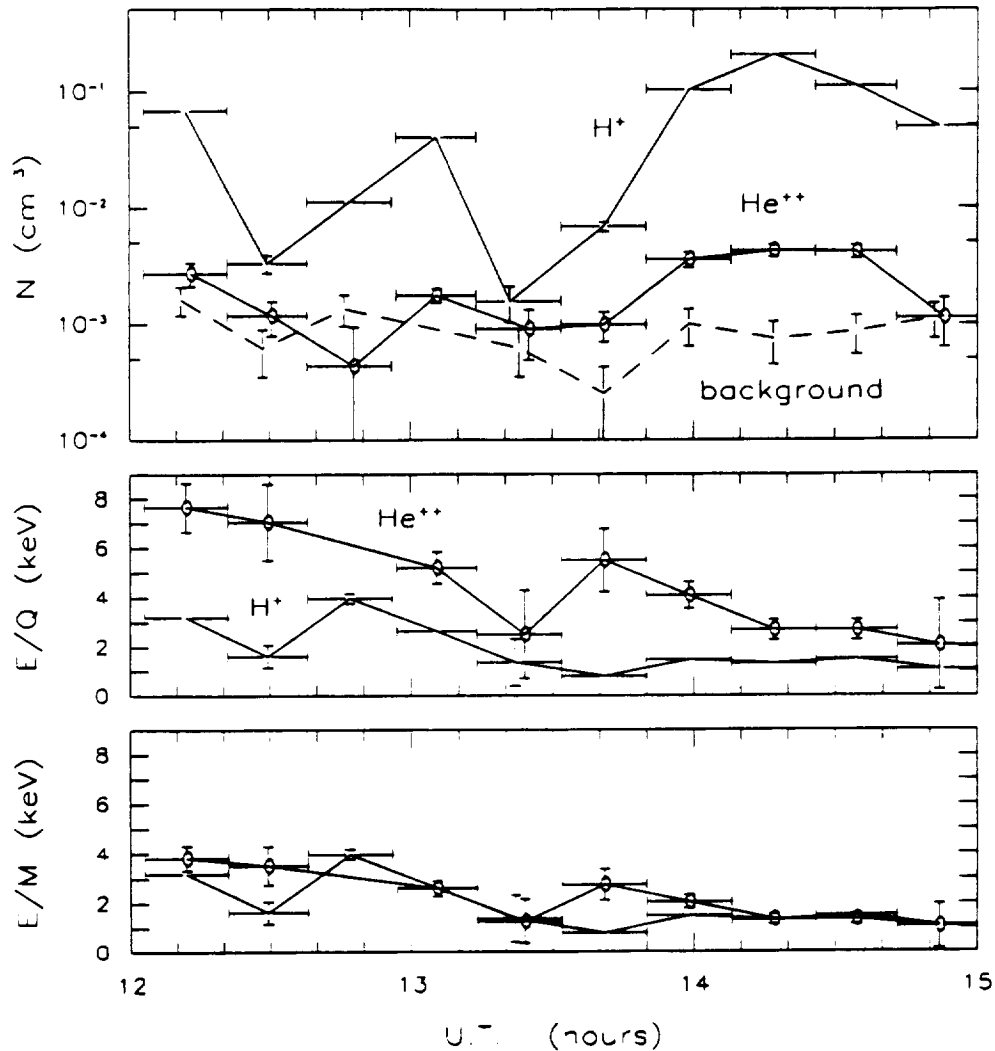
Figure 10. A 3-hour segment of data taken near local midnight on March 13, 1979, at 10 to $14R_E$. Top panel shows densities of H^+ (line without symbols) and He^{++} (open circles), with background already subtracted, as well as the "density" of the background alone (dashed line) using weights corresponding to He^{++} ions. Lower panels show mean energies normalized by (middle) ionic charge or (bottom) mass. Horizontal bars indicate energy-mass scan cycle, vertical bars show standard deviation carried over from counting statistics.

positive ratios at low beta. This bias cannot be instrumental, because the detector response to penetrating radiation is independent of the M/Q setting of the optical parts and, as already stated, the formulas for density calculations would produce negative numbers as often as positive ones if count rates in the background channel and the ion channels were from the same statistical distribution.

Granted that there is a geophysical explanation for Figures 5 and 6, what specific physical quantity separates the different ions? One candidate might be the mean or median gyroradius of each species. At a geocentric distance $R >$ $10R_E$, and at beta <0.1 the tail magnetic field, as measured by the ISEE 1 magnetometer, typically ranges between 20 and 60 nT (depending mostly on distance from Earth). This means that a 3-keV H^+ ion, for example, has a gyroradius of 130 to 400 km at 90° pitch angle, and therefore a transverse range of 260 to 800 km during each gyration. This is small compared to the cross section of the tail, but not necessarily

small compared to the transition region between the plasma sheet and tail lobes [e.g., *Parks et al.*, 1992, and references therein].

To make this point more tangible, assume the following: (1) Each density $n(i)$ of species i falls off with increasing distance dz from the plasma sheet proper with the functional dependence $\exp (-dz/H)$, starting with $dz = 0$ at a point where beta = 0.1 (magnetic field already near its lobe value). (2) The "scale height" $H = H(i)$ is proportional to the mean gyroradius $g(i)$, and the proportionality constant is the same for all species. (3) The mean energy of each species is independent of dz, that is $H(i)$ is approximately constant. (4) Beta is dominated by the H^+ ions, which have the mean radius $g(H^+)$. Under these assumptions the coordinate dz can be approximated by

$$dz \approx H(H^+) \times \log \, [\text{beta}(0)/\text{beta}(dz)]/ \, \log \, (2.718)$$

and the ratio $r(i) = n(i)/n(H^+)$ is related to beta by

$$\log [r(i)] = A(i) - C(i) \times \log (\text{beta}) \qquad (1)$$

where A and C are constants and

$$C(i) = [g(i) - g(\text{H}^+)]/g(i). \qquad (2)$$

Considering that the gyroradius at a given pitch angle is proportional to the square root of the product of mass and energy and inversely proportional to charge, it would appear from the left panels of Figure 7 ($AE < 100$ nT), that the He^{++} ions should have a mean gyroradius twice that of H$^+$ ions (4 times the energy), assuming roughly isotropic velocity distributions (Figure 8), and the O$^+$ ions one that is about 4 times that of H$^+$ ions (about the same energy as the H$^+$). This means that the values of $C(i)$ for He^{++}/H$^+$ and O$^+$/H$^+$ in (2) ought to be about 1/2 and 3/4, respectively. Those numbers are in fact very close to the slopes of the respective regression lines in the left panels of Figure 5 (-0.56 and -0.80), a result that is surprising in view of the extreme simplicity of the assumptions.

Removing (3) and taking into account that the mean energies $E(i)$ of H$^+$, He^{++}, and O$^+$ ions decrease with decreasing beta, that is with increasing dz, means adding a third term $C(i) \times \log [E(\text{H}^+, dz)/E(\text{H}^+, 0)]$ on the right side of (1), but A and C are still constants as long as $E(i)/E$ (H$^+$) is constant. Inserting typical numbers for E (H$^+$) from Figure 3 yields only small absolute values for this third term, at least an order of magnitude smaller than the second right-hand term in (1), so this equation is still a fair approximation, within the remaining assumptions, for the He^{++}/H$^+$ and O$^+$/H$^+$ ratios at $AE < 100$ nT.

On the other hand, (1) predicts that the He$^+$/H$^+$ ratio should have a slope intermediate between those of the He^{++}/H$^+$ and O$^+$/H$^+$ ratios, even after proper consideration of energies (A and C are not constant for He$^+$), while the left panels of Figure 5 (and Figure 6) show the steepest slope for the He$^+$/H$^+$ ratio. Furthermore, as beta receives greater contributions from ions other than the H$^+$ ions, especially from O$^+$ ions at active times, the slope of the log $[r(i)]$ versus log(beta) ought to increase, and that is not borne out in the right panels of Figure 5, so this simple "model" probably has severe limitations. All it really does is make it plausible that Figures 5 and 6 have a geophysical explanation. It should also be pointed out that the far more elaborate model of *Kiessling and Ziegler* [1989] does not have gyroradii as separate input parameters, although it does make the implicit assumption that the O$^+$ ions have four times larger gyroradii than the H$^+$ ions by assuming that both species have the same temperature (independent of beta).

5. Conclusions

To begin with, the large O$^+$/H$^+$ ratios in Figures 5 and 6 provide further evidence that ions of terrestrial origin constitute a large fraction of the tenuous energetic plasma in the tail lobes. This is keeping with the reasoning of *Sharp et al.* [1981], who based theirs on the large oxygen content of magnetic field-aligned ion streams. If one defines the lobes by beta <0.1 in these figures, it appears that during disturbed conditions ($AE > 200$ nT) the O$^+$ concentration typically exceeds that of H$^+$ ions, and is quite compatible with the finding by Sharp et al. that O$^+$ ions comprise about 2/3 to 3/4

of the tail lobe ion streams for $Kp > 3+$ (their Table 1). Since Figures 5 and 6 are based on all ion flux entering the instrument, not merely the peak flux, the large O$^+$ concentration measured here can be considered a generalization of the result of Sharp et al.

Where do H$^+$ ions fit in this picture? What is their principal origin? As far as their energies are concerned, they are much better correlated with the He^{++} ions than they are with either the O$^+$ or He$^+$ ions, according to Figure 7, which suggests that a majority of the H$^+$ ions in the Earth's tail are of solar rather than terrestrial origin, most of the time. This impression is strengthened by the observation that the H$^+$ and He^{++} ions tend to have about the same energy per nucleon in the top panels of Figure 7 (see specific example in Figure 10), a relationship that is characteristic of H$^+$ and He^{++} ions in the solar wind.

It should be mentioned that the slight negative slope of the He^{++}/H$^+$ regression lines in Figure 7 is probably an instrumental effect, caused by a combination of higher ion energies at higher beta (Figure 3) and the upper energy cutoff at 16 keV/e. Since the latter is measured in energy per charge, it leads to a more rapid loss of He^{++} than H$^+$ ions from the measured energy range if these ions are energized in proportion to either ionic mass or initial energy (see more extensive discussion of this subject by *Lennartsson and Shelley* [1986]). The same effect is probably responsible for the slight downward shift of the regression line at $AE > 200$ nT, since the H$^+$ and He^{++} energies are higher during active times (Figure 3).

Assuming that the H$^+$ ions are indeed mostly of solar origin, and ignoring for a moment the He^{++} ions, it follows from the bottom panels of Figures 5 and 6 that the solar ions usually outnumber the terrestrial ions in the plasma sheet, at beta >0.1. How do the solar ions reach the near-Earth plasma sheet? Do all of these ions arrive from the distant tail by the combined means of earthward jetting along the magnetic field lines and earthward convection in a predominantly dawn-dusk oriented electric field [e.g., *Speiser*, 1965], or do they enter in large part by cross-tail convection from the dawn and dusk flanks, as argued in *Lennartsson* [1992]? The answer to that question depends on the actual geometry and temporal behavior of the tail electric field, neither of which is well known at present. However, there are some features of these data that seem to favor the second means of transportation, that is the cross-tail convection.

As Figure 4 shows, it is easy to find rapid (hundreds of km s^{-1}) earthward flows of H$^+$ ions, especially during disturbed conditions ($AE > 200$ nT). However, these flows are not the normal state of motion of the H$^+$ ions, not even at low beta; the normal state is to have slow (tens of km s^{-1}) bulk motion, including both earthward and tailward components. If the H$^+$ ions were mostly arriving from the distant tail, say from $100R_E$ downtail [*Zwickl et al.*, 1984], moving along magnetic field lines while at the same time convecting into the plasma sheet, that is convecting toward higher beta, they would tend to disperse according to field-aligned speed, leaving the faster ions at the lower beta. There is really no evidence of that in Figure 4; faster and slower flows occur at the same beta, at least at beta <0.1, and the slower flows are dominant everywhere. This situation would seem to imply that the bulk of the H$^+$ ions must be able to reach the near-Earth plasma sheet from somewhere besides the distant tail, and one possible mode of access would be by inward
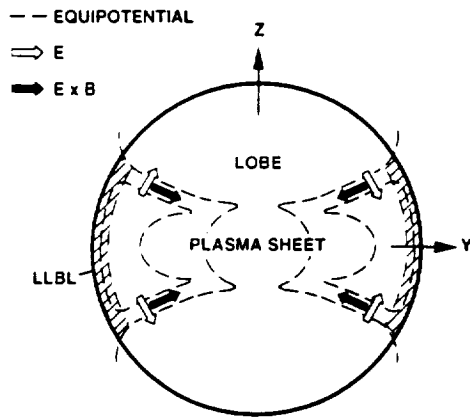
Figure 11. Hypothetical electric equipotentials (dashed lines) allowing inward tail convection from dawn and dusk flanks. These may originate in the low-latitude boundary layer (LLBL), as indicated by closed contours [*Lennartsson*, 1992], or in the solar wind, as indicated by open contours (assuming dawn-dusk directed E field in solar wind).

convection from the tail flanks, in an electric field that is locally north-south directed in a proper sense, for example as outlined in Figure 11.

It should be noted that the predominantly small V_X values at low beta in Figure 4 cannot be ascribed to poor counting statistics, since they cannot be consistently smaller than their absolute errors. Neither can they be ascribed to infrequent sampling of the earthward magnetic field-aligned direction, because the pitch angle range of the data is generally the widest at the lowest beta, and even when the data are limited to those with the most complete pitch angle coverage, as done in Figure 8, there is no significant field-aligned anisotropy in the H^+ population as a whole (top panels). So even though rapid earthward flows are common, a nearly isotropic velocity distribution is more common yet among H^+ ions at all beta. It is also worth mentioning that the particle counter in the energy-analysis section of the instrument does not detect a significantly more frequent occurrence of rapid earthward flows than does the "mass detector," even though its angular response is more favorable (in the northern lobe), counting ions moving in the spin plane or slightly downward (not shown).

Returning to the He^{++} ions, which may all be of solar origin, it should be mentioned that they have V_X values similar to those of the H^+ ions (not shown), including numerous negative ones (see examples in the work by *Lennartsson* [1992]), although the scatter is enhanced by frequently poor counting statistics. Of greater interest, however, is the difference between the He^{++} and H^+ ions in terms of their density gradients, as implied by Figures 5 and 6 (top panels). It is hard to imagine how this could arise from velocity dispersion among ions streaming earthward from the distant tail, since there is no indication that He^{++} ions are moving any faster than H^+ ions in general (about same E/M in Figure 7). Furthermore, this spatial relationship between the He^{++} and H^+ ions is basically similar to the relationship between the O^+ and H^+ ions, even though the O^+ ions are flowing almost exclusively tailward at low beta

(not shown) and have generally small velocities as well (fairly low energies in Figure 7 despite the large ionic mass).

As suggested by the simple exercise in the preceding section, the varying density gradients may be physically related to the different gyroradii of different ions. If that is true, it would seem to require that the gyrocenter motion of all ions is largely perpendicular to the density gradients, that is parallel to the boundary between the plasma sheet and the lobes. That state of motion could be set up in accordance with Figure 11, for example.

Since the mass-dependent gradients in Figures 5 and 6 are qualitatively similar to the theoretical result of *Kiessling and Ziegler* [1989] for H^+ and O^+ ions, whether or not the ion gyroradii are truly the ordering parameters, it is reasonable to assume that there may also be some fundamental similarities between actual and modeled particle drifts. It is therefore interesting to note that their model, which has only two spatial coordinates, GSM X and Z, assumes purely one-dimensional bulk motion along the Y axis, that is along surfaces of constant magnetic field and constant beta. Despite the two-dimensional character of their model, that state of motion is conceptually similar to having ions convect according to Figure 11.

The obvious test to make with the existing data is to examine how the calculated bulk velocities in the GSE Y direction vary across the tail. A preliminary study along those lines has been made, using the ion beta as a measure of latitude, but the results are not yet conclusive. The calculated V_Y values are typically in the range of tens of km s^{-1}, and are to some extent consistent with Figure 11 (not shown), but it appears that beta is inadequate as a measure of location across the shear boundary in the velocity field, and further study is required. In order to extract true bulk velocities it is also necessary to consider the effects of a gradient in the spatial distribution of ion gyrational motion (due to the density gradients).

Finally, it is natural to view Figures 5 and 6 against the now well-documented "deficiency" in the magnetospheric content of He^{++} ions when compared to the solar wind [e.g., *Young et al.*, 1982; *Gloeckler and Hamilton*, 1987]. The central plasma sheet was found to have a higher He^{++}/H^+ ratio than the inner magnetosphere by *Lennartsson and Shelley* [1986], reaching average values of about 3% during quiet conditions, but still lower than the typical solar wind ratio of about 4% during the same phase of the solar cycle (rising phase; see for example *Feldman et al.* [1978]). According to Figures 5 and 6, the He^{++}/H^+ ratio is instead enhanced over solar wind values in the tail lobes. Does this mean that solar wind He^{++} ions are partially stripped away from the accompanying H^+ ions during entry into the geotail and subsequently left behind in the lobes? This scenario cannot be excluded at this point, but if Figure 11 properly depicts the plasma convection, then the He^{++} ions would eventually rejoin the H^+ ions when the convection turns into the central plasma sheet. Another possible explanation for the reduced He^{++}/H^+ ratio in the central plasma sheet (and inner magnetosphere) is of course the admixture of terrestrial H^+ ions. Being that the H^+ and He^{++} ions often have about equal velocity distribution in the tail (Figure 7), this admixture may start at an early stage of solar plasma entry, for example in the cusp regions, as perhaps suggested by the numerical modeling of *Delcourt et al.* [1989].

Appendix

A1. Instrumentation

The ISEE 1 spacecraft (along with the ISEE 2) was launched on October 22, 1977, into an orbit with apogee at almost $23R_E$ (geocentric), perigee at about 300 km altitude, an inclination of 29°, and an orbital period of 57 hours. It was placed in a spinning mode with the axis nearly perpendicular to the solar ecliptic plane and with a period of approximately 3 s.

The Lockheed ion composition experiment on the ISEE 1 is one of a family of instruments using the same type of ion optics and covering nearly the same range of energies (0 eV/e to about 17 keV/e) which have also been flown on GEOS 1 and 2, DE 1, and AMPTE/CCE [Shelley et al., 1978]. The ISEE 1 instrument consists of two nearly identical mass spectrometers with the respective fields of view centered 5° above and 5° below the spin plane, that is about 5° above and below the solar ecliptic plane. Data used in this study are from one of these, the one looking below the spin plane (seeing ions moving upward). Each field of view is about 10° wide along the spin plane, and some 10° to 50° wide transverse to this plane, being the widest at the low energy end (due to preacceleration) and gradually decreasing toward 10° with increasing energy. Information on the instantaneous pitch angles (at center of field of view) is provided by the ISEE 1 flux gate magnetometer [Russell, 1978].

Each spectrometer consists of an electrostatic analyzer to select energy per charge, followed by a combined electrostatic and magnetic analyzer to select mass per charge. Both analyzer sections have particle detectors, so at each energy setting the experiment provides both the total ion flux and the partial flux at a selected mass per charge. On ISEE 1 each combination of energy and mass is maintained for at least 1/16 s in high telemetry bit rate and 1/4 s in low (normal) bit rate. Different combinations are stepped through in a cyclic fashion according to patterns controlled by a random access memory which is programmable from the ground. The various ISEE 1 patterns, or "modes," used inside the magnetosphere require anywhere from 2 to 20 min to complete. The mass selections usually include one that blocks all ions from reaching the second detector, allowing intermittent measurements during each cycle of the noise associated with penetrating radiation. These measurements are later used to correct the count rates of mass analyzed ions. The total count rate in the first detector is not corrected this way, but this detector is much less susceptible to penetrating radiation because of its small size (spiraltron).

The maximum energy range of the ISEE 1 instrument is 0 eV/e (or spacecraft potential) to 17.9 keV/e, divided into 32 contiguous channels, although only a subset of these may be used in a given mode. The lowest channel, from 0 eV/e to about 100 eV/e, is normally limited to energies above 10 eV/e by a retarding potential analyzer (RPA) in the entrance. That same RPA is used to provide "cold plasma" data from 0 to 100 eV/e (retarding within the lowest channel) during parts of some scan cycles. Because of measurement uncertainties associated with spacecraft charging and plasma convection, the lowest-energy channel is treated separately when calculating velocity moments. Data from the highest-energy channel (above 16 keV/e) are excluded altogether here, because of a slight variation over time of the mass response of the ISEE 1 instrument in that channel. The numerical procedures used for weighting and summing counts from the various energy channels are such that the velocity moments correspond to an energy range of either 100 eV/e to 16 keV/e (in all figures) or 10 to 100 eV/e (discussed separately), the latter assuming no spacecraft charging.

The data used here have been obtained in several different energy-mass scan modes, but only in modes spanning at least the 0.1- to 16-keV/e energy range, whether that range is covered in a contiguous fashion (normally true) or not (see below), and only in modes which provide H^+ data from the mass analyzer, as opposed to modes which rely on "total ion" counts for approximate H^+ measurements. Any sampling that has not been corrected for background noise, because of gaps in the telemetry, for example, has been discarded.

A2. Data Format

This study makes use of an archival data set recently completed for NASA's Explorer Project and placed in the NSSDC under index number 77-102A-12I. The format of these data is designed to be a compact representation with roughly the same time resolution as that provided by the instrument energy-mass scan cycle. Although these data include various spectral information, this study is mainly based on files which contain velocity moments. Only a brief outline of the format can be provided here; a detailed explanation (user guide) may be obtained from the NSSDC. The time coverage of these data spans the so called "prime period" of ISEE operations, from the time of launch of ISEE 1 and 2 through the end of February 1980.

The main type of file used here contains separate velocity moments for the four principal ion species, H^+, He^{++}, He^+, and O^+, or in some cases a subset of these ions, depending on the instrument operating mode. The moments have been calculated once each energy-mass scan cycle, using two different methods to be explained below. In cases where the energy scans have left some channels unsampled, sometimes every other channel, an interpolation procedure has been employed, essentially assuming a linear variation of the differential flux. Each moment has a statistical uncertainty (standard deviation) assigned to it, calculated with standard formulas for error propagation [e.g., Bevington, 1969, pp. 56–64] assuming Poisson counting statistics and including the uncertainty in background subtraction [Lennartsson and Sharp, 1982].

A second type of file has velocity moments for "total ions," based on the total ion count rate in the electrostatic analyzer and assuming that this rate is due entirely to H^+ ions. These moments have been calculated once per energy scan, providing a time resolution of a couple of minutes or better, and usually have nearly continuous time coverage. The reason for using "total" moments here is to help interpret the mass-resolved moments (see text).

To calculate full three-dimensional velocity moments from the raw ISEE 1 data, the ion fluxes measured within the near-ecliptic field of view have been extrapolated to other angles using either of two sets of approximating assumptions:

1. The principal ion flow is parallel to the solar ecliptic plane and the ion fluxes have rotational symmetry around the flow vector, regardless of the magnetic field orientation. The direction of the flow vector within this plane is deter-

mined by the measured flow within the instrument field of view. The single angular variable in this case is divided among twelve 30° spin angle bins, roughly approximating the inherent angular resolution of the ISEE 1 instrument in normal low-bit-rate operation.

2. Fluxes are gyrotropic (independent of gyration angle) over the sampled range of pitch angles, and isotropic outside of this range, maintaining the values measured at the smallest and largest pitch angles, respectively. The pitch angles are divided among nine 20° bins. This assumption is only applied to number densities, mean energies, parallel and perpendicular to the magnetic field, and energy densities. It ignores any net bulk flow perpendicular to the magnetic field.

The moments reported here are those obtained with 1, except when they refer specifically to components parallel and perpendicular to the magnetic field, thus necessitating the use of 2. The two sets of assumptions usually provide about the same densities and total mean energies, within statistical uncertainties, but the numbers obtained with 1 are believed to be at least marginally more accurate in most cases. Although the drift direction in 1 is determined from average fluxes in 30° wide bins, the weighting involved in the integrations usually provides an accuracy much better than 30°.

The moment data have been supplemented with a third type of file, containing a form of energy-angle spectra for the same four ion species (and for O^{++} ions). These spectra consist of spin-averaged count rates in each energy channel (typically all 32 channels), averaged over a single energy-mass scan cycle, combined with information about the maximum count rate at each energy during that cycle. This information includes the time and spin angle of the maximum, the maximum rate, and the angular range of counts greater than 1/3 of the maximum rate. These have been used to verify that the moments still have reasonable values when count rates are narrowly focused in angle or energy and are otherwise low, as often happens in the tail lobes [*Sharp et al.*, 1981].

References

Akasofu, S.-I., E. W. Hones, Jr., S. J. Bame, J. R. Asbridge, and A. T. Y. Lui, Magnetotail and boundary layer plasmas at a geocentric distance of ~18R_E: VELA 5 and 6 observations, *J. Geophys. Res.*, *78*, 7257, 1973.

Bevington, P. R., *Data Reduction and Error Analysis for the Physical Sciences*, McGraw-Hill, New York, 1969.

DeCoster, R. J., and L. A. Frank, Observations pertaining to the dynamics of the plasma sheet, *J. Geophys. Res.*, *84*, 5099, 1979.

Delcourt, D. C., C. R. Chappell, T. E. Moore, and J. H. Waite, Jr., A three-dimensional numerical model of ionospheric plasma in the magnetosphere, *J. Geophys. Res.*, *94*, 11,893, 1989.

Eastman, T. E., L. A. Frank, and C. Y. Huang, The boundary layers as the primary transport regions of the earth's magnetotail, *J. Geophys. Res.*, *90*, 9541, 1985.

Feldman, W. C., J. R. Asbridge, S. J. Bame, and J. T. Gosling, Long-term variations of selected solar wind properties: Imp 6, 7, and 8 results, *J. Geophys. Res.*, *83*, 2177, 1978.

Gloeckler, G., and D. C. Hamilton, AMPTE ion composition results, *Phys. Scr.*, *T18*, 73, 1987.

Hardy, D. A., H. K. Hills, and J. W. Freeman, Occurrence of lobe plasma at lunar distance, *J. Geophys. Res.*, *84*, 72, 1979.

Hones, E. W., Jr., J. R. Asbridge, and S. J. Bame, Time variations of the magnetotail plasma sheet at 18R_E determined from concurrent observations by a pair of Vela satellites, *J. Geophys. Res.*, *76*, 4402, 1971.

Hones, E. W., Jr., T. A. Fritz, J. Birn, J. Cooney, and S. J. Bame, Detailed observations of the plasma sheet during a substorm on April 24, 1979, *J. Geophys. Res.*, *91*, 6845, 1986.

Kamei, T., and H. Maeda, Auroral electrojet indices (*AE*) for January-June 1978, Data Book 3, World Data Cent. C2 for Geomagn., Kyoto, Jpn., April 1981.

Kiessling, M., and H. J. Ziegler, A theory of self-consistent two-dimensional tail equilibria for quasi-neutral $e^- H^+ O^+$ mixtures, *J. Geophys. Res.*, *94*, 261, 1989.

Lennartsson, W., A scenario for solar wind penetration of Earth's magnetic tail based on ion composition data from the ISEE 1 spacecraft, *J. Geophys. Res.*, *97*, 19,221, 1992.

Lennartsson, W., and R. D. Sharp, A comparison of the 0.1-17 keV/e ion composition in the near equatorial magnetosphere between quiet and disturbed conditions, *J. Geophys. Res.*, *87*, 6109, 1982.

Lennartsson, W., and E. G. Shelley, Survey of 0.1- to 16-keV/e plasma sheet ion composition, *J. Geophys. Res.*, *91*, 3061, 1986.

Parks, G. K., et al., Low-energy particle layer outside of the plasma sheet boundary, *J. Geophys. Res.*, *97*, 2943, 1992.

Press, W. H., B. P. Flannery, S. A. Teukolsky, and W. T. Vetterling, *Numerical Recipes*, Cambridge University Press, New York, 1986.

Russell, C. T., The ISEE 1 and 2 fluxgate magnetometers, *IEEE Trans. Geosci. Electron.*, *GE-16*, 239, 1978.

Sharp, R. D., D. L. Carr, W. K. Peterson, and E. G. Shelley, Ion streams in the magnetotail, *J. Geophys. Res.*, *86*, 4639, 1981.

Shelley, E. G., R. D., Sharp, R. G. Johnson, J. Geiss, P. Eberhardt, H. Balsiger, G. Haerendel, and H. Rosenbauer, Plasma composition experiment on ISEE-A, *IEEE Trans. Geosci. Electron.*, *GE-16*, 266, 1978.

Speiser, T. W., Particle trajectories in model current sheets, 1, Analytical solutions, *J. Geophys. Res.*, *70*, 4219, 1965.

Young, D. T., H. Balsiger, and J. Geiss, Correlations of magnetospheric ion composition with geomagnetic and solar activity, *J. Geophys. Res.*, *87*, 9077, 1982.

Zwickl, R. D., D. N. Baker, S. J. Bame, W. C. Feldman, J. T. Gosling, E. W. Hones, Jr., D. J. McComas, B. T. Tsurutani, and J. A. Slavin, Evolution of the Earth's distant magnetotail: ISEE 3 electron plasma results, *J. Geophys. Res.*, *89*, 11,007, 1984.

O. W. Lennartsson, Lockheed Missiles and Space Company, Incorporated, Research and Development, Palo Alto, CA 94304-1191. (e-mail.SPAN.lockhd::Lenn)

Experimental Investigation of Possible Geomagnetic Feedback From Energetic (0.1 to 16 keV) Terrestrial O⁺ Ions in the Magnetotail Current Sheet

O. W. LENNARTSSON, D. M. KLUMPAR, E. G. SHELLEY, AND J. M. QUINN

Division of Research and Development, Lockheed Missiles and Space Company, Incorporated, Palo Alto, California

Data from energetic ion mass spectrometers on the ISEE 1 and AMPTE/CCE spacecraft are combined with geomagnetic and solar indices to investigate, in a statistical fashion, whether energized O⁺ ions of terrestrial origin constitute a source of feedback which triggers or amplifies geomagnetic activity, as has been suggested in the literature, by contributing a destabilizing mass increase in the magnetotail current sheet. The ISEE 1 data (0.1-16 keV/e) provide in situ observations of the O⁺ concentration in the central plasma sheet, inside of 23 R_E, during the rising and maximum phases of solar cycle 21, as well as inner magnetosphere data from same period. The CCE data (0.1-17 keV/e), taken during the subsequent solar minimum, all within 9 R_E, provide a reference for long-term variations in the magnetosphere O⁺ content. Statistical correlations between the ion data and the indices, and between different indices, all point in the same direction: there is probably no feedback specific to the O⁺ ions, in spite of the fact that they often contribute most of the ion mass density in the tail current sheet.

1. INTRODUCTION

Singly charged oxygen is a variable but usually substantial component of the magnetospheric plasmas at most energies [*Shelley et al.*, 1972; *Ghielmetti et al.*, 1978; *Balsiger et al.*, 1980; *Sharp et al.*, 1981; *Lundin et al.*, 1982; *Lennartsson and Shelley*, 1986; *Möbius et al.*, 1987; *Gloeckler and Hamilton*, 1987; *Chappell et al.*, 1987]. It is perhaps, besides H⁺ and He⁺⁺ ions, the most important ion component from a scientific point of view, for at least two reasons. One is its principal source, Earth's atmosphere [*Young et al.*, 1982; *Kremser et al.*, 1988], which makes it a unique measure of electrical solar-terrestrial interactions. This is the one aspect that has received the closest attention in the literature so far. Another reason, however, is the large mass or mass per charge of the O⁺ ions compared to that of the H⁺ ions. A mere 10% admixture of O⁺ ions in an otherwise pure H⁺ population will more than double the mass density of the plasma, even though the number density and charge density remain almost the same. And a 50-50 mixture of O⁺ and H⁺ ions, often reached in the inner magnetosphere [*Lennartsson and Sharp*, 1982] and sometimes in the central plasma sheet as far out as 20 R_E [*Peterson et al.*, 1981], will have almost an order of magnitude greater mass density than the corresponding number of only H⁺ ions. This property of the O⁺ component may have significant consequences for the plasma dynamics; it certainly has for hydromagnetic wave propagation [e.g., *Singer et al.*, 1979].

Although the energetic (keV) O⁺ ions observed in the near-equatorial magnetosphere are commonly perceived to be a product of geomagnetic storm or substorm activity, a good case has been made for feedback effects as well [e.g., *Baker et al.*, 1982, 1985; *Delcourt et al.*, 1989; *Daglis et al.*, 1990, 1991; *Moore and Delcourt*, 1992; *Swift*, 1992]. *Baker et al.* [1982] argued that the addition of such O⁺ ions in the tail current sheet, after the onset of a substorm, will have a

destabilizing effect on this sheet, especially at $-15 R_E <$ GSM $X < -10 R_E$, the reason being that the large mass per charge of the O⁺ ions may cause the sheet ion population to become increasingly demagnetized and therefore more susceptible to ion tearing mode instabilities. This course of reasoning allows for the initial increase in the tail O⁺ population, after a period of geomagnetic quiescence, to be induced entirely by external forces, but it suggests that the increased concentration of O⁺ ions will promote consequent substorm onsets, thereby prolonging and strengthening many active periods.

One observational fact that may seem to fit with that kind of scenario is the tendency of very strong substorms, those with a peak AE index of 1000 nT or greater, to occur in clusters during extended periods (often a day or longer) of elevated AE (see, for example, *Kamei and Maeda* [1981] and *Baker et al.* [1985]). On the other hand, more long-term records of geomagnetic and solar activity, covering several years, may not seem to fit the same trend, because the energetic O⁺ population has been found to vary substantially in density over the course of a solar cycle without causing a parallel long-term variation of geomagnetic activity [*Young et al.*, 1982; *Yau et al.*, 1985; *Lennartsson*, 1989]. None of the long-term studies of O⁺ ions has been specifically directed towards the feedback aspect, however, so there is still room for doubt either way.

This study attempts to clarify, to the extent possible with statistical methods, whether there is a geomagnetic feedback specific to the O⁺ ions, by comparing extensive sets of near-equatorial ion composition data with common geomagnetic and solar activity indices. In order to utilize the long-term observations now available from similar experiments, data obtained during the rising and maximum phases of solar cycle 21 by a mass spectrometer on the International Sun-Earth Explorer (ISEE 1) spacecraft are intercompared with data obtained near the end of the same cycle, at the minimum phase, by the same kind of spectrometer on the Charge Composition Explorer (CCE) spacecraft of the Ac-

PRECEDING PAGE BLANK NOT FILMED

tive Magnetosphere Particle Tracer Explorer (AMPTE) mission.

The focus of this study is on the consequences, if any, of increasing the average mass per ion in the central plasma sheet by adding O^+ ions, or replacing H^+ ions with O^+ ions. It is recognized that the O^+ ions, along with other ions of terrestrial origin, energetic or not, must have some role in magnetosphere dynamics simply by contributing a positive plasma component but that aspect is more complex and does not necessarily distinguish the O^+ as a species. It is the exceptional capability of the O^+ to enhance the plasma mass density that is of principal interest here.

2. INSTRUMENTATION

The ISEE 1 spacecraft (along with the ISEE 2) was launched on October 22, 1977, into an orbit with apogee at almost 23 R_E (geocentric), perigee at ~300 km altitude, an inclination of 29°, and an orbital period of 57 hours. It was placed in a spinning mode with the axis nearly perpendicular to the solar ecliptic plane and with a period of approximately 3 s. The AMPTE CCE, one in a stack of three separate spacecraft, was launched on August 16, 1984, and directed into a very nearly equatorial orbit with apogee at almost 9 R_E, perigee at ~1000 km altitude, an inclination of less than 5°, and an orbital period of 15.6 hours. The AMPTE CCE is also in a spinning mode, but its spin axis is parallel to Earth's equatorial plane, pointing some 10° to 30° from the Sun direction, and its spin period is 6 s.

The Lockheed ion composition experiments flown on ISEE 1 and AMPTE/CCE are two of a family of instruments using the same type of ion optics and covering nearly the same range of energies (0 eV/e to ~17 keV/e) which have also been flown on GEOS 1 and 2 and on DE 1 [Shelley et al., 1978, 1985]. The ISEE 1 instrument consists of two nearly identical mass spectrometers with the respective fields of view centered 5° above and 5° below the spin plane, that is about 5° above and below the solar ecliptic plane. Data used in this study are from one of these, the one looking below the spin plane. The CCE instrument has a single mass spectrometer with the field of view centered in the spin plane, which in that case is roughly perpendicular to the solar ecliptic plane, oriented somewhat like the GSE Y-Z plane. Each field of view is ~10° wide along the spin plane, and some 10° to 50° wide transverse to this plane, being the widest at the low-energy end (due to preacceleration) and gradually decreasing toward 10° with increasing energy. Information on the instantaneous pitch angles (at center of field of view) is provided by the ISEE 1 fluxgate magnetometer [Russell, 1978] and the AMPTE CCE Magnetic Field Experiment [Potemra et al., 1985].

Each spectrometer consists of an electrostatic analyzer to select energy per charge, followed by a combined electrostatic and magnetic analyzer to select mass per charge. Both analyzer sections have particle detectors, so at each energy setting the experiments provide both the total ion flux and the partial flux at a selected mass per charge. On ISEE 1 each combination of energy and mass is maintained for at least 1/16 s in high telemetry bit rate and 1/4 s in low (normal) bit rate, on CCE the corresponding time is 1/32 s. Different combinations are stepped through in a cyclic fashion according to various patterns controlled by a random access memory which is programmable from the ground. The ISEE

1 patterns, or "modes," used inside the magnetosphere usually require from 2 to 17 min to complete. Most commonly used CCE patterns require ~2 min per cycle. The mass selections include one that blocks all ions from reaching the second detector, allowing intermittent measurements of the noise associated with penetrating radiation. These measurements are later used to correct the count rates of mass analyzed ions.

The maximum energy range is 0 eV/e (or spacecraft potential) to 17.9 keV/e, divided into 32 contiguous channels, although only a subset of these may be used in a given mode (typically only 15 channels on CCE). The lowest channel, from 0 eV/e to ~100 eV/e, is normally limited to energies above 10 eV/e on ISEE 1 and above 30 eV/e on CCE by an RPA (retarding potential analyzer) in the entrance. That same RPA is used to provide "cold plasma" data from 0 to 100 eV/e (retarding within the lowest channel) during part of some measurement cycles. Because of measurement uncertainties associated with spacecraft charging and plasma convection, the lowest energy channel is treated separately when calculating velocity moments. Data from this channel are not included in the statistical material here but are discussed briefly in a separate section. In the case of ISEE 1, data from the highest-energy channel (above 16 keV/e) are also excluded from moment calculations, because of a slight variation over time of the mass response in that channel. Whenever the energy scans have left some intermediate energy channels unsampled, an interpolation procedure has been employed, assuming a linear variation of the differential flux. Given these considerations, and given the numerical procedures used for weighting and summing counts from the various energy channels, the velocity moments displayed in the following figures correspond to an energy range of ~100 eV/e to 16 keV/e for ISEE 1 and 100 eV/e to 17 keV/e for AMPTE/CCE.

3. DATA FORMATS

This study is the first extensive application of two archival data sets recently completed for NASA's Explorer Project. The formats of these data are designed to be a compact representation, with roughly the same time resolution as that provided by the instrument energy-mass scan cycle. Although these data sets include various spectral information, only the files containing velocity moments have been used here.

The ISEE 1 data files contain separate velocity moments for the four principal ion species, H^+, He^{++}, He^+, and O^+, calculated once each energy-mass scan cycle, using two different methods to be explained below. Each moment has a statistical uncertainty (standard deviation) assigned to it, calculated with standard formulas for error propagation assuming Poisson counting statistics and including the uncertainty in background subtraction. In addition, there are velocity moments for "total ions," based on the total ion count rate in the electrostatic analyzer and assuming that this rate is due entirely to H^+ ions. These moments are calculated once per energy scan, providing a time resolution of a couple of minutes or better, and usually have nearly continuous time coverage. The reason for including "total" moments here is to help separate mass-resolved moments taken in different plasma regimes (see next section).

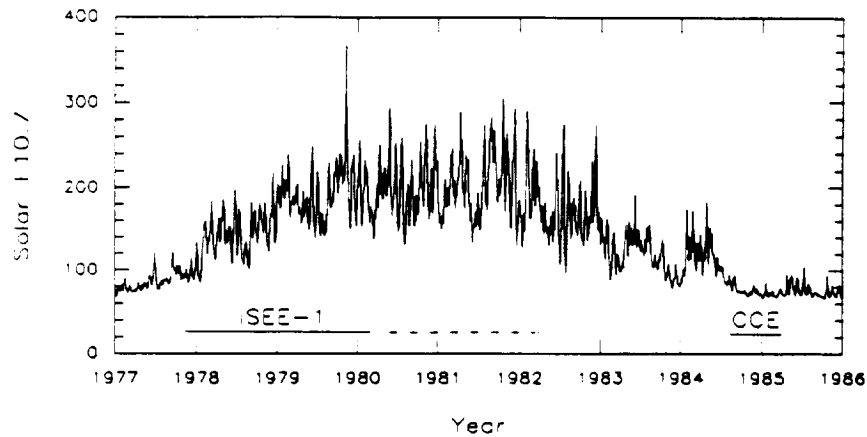To calculate full three-dimensional velocity moments from

Fig. 1. Time ranges of available ion composition data in relation to solar activity. Only the solid line (archived) portion of the ISEE 1 data is used here (years labeled at beginning).

the raw ISEE 1 data, the ion fluxes measured within the near-ecliptic field of view have been extrapolated to other angles using either of two sets of approximating assumptions:

1. The principal ion flow is parallel to the solar ecliptic plane and the ion fluxes have rotational symmetry around the flow vector, regardless of the magnetic field orientation. The direction of the flow vector within this plane is determined by the measured flow within the instrument field of view. The single angular variable in this case is divided among 12 30° spin-angle bins, roughly approximating the inherent angular resolution of the ISEE 1 instrument in normal low-bit-rate operation.

2. Fluxes are gyrotropic (independent of gyration angle) over the sampled range of pitch angles, and isotropic outside of this range, maintaining the values measured at the smallest and largest pitch angles, respectively. The pitch angles are divided among nine 20° bins. This assumption is only applied to number densities, mean energies, parallel and perpendicular to the magnetic field, and energy densities. It ignores any net bulk flow perpendicular to the magnetic field.

The two sets of assumptions typically yield about the same number densities and total energy densities, within statistical uncertainties, except for cases of substantial ecliptic ion drift across the magnetic field (substantial when compared to thermal velocities), when 1 appears to provide more accurate values, especially for number densities. This has been verified by comparing the ion densities with electron densities derived from ISEE 1 and 2 wave experiments on several occasions. Although the drift direction in 1 is determined from average fluxes in 30° wide bins, the weighting involved in the integrations usually provides an accuracy much better than 30°. For simplicity, the ISEE 1 number densities illustrated here are those derived from 1 when referring to the magnetotail (plasma sheet) and from 2 when referring to the inner magnetosphere (for comparison with CCE densities).

The AMPTE/CCE moment files use a common integration time of 6.4 minutes for both the mass resolved data and the total ion data. The CCE velocity moments have all been calculated according to approximation 2 above, including a standard deviation for each moment, except that the counts were initially separated between the right and left side of the magnetic field direction, in order to allow a cross-B velocity

to be calculated (along with a parallel velocity). Because of the attitude and orbit of the spacecraft, the CCE instrument normally samples fluxes along the magnetic field direction. In addition to the H⁺, He⁺⁺, He⁺, and O⁺ ions these files also include O⁺⁺ ions. It is clear from these data that the O⁺⁺ ions, as was assumed during the preparation of the ISEE 1 files, are generally much less abundant than the O⁺ ions at these energies, typically by 1 to 2 orders of magnitude (see also Young et al. [1982]). The same appears to hold at higher energies as well, according to data from the CHEM experiment on AMPTE/CCE [Kremser et al., 1988].

4. DATA SELECTION

The time coverage of the ISEE 1 and AMPTE/CCE data sets through solar cycle 21 is illustrated in Figure 1, along with the daily index of 10.7-cm wavelength solar radio flux. This index is commonly used as a proxy for the solar extreme ultraviolet (EUV) radiation [Hinteregger, 1981] and is therefore an indirect measure of the solar radiant effects on the terrestrial O⁺ source [e.g., Young et al., 1982, and references therein]. Figure 1 shows the reason for intercomparing the two data sets; the ISEE 1 set was acquired during strongly varying solar activity, including the peak, the CCE set during weak and extremely steady solar activity. The significance of this will be clarified later.

Of all the ISEE 1 data available, only three subsets have been used here, one obtained in the central plasma sheet, the other two in the inner magnetosphere, in the same spatial region as the CCE data. The spatial distribution of the plasma sheet samplings is illustrated in Figure 2 in GSM coordinates, with each point representing one instrument energy-mass cycle. The samplings are all from geocentric distances beyond 10 R_E and have been further limited to −10 R_E < GSM Y < 10 R_E and GSM X < −5 R_E. The main reason for choosing this particular region is that the plasma sheet O⁺ density has been found to have a rather broad maximum within 10 R_E of either side of local midnight during periods of hourly AE > 200 nT (see Figure 7d of Lennartsson and Shelley [1986]).

The central plasma sheet has been defined by the following conditions:

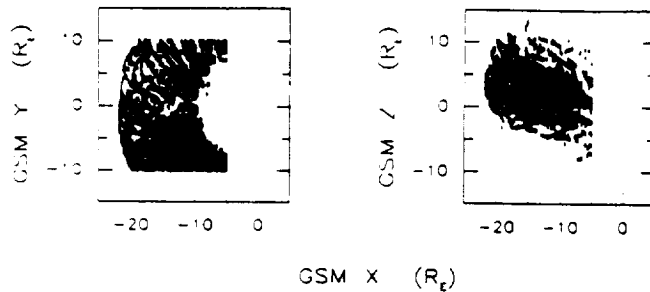1. The sum of the H⁺, He⁺⁺, He⁺, and O⁺ densities is at least 0.1 cm⁻³.

Fig. 2. Spatial extent of selected plasma sheet data set (ISEE 1) in Geocentric Solar Magnetospheric (GSM) coordinates.

2. The plasma beta value produced by these same ions is at least 0.1.

3. The multiple densities derived from the total ion count rates during the course of each energy-mass scan cycle, assuming only H⁺ ions (see previous section), are all at least 0.05 cm⁻³.

These conditions differ slightly from those used by *Lennartsson and Shelley* [1986] but lead to essentially the same selection, given the spatial constraints. The present data set is further constrained by the requirement that concurrent AE indices be available, resulting in the exclusion of samplings from 1977 (see *Kamei and Maeda* [1981], and subsequent data books). The resulting number of samples is 4056 (~1000 hours).

For this study the CCE samplings have first been binned and averaged into a time-space matrix of 1 hour UT by 1 hour MLT by one dipole L unit, in order to make the set more compact. The spatial distribution of the elements (average coordinates) is illustrated in Figure 3 in SM coordinates (same as GSM, except for a rotation around the Y axis to make the Z axis equal to the northward dipole axis). The samplings have been limited to $L > 6$ in order to ensure that the ion composition is controlled by the particle sources rather than by charge exchange decay [*Lennartsson and Sharp*, 1982]. In addition, the samplings have been confined to the inside of the magnetopause, by elimination of data that might be interpreted as magnetosheath or solar wind (based in part on total moments). The reason for dividing the data by year is that AE indices, at this writing, are not available on magnetic tape for 1985. The set is made up of 7998 individual 6.4-min samplings from 1984, and 8211 such
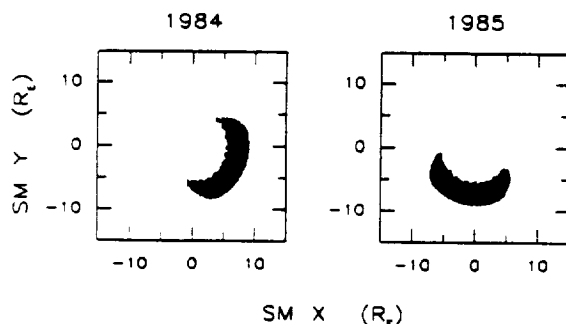
Fig. 3. Spatial extent of selected CCE data sets in Solar Magnetic (SM) coordinates. These extend in geomagnetic latitude from −16° to +12°. Equivalent regions are used for ISEE 1 data as well (see text).

samplings from 1985, binned and averaged into 1732 and 1728 matrix elements, respectively.

The two spatial regions thus defined by the CCE data have in turn been used to select two "inner magnetosphere" sets of ISEE 1 data as well (similarly excluding magnetosheath and solar wind). The resulting number of samples in these ISEE 1 sets is 581 (corresponding to 1984 CCE set) and 693 (1985 CCE set).

5. STATISTICAL RESULTS

Whether auroral substorms, as defined by enhancements in the AE index, for instance, are triggered by an increasing concentration of O⁺ ions in the tail current sheet [e.g., *Baker et al.*, 1982], or always start independently of the O⁺, may seem to be a simple question of timing. The answer is not readily found by studying individual events, however, because the O⁺ data from within the plasma sheet are rather spotty during active periods, due to plasma sheet motion and thinning, and the substorm activity is often recurring too rapidly to allow a unique association between enhancements in the AE and in the O⁺ density. The only firm conclusion that can be drawn from previous event studies is that there are numerous cases where the ISEE 1 is in the central plasma sheet at a substorm expansion onset and does not observe a large concentration of O⁺ (>10%) until after onset (R. D. Sharp, unpublished manuscript, 1982; see also *Baker et al.* [1985]). Hence we have had reasons to believe that substorms can occur before the O⁺ density is enhanced in the tail, but we still do not know whether they occur more easily if the O⁺ density is already high, or if they are stronger in that case.

5.1. *Relative Timing*

As a first step in addressing this question, the entire set of ISEE 1 plasma sheet data, as defined above (see Figure 2), was scoured for evidence that the O⁺/H⁺ density ratio might sometimes undergo a significant increase shortly before such an increase takes place in the AE index. Several different approaches were tried, using different definitions of "significant increase" and "shortly before." The result was essentially negative; there was no clear evidence that any increment in the AE could be uniquely associated with a preceding, or even simultaneous, increase in the O⁺/H⁺ ratio, and this was due in part to the difficulties already mentioned. One approach, for example, was to use hourly AE indices and pose the following problem:

Find each sampling with an O⁺/H⁺ ratio greater than 30%, which is preceded by at least a 3-hour period of samplings with O⁺/H⁺ consistently less than 20%, allowing no more than 60 min for data gaps during that period, and check whether the concurrent or succeeding hourly AE is greater, by any amount, than the preceding 3-hour average AE. The result: No case of a succeeding increase in the hourly AE, but one case of a concurrent increase. In that one case the 1-min AE indices were examined next, and the AE proved to increase ahead of the increase in the O⁺/H⁺ ratio.

5.2. *Correlation Between AE and Average Ion Mass in Plasma Sheet*

Figure 4 shows a purely statistical approach, where each plasma sheet sampling is represented by its linearly averaged
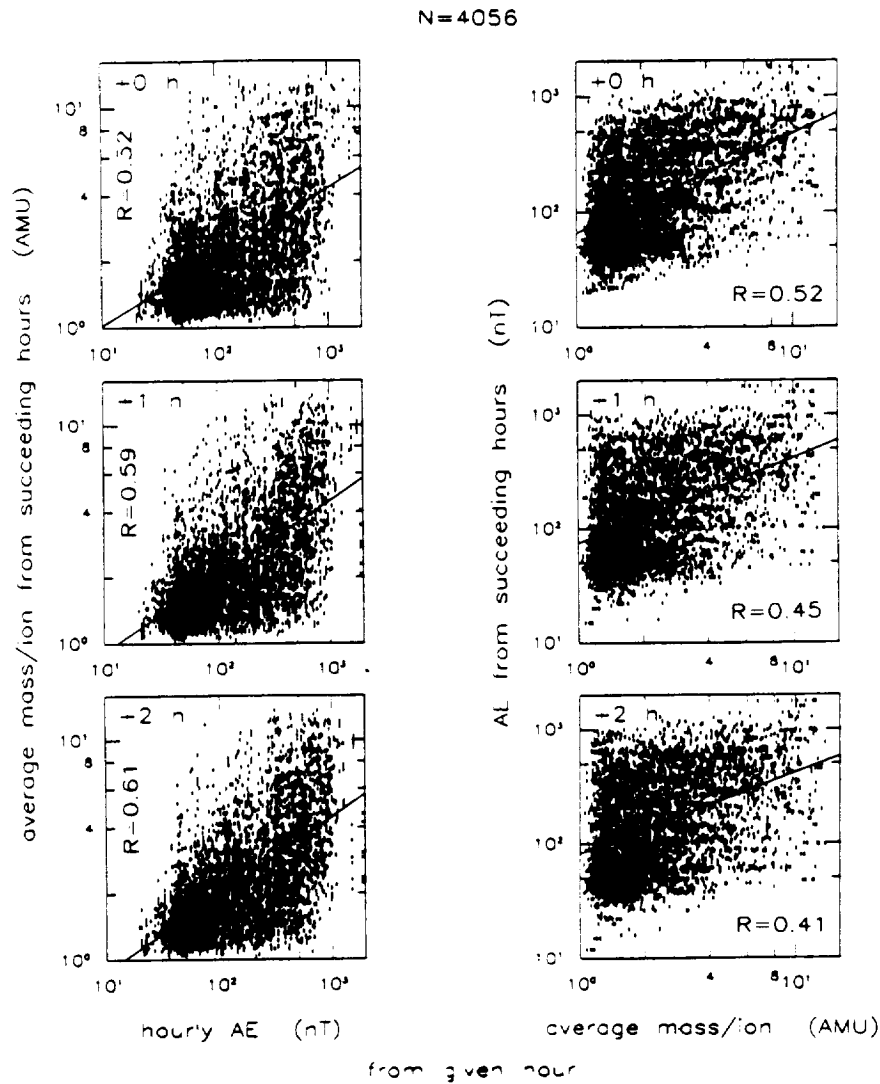
N=4056

Fig. 4. Scatterplots of average ion mass in plasma sheet versus hourly AE (left) and vice versa (right). The top panels compare AE readings and mass samplings from same hour, the lower panels compare AE or mass with mass and AE from the first (middle) and second (bottom) succeeding hour. The regression lines in this and following figures have a correlation coefficient as indicated by parameter R. The parameter N indicates the number of data points in each panel.

ion mass, weighted by the respective densities of H^+, He^{++}, He^+, and O^+ ions (thus having a range of 1.0 to 16.0 amu), and is associated with hourly AE indices from the same (top panels) or adjacent hours. Because the He^{++} ions are always in minority here (almost always less than 10% of total number density), the average mass is also approximately the average mass per charge, which may be the physically more significant quantity (or mass divided by the square of the charge). This mass, whether associated with ion or charge, is not expected to be significantly defective by not including O^{++} ions (see end of section 3).

In the left panels of Figure 4 the average mass is treated as a function of the hourly AE index, allowing up to 2 hours delay from each AE reading to the plasma sheet sampling. The slanted straight line in each panel is the linear least squares fit of log (mass) versus log (AE). The reason for using a linear fit here is that when the AE is binned, rather than scattered, the logarithm of the average mass in each AE bin is approximately a linear function of the logarithm of AE

(not shown). The correlation coefficient, denoted by the letter R, is significant in each case, given the large number of points (4056). The generally greater mass/ion during active times is due to a combination of increasing O^+ density and decreasing H^+ and He^{++} densities [see Lennartsson and Shelley, 1986]. The He^+ ions contribute a negligible density in the central plasma sheet at most times. It can be seen that the correlation is somewhat better with a 2-hour delay than with a shorter delay, or no delay. The correlation with a 2-hour delay is in fact at its maximum; it declines again with longer delays, reaching a value of $R = 0.45$ with a 5-hour delay, for instance (not illustrated).

In the right panels of Figure 4 the AE index is similarly treated as a function of the average mass, using the same set of plasma sheet samplings. In this case the correlation coefficient declines monotonically with increasing delay, reaching $R = 0.45$ already with a 1-hour delay (and $R = 0.31$ with a 5-hour delay). Clearly, the AE is less well correlated with preceding values of the average ion mass

TABLE 1. Autocorrelation of Log (Hourly AE) in 1978–1979 ($N = 17520$)

Lag Time, hours	Correlation Coefficient
1	0.87
2	0.70
3	0.61
4	0.55
5	0.51
6	0.46

than vice versa. Note also that the regression line in the top right panel is different from the corresponding line in the top left panel, even though the two correlation coefficients are the same (by definition).

Figure 4 displays all plasma sheet samplings corresponding to Figure 2, including both dawn and dusk halves. It may be true that conditions in the dusk half are usually the most relevant to substorm onset, as argued by Baker et al. [1982], but these ion composition data show no significant asymmetry between dusk and dawn and do not justify limiting the statistical material to the dusk side only. By including the dawn half it is possible to admit more samplings from early 1978 and early 1980 and thus cover a wider range of solar surface activity (see Figure 1). This is a desirable objective in the next section. It may suffice to mention that if the scatterplots of Figure 4 are limited to the dusk half, where there are 1366 samplings, the least squares fits are virtually identical to those in Figure 4, and the correlation coefficients differ by at most 0.02.

It is quite possible that the nonzero correlation of the AE with the preceding values of the average ion mass in the right panels of Figure 4, with 1- and 2-hour delays, is purely accidental, because the AE has a very high degree of autocorrelation over long periods of time. This is illustrated by Table 1, which lists the correlation coefficients for hourly AE values taken from one to six hours apart during 1978 and 1979 (17520 hours). As can be seen, the AE at any one time is still better correlated with the AE from as much as 6 hours earlier than it is with the average ion mass during the immediately preceding hour.

5.3. Solar Cycle Effects

Figure 5 relates the average ion mass in the central plasma sheet to solar surface activity, as measured by the $F_{10.7}$, as well as geomagnetic activity. The ion mass samplings in the left panel are from geomagnetically "quiet" times, defined by requiring that the hourly AE index be consistently less than 100 nT over a 3-hour period, where the middle hour contains the mass sampling. The right panel has samplings from "disturbed" times, similarly defined by hourly AE indices being consistently greater than 200 nT over that same 3-hour period. By considering AE indices taken both before and after the mass sampling it is ensured that no bias is placed on the causal relationship between the AE and the ion mass, although the strong autocorrelation of the AE index makes the precise timing less important (see Table 1). In any case the average ion mass is found to increase with increasing solar activity, regardless of substorm activity level, and this is mainly a consequence of an increasing O⁺ density (see also Young et al. [1982] and Lennartsson [1989]). The regression lines are again based on log (mass), because a logarithmic y scale and a linear x scale provide a roughly linear dependence when data points are binned in x and averaged in y (not shown).

Although the correlation coefficient is only about 0.3 in both panels of Figure 5, the large number of data points makes it significant. It can be seen, by using standard statistical tests [Bevington, 1969, pp. 119–127; Press et al., 1986, pp. 484–487], that the probability of having no actual correlation between the ion mass and the solar activity is negligible (less than 10^{-8}). Essentially, the same statistical results are reached even if the samplings are limited to the dusk half of the plasma sheet, thereby reducing the number of data points as well as the range of $F_{10.7}$. In that case, $N = 339$ and $R = 0.25$ in the left panel ($AE < 100$ nT) and $N = 348$ and $R = 0.36$ in the right panel ($AE > 200$ nT), and the respective regression lines remain identical within one standard deviation of either the slope or the vertical location.

By contrast, the substorm activity, as measured by the AE or Kp indices, does not increase with increasing solar surface activity during this time period, neither in terms of frequency of substorm onsets nor in terms of peak ampli-
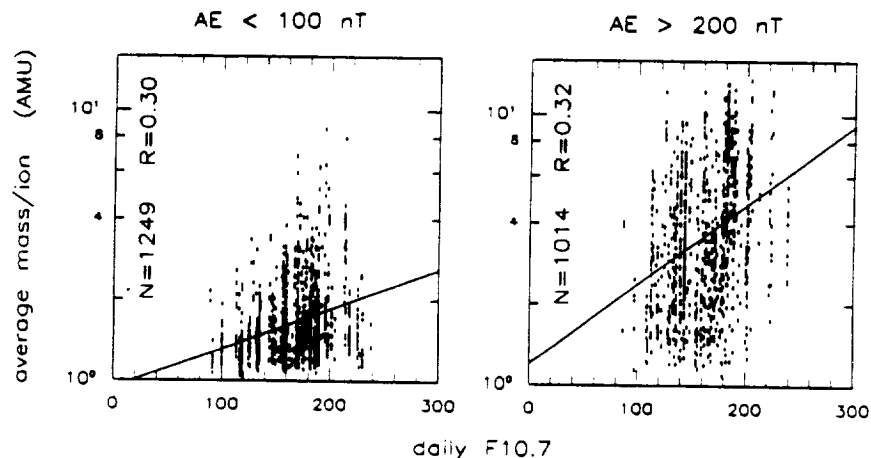

Fig. 5. Comparison of ion mass in plasma sheet with the Ottawa daily $F_{10.7}$ index (solar radio flux) during geomagnetically (left) quiet and (right) disturbed conditions (see text for selection of AE). The ion samplings have been ordered by Ottawa local time here, rather than by the usual universal time.
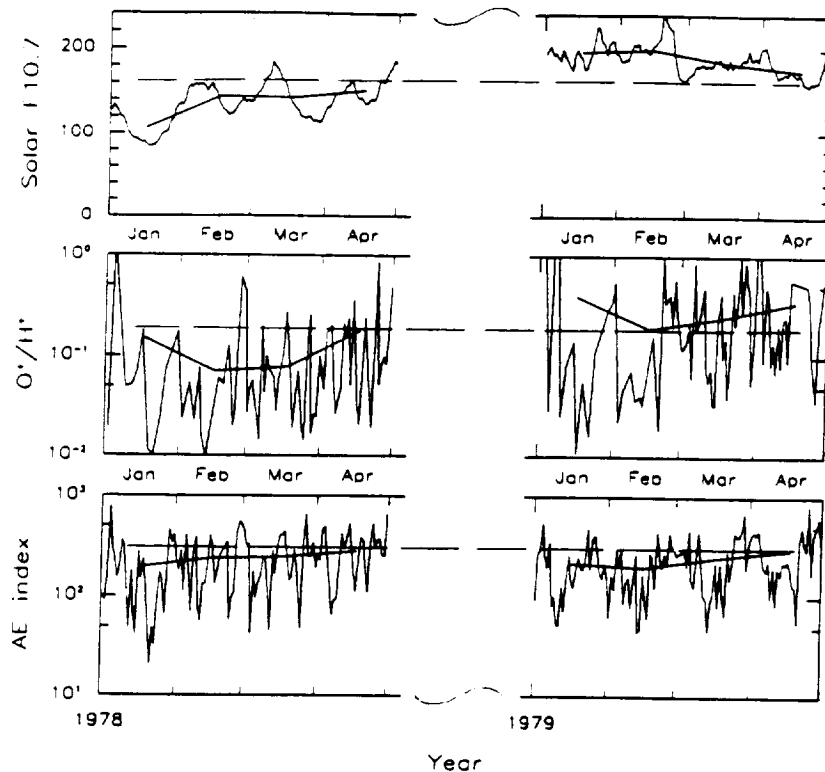
Fig. 6. (Top) Daily (jagged line) and monthly $F_{10.7}$; (middle) daily and monthly averaged plasma sheet O^+/H^+ density ratio; (bottom) daily and monthly averaged AE index. The dashed horizontal lines are for visual reference.

tude. This is partly illustrated for the AE index by Figure 6, which covers two 4-month intervals with similar ISEE 1 samplings of the plasma sheet (as defined in Figure 2), one in 1978, the other in 1979. The daily solar $F_{10.7}$ (top panel), and presumably also the concurrent EUV flux, is almost consistently higher in the later interval, resulting in a generally greater O^+/H^+ density ratio in the central plasma sheet, also represented by "daily" numbers here (middle panel), obtained by averaging all available samplings each day. These trends are still more distinct in terms of monthly averages, shown here by points centered on each month and connected by straight lines. However, the AE index (bottom panel) shows no signs of increasing from 1978 to 1979, neither as a daily nor as a monthly average (see also Figure 3 in the work by *Young et al.* [1982]). As far as the frequency of substorm onsets is concerned, a visual inspection of 1-min AE records (see *Kamei and Maeda* [1981] and subsequent data books) reveals no obvious increase from 1978 to 1979 (not illustrated here).

It may be argued that Figure 6 does show some change from 1978 to 1979 in the daily averaged AE index, since in 1979, but not in 1978, the AE appears to be modulated at a rate resembling the solar rotation period, which ranges from 25 to 36 days, depending on latitude and physical feature [*Hansen et al.*, 1969, and references therein]. This is probably not caused by a solar-induced periodicity in the O^+ density, however, since the $F_{10.7}$ index is much less periodic in 1979 than in 1978. The fact that the O^+/H^+ ratio in Figure 6 does not show a clear solar rotation modulation, not even in 1978, can probably be ascribed to the rapidly varying sampling conditions, including the spacecraft motion along the orbit (at least 7 R_E per day) and the orbital drift relative to the tail ($\sim$12 R_E per month at apogee).

Returning to Figure 1, it is clear that the $F_{10.7}$ index continues to have strong oscillations for the next couple of years, including those caused by solar rotation, but it does not begin to change in a more long-term fashion again until 1983, when it starts declining, and it is not until the second half of 1984 that it reaches a low and steady level, coincident with the AMPTE/CCE data interval. At this time the $F_{10.7}$ is very close to its minimum daily (65.8 on October 8, 1985) and monthly values (69.4 in September 1986, which is the canonical end of solar cycle 21). Accordingly, the CCE data set should have substantially lower O^+ concentrations than the ISEE 1 set, even if the ISEE 1 set is averaged over most of the rising phase (to improve statistics). The CCE data contain no samplings from the plasma sheet region shown in Figure 2, but it is known from the ISEE 1 data that O^+ ions in the inner magnetosphere ($R < 10$ R_E) have virtually the same response to the $F_{10.7}$ index as do the plasma sheet O^+ ions [*Lennartsson*, 1989]. Hence, if the CCE data do show much lower O^+/H^+ ratios than do the ISEE 1 data, given the same inner magnetosphere sampling region for both sets, then it is fair to assume that the plasma sheet O^+/H^+ ratios are also substantially reduced at solar minimum (reversing the time sequence in Figure 6).

Figure 7 shows one kind of comparison between ISEE 1 and CCE data within the bounds of available AE indices. In this case each ion sampling has been associated with the average of 6 successive hourly AE indices, the last of which is concurrent. There is no special reason for choosing a 6-hour period per se, but the statistical correlation is somewhat better when an average of several hourly AE values is used rather than some single preceding value. Using preceding rather than succeeding AE values here seems intuitively
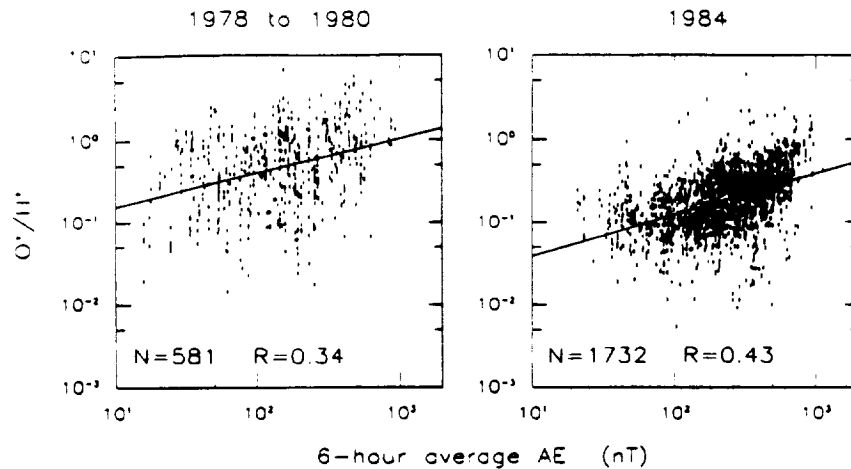
Fig. 7. Comparison of O^+/H^+ density ratio in the equatorial magnetosphere (dawn to noon; see left panel of Figure 3) with the preceding 6-hour average AE index during (left) rising-to-maximum and (right) minimum solar activity. The grand average AE during the two data sampling intervals was (left) 203 ± 7 nT and (right) 280 ± 5 nT.

right [cf. *Strangeway and Johnson*, 1984], regardless of the role of O^+ ions in the plasma sheet, and that choice is also justified by improved correlation.

Figure 7 confirms that the O^+/H^+ ratio has declined quite substantially in late 1984, near solar minimum, as compared to typical values during the rising phase of 1978 to early 1980. Even though the two instruments have different pitch angle coverage in this region of space (sections 2 and 3), the difference in the O^+/H^+ ratio between the left (ISEE 1) and right (CCE) panels is quite consistent with a time reversal of the results obtained between 1978 and 1980 at geosynchronous altitude ($L \approx 6.6$) by the GEOS 2 instrument (measuring nearly perpendicular to the magnetic field). If a median $F_{10.7}$ of 175 is assigned to the ISEE 1 data [*Lennartsson*, 1989] and an $F_{10.7}$ of 70 to the CCE data (Figure 1), the logarithmic regression formula in Table 3b of *Young et al.* [1982] predicts a reduction in the ratio by a factor of ~3.5 in 1984 for geomagnetically quiet conditions. Comparing the two regression lines in Figure 7 at low AE yields a somewhat larger reduction by a factor of 4.1, but the difference is probably within the margins of error, considering that the ISEE 1 data in Figure 7 span such a wide range of $F_{10.7}$. In any case there is a clear downward displacement of the regression line in 1984, and there is relatively less scatter about this line, resulting in a higher correlation coefficient. The improved correlation with the AE index is consistent with the strongly reduced fluctuations in the daily $F_{10.7}$ index (Figure 1), provided the O^+/H^+ ratio, as implied by Figure 5, depends not only on long-term but also on day-to-day variations in the solar irradiation.

In spite of this substantial long-term reduction in the O^+/H^+ ratio, there is no corresponding reduction in substorm activity. Instead, there is a modest but statistically significant increase over the same time period, as measured by for instance daily averages of the AE index (see *Kamei and Maeda* [1981], and subsequent data books). This trend is reflected in Figure 7 by the different grand average AE values during the two intervals of ion sampling (203 nT in the ISEE 1 interval, 280 nT in the CCE interval, the two mean values differing by more than ten times the standard deviation of either mean).

These opposing effects are even more clearly demon-

strated by means of the Kp index, which allows all of the CCE data to be used (and more than twice as much of the ISEE 1 data; see end of section 4). In Figure 8 each ion sampling has been associated with the linear average of the concurrent and the two immediately preceding Kp indices, assigning the numerical values $+1/3$ and $-1/3$ to the graduating plus and minus symbols on the Kp index. The resulting 9-hour average Kp has been binned, as shown, and the density ratios have been averaged within each bin. The grand average Kp during the two sets of ion samplings is indicated in the respective panel, in conventional notation, and further described in the caption. When expressed in decimal numbers, the two mean values differ by 50 times the standard deviation of either mean.

To place these results in a broader perspective, the hourly and daily averaged AE for all of 1978 through 1984 have been plotted versus the daily $F_{10.7}$ in Figure 9 (except for 1 day of missing $F_{10.7}$ index in 1983). Although small in magnitude, the resulting correlation coefficients are statistically significant, considering the large number of points [*Bevington*, 1969, pp. 119–127; *Press et al.*, 1986, pp. 484–487]. The fact that the two regression lines have almost exactly the same slope (same within two decimal places), even though the two sets of data points differ in size by a factor of 24, makes it almost certain that the correlation is real and not merely due to numerical rounding errors. The negative sign of the correlation is consistent, in a superficial sense, with the long-term anticorrelation just found between the O^+/H^+ ratio and the AE (Figure 7) and Kp (Figure 8), since the O^+ density is positively correlated with the $F_{10.7}$ (Figure 5; see also *Young et al.* [1982] and *Lennartsson* [1989]). This does not by itself imply a physical relationship between the AE and the $F_{10.7}$, however, because Figure 9 spans the better part of a solar cycle, and the important physical parameter may be solar cycle phase, or simply time. Indeed, if the AE is sorted by the $F_{10.7}$ on a year-by-year basis, the correlation does not even show a persistent sign. This is illustrated by Table 2.

5.4. Effects of Including Lowest Energy Channel

The possible role of ions with energies below 100 eV/e is primarily an issue with data obtained in situ, that is the ISEE
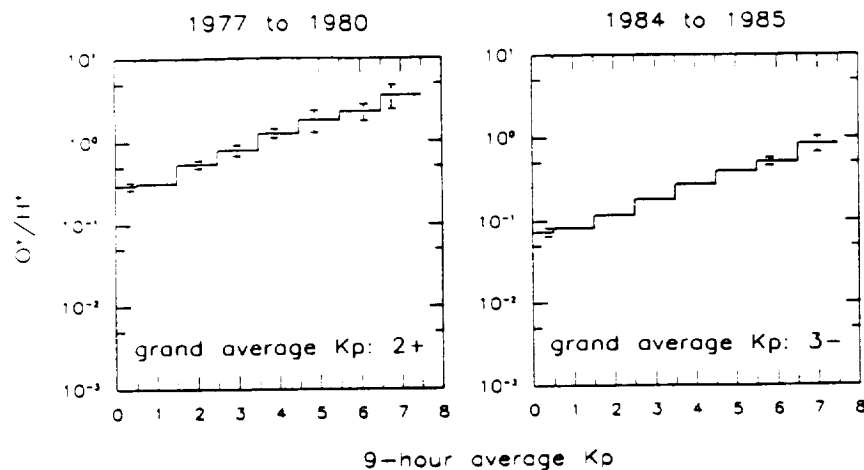
Fig. 8. Averages of same ratio as a function of the preceding 9-hour average Kp index, covering similar phases of the solar cycle, but including a larger spatial region (left and right panels of Figure 3 combined). The error bars indicate the standard deviation (plus and minus) of the average ratio in each Kp-bin, and is drawn at the average Kp within the bin (when greater than the line width). The grand average Kp in each panel represents an actual decimal number of (left) 2.26 ± 0.01 and (right; see text) 2.76 ± 0.01.

l plasma sheet data (Figure 2). The nominal range of 10–100 eV/e, not including variable RPA settings, has been measured in ~90% of the 4056 plasma sheet samplings, and these measurements almost always cover all 12 spin angle sectors at least once.

Count rates in this single energy channel have been converted to partial ion number densities assuming rotational symmetry of the ion flux around the same flow vector used for the main velocity moments (assumption 1 in section 3). This average flow vector, one for each ion species, has been based on count rates in all the other energy channels (except the highest one) and does not always approximate the true flow direction of the 10- to 100-eV/e ions. This can be a significant problem when the flux of low-energy ions is strongly focused in spin angle, in which case an error in the axis of symmetry leads to exaggerated densities.

Adding these partial densities, when measured, to the main densities has almost no effect on the statistical picture, however. In most samplings from the central plasma sheet the O^+ and He^+ densities are increased by less than 15%

and the H^+ and He^{++} densities by less than 5%. Table 3 shows the average increases. Part of the reason for these modest numbers may be that the low-energy cutoff is actually higher than 10 eV/e in much of the plasma sheet data, perhaps more typically between 10 and 20 eV/e, because of positive spacecraft charging associated with photo electron emission (see Figure 1 of *Mozer et al.* [1983]).

When Figures 4 and 5 are reproduced with the lowest-energy channel included (not shown), the new scatter patterns are virtually identical to the old ones. There is a barely perceptible flattening of the regression lines, corresponding quantitatively to a change in the third decimal place of the respective slopes. This flattening is accompanied by a slight reduction in the correlation coefficients as well, and this is again limited to the third decimal place in all cases but the left panel of Figure 5, where R is reduced to 0.28. Although very small, the reductions in the slopes and correlation coefficients of each regression line both indicate disordering. Hence, as far as the ion composition is concerned, adding the 10- to 100-eV/e partial densities in the central plasma
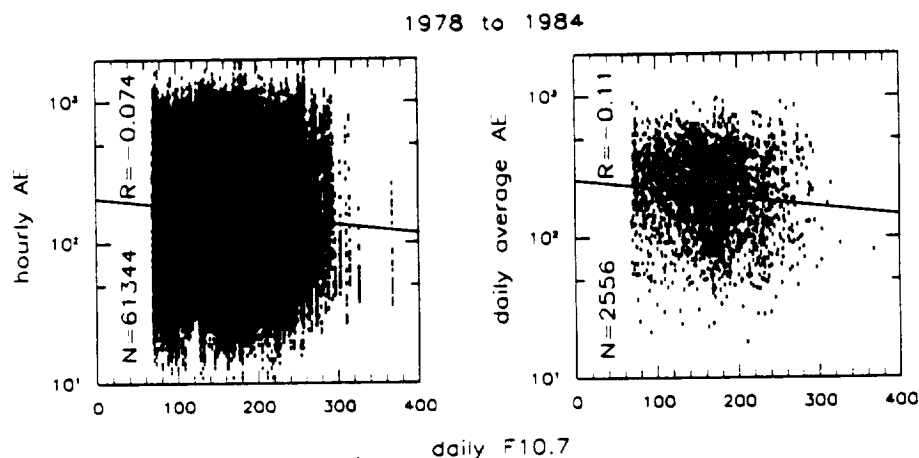

Fig. 9. Comparison of hourly (Ottawa LT; left) and daily (UT; right) AE indices with the daily solar $F_{10.7}$ index during a 7-year period (year-by-year comparison is made in Table 2).

TABLE 2. Correlation of Log (Hourly AE) With Daily $F_{10.7}$

	Year						
	1978	1979	1980	1981	1982	1983	1984
Number values	8760	8760	8784	8760	8760	8736	8784
Correlation coefficient	0.002	−0.118	0.041	0.074	0.074	0.026	0.065

sheet makes no significant physical difference, but it appears to slightly increase the measurement errors, which is the main reason for keeping the low-energy cutoff at 100 eV/e in this study.

6. CONCLUDING REMARKS

The preceding section makes no mention of the mean energy of the O⁺ ions, and there is actually no new information from this study that warrants a discussion beyond what was presented by Lennartsson and Shelley [1986] and Lennartsson [1989]. The only potentially critical issue here is whether the O⁺ energy in the central plasma sheet decreases with increasing O⁺ density, so as to offset the expected increase in the ion inertial effects. It was found previously that the O⁺ mean energy in the 0.1- to 16-keV range is indeed slightly anti-correlated with both geomagnetic [Lennartsson and Shelley, 1986] and solar activity [Lennartsson, 1989], that is anticorrelated with density, but the effect appears far too small to be of any significance here. Specifically, the O⁺ mean energy in the central plasma sheet is typically ~4 to 5 keV during low geomagnetic and solar activity and ~3 to 4 keV during moderate to strong activity.

Returning to the far greater variations in the O⁺ density, and in the O⁺/H⁺ density ratio, the challenge is now to interpret their various statistical relations with geomagnetic and solar activity. If one makes the very reasonable assumption that Figures 7 and 8 show a long-term trend that applies also to the central plasma sheet, it is clear that the frequency of occurrence of very large O⁺/H⁺ ratios in the tail current sheet can be substantially reduced over time with no hindrance to substorms. On the contrary, substorm activity increases. Is this increased activity actually caused by the relative decrease in O⁺ content? Considering Figure 5, such a scenario is consonant with the negative correlation between the AE and the $F_{10.7}$ in Figure 9. However, Table 2 shows that this negative correlation, when ordered by calendar year, is not an ordinary feature, but is limited to one (1979) of seven years. This makes it much more likely that the long-term variation of the AE is controlled by a solar process which depends on the solar cycle phase but is not well measured by the $F_{10.7}$, nor by the EUV flux.

Figure 10 may provide additional clues. It appears from Figure 10 that the year 1979 is unique in the sense that the

TABLE 3. ISEE 1 Average Incremental Density From 10- to 100-eV/e Channel in Plasma Sheet

Ion	Increment, %
H⁺	2.8
He⁺⁺	1.3
He⁺	8.2
O⁺	7.2

AE activity then approaches its absolute minimum in the 7 years considered, a minimum reached in early 1980. Since this occurs while the $F_{10.7}$ is approaching its absolute maximum (Figure 1), it probably accounts for the net negative correlation in Figure 9 (even without the singular $F_{10.7}$ peak in early November 1979). It certainly accounts for the long-term increase in the AE and the Kp in Figures 7 and 8. Whether the early 1980 minimum in the monthly average AE is entirely due to solar processes, or somehow depends on solar-induced changes in the magnetosphere particle populations, it is clearly contrary to having substorm activity enhanced by increased O⁺ concentration in the tail current sheet (see also Figure 6).

If there is any significant feedback from the O⁺, due to its large ionic mass, it must be negative: The O⁺ either inhibits the onset of substorms, acts as a damper on substorms in progress, or helps to release tail stresses at an earlier and "less harmful" stage. However, Figure 10 appears to exclude that scenario as well, since the monthly average AE starts increasing again long (2 years) before the solar $F_{10.7}$ enters its declining phase (Figure 1), which is presumably when the O⁺ concentration declines in the plasma sheet (Figure 5).

Short-term correlations are less definitive, for reasons that have been outlined above, but they appear to point in the same direction. Figure 4 suggests that the O⁺/H⁺ ratio in the plasma sheet does depend on the previous history of the AE, at least over a 2-hour interval (maximum R with two hours delay), but it gives no hint of a similar dependence of the AE on the O⁺ concentration, since the correlation in the right panels declines monotonically with time and is anyway much weaker than the autocorrelation of the AE (Table 1). Furthermore, the pattern of scattered points in Figure 4 has an almost triangular shape in the left panels, especially in the bottom panel, with one corner at small ion mass but large AE. This shape implies, ideally, that the AE can take on any large value without O⁺ ions being present, and it can do that without increasing the O⁺/H⁺ ratio uniformly throughout the central plasma sheet, but the O⁺/H⁺ ratio cannot reach very large values anywhere unless the AE is already large.

6.1. Possible Role of Very Low Energy Ions

Whether the low-energy cutoff is 10 or 100 eV/e, or some intermediate value imposed by positive spacecraft charging, does not appear to make much difference in the central plasma sheet (Table 3), but there may still be a "hidden" ion population with mean energies of a few eV, or less, associated with the terrestrial polar wind and consisting mostly of H⁺ ions [e.g., Chappell et al., 1987]. The question is, how large is this polar wind population of H⁺ ions compared with the more energetic H⁺ population measured on the ISEE 1 spacecraft? Does it have a significant effect on the average ion mass? So far there have been no direct measurements of
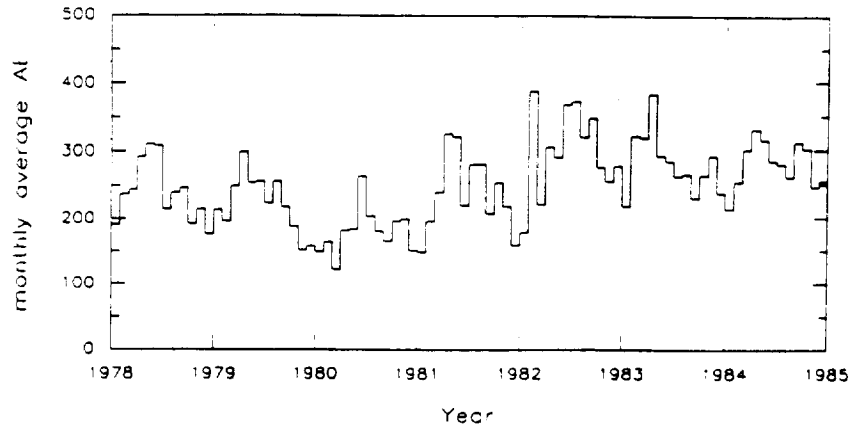
Fig. 10. Long-term variation of monthly averaged AE index (nanoteslas).

ions with only a few eV energy in the plasma sheet, beyond 10 R_E, nor have there been any large-scale attempts to infer "hidden" ions by comparing measured partial ion densities with total electron densities deduced from wave experiments, but the subject has been addressed indirectly by modeling particle trajectories, notably by Delcourt et al. [1989].

The numerical model of Delcourt et al. takes into account all presently known sources of terrestrial ion outflows, using the most recent measurements or estimates of source parameters, but it is restricted to radial distances less than 17 R_E, and its plasma sheet does not receive ions whose trajectories intersect the magnetopause or reach beyond 17 R_E downtail. As emphasized by the authors, the trajectory interrupts, especially downtail, set artificial and severe limits on the potential contribution to the plasma sheet density of H⁺ ions with initial energies of 10 eV (cusp source) or greater (auroral zone and polar cap sources) and are the main reason why the calculated H⁺ density between 10 and 17 R_E, including all energies, is only ~0.01 to 0.08 cm⁻³ (Figure 18 in their paper). However, these limits are less severe for the polar wind H⁺ ions, which are all assumed to have an initial energy of only 1 eV, so this model may provide a probable upper limit on their specific contribution in Earth's plasma sheet.

According to Figure 4 in the paper by Delcourt et al.. ~43% of the polar wind H⁺ ions remain within the model boundaries during geomagnetically quiet conditions, whereas 41% are lost downtail, because of weak equatorward convection, and 16% are lost at the magnetopause. The 43% that remain are sufficient to dominate the H⁺ density earthward of the 17 R_E boundary, but the density between 10 and 17 R_E is only about 1/10 of the energetic H⁺ density measured on the ISEE 1 (Figure 18 in same paper; see also Lennartsson and Shelley [1986]). Fewer of the polar wind ions are lost downtail during disturbed conditions (stronger convection), only ~6%, but the ionospheric source is assumed to be weaker then, by a factor of 2/3 (their Table 2), and a somewhat greater fraction is lost at the magnetopause (23%), so the model H⁺ density in the plasma sheet is still smaller, by a factor of 5 to 10, than the energetic H⁺ density measured on the ISEE 1. Hence, even with all of the lost polar wind H⁺ ions somehow recovered and added to its plasma sheet. this model seems to imply that the density of very low energy H⁺ ions (few eV) is smaller than the known

density of energetic H⁺ ions in Earth's plasma sheet, possibly substantially smaller.

It is worth noting that the polar wind is expected, on theoretical grounds, to be stronger, by approximately a factor of 3, at the minimum of the solar cycle than at the maximum of same [Chappell et al., 1987, and references therein], which is the opposite of the observed long-term trend of the O⁺ flux. To the extent that polar wind H⁺ ions do affect the ion composition in the tail current sheet, they probably amplify the difference in the O⁺/H⁺ ratio between solar maximum and minimum, thereby enhancing the long-term anticorrelation between average ion mass and geomagnetic activity implied by Figures 7 and 8 above.

6.2. Corollary

Since the energetic O⁺ ions do reach the central plasma sheet, well beyond 10 R_E, and do so in sufficient numbers to have a very significant and strongly variable influence on the average mass of keV ions (Figures 4 and 5), they must have significant and variable effects on any tail instability that depends in a decisive fashion on this mass, including any such instability powerful enough to influence the geomagnetic indices. The statistical results of this study suggest therefore that the average ion mass is an unimportant parameter in the equations that govern magnetotail stability. It is clear, at least from the long-term behavior of the AE and Kp indices (Figures 6, 7, 8, and 10), that a more frequent occurrence of large average mass/ion, or mass/charge, in the tail current sheet is not sufficient cause for stronger dissipation of auroral energy. The statistical data are more compatible with reduced energy dissipation when the ion mass becomes extremely large near solar maximum. However, the lack of a consistent correlation over time between solar and geomagnetic indices seems to rule out all significant feedback (Table 2 and Figures 1 and 10). These considerations are nominally based on ion composition data from the 0.1- to 16-keV/e energy range, but probably apply to the bulk of the plasma sheet ions.

magnetometer data and to the National Oceanic and Atmospheric Administration for the use of magnetic tape records of the geophysical and solar indices. This work was supported by NASA under contracts NAS5-30565, NAS5-31209, and NAS5-33047 and by Lockheed Independent Research.

The Editor thanks J. H. Waite and H. D. Balsiger for their assistance in evaluating this paper.

REFERENCES

Baker, D. N., E. W. Hones, Jr., D. T. Young, and J. Birn, The possible role of ionospheric oxygen in the initiation and development of plasma sheet instabilities, Geophys. Res. Lett., 9, 1337, 1982.

Baker, D. N., T. A. Fritz, W. Lennartsson, B. Wilken, and H. W. Kroehl, The role of heavy ionospheric ions in the localization of substorm disturbances on 22 March 1979: CDAW-6, J. Geophys. Res., 90, 1273, 1985.

Balsiger, H., P. Eberhardt, J. Geiss, and D. T. Young, Magnetic storm injection of 0.9- to 16-keV/e solar and terrestrial ions into the high altitude magnetosphere, J. Geophys. Res., 85, 1645, 1980.

Bevington, P. R., Data Reduction and Error Analysis for the Physical Sciences, McGraw-Hill, New York, 1969.

Chappell, C. R., T. E. Moore, and J. H. Waite, Jr., The ionosphere as a fully adequate source of plasma for the Earth's magnetosphere, J. Geophys. Res., 92, 5896, 1987.

Daglis, I. A., E. T. Sarris, and G. Kremser, Indications for ionospheric participation in the substorm process from AMPTE/ CCE observations, Geophys. Res. Lett., 17, 57, 1990.

Daglis, I. A., E. T. Sarris, and G. Kremser, Ionospheric contribution to the cross-tail current enhancement during the substorm growth phase, J. Atmos. Terr. Phys., 53, 1091, 1991.

Delcourt, D. C., C. R. Chappell, T. E. Moore, and J. H. Waite, Jr., A three-dimensional numerical model of ionospheric plasma in the magnetosphere, J. Geophys. Res., 94, 11,893, 1989.

Ghielmetti, A. G., R. G. Johnson, R. D. Sharp, and E. G. Shelley, The latitudinal, diurnal, and altitudinal distributions of upward flowing energetic ions of ionospheric origin, Geophys. Res. Lett., 5, 59, 1978.

Gloeckler, G., and D. C. Hamilton, AMPTE ion composition results, Phys. Scr., T18, 73, 1987.

Hansen, R. T., S. F. Hansen, and H. G. Loomis, Differential rotation of the solar electron corona, Sol. Phys., 10, 135, 1969.

Hinteregger, H. E., Representations of solar EUV fluxes for aeronomical applications, Adv. Space Res., 1, 39, 1981.

Kamei, T., and H. Maeda, Auroral electrojet indices (AE) for January–June 1978, Data Book 3, World Data Center C2 for Geomagn., Kyoto, Japan, April 1981.

Kremser, G., W. Stüdeman, B. Wilken, G. Gloeckler, D. C. Hamilton, and F. M. Ipavich, Observations of energetic oxygen and carbon ions with charge states between 3 and 6 in the magnetosphere, Ann. Geophys., 6, 325, 1988.

Lennartsson, W., Energetic (0.1–16 keV/e) magnetospheric ion composition at different levels of solar F10.7, J. Geophys. Res., 94, 3600, 1989.

Lennartsson, W., and R. D. Sharp, A comparison of the 0.1–17 keV/e ion composition in the near equatorial magnetosphere between quiet and disturbed conditions, J. Geophys. Res., 87, 6109, 1982.

Lennartsson, W., and E. G. Shelley, Survey of 0.1- to 16-keV/e plasma sheet ion composition, J. Geophys. Res., 91, 3061, 1986.

Lundin, R., B. Hultqvist, N. Pissarenko, and A. Zakharov, The plasma mantle: Composition and other characteristics as ob-

served by means of the Prognoz-7 satellite, Space Sci. Rev., 31, 247, 1982.

Möbius, E., M. Scholer, B. Klecker, D. Hovestadt, G. Gloeckler, and F. M. Ipavich, Acceleration of ions of ionospheric origin in the plasma sheet during substorm activity, in Magnetotail Physics, edited by A. T. Y. Lui, Johns Hopkins University Press, Baltimore, 231, 1987.

Moore, T. E., and D. C. Delcourt, Transport and energization of ionospheric plasma (abstract), EOS Trans. AGU, 73(43), Fall Meeting suppl., 471, 1992.

Mozer, F. S., E. W. Hones, Jr., and J. Birn, Comparison of spherical double probe electric field measurements with plasma bulk flows in plasmas having densities less than 1 cm⁻³, Geophys. Res. Lett., 10, 737, 1983.

Peterson, W. K., R. D. Sharp, E. G. Shelley, and R. G. Johnson, Energetic ion composition of the plasma sheet, J. Geophys. Res., 86, 761, 1981.

Potemra, T. A., L. J. Zanetti, and M. H. Acuña, The AMPTE CCE Magnetic Field Experiment, IEEE Trans. Geosci. Remote Sens., GE-23, 246, 1985.

Press, W. H., B. P. Flannery, S. A. Teukolsky, and W. T. Vetterling, Numerical Recipes, Cambridge University Press, New York, 1986.

Russell, C. T., The ISEE 1 and 2 fluxgate magnetometers, IEEE Trans. Geosci. Electron., GE-16, 239, 1978.

Sharp, R. D., D. L. Carr, W. K. Peterson, and E. G. Shelley, Ion streams in the magnetotail, J. Geophys. Res., 86, 4639, 1981.

Shelley, E. G., R. G. Johnson, and R. D. Sharp, Satellite observations of energetic heavy ions during a geomagnetic storm, J. Geophys. Res., 77, 6104, 1972.

Shelley, E. G., R. D. Sharp, R. G. Johnson, J. Geiss, P. Eberhardt, H. Balsiger, G. Haerendel, and H. Rosenbauer, Plasma composition experiment on ISEE-A, IEEE Trans. Geosci. Electron., GE-16, 266, 1978.

Shelley, E. G., A. Ghielmetti, E. Hertzberg, S. J. Battel, K. Altwegg-Von Burg, and H. Balsiger, The AMPTE CCE Hot Plasma Composition Experiment (HPCE), IEEE Trans. Geosci. Remote Sens., GE-23, 241, 1985.

Singer, H. J., C. T. Russell, M. G. Kivelson, T. A. Fritz, and W. Lennartsson, Satellite observations of the spatial extent and structure of PC 3, 4, 5 pulsations near the magnetospheric equator, Geophys. Res. Lett., 6, 889, 1979.

Strangeway, R. J., and R. G. Johnson, Energetic ion mass composition as observed at near-geosynchronous and low altitudes during the storm period of February 21 and 22, 1979, J. Geophys. Res., 89, 8919, 1984.

Swift, D. W., The role of ionospheric plasma in substorm models (abstract), Eos Trans. AGU, 73(43), Fall Meeting suppl., 472, 1992.

Yau, A. W., E. G. Shelley, W. K. Peterson, and L. Lenchyshyn, Energetic auroral and polar ion outflow at DE 1 altitudes: Magnitude, composition, magnetic activity dependence, and longterm variations, J. Geophys. Res., 90, 8417, 1985.

Young, D. T., H. Balsiger, and J. Geiss, Correlations of magnetospheric ion composition with geomagnetic and solar activity, J. Geophys. Res., 87, 9077, 1982.

D. M. Klumpar, O. W. Lennartsson, J. M. Quinn, and E. G. Shelley, Lockheed Missiles and Space Company, Inc., Research and Development, Dept. 91–20, Bldg. 255, 3251 Hanover Street, Palo Alto, CA 94304.